ISSN 1880-8468

Technical Report of
International Development Engineering

国際開発工学報告

TRIDE-2014-04 June 5, 2014

Abstracts of Master Theses
Presented in February 2014

Department of International Development Engineering,
Graduate School of Science and Engineering,
Tokyo Institute of Technology
http://www.ide.titech.ac.jp/TR

Preface

Master theses of Department of International Development Engineering, Tokyo Institute of Technology were presented successfully on August 5, 2013 and February 13, 2014, respectively. This technical report consists of the abstracts of those theses.

Technical Report of International Development Engineering
TRIDE-2014-03m

Table of Contents

STAKEHOLDERS' PERSPECTIVES ON ADOPTION AND DIFFUSION OF CASBEE IN THE JAPANESE BUILDING MARKET

Student Number: 11M51525 Name: Sheau-Chyng WONG Supervisor: Naoya ABE

CASBEE was developed in 2001 for the promotion of sustainable building practices in Japan. Since then, only limited studies have been conducted to understand the perspectives of CASBEE's stakeholders. In a building market where numerous sustainable building policies and schemes coexist, CASBEE's status and practicality has yet to be validated. This study examined four main aspects – perceptions, motivations, incentives and barriers – towards the adoption and promotion of CASBEE from the project stakeholders' perspectives. Data were collected through surveys administered to CASBEE Accredited Professionals and local governments. The findings show that CASBEE's adoption is limited in the building market and that substantial gaps exist between the perspectives of stakeholders. This study contributes to the policymaking for the Japanese sustainable building market by providing recommendations for the development and implementation of CASBEE.

1 Introduction

Comprehensive Assessment System for Built Environment Efficiency (CASBEE) is a building performance assessment method (green building rating system) originally developed as an architectural design tool in Japan. Since its introduction in 2001, CASBEE's role has expanded into various areas. CASBEE's current key applications in Japan include use by: 1) architects and engineers as a building design tool; 2) local governments for their 'Sustainable Building Reporting System' (SBRS) policy; and 3) building owners or developers as an environmental labeling tool for asset assessment. [3]

Nonetheless, no official studies have previously been conducted to fully understand the perceptions, barriers or motivations towards the adoption and promotion of CASBEE from the perspectives of its direct users i.e., stakeholders. The number of CASBEE-certified buildings has remained small relative to the volume of construction in Japan. This phenomenon could be attributed to the social and psychological barriers within the building industry, which must be overcome in order to bring structural changes throughout the industry [2].

Since 2007, the Japanese central government has introduced a series of green incentive programs to promote 'sustainable buildings', 'energy-efficient buildings', 'low-carbon buildings' and 'long-life quality housing' [1]. The simultaneous operation of these programs, sometimes with overlapping agenda, would conceivably cause confusion in the building market.

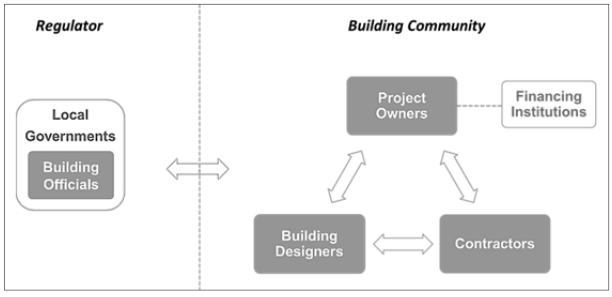

Figure 1 CASBEE's Direct Project Stakeholders
Source: by author.

This study has identified the following groups as the direct project stakeholders of CASBEE: project owners (building owners/developers), building designers (architects/engineers), building contractors and local governments. The core interests of these stakeholders are highly diverse, oftentimes conflicting, and therefore their motives towards sustainable construction and an environmental labeling tool could vary significantly (Figure 1). This study recognizes that the interests of all stakeholder groups must be addressed and aligned before the CASBEE system can be effectively utilized for the promotion of sustainable building practices in Japan.

2 Objectives

The purpose of this study is to examine the direct project stakeholders' perspectives towards the adoption and diffusion of the CASBEE system in the Japanese building market. The following research objectives have therefore been established:

1. To uncover the direct project stakeholders' *perceptions* of CASBEE.
2. To identify the favorable factors (*motivations*, *incentives*) and unfavorable factors (*barriers*) for the adoption and diffusion of CASBEE in the Japanese market from the perspectives of different direct project stakeholders; and to find the gap between the perspectives of these stakeholders and identify the opportunities to bridge the gap.
3. To provide recommendations regarding the development and implementation of CASBEE.

3 Research Design

This study employed a quantitative data collection method to examine the stakeholder's perspectives. First, questionnaire surveys were conducted among the direct project stakeholders of CASBEE. The survey data were then interpreted using a straightforward descriptive analysis based on the frequency results. Finally, Multiple Correspondence Analysis was utilized to further analyze the data and summarize the main characteristics of the data set.

3.1 Questionnaire Surveys

Two separate surveys were conducted in early 2013 to collect feedback from the following groups: 1) local governments currently adopting CASBEE for SBRS purpose; and 2) CASBEE Accredited Professionals (CASBEE-AP) representing the building community. The two main classifications of CASBEE-AP, CASBEE-AP for Building and CASBEE-AP for Detached House, are typically acquired by building professionals from the nonresidential sector and residential sector respectively, and therefore they could be considered representations of the two building sectors. The key survey topics and questions are summarized in Table 1.

Table 1 Key Survey Topics/Items

Topic	Survey Topics/Items
General *(individuals)* *(governments)*	▪ Region of company or government ▪ Job title, professional certification, years of work experience, size of company ▪ Number of support staff in charge of SBRS, and accredited as CASBEE-AP respectively
Sustainable building policies	▪ Tools to promote sustainable building ▪ Influential factors in sustainable building policy
Perceptions	▪ 'Impression of CASBEE' with respect to its benefits for society and business. ▪ 'Level of engagement' with CASBEE measured by its regular use and recommendation of CASBEE in projects
Barriers	▪ Most important barriers to the application of CASBEE standards ▪ Additional time or cost on the design or construction of a CASBEE building ▪ Design experience with CASBEE project in terms of level of difficulty and effort
Motivations	▪ Most important motivations for the application of CASBEE standards
Incentives	▪ Incentives that are most attractive for applying CASBEE standards ▪ Incentives currently offered by local governments

3.2 Exploratory Data Analysis

3.2.1Test of Independence

The Pearson's chi-squared (χ^2) test was used to determine whether significant dependency exists between two variables, e.g., motivation and size of firm. This study considers two variables to be 'significantly dependent' when the *p-value* from the chi-squared test was found to be below 5%.

3.2.2Multiple Correspondence Analysis (MCA)

Multiple Correspondence Analysis is a multivariate analytical method commonly applied to contingency tables to uncover associations between categorical variables. In this study, MCA was applied to the survey data to characterize stakeholder groups with CASBEE's factors (barrier, motivation, incentive and perception); and, to associate this characterization with the descriptive variables (CASBEE accreditation, location, etc.).

4 Results and Discussion

4.1 Survey 1

Questionnaires were mailed to all 24 (sample size) Japanese prefectural or city municipalities that are implementing a CASBEE-based SBRS policy. In total, 23 questionnaires were returned but only 15 of them contain complete, effective answers, yielding an effective survey response rate of 62.5%.

4.2 Findings

The highest numbers of respondents (local governments) are located within the Kansai region (7), Kanto (6) and Chubu (4). Less than half of these governments have one or more CASBEE-AP's, which imply that the CASBEE-based SBRS policy in some jurisdictions may be purely administrative.

As illustrated by Figure 2, to promote sustainable building, local governments most frequently 'provide publicity for green buildings' and 'develop green building policies or regulations'; educational type activities such as 'seminars in green building technology' are much less frequently used. It would later be shown in Survey 2 that the publicity efforts are insufficient to raise awareness of CASBEE among the general public.

As evident in Figure 2, the sustainable building policy of local governments is highly influenced by political factors such as 'central government guidance' and 'comprehensive promotion of sustainable building… and other environmental issues'. They are also guided by the interests of 'the department-in-charge' and 'elected officials', rather than the 'local business leaders' or 'developers/ industry', which may infer a lack of communication between the local governments and their building community.

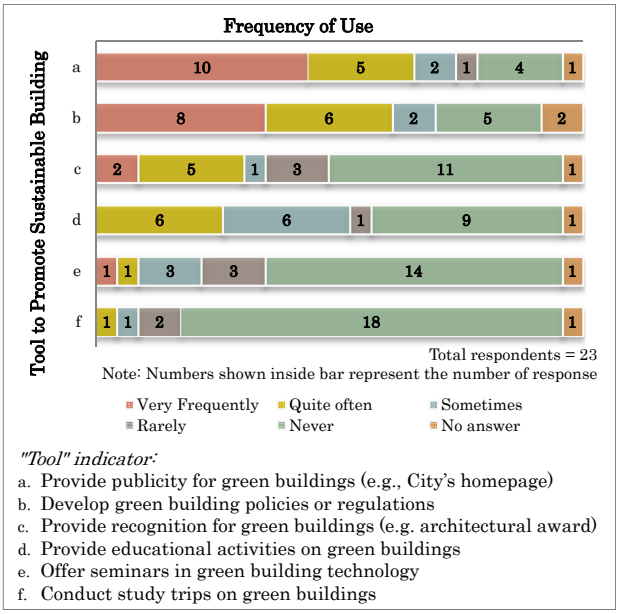

Figure 2 Results on "Tool to Promote Sustainable Building" (Survey 1)

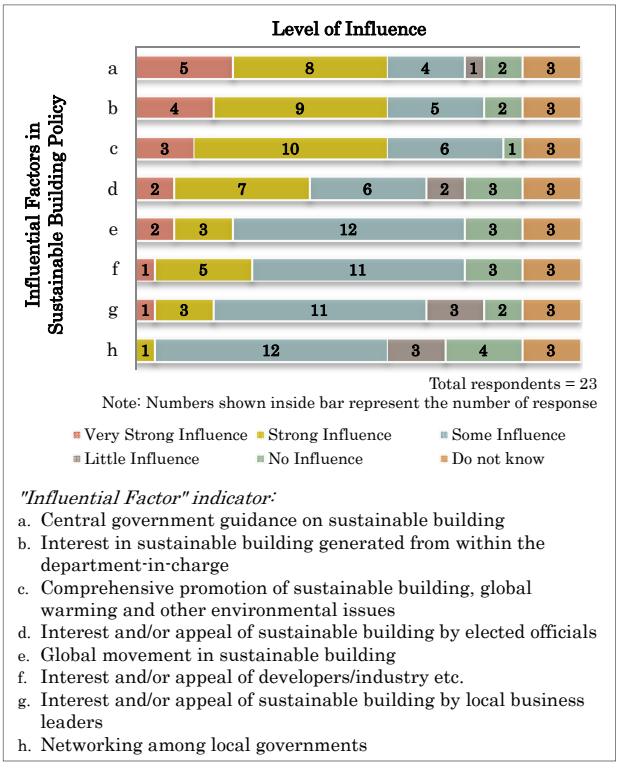

Figure 3 Results on "Influential Factors in Sustainable Building Policy" (Survey 1)

The incentive most frequently offered by the local governments in conjunction with the SBRS program is 'preferential interest rates' (mostly limited to residential buildings), followed by 'recognition for building owners and developers'. Unfortunately, no government is offering 'priority reviews', an incentive most desired by the building community according to survey 2 (Table 3).

4.3 Survey 2

The request to participate in the survey was successfully delivered to 3,921 (sample size) out of the 4,408 email addresses of CASBEE-AP's published on the CASBEE's homepage (as of March 2013). In this email, a link to an online survey site was provided. A total of 440 respondents completed the web questionnaire forms, but only 436 were considered effective, yielding an effective survey response rate of 11%.

The respondents comprised 320 (73%) architects/engineers, 80 (18%) contractors, 12 (3%) building owners and 24 (6%) other professionals. Among all, 243 (56%) are accredited as CASBEE-AP for Building and 267 (61%) as CASBEE-AP for Detached House (dual certification is possible). The highest proportions of respondents work in Kanto (38%), Chubu (22%) and Kansai (14%). The respondents are relatively evenly distributed across firm size, and the majority (54%) has over 20 years of work experience.

4.4 Findings

The results have confirmed that the practical application of CASBEE has been extremely limited in the building market in Japan. About 50% of the respondents indicated that they have no practical experience in using CASBEE. The response patterns on "perceptions" (Figure 4) suggest that although most respondents are motivated to utilize CASBEE in practice conceivable because they believe CASBEE is beneficial for the society, they are not given the opportunities or the right business environment to use CASBEE in practice.

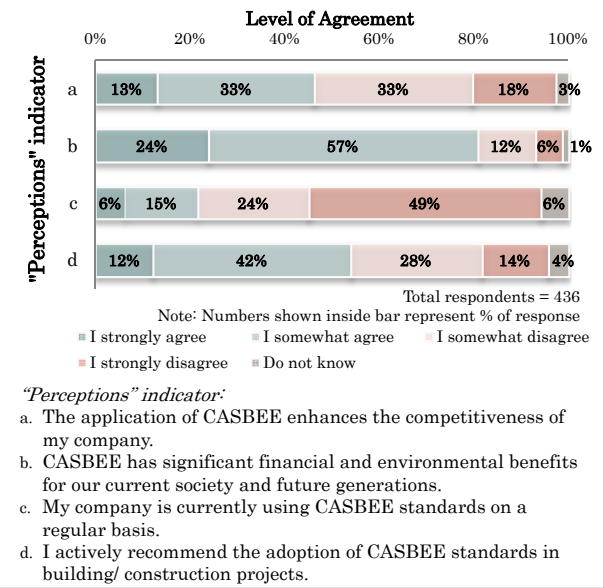

Figure 4 Survey Results on "Perceptions" (Survey 2)

Table 2 shows the ranking results on the top motivations for the CASBEE-AP's to apply CASBEE in their work. It can be observed that the motivations lean towards 'intangible motivations' (promotion of environmental initiatives), rather than tangible rewards or monetary incentives (preferential interest rates etc.). This could be further evidence that the practical application of CASBEE in projects is not supported by the current business environment; it also leads to the speculation that real tangible or monetary benefits of CASBEE buildings have remained absent from the market.

The incentives most desired by the respondents are listed in Table 3. The top three types of incentives ('priority review of CASBEE projects', 'preferential interest rates' and 'financial incentives for building owners') could be regarded as financial or tangible incentives that substantially benefit the project owners rather than the design or construction team. The implicit suggestion is that the adoption of CASBEE, or any 'unconventional innovation' that complicates the building process, must be first and foremost be endorsed by the owners; the right market incentives are needed to motivate the owners to adopt CASBEE in their projects.

Table 2 Ranking Result on "Most Important Motivation"

	Motivation	% Respondents
1	Promotion of environmental initiatives	48
2	Lower building life-cycle or energy costs	12
3	Compliance with local governments' SBRS policy	10
4	Client demand	8
5	Preferential interest rates offered by banks	6
6	Corporate social responsibility (CSR)	5
7	Higher value of green/CASBEE buildings	4
8	Increased longevity of buildings	3
9	Other	2
10	Recognition for buildings	1
11	Financial payback / higher return on investment	1
12	Competitive advantage of CASBEE buildings	0
13	Reduced liability and risk of green/CASBEE buildings	0
13	Help to promote sustainable building market	0

Table 3 Ranking Result on "Most Attractive Incentive"

	Incentive	% Respondents
1	Priority reviews of CASBEE projects	22
2	Preferential interest rates offered by banks	21
3	Financial incentives for building owners, e.g., property tax reduction, subsidy	16
4	Promotion and advertising of CASBEE buildings	10
5	Density bonus for CASBEE building as allowed by local government	9
6	Recognition for building owners and developers	5
7	Financial incentives / rewards for building designers	5
8	Reduction of building permit fees	5
9	Recognition for building designers	4
10	Recognition for builders / contractors	2
11	Other	1

Table 4 Ranking Result on "Most Important Barrier"

	Barrier	% Respondents
1	Lack of public outreach / education / training	24
2	Complexity of certification process	15
3	Complexity of CASBEE certification standards	11
4	Higher upfront construction costs	11
5	Amount of time required for certification	10
6	Lack of certified materials or resources meeting CASBEE standards	7
7	Confusion among different programs/versions of CASBEE	5
8	Learning curve of CASBEE system	5
9	Certification fees	3
9	Lack of demand for green/CASBEE buildings	3
9	Other	3
12	Insufficient incentive for using CASBEE	2
13	Increased liability and risk of green/CASBEE buildings	0

As evident from Table 4, the main challenges of utilizing CASBEE from the building community's perspectives are two-fold. First, insufficient publicity has contributed to lack of awareness of CASBEE among the general public, which explains the low demands for CASBEE projects. Second, the complex nature of the CASBEE system (standards, certification process etc.) inevitably imposes additional time and cost on building owners, designers and contractors. The latter point was further confirmed by a sub-set of survey questions concerning the time and cost burden associated with CASBEE application.

4.5 Discussion

Comparing the two survey results shows that substantial gaps exist between the perspectives of the local governments and those of the building community. In particular, the incentives to

promote CASBEE seem to be misplaced; certain incentives most desired by the building community are not available.

Furthermore, the publicity efforts of CASBEE by the local governments appear to be insufficient or be misdirected, and therefore fell short of raising the awareness among the general public, who constitute the majority of project owners. The aggregate findings may infer a general lack of communication between the local governments and their building community.

5 Exploratory Data Analysis and Interpretations

The χ2-tests have revealed that significant dependency exists between most aspects and CASBEE-AP type and/or region (Table 5). The test results of other descriptive variables, e.g., profession, company size, years of work experience, are not shown but these variables will be included in the discussions if significant associations with any of the factors were found.

Table 5 P-values for χ2-tests between Variables (Survey 2)

	sample size	CASBEE-AP Building	CASBEE-AP Detached House	Region
Perception (a)	436	0.164	0.041**	0.433
Perception (b)	436	0.230	0.122	0.119
Perception (c)	436	0.004***	0.000***	0.296
Perception (d)	436	0.078	0.030**	0.561
Barrier	241	0.079	0.001***	0.739
Motivation	434	0.000***	0.000***	0.009***
Incentive	435	0.000***	0.000***	0.001***

Note: *** indicates p-value <1% significance level; ** indicates p-value <5% significance level.

5.1 Perceptions

The MCA analysis revealed that CASBEE is more positively perceived by CASBEE-AP's for Building (nonresidential sector). Furthermore, the nonresidential sector has higher level of engagement with CASBEE as illustrated in Figure 5.

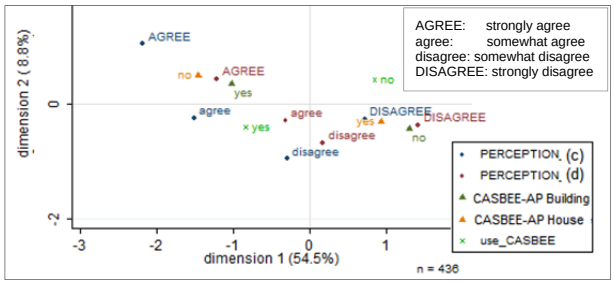

Figure 5 MCA Plot of "Perceptions: Level of Engagement" and "CASBEE-AP Type"

5.2 Motivations

According to the MCA analysis, the top-ranked motivations 'promotion of environmental initiatives' and 'lower building life-cycle or energy costs' tend to be associated with the respondents from relatively small companies in the Chubu and Kanto areas; 'compliance with local government's SBRS' tends to motivate CASBEE-AP's for Building who work for relatively large companies located in Kansai, which have the highest number of local government implementing SBRS.

5.3 Incentives

The MCA results showed that 'preferential interest rates' and 'financial incentives for building owners' tend to be favored by CASBEE-AP's for Detached House. By contrast, 'promotion… of CASBEE buildings' and 'density bonus' are more appealing to CASBEE-AP's for Building. Furthermore, the respondents from different regions have vastly different preferences on incentives (Figure 6).

5.4 Barriers

The MCA results demonstrated that the CASBEE-AP's for Detached House are more strongly affected by 'lack of public outreach/education/training' compared with other barriers. In contrast, CASBEE-AP's for Building consider 'complexity' issues such as 'complexity of certification process' and 'complexity of CASBEE standards' as the bigger obstacles.

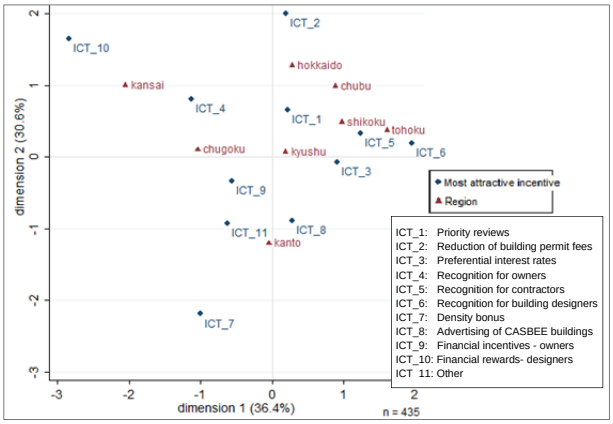

Figure 6 MCA Plot of "Most Attractive Incentive" and "Region"

6 Conclusions and Recommendations

Overall, this study has revealed significant differences in perspectives between building sectors and between regions within the building community. The residential sector holds more negative views of CASBEE and has fewer opportunities to use CASBEE conceivably due to the lack of CASBEE knowledge amongst their clients and the time and cost burden. The regional differences might stem from the varying social, economic and political conditions of regions. The gaps between the perspectives of the local governments and their building community are most evident from the aspects of misplaced incentives and insufficient publicity efforts.

In conclusion, the research points toward the underdevelopment of a favorable business environment for CASBEE's dissemination. It is recommended that promotional efforts to raise public awareness of CASBEE be made priority. The central and local governments should create a mix of incentives that meet regional and sectoral needs, in conjunction with the consolidation and streamlining of the variety of incentive programs that coexist in the building market today to improve the effectiveness of their sustainable building policies.

7 Limitations and Future Research

By studying CASBEE's adoption and diffusion from the perspectives of its direct project stakeholders, this study has gained valuable yet partial insights into sustainable building market in Japan. In particular, the perspectives of the project owners' group could not be adequately clarified due to its small sample size. Future studies should extend the present findings by exploring the project owners' perspectives or the regional and sectoral differences in sustainable building practice. Examinations of aspects such as level of public interest in green building and levels of bureaucracy in the development of green building policy may also provide comprehensive evaluation of sustainable building schemes in Japan from both regulatory and voluntary aspects.

References

[1] Hashimoto, K. (2013). Status and Prospect of the Policy on Housing and Building toward Low-carbon Society. Keynote session of 3rd Eco House & Eco Building Expo. Tokyo, Japan.

[2] Hoffman, A. J., & Henn, R. (2008, December). Overcoming the Social Barriers and Psychological Barriers to Green Building. Organization & Environment, 21(4), 390-419.

[3] Japan GreenBuild Council / Japan Sustainable Building Consortium. http://www.ibec.or.jp/CASBEE/index.htm.

Lifetime Cost Reduction Study of A Ground Source Heat Pump System in Mongolia

Student Number: 11M51258 Name: Dagva Byambatuya Supervisor: Abe Naoya

This study aimed at quantifying the lifetime cost reduction of Ground Source Heat Pump (GSHP) system by focusing on an actual installed system in Mongolia. The comparison between a recently built GSHP system and a typical traditional heat generating system, which utilizes coal, a main source of air pollutants extensively, is thoroughly conducted to identify the critical risk factor in terms of the change of the total present value of the lifetime cost reduction. The study is supposed to be a reference case for further investors and policy makers of the technology application in the country.

1. Introduction

Ulaanbaatar (UB) is the coldest capital city in the world. In Mongolian harsh winter, the air pollution in UB gets distinctly worse mainly because of fossil fueled space heat production by such as simple household ger[1] stoves, heat only boilers (HOB), and thermal power plant etc. Because of the air pollution in UB, 1600 people die every year and the levels of premature death, chronic bronchitis, and cardiovascular diseases are increasing rapidly as World Health Organization identified. Therefore, Mongolia needs to promote more efficient and greener technologies to produce heat for reducing the air pollution. One of the best solutions can be using Ground Source Heat Pump (GSHP) technology for space heating to overcome extremely harsh winter in UB.

GSHP uses the earth as a heat source for heating or as a heat sink for cooling, depending on the season (Figure1). This characteristic has made it possible for all countries to use the heat of the earth for heating and/or cooling, as proper. The required energy amount to run a GSHP system, which is mainly certain amount of electricity to run a pump for fluid circulation, is from one-third to one-fifth the required energy amount transported from a lower temperature level to a higher one (John, 2011). Thus the technology allows us to reduce consumption of fossil fuels (coal), protect valuable natural resources, lower emissions and get economic efficiency.

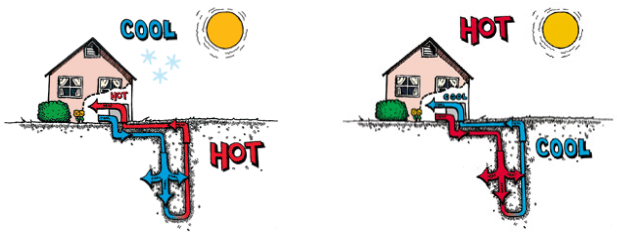

Figure1. GSHP system operations
(Source: IGSHPA, 2013)

[1] Ger is a circular domed Mongolian tradition dwelling that is portable and self-supporting.

GSHPs are now the fastest growing application of direct geothermal energy use, with about 3 million GSHP installed units globally at the start of 2010 (IEA 2010). GSHPs have faced an enormous market development in some European countries during the last years as shown in Figure 2.

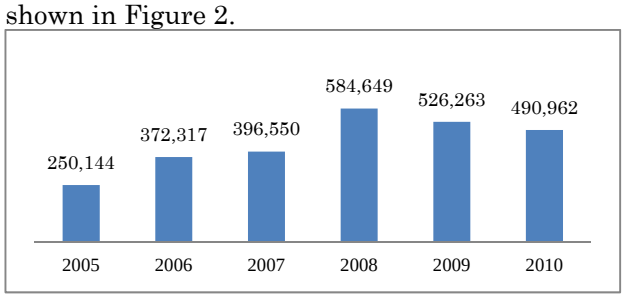

Figure2. Development of GSHP sales numbers in Europe (Austria, Finland, Denmark, Italy, Norway, Sweden, Czech, and United Kingdom)
Source: (Dumas, 2011)

The number of installed GSHP in Japan has started to increase about a decade ago (Figure3). The total number of GSHP has reached 990 for the heating and cooling system and for the snow melting system by the beginning of the year 2013 (Ministry of Environment of Japan, 2013).

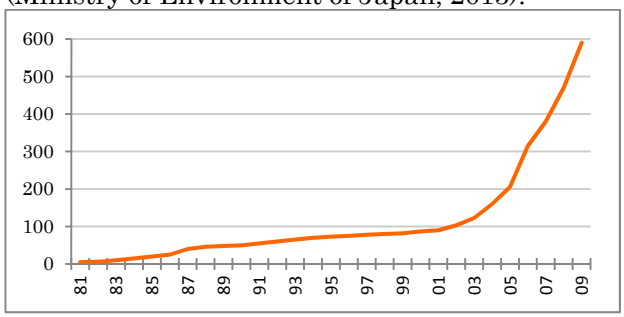

Figure3. GSHP cumulative increases, Japan
(Source: Geo Heat Promotion Association of Japan, 2013)

The National Renewable Energy Centre (NREC) of Mongolia, a state owned enterprise, has already initiated in implementing a pilot project on GSHPs using government funding. This study is focusing on a kindergarten GSHP system implemented as the pilot project.

2. Objectives of the study

The main goal of this study is to quantify the lifetime cost reduction of GSHP system in Mongolia and provide a reference case for further investors and policy makers of the technology application in the country. The GSHP system at the "Ireedui" Kindergarten of "Tuv" province near UB is analyzed as a case study in comparison with the previous heating solution, heat only boiler (HOB), in this study.

Having reviewed the current state of GSHP in various countries, including in Mongolia, the objectives of the study are set as:

1) To estimate present values of lifetime cost reduction (PV-LCR) by the adoption of GSHP for 12-year, 13-year, 14-year, 15-year, 20-year, 25-year and 30-year lifetime respectively by comparing present values of lifetime costs (PV-LC) of HOB and GSHP system for the respective lifetimes.

2) To determine the payback period[2] of the GSHP system done by its operational cost saving.

3) To identify the most sensitive cost variables on PV-LCR of the GSHP system through sensitivity analysis and to determine the riskiest variable causing uncertainty on PV-LCR of the GSHP system.

4) To identify perspective of the users of the GSHP system.

3. Data collection

A site survey was conducted in April, 2013 in UB and Tuv Province, Mongolia aiming to get all the qualitative and quantitative information used for the study. The main approach of the survey was interviewing with professionals and officials at various organizations and site visit.

The main data of initial investment, electricity usage (for operation cost estimation), and maintenance of the GSHP system were provided by NREC. The data in regards of the previous heating solution, HOB, cost was provided by the "Ireedui" kindergarten. Assumption input for conducting risk analysis (explained in Data analysis) ideas of the GSHP adoption were obtained through the survey.

Major cost of initial investment of the GSHP system was spent for drilling (36%) and materials purchase (39%) (Figure4).

Perception of the GSHP system by the users was identified by individual interviews at the kindergarten. The satisfaction level of the users was high (with mean score 4.8 out of 5) and their attitude toward the existing system was positive mainly because of its reliable operation, low operation cost, and convenient (constant) indoor temperature.

[2] Payback period refers to the year when initial investment cost of GSHP recovered by PV-LCR at this study.

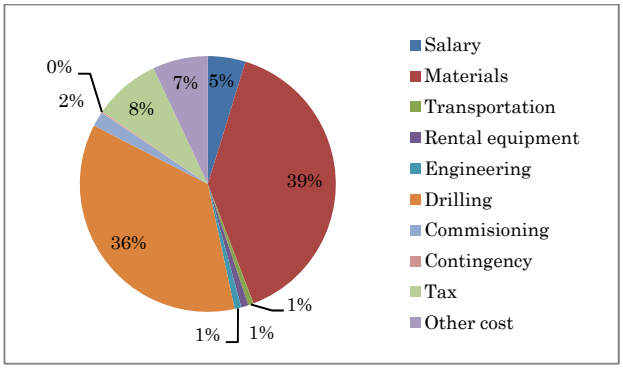

Figure4. Share of percentage of each cost of initial investment. Note: Raw data provided by NREC

4. Data analysis

The financial analysis was implemented by developing discounted cash flow (DCF) model at the MS-Excel software. A typical DCF model for a potential investment makes forecasts of costs and revenues over the life of the project and discounts those back to present values.

$$NPV(r) = \sum_{i=0}^{n} \frac{\overline{F_i}}{(1+r)^{i-1}}$$

F_i - Expected values of net cash flows in each period; r - Discount rate

In this study, only lifetime costs both for before (HOB) and after (GSHP) case were forecasted and the values were discounted to present values because there is no substantial revenue for the owner. Lifetime cost of HOB includes only heating service charge paid by the kindergarten. Lifetime cost of GSHP includes its initial investment, operation and maintenance costs. Present value of life time cost of HOB is denoted as PV-LC-Before and present value of lifetime cost of GSHP is denoted as PV-LC-After respectively. Afterwards by comparing the PV-LC-Before and PV-LC-After, estimated present value life time cost reduction (PV-LCR) becomes the main focus in this study.

After the financial analysis, sensitivity analysis was carried out, which is the first step to conduct risk analysis. In order to conduct the sensitivity analysis all the cost variables that are significant to the outcome of the project, PV-LCR, were tested. The variables that have great impacts on the PV-LCR were identified as materials and drilling cost (Figure5). Appropriate probability distribution and likely range of values were assigned to the two variables based on either past data or experts' opinions (Table2.) to determine the most crucial variables on PV-LCR. Monte Carlo simulation was used to generate a probability distribution of the outcome, PV-LCR, through the help of Crystal Ball™ with 1,000 trials.

Table2. Probability distribution (triangular) assumption made for material and drilling cost

Material cost	Min	$105,411
	Likeliest	$147,575
	Max	$189,739
Drilling cost	Min	$67,463
	Likeliest	$134,926
	Max	$269,852

5. Results

Financial analysis: Present values of lifetime cost were calculated for 12-year, 13-year, 14-year, 15-year, 20-year, 25-year and 30-year separately both for GSHP (PV-LC-Before) and HOB (PV-LC-After) to make comparison of them. GSHP system is expensive to install but it has considerably lower operating and maintenance costs than that of conventional HOB system. For this reason it can do saving (PV-LCR) by its extremely low operation cost (Table3.).

Table3. PV-LC-before and after; PV-LCR

	PV-LC-Before (A)	PV-LC-After (B)	PV-LCR (C)=(B)-(A)
12-year	$ -435,241	$ -429,807	$5,434
13-year	$ -491,482	$ -436,073	$55,409
14-year	$ -551,935	$ -442,604	$109,331
15-year	$ -616,918	$ -449,415	$167,503
20-year	$ -1,022,564	$ -488,068	$534,495
25-year	$ -1,604,679	$ -535,680	$1,068,999
30-year	$ -2,440,034	$ -594,326	$1,845,708

Sensitivity analysis: Six cost parameters such as cost for salary of construction workers, material, rental equipment utilization (Rental), drilling, electricity usage, and maintenance (Maint) were tested. To compare the all six different costs, elasticity of them are calculated and presented in Figure5. The most sensitive variables are material and drilling cost.

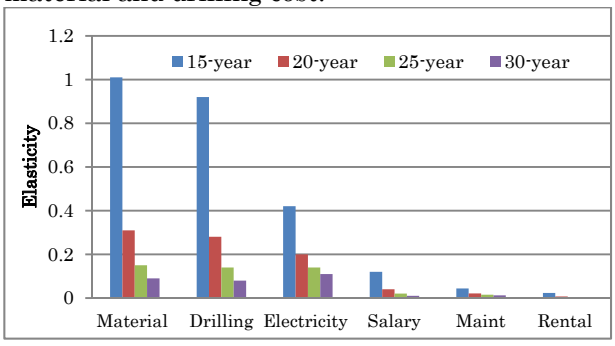

Figure5. Elasticity of costs on PV-LCR

Monte Carlo Simulation: After identifying the most sensitive variables, the probability distributions (Table2) were assigned. Then PV-LCR forecast distributions were generated for 12-year, 13-year, 14-year, 15-year, 20-year, 25-year, and 30-year lifetime by Monte Carlo simulation @Crystal ball software. Forecasted PV-LCR distributions for 12-year and 30-year lifetime are illustrated in Figures8 and 9 as examples. All the result of the simulation is summarized in Table5 and its values are illustrated in Figure6.

Table5. PV-LCR for the seven different lifetimes

PV-LCR / Life-time	At the base DCF model	Mean (after Monte Carlo simulation)	Minimum (after Monte Carlo simulation)	Maximum (after Monte Carlo simulation)
12-year	$5,434	$ -21,054	$ -152,010	$109,056
13-year	$55,409	$28,922	$ -102,034	$159,031
14-year	$109,331	$82,844	$ -48,112	$212,953
15-year	$167,503	$141,016	$10,060	$271,125
20-year	$534,495	$508,008	$377,052	$638,117
25-year	$1,068,999	$1,042,511	$911,555	$1,172,621
30-year	$1,845,708	$1,819,221	$1,688,265	$1,949,330

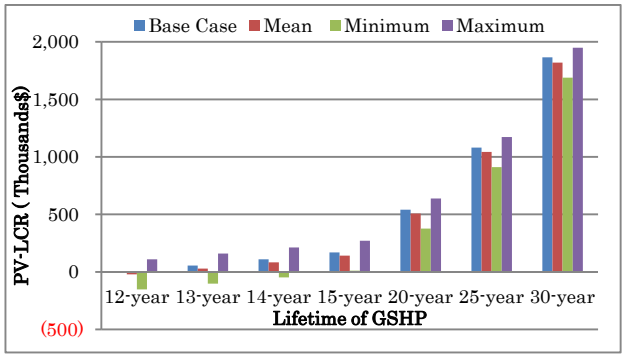

Figure6. PV-LCR for the seven different lifetimes

The probabilities that PV-LCR will be more than "Zero" for 12-year, 13-year, 14-year, 15-year, 20-year, 25-year and 30-year lifetimes are shown in Table4.

Table4. Probability of PV-LCR to be more than "Zero"

Lifetime (year)	12	13	14	15	20	25	30
Probability (%)	37	72	94	100	100	100	100

After the simulation, material and drilling cost contribution shares on PV-LCR variance were found 86.7% for drilling cost and 13.3% for material cost (Figure7).

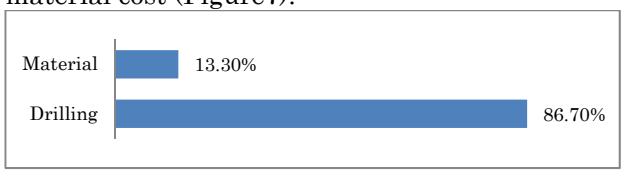

Figure7. Material and drilling cost contributions for the variance on PV-LCR

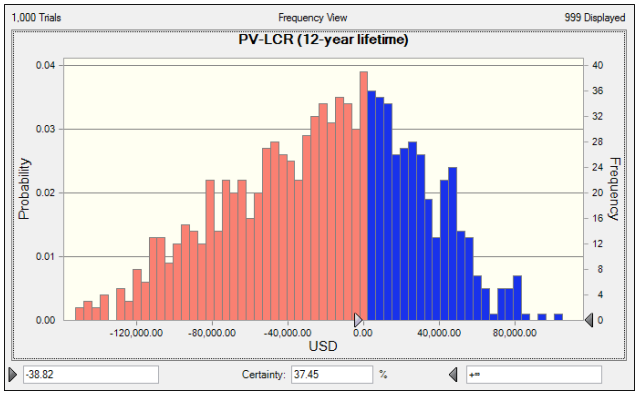

Figure 8. PV-LCR distribution for 12-year of lifetime

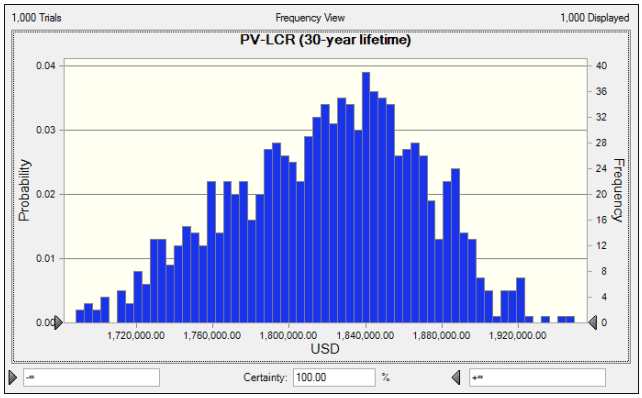

Figure 9. PV-LCR distribution for 30-year of lifetime

6. Conclusions

1) PV-LCR values are quantified for lifetimes of 12-year, 13-year, 14-year, 15-year, 20-year, 25-year and 30-year of the GSHP system; include base DCF model results and its mean, minimum, and maximum values after Monte Carlo simulation as presented in Table5. The general trend is PV-LCR increases distinctively if life time of the GSHP increases (Figure6). At the base DCF model, PV-LCR becomes positive at the 12th-year of operation as \$5,434. After conducting the Monte Carlo simulation, the mean value of PV-LCR becomes positive starting from 13th-year as \$28,922 and the minimum value of PV-LCR becomes positive from 15th-year of operation as \$10,060.

2) The certainty of PV-LCR can be more that "zero" is 37% at the 12th-year, 72% at the 13th-year, 94% at the 14th-year and more than 100% from the 15th-year of the operation (Table4). The minimum value of PV-LCR is \$ -48,112 at the 14th year and \$10,060 at the 15th year becoming positive value (Table5). Thus the payback period done by its operational cost saving is 15 years. To make sure to have positive PV-LCR, the system needs to last more than 15 years.

3) According to the sensitivity analysis, the most sensitive variables are material and drilling cost. As a result of conducting risk analysis (after Monte Carlo simulation), drilling cost is the riskiest variable sharing 86.7% of sensitivity (Figure7); thus it is capable of causing high uncertainty on PV-LCR.

4) It is assumed that GSHP is suitable for Mongolia technologically because the pilot project has been working properly since its commissioning in 2010 as identified by the site survey. The regular user's attitude at the kindergarten building toward the existing GSHP system was quite positive mainly because of its reliable operation, low operation cost, and convenient (constant) indoor temperature.

Recommendations: Lifetime of a GSHP system is extremely important and should be maximized. If lifetime of the GSHP increases, elasticity of each cost on PV-LCR reduces (Figure5) and PV-LCR increases distinctively (Figure6). Considering lifetime and performance of a GSHP depends greatly on designing and installation (early stage works), they have to be done at high quality. The cost of a GSHP installation is very important; however, the more important concern relates to the quality of the design and installation. A low-cost designing and installation might not be a better choice except it can perform well over a long time. Drilling cost highly depends on soil physical properties (texture, density, porosity etc.) and weather (season). Thus physical properties of soil need to be investigated in advance and drilling work should be planned appropriately in a proper period of time (season) of a year.

Areas for further study: More improved input assumptions for more variables for the Monte Carlo simulation should be developed. Assessments concerning various aspects such as health and environmental impact of GSHP adoptions were not performed in this study. It is highly recommended to perform an economic analysis covering various aspects as above to determine the impacts of GSHP technology if widely adopted since the technology has other impacts besides operational cost savings. It will require comprehensive and systematic approach. An extensive study titled "Air Quality Analysis of Ulaanbaatar", which can be one of the useful references for the further recommended analysis, was conducted by The World Bank in 2011.

References

John, S., 2011. *Residential Geothermal Systems, Heating And Cooling Using The Ground Below*. 2nd ed. New York.

IEA, 2010. *Renewable Energy Essentials: Geothermal*. International Energy Agency.

Dumas, P., 2011. *Increasing deployment of GSHP in Europe - market, incentives, regulations - and savings*. Presentation Material. Brussels, Belguim: European Geothermal Energy Council.

IGSHPA, 2013. [Online] Available at: http://www.igshpa.okstate.edu/geothermal/ [January 2013].

ECO-EFFICIENT MODAL SPLIT OF INTERREGIONAL FREIGHT TRANSPORT IN GMS

Student Number: 11M18060 Name: Tomoaki Kato Supervisor: Shinya Hanaoka

大メコン圏の地域間貨物輸送における環境を考慮した機関分担率の算出

加藤　智明

本研究では、大メコン圏の地域間貨物輸送を対象に、輸送費用、輸送時間、二酸化炭素排出量を目的関数とし、機関分担率を決定変数とする目標計画問題を定式化した。バンコクーハノイとバンコクーヤンゴンの 2 つの路線をケーススタディとして、既存輸送機関の改善と貨物鉄道新規建設の 2 つの開発シナリオと、目的関数の削減目標値を設定し、目標に対する最適な機関分担率の算出を行った。その結果、路線や削減項目、削減目標ごとの最適機関分担率の傾向や差異が定量的に明らかになった。具体的には、バンコクーヤンゴン路線では、輸送距離が著しく長いために海上輸送距離の優位性が低く、トラック輸送や鉄道輸送の分担率が相対的に高いこと、また、両路線共、時間と排出量の同時削減を目指す場合には鉄道輸送が高い分担率を担うことが望ましいことなどが示された。

1. Introduction

Nearly 40% of greenhouse gas emissions, which are perceived as the causes of the climate change, originated from Asian region. Transport sector occupied over 20% of the world total CO_2 emissions and was the second most emitting sector following electricity and heat. Therefore it is our great challenge to establish low-carbon transport system which is one of main components of Low carbon Asia [1].

For interregional transport, strategies to realize low-carbon transport system are classified into three: AVOID, SHIFT and IMPROVE [1]. The present study is focused on SHIFT, which is the shift to lower emission transport modes such as water or railway transport. Modal split expresses the share taken by each transport mode and is an important indicator of SHIFT. But few studies have attempted a quantitative discussion of optimal modal split despite the fact that many previous studies pointed out the significance of water or railway intermodal transport. Therefore it is required to set modal split targets as one of indicators of modal shift.

The study area, Greater Mekong Subregion (GMS), is currently at a crucial stage of the modal shift of its interregional freight transport. The first reason is a dramatic growth of regional freight demands driven by the economic growth in this region. Secondary this region has been putting considerable resources into the development of the major economic corridors such as East-West Corridor, North-South Corridor, and Southern Corridor. Consequently the hard infrastructure for truck transport in this region has been substantially improved compared to before. Thirdly not only the hard infrastructure but also soft infrastructure has been being developed. All GMS countries signed Cross Border Trade Agreement with the intension to promote smoother movement of people and goods crossing the borders. Mainly these three important changes of situation are expected to cause freight modal shift from maritime transport, which has been dominating interregional freight transport in GMS, to truck transport. Truck transport has substantial advantages over other transport modes in terms of logistics performance such as lead time, flexibility and frequency. From the viewpoint of environmental impact, however, its emission factor is far larger than those of other modes. Therefore it is important to present the vision of eco-efficient modal split based on backcasting approach, which stands for drawing a pathway from a desirable future to present, not like forecasting.

Against this background, the objectives of this study are set as follows.

1) To formulate the model of interregional freight modal split to reflect logistics performances and environmental impacts.
2) To calculate optimal modal splits in GMS based on several scenarios regarding transport modes and reduction targets of cost, time and emissions by using goal programming.

2. Methodology

2.1 Freight demand and mode of focus

This study examines three transport modes: maritime-truck intermodal, truck only and railway-truck intermodal. Intermodal transports are the combination of main transport (line-haul transport) such as vessels or railways and truck transport connecting between origins/destinations and terminals (pre/post-haulage transport) In GMS, railway intermodal transport is hardly used for interregional freight transport at the moment. But in long term, there is a possibility of new railway construction. Therefore it is worthwhile to take into account hypothetical railways.

Regarding freight demand of focus, cargoes which is transported in standardized containers for distance of over 500km is of interest because some previous studies have revealed that such freight demand is adaptable to modal shift [2].

2.2 Case study routes

(1) Bangkok – Hanoi route

With the opening of the Second Thai – Lao Friendship Bridge in 2006, truck transport from Bangkok to Hanoi via East-west corridor is available. Maritime-truck intermodal transport, however, is predominant on this route. It ships from Bangkok city to Laem Chabang Port by truck. The cargo will reach Hai Phong Port, which is approximately 100km away from Hanoi after transshipment at Ho Chi Minh Port. Railway transport route is a hypothetical route and it's not fully connected at the moment.

(2) Bangkok – Yangon route

Trucks go north up to Tak and reach Yangon via western section of East-west corridor. Even though the land transport route is much shorter in distance than maritime transport, some sections in Myanmar still have very poor road condition. Therefore maritime route, which is a roundabout by Strait of Malacca, deals with almost all of freight demands. The railway route is also a hypothetical route.

2.3 Modal split calculation

Calculation of modal split is shown in figure 1 in the next page. The procedure is divided into two stages: baseline analysis and estimation of optimal modal split using goal programming approach.

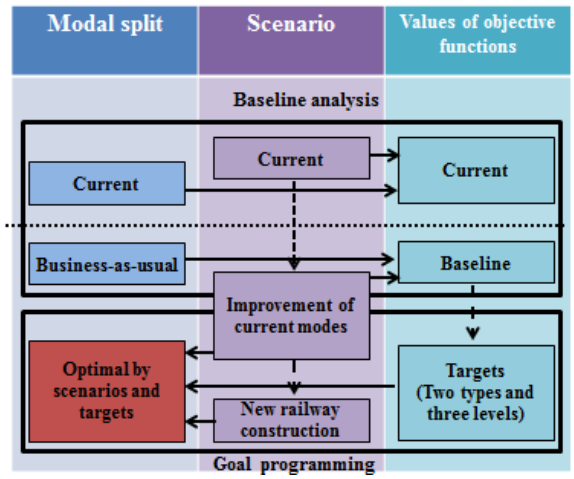

Figure 1 Flow of modal split calculation

2.4 Scenario building

This study estimates several different optimal modal splits depending on scenarios and targets. Two types of scenarios regarding transport modes are built to determine the model inputs. Those are (i) improvement of existing modes, and (ii) new construction of freight railway in addition to the improvement of existing modes.

Improvement of existing modes specifically assumes following situations:

1. Improvement of road conditions such as improved pavement and multiple lanes
2. Facilitations for night driving
3. Free entrance of foreign-registered vehicles
4. Single window/stop
5. Improvement of terminal operation efficiency
6. Rerouting of maritime transport

Since railway transport routes are hypothetical, some of inputs are based on similar examples in other countries.

2.5 Formulation of objective functions

Following three objective functions are taken into account as indicators of logistics performance and environmental efficiency. Formulations were done by reference to Hanaoka et al (2011) [3].

(a) Transport cost

$$f_1 = \sum_i s_i (Cm_i \times dm_i + tc_i + pc_i + Cae_i \times dae_i) \quad (1)$$

$$\sum_i s_i = 1 \quad (2)$$

$$s_i \geq 0 \quad (3)$$

i : transport mode (1:maritime-truck intermodal, 2: truck only, and 3: railway-truck intermodal)

s_i : modal split of mode i

Cm_i : line-haul transport cost of mode i (USD/ton-cargo*km)

dm_i : line-haul transport distance of mode i (km)

tc_i : terminal operation cost of mode i (USD/ton-cargo)

pc_i : custom processing cost of mode i (USD/ton-cargo)

Cae_i : pre/post-haulage transport cost of mode i (USD/ton-cargo*km)

dae_i : pre/post-haulage transport distance of mode i (km)

(b) Transport time

$$f_2 = \sum_i s_i \left(\frac{dm_i}{vm_i} \times \frac{1}{cm_i} + tt_i + pt_i + \frac{dae_i}{vae_i} \times \frac{1}{cae_i} \right) \quad (4)$$

$$\sum_i s_i = 1 \quad (5)$$

$$s_i \geq 0 \quad (6)$$

i : transport mode (1:maritime-truck intermodal, 2: truck only, and 3: railway-truck intermodal)

s_i : modal split of mode i

vm_i : line-haul transport velocity of mode i (km/hr)

dm_i : line-haul transport distance of mode i (km)

cm_i : line-haul transport capacity of mode i (ton-cargo)

tt_i : terminal operation time of mode i (hrs/ton-cargo)

pt_i : custom processing time of mode i (hrs/ton-cargo)

vae_i : pre/post-haulage transport velocity of mode i (km/hr)

dae_i : pre/post-haulage transport distance of mode I (km)

cae_i : pre/post-haulage transport capacity of mode i (ton-cargo)

(c) CO_2 emission

$$f_3 = \sum_i s_i (\mu m_i \times dm_i + \mu t_i + \mu ae_i \times dae_i) \quad (7)$$

$$\sum_i s_i = 1 \quad (8)$$

$$s_i \geq 0 \quad (9)$$

i : transport mode (1:maritime-truck intermodal, 2: truck only, and 3: railway-truck intermodal)

s_i : modal split of mode i

μm_i : emission factor of line-haul transport of mode i (kg-CO_2/ton-cargo*km)

dm_i : line-haul transport distance of mode i (km)

μt_i : emission factor of terminal operation of mode i (kg-CO_2/ton-cargo)

μae_i : emission factor of pre/post-haulage transport of mode i (kg-CO_2/ton-cargo*km)

dae_i : pre/post-haulage transport distance of mode i (km)

2.6 Goal programming

Goal programming is a special form of linear programming in which multiple and conflicting objectives are expressed as constraints. As each of these objectives has a goal or target value to be achieved, unwanted deviations from this set of target values are then minimized in a regret function [4]. Goal programming problems of this study is formulated as below. Three objective functions presented above are converted into constraints. Modal split s_i and all the deviations are decision variables. The regret function to be minimized in this problem is expressed as the sum of squared "degree of unsatisfaction" (defined as over-attainments divided by target values) of each indicator. LINGO 14.0, a comprehensive mathematical calculation tool, is used for solving the goal programming problem.

$$\min R = \left(\frac{d_c^+}{T_c}\right)^2 + \left(\frac{d_t^+}{T_t}\right)^2 + \left(\frac{d_e^+}{T_e}\right)^2 \quad (10)$$

s.t.

$$\sum_i s_i\left(Cm_i \times dm_i + tc_i + pc_i + Cae_i \times dae_i\right) + d_c^- - d_c^+ = T_c \quad (11)$$

$$\sum_i s_i\left(\frac{dm_i}{vm_i} \times \frac{1}{cm_i} + tt_i + pt_i + \frac{dae_i}{vae_i} \times \frac{1}{cae_i}\right) + d_t^- - d_t^+ = T_t \quad (12)$$

$$\sum_i s_i\left(\mu m_i \times dm_i + \mu t_i + \mu ae_i \times dae_i\right) + d_e^- - d_e^+ = T_e \quad (13)$$

$$d_c^- \times d_c^+ = 0 \quad (14)$$

$$d_t^- \times d_t^+ = 0 \quad (15)$$

$$d_e^- \times d_e^+ = 0 \quad (16)$$

$$\sum_i s_i = 1 \quad (17)$$

$$d_c^-, d_c^+, d_t^-, d_t^+, d_e^-, d_e^+, s_i \geq 0 \quad (18)$$

T_c : target value of transport cost (USD/ton-cargo)

T_t : target value of transport time (hrs/ton-cargo)

T_e : target value of CO_2 emission (kg-CO_2/ton-cargo)

d_c^- : over-attainment of transport cost (USD/ton-cargo)

d_c^+ : under-attainment of transport cost (USD/ton-cargo)

d_t^- : over-attainment of transport time (hrs/ton-cargo)

d_t^+ : under-attainment of transport time (hrs/ton-cargo)

d_e^- : over-attainment of CO_2 emission (kg-CO_2/ton-cargo)

d_e^+ : under-attainment of CO_2 emission (kg-CO_2/ton-cargo)

2.7 Target setting

Since target values of the goal programming problem are given values, target setting done based on the baseline. Two ways of target setting are attempted, which are (a) reduction of cost and emission, and (b) reduction of time and emission. In order to observe the difference by reduction levels, three levels of reduction are set respectively. The details of the reduction levels are shown below.

Table 1 Level of cost and CO_2 emission reduction

	Cost	Time	Emission
Level 1	10% down	Baseline	10% down
Level 2	20% down	10% up	20% down
Level 3	25% down	20% up	40% down

Table 2 Level of time and CO_2 emission reduction

	Cost	Time	Emission
Level 1	Baseline	10% down	10% down
Level 2	10% up	20% down	20% down
Level 3	20% up	35% down	40% down

3. Results and discussion

3.1 Inputs

Three input sets according to the built scenarios are prepared for each case study. The values are determined based on the surveys of JETRO and some other literature reviews. Presentation of specific values of inputs is omitted here due to the limitation of space.

3.2 Baseline analysis

As for Bangkok – Hanoi route, current modal split are assumed as 95% for maritime transport and 5% for truck transport. Predicted modal split used in the baseline scenario is determined as 67.3% for maritime transport and 32.7% for truck transport by reference to the example of Japan.

It is assumed as the current modal split on Bangkok – Yangon route is fully occupied by maritime transport. Similarly to Hanoi route, predicted modal split is determined as 53.4% for maritime transport and 46.6% for truck transport by reference to the example of Japan.

The table 3 and 4 compare values of the objective functions in current status and baseline scenario.

Table 3 Current and baseline scenario (Hanoi route)

	Transport cost (USD/ton-cargo)	Transport time (hrs/ton-cargo)	CO_2 emissions (kg-CO_2/ton-cargo)
Current status	116.06	11.32	52.99
Baseline scenario	113.44	4.94	82.3
Rate of change	-2.26%	-56.35%	+55.3%

Table 4 Current and baseline scenario (Yangon route)

	Transport cost (USD/ton-cargo)	Transport time (hrs/ton-cargo)	CO_2 emissions (kg-CO_2/ton-cargo)
Current status	137.77	7.46	53.75
Baseline scenario	157.37	4.34	71.11
Rate of change	+14.23%	-41.77%	+32.29%

For Bangkok – Hanoi route, the baseline is slightly lower in cost, considerably lower in time and considerably higher in emission compared to the current status. Despite the increase of share of truck transport, which is more expensive mode, cost slightly decreases probably because cost of both transport modes are substantially reduced by the infrastructure improvement. Particularly the effect of maritime rerouting is influential. For Bangkok – Yangon route, comparison between the current status and the baseline shows different trend in cost from Bangkok – Hanoi route mainly because of remarkable increase of truck transport share.

3.3 Optimal modal splits

The optimal modal splits are calculated by the scenarios, targets and routes. The results are shown in the figure 2 in the next page. Since not all targets are achieved, the degrees of unsatisfaction are also shown in figure 3 in the next page. 50% of unsatisaction, for example, means that the actual value is 1.5 times greater than the target value. The degree of unsatisfaction is shown as 0 if the target is achieved or lower than the target.

When the reduction of cost and CO_2 emission is aimed, the results of optimal modal splits in (i) improvement of existing modes scenarios are consistent with the expectation. That is, the higher the reduction level the larger share of maritime transport. On the other hand, the shares of truck transport remain relatively high for time and emission reduction targets, but the targets are not well achieved. In (ii) new rail construction scenario, the share of truck transport is substituted by railway transport and the achievements are improved. A remarkable difference can be observed in the trends of railway share between reductions targets. The railway share increases as the reduction level goes higher in time and emission reduction.

The share of truck transport is fairly high in case of time and emission reduction, while the trend is similar to that of Bangkok – Hanoi route when the reduction of cost and CO_2 emission is aimed. The change in share is very small even if the reduction targets go higher. In

(ii) new rail construction scenario, and the highest reduction levels, the modal share was occupied by two modes, those are truck and railway in time and emission reduction case, and maritime and railway in cost and emission reduction case. In lower targets, on the other hand, no mode has little shares. Comparing to Bangkok – Hanoi route, the maritime transport generally occupies smaller shares. This implies that the maritime transport holds relatively weak advantage over the land transport modes due to its much longer transport distance.

As an overall trend, achievements of time and emission reduction targets are worse than those of cost and emission reduction targets. That is because time and emission are often in the relationship of trade-off. This study quantitatively reveals the efficiency of the new railway construction.

4. Conclusion

In this study, interregional freight modal split in GMS was formulated as a goal programming problem which aimed to achieve the targets of transport cost, transport time and CO_2 emission in order to calculate eco-efficient modal split. Two case study routes, Bangkok – Hanoi and Bangkok – Yangon, were examined by the scenarios and targets. As a result, the optimal modal splits for respective scenarios, targets and routes were calculated and the trends and differences between them were also revealed. More specifically, on Bangkok – Yangon route, maritime transport holds relatively weak advantage over the land transport modes due to its much longer transport distance. The results also implied the efficiency of the new railway construction on the both case study routes particularly when .the reduction of time and CO_2 emission is aimed.

References

[1]Hayashi, Y. and Nakamura, K.: Climate change, mobility and cost of transport, Transport Policy, 2013.

[2] 高橋宏直：モーダルシフト化率の推計方法と動向分析、国土技術総合研究所資料、No. 407、2007.

[3] Hanaoka, S. et al.: Measurement of energy-saving effect by intermodal freight transport in Thailand, World Review of Intermodal Transportation Research, Vol.3, No.4, pp.320-337, 2011.

[4] Yang, X. et al: Analysis of intermodal freight from China to Indian Ocean: A goal programming approach, Journal of Transport Geography, Vol.19, pp.515-527, 2011.

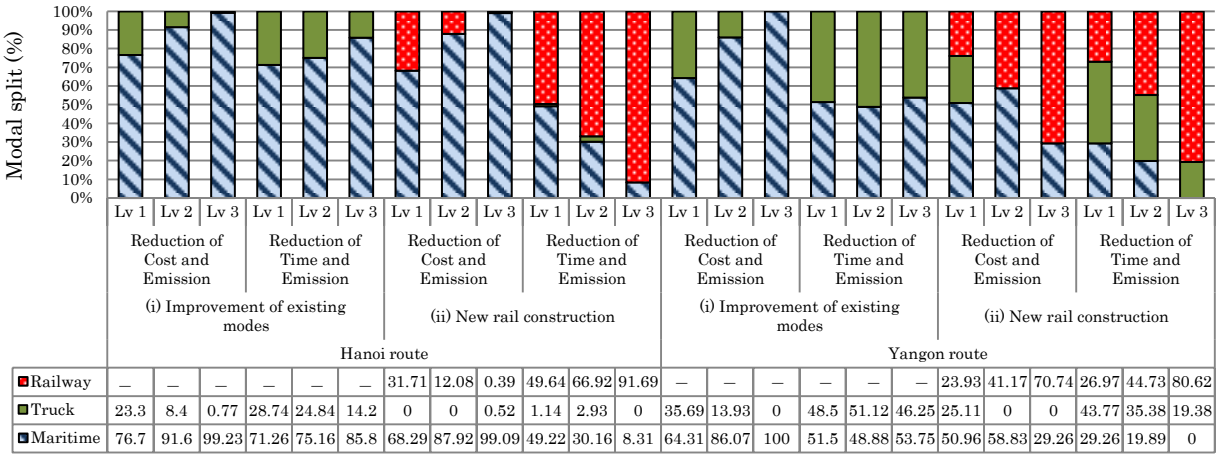

	Hanoi route												Yangon route											
	Lv 1	Lv 2	Lv 3	Lv 1	Lv 2	Lv 3	Lv 1	Lv 2	Lv 3	Lv 1	Lv 2	Lv 3	Lv 1	Lv 2	Lv 3	Lv 1	Lv 2	Lv 3	Lv 1	Lv 2	Lv 3	Lv 1	Lv 2	Lv 3
Railway	–	–	–	–	–	–	31.71	12.08	0.39	49.64	66.92	91.69	–	–	–	–	–	–	23.93	41.17	70.74	26.97	44.73	80.62
Truck	23.3	8.4	0.77	28.74	24.84	14.2	0	0	0.52	1.14	2.93	0	35.69	13.93	0	48.5	51.12	46.25	25.11	0	0	43.77	35.38	19.38
Maritime	76.7	91.6	99.23	71.26	75.16	85.8	68.29	87.92	99.09	49.22	30.16	8.31	64.31	86.07	100	51.5	48.88	53.75	50.96	58.83	29.26	29.26	19.89	0

Figure 2 Results of optimal modal split calculations

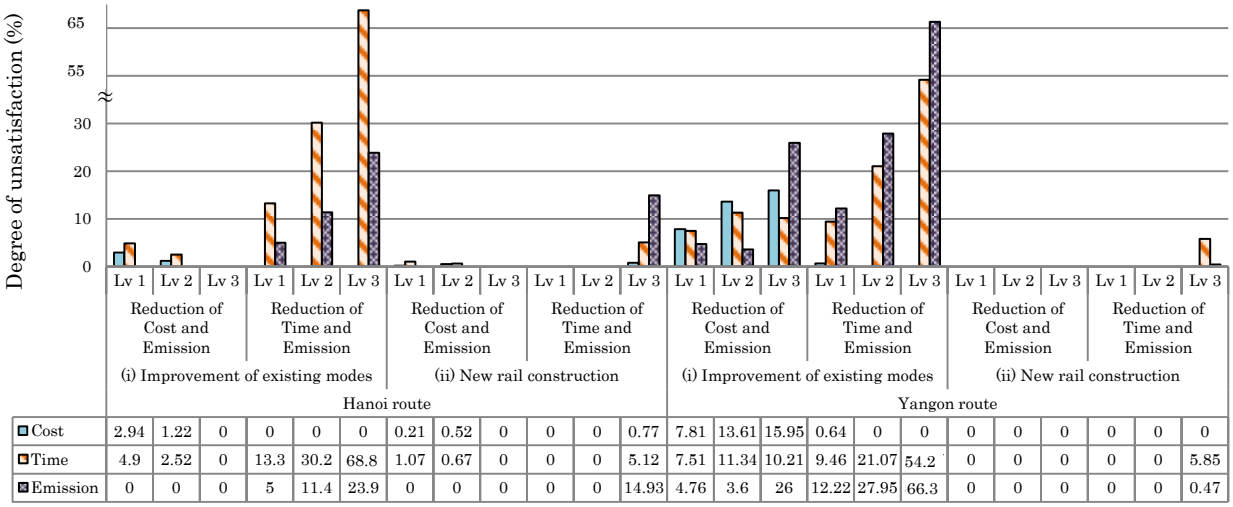

	Hanoi route												Yangon route											
	Lv 1	Lv 2	Lv 3	Lv 1	Lv 2	Lv 3	Lv 1	Lv 2	Lv 3	Lv 1	Lv 2	Lv 3	Lv 1	Lv 2	Lv 3	Lv 1	Lv 2	Lv 3	Lv 1	Lv 2	Lv 3	Lv 1	Lv 2	Lv 3
Cost	2.94	1.22	0	0	0	0	0.21	0.52	0	0	0	0.77	7.81	13.61	15.95	0.64	0	0	0	0	0	0	0	0
Time	4.9	2.52	0	13.3	30.2	68.8	1.07	0.67	0	0	0	5.12	7.51	11.34	10.21	9.46	21.07	54.2	0	0	0	0	0	5.85
Emission	0	0	0	5	11.4	23.9	0	0	0	0	0	14.93	4.76	3.6	26	12.22	27.95	66.3	0	0	0	0	0	0.47

Figure 3 Results of degree of unsatisfaction

Empirical Research on Effectiveness of Improved Packaging Technologies for Transport Damage on Agricultural Products in Vietnam

Student Number: 11M18108　Name: Yuki TAKEHISA　Supervisor: Shinya HANAOKA

ベトナムにおける農産物輸送時損傷に対する梱包技術改善の有効性の実証

竹久 祐貴

本研究では、輸送段階で生じる農産物損傷に対する梱包技術改善の有効性を明らかにすることを目的に、ベトナム現地の農家、輸送業者、小売業者の協力を得てトマトを対象に梱包実験を行い、改善梱包の採算性に関する分析を行った。その結果、MA 梱包とメッシュバッグを導入することで、損傷の割合が低下することが分かった。また、内装に新聞紙、個装にメッシュバッグを使用した改善梱包の場合に得られる利益が最も高いことが分かった。

1. Introduction

Roughly one third of food produced for human consumption is estimated to lose or waste globally, which amount to about 1.3 billion ton on 2011[1)]. Those losses are called food losses that defined as the decrease in edible food mass throughout the part of the supply chain that specifically leads to edible food for human consumption[2)]. Food losses are divided into two categories. First one is postharvest losses that occurred on transport, storage, processing and so on. Second one is food waste that occurred on retail and household.

Unlike developed countries, postharvest losses are serious problem rather than food waste. Main causes for food losses in developing countries are basically attributed to technological limitations such as poor harvesting techniques, poor storage and cooling facilities, poor transport systems and so on[1)]. In addition to technological limitations, socioeconomic factors such as inadequate marketing systems, inadequate transportation modes, unavailability of needed materials and tools, lack of information, governmental regulations and legislations are also related[3)].

In order to reduce the postharvest losses in developing countries, this research focuses on improved packaging. Some field tests of improved packaging show that it generates increased incomes more than 30% to introduce plastic box instead of sack and add carton as cushion[3)]. In previous research, they achieved to identify some effective improved packaging. However, there are few researches refer to costs and financial benefits of improved packaging. Furthermore, the combination of individual packaging, inner packaging and outer packaging has not been well researched yet.

Therefore, the research objectives are first to measure the performance of improved packaging with consideration of packaging combination during transport in developing countries and second to calculate the profitability of improved packaging.

2. Evaluation for improved packaging

(1) Calculation for the ratio of damage

The ratio of damaged is calculated by following equation.

$$R_i = \frac{QD_i}{TQ_i} \quad (1)$$

Suppose that R_i is the ratio of damage in improving packaging i (%), QD_i is the quantity of damage in improved packaging i (kg), TQ_i is the total quantity in improved packaging i (kg). Current packaging is also calculated by same equation.

(2) Calculation for the profitability of improved packaging

Profitability of improved packaging is calculated by following equations.

$$Benefit_i = Profit_i - Profit_c \quad (2)$$

$$Profit_i = Revenue_i - Cost_i \quad (3)$$

Suppose that $Benefit_i$ is benefit when introducing the improved packaging i compared to current packaging (VND), $Proft_i$ is the profit in improved packaging i (VND), $Profit_c$ is the profit in current packaging (VND).

Revenue and cost are calculated by following equation

$$Revenue_i = Sellng\ price \times QT_i \times (1 - R_i) \quad (4)$$

$$Cost_i = PMC_i + PLC_i \quad (5)$$

$$PLC_i = Labor\ time_i \times ALC \quad (6)$$

Suppose that PMC_i is the packaging material cost (VND), PLC_i is the labor cost for packaging i (VND), ALC is the average labor cost (VND/sec). Current packaging is also calculated by same equation.

3. Research target

(1) Country and product

Vietnam, Tomato are selected since Vietnam is severely constrained by tomato losses which amount to 14.6 million dollars in 2004[4]. Tomato is selected because amount of production is high in Vietnam and also high perishability.

(2) Definition of damaged tomato

For this research, damaged tomato is defined as dent, peeling and crack on the tomato's surface (Fig.1).

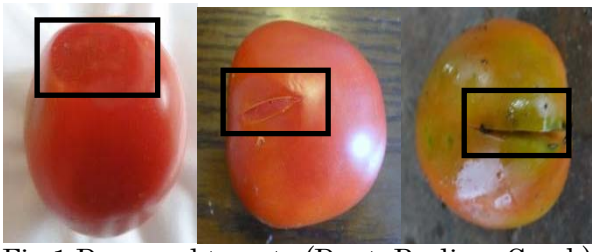

Fig.1 Damaged tomato (Dent, Peeling, Crack)

The causes of damaged tomato are divided into 2 categories.

a) Weakening of the tomato's surface

The quality of tomato decreases after harvesting due to water loss, respiration. That results in making tomato's surface easier to be damaged.

b) Extraneous impact

Extraneous impact is caused by 3 factors such as pressure from tomato weight, friction with other tomatoes and outer packaging, strong impact from the unpaved road.

4. Tomato supply chain

For consumer in Hanoi, they are basically supplied by neighborhood production area. However, Da Lat in southern part becomes main supply chain on July, August due to seasonality. Supply chain from Da Lat to Hanoi is selected since field survey was conducted on that period. The distance between them is about 1600 km (Fig.2).

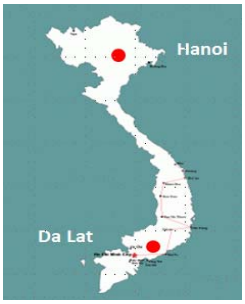

Fig.2 Hanoi and Da Lat in Vietnam

From Da Lat to Hanoi, there are many stakeholders involved to transport. This research focuses on supply chain with blue line shown in Figure.3.

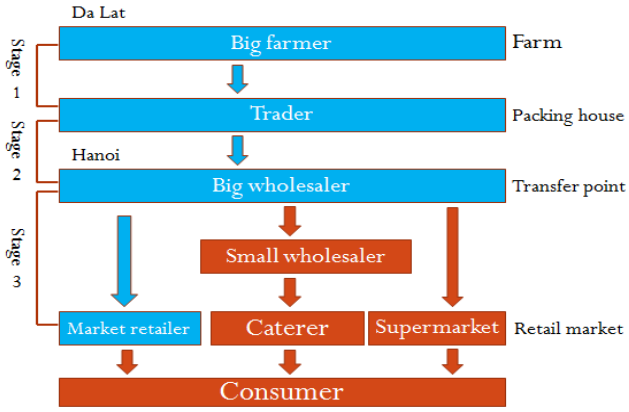

Fig.3 Tomato supply chain

As for their role, big farmer produce tomato and package tomato to transport from farm to packaging house in Da Lat. In the packaging house, they remove damaged tomato and repack tomato to transport to Hanoi. Trader is only in charge of transporting from packaging house to transfer point in Hanoi. Big wholesaler receives tomato from trader, they sell it to market retailer in transfer point. Market retailer transports to retail market to sell to consumer.

The supply chains are divided into 3 stages. Each stage has different road condition, transport mode, transport time (Table.1).

Table.1 Condition in each stage

	Stage 1	Stage 2	Stage 3
Road condition	Unpaved	Paved	Paved
Transport mode	Small truck	large truck	Motorbike
Transport time	1 hour	50 hours	1 hour

5. Experiment of improved packaging

(1) Types of packaging

Packaging is divided into 3 categories. There are outer packaging, inner packaging and individual packaging.

(2) Current packaging

For current packaging, plastic crate is used as outer packaging and newspaper is used as inner packaging. Capacity of plastic box is 25 kg.

(3) Improved packaging

Improved packaging is proposed based on current packaging, effectiveness for reducing the damage, packaging availability in Vietnam. The number of combination of improved packaging is 5 in total (Table.2).

a) Carton

Carton could be used as inner packaging that put inside of plastic craters. It has cushion to reduce extraneous impact.

b) Mesh bag

Mesh bag is used as individual packaging that reduce extraneous impact (Fig.5). The capacity is about 1.3kg. It is currently using in supply chain for supermarket.

c) MAP (Modified Atmosphere Packing)

MAP is used as individual packaging that automatically modifies the composition of internal atmosphere of a package in order to reduce the speed of weakening of the surface (Fig.4). It also reduces the extraneous impact since it's made by thick plastic bag. The capacity is about 1.0 kg.

Fig.4 Mesh bag (left) and MAP (right)

Table.2 Combination of improved packaging

	Outer	Inner	Individual
Current	Plastic	Newspaper	
Improved1	Plastic	Newspaper	MAP
Improved2	Plastic	Newspaper	Mesh bag
Improved3	Plastic	Carton	
Improved4	Plastic	Carton	MAP
Improved5	Plastic	Carton	Mesh bag

(4) Procedure of packaging experiment

The procedure of packaging experiment is following steps.

a) Making improved packaging

2 plastic crates are used for packaging experiment. Specifically, Current, Improved1, Improved2 are put together in one plastic crate and Improved3, Improved4, Improved5 are put together in other one plastic crate (Fig.5).

Fig.5 Packaging for experiment

b) Transport

After sorting tomato into plastic crates, packaging is loaded on truck or motorbike. Then packaging is transported.

c) Measurement for damaged tomato

After transport, damaged tomato is checked by visual contact. After sorting, weight of damaged tomato is measured.

6. Results

(1) The performance of improved packaging

From Table 4, we could see the performance of improved packaging. As for inner packaging, carton doesn't reduce the damage compared to newspaper. It means that newspaper is enough to reduce the damage or inner packaging doesn't have important role to reduce.

As for individual packaging, MAP, Mesh bag reduce the damage compared to without individual packaging. Both packaging seems to have same effect on the damage.

(2) Goodness of fit test

Goodness of fit test was conducted to test the hypothesis that carton has same effect with newspaper and also Mesh bag has same effect with MAP. As for comparison between newspaper and Mesh bag, we assume that the effect of newspaper is correct. The calculation is shown in Table 4. As for individual packaging, same calculation was conducted in both stage 1 and stage by assuming that the effect of Mesh bag is correct (Table.5). From the results, we could see that no significant difference between newspaper and carton, and between Mesh bag

and MAP.

(3) The effect of road condition on damage

From Table 4, we could see that the ratio of damage in stage 1 is highest since the road condition in stage 1 is not paved (Fig.6)

Fig.6 Paved road (left) and Unpaved road(right)

(4) Profitability of improved packaging

From Figure 7,8 we could understand that most profitable packaging is improved 2 that use newspaper as inner packaging and Mesh bag as individual packaging since it uses individual packaging and costs is cheapest. It's profitable in both stage 1 and stage 2.

On the other hand, other packaging is all unprofitable since cost is higher than benefit of improved packaging (Fig.7). In particular, Cost of MAP and Carton account for big proportion of cost (Fig.8).

Table.3 The ratio of damage

	Stage1	Stage2	Stage3
Current	25.0%	5.0%	13.2%
Improved1	7.5%	0%	1.3%
Improved2	8.3%	0%	NA
Improved3	27.3%	8.6%	NA
Improved4	10.0%	0%	NA
Improved5	6.7%	0%	NA

Table.4 Comparison between newspaper and carton in goodness of fit test

	Newspaper	Carton
Observed frequency	4	6.72
Ratio of damage	0.25	0.25
Expected frequency	4	4
χ^2	0	1.84

Table.5 Comparison between Mesh bag and MAP in goodness of fit test

	Stage 1		Stage 2	
	Mesh bag	MAP	Mesh bag	MAP
Observed frequency	0.3	0.332	0.4	0.268
Ratio of damage	0.075	0.075	0.1	0.1
Expected frequency	0.3	0.3	0.4	0.4
χ^2	0	0.042	0	0.001

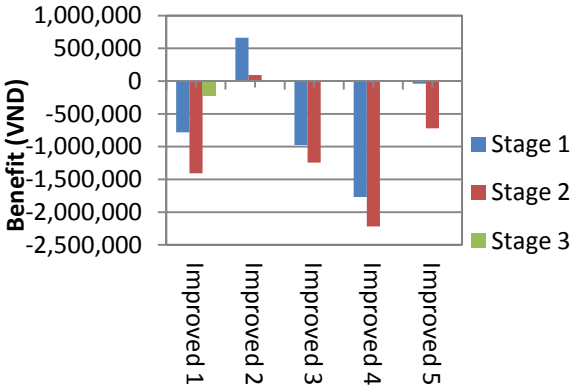

Fig.7 Benefit of improved packaging for 1000kg of tomato

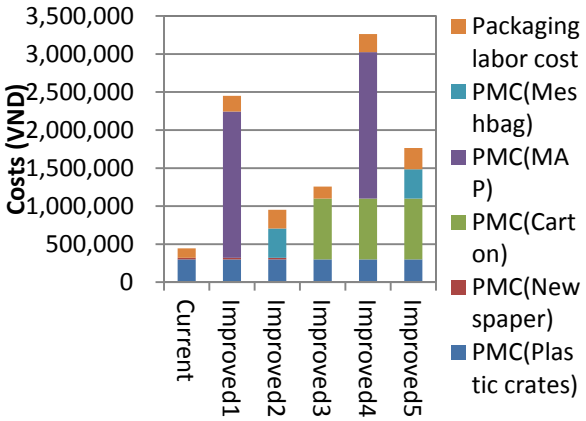

Fig.8 Cost of packaging for 1000kg of tomato

7. Conclusions

In this paper, the packaging experiment was conducted to measure the performance of improved packaging and calculate the profitability. We conclude that postharvest losses could be reduced and made benefit by introducing the improved packaging that use newspaper as inner packaging and Mesh bag as individual packaging.

Reference

1) FAO. (2008), GLOBAL FOOD LOSSES AND FOOD WASTE
2) Parfitt, J., Barthel, M. and Macnaughton, S. (2010), Food waste within food supply chains: quantification and potential for change to 2050, Phil. Trans. R. Soc., vol. 365, pp. 3065-3081
3) Saran, S. and Roy, S.K. (2012), Appropriate postharvest technologies for small scale horticultural farmers and marketers om Sib-Saharan Africa and South Asia – Part 2. Field trial results and identification of research needs for selected crops, Proc. XXVIIIth IHC
4) Weinberger, K.C., Genova, I.I. and Acedo, A. (2008), Quantifying postharvest loss in vegetables along the supply chain in Vietnam, Cambodia and Laos, Int. Postharv. Technol. Innov. 1:288-297

AIRPORT DESIGN GUIDELINE AS A HUMANITARIAN LOGISITCS BASE

Student Number: 11M51241 Name: Sunkyung CHOI Supervisor: Shinya HANAOKA

Airports play a critical role as a node for humanitarian logistics when natural disaster hits a region. However, there are no guidelines governing space allocation of an airport. This paper proposes a design guideline for an airport as a humanitarian logistics base concerning two components mainly: 1) base camp (space for emergency workers), 2) staging area (area to deal with sorting, storing, loading and unloading relief goods). We develop a methodology to estimate total area of the base and visualize layout by space planning. The result suggests approximate size and layout of a base camp and a staging area to be included as a humanitarian logistics base. The space planning methodology is further applied to Shizuoka airport as a case study.

1. Introduction

Following the March 2011 earthquake and tsunami, there was a certain need to revisit disaster management planning of infrastructures regarding natural disaster. Since disasters come in all different sizes and impacts, it is difficult to predict and response well in some situations.Therefore, it is important to build a sound disaster preparedness plans in many disaster prone cities and countries, this research would lead academics and practitioners to attain attention for disaster management planning.

In emergency logistics or humanitarian logistics, it is known that air transport is more used than normal cases since destructive damage in land transportation modes and the other transportation modes. As a node for enabling immediate disaster response, some argues that it is preferable if staging area can be set up within an airport since most regional airports have vacant space which enables various activities, accessibility, hard stand area for loading/unloading goods, and helipads.

Despite critical role of airports in humanitarian logistics, some limitations still lie in airports space usage in post-disaster. Such space constraints are mentioned in Hanaoka *et al.* (2013)[1]. The author argues that airports need to deal with the space constraints in order to be prepared well enough to deal with humanitarian logistics operation in airports. In this study, two space constraint issues are to be answered by research question. Two issues are space for emergency workers and place for relief goods.

The fundamental question that the author intended to address is how to plan space allocation of a humanitarian logistics base in an airport. By answering this question, this research aims to propose a design guideline for an airport as a humanitarian logistics base. There are three objectives that derived from the research goal.

1) Estimate area of required facilities in a humanitarian logistics base
2) Make a bubble diagram for each facility
3) Draw a schematic plan for Shizuoka airport based on scenario analysis

By achieving objectives, this research would make an attempt to deal with space limitation issues in an airport in post-disaster and assist effective decision making in planning a humanitarian logistics base in an airport with regard to space planning.

2. Methodology

2.1 Methodology framework

A proposed methodology would be formulated by unfying ideas of practical projects and acadmic researches. Current practices of humanitarian logistics are mostly led by government operation. Kapucu *et al.* (2007)[2] mentions that there are no officially-documented guidelines regarding staging area selection as emergency management planning. Therefore, This research follows a methodology framework as in Figure1 in order to assist design guideline for space allocation of an airport as a humanitarian logistics base.

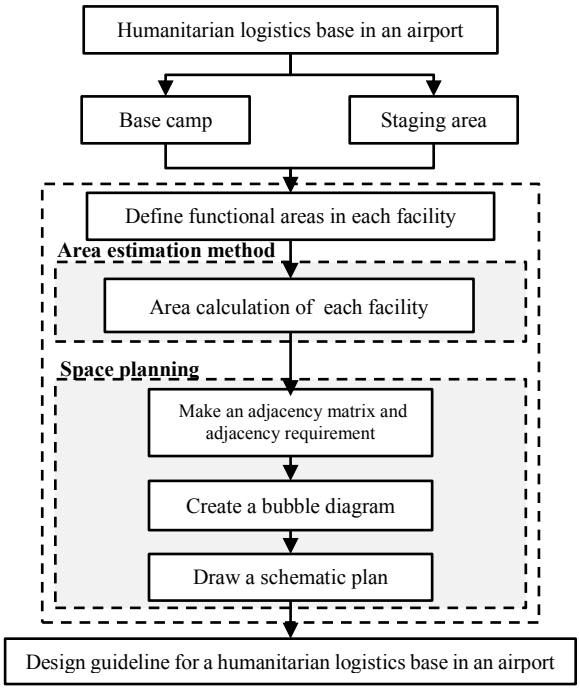

Figure1: Framework for a humanitarian logistics base

2.2 Area estimation method

2.2.1 Calculation method for a base camp

Data was collected through government's project papers and practical emergency planning in Florida, U.S.A.[3] Figure 2 explains flow for a base camp estimation. In this paper, required number of emergency workers (m) is defined as 100, 250, 500, 750 and 1000 in this study in order to support standardized guideline for base design. The following equation (1) and (2) is for calculating each functional area to be included in a base camp.

Unit area u is defined as $30m^2$ for minimum estimation and $50m^2$ for maximum unit area (MLIT, 2003)[4]. R_k is estimated based on current practices of base camp design in Florida State Emergency Planning of United States. Total area of base camp is a sum of all functional areas within the area. Functional areas are noted as A_k^m, when considering m number of emergency workers.

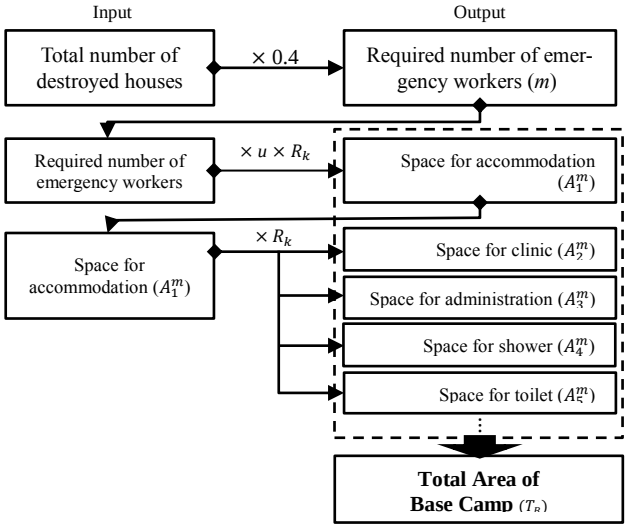

Figure 2: Calculation flow for a base camp

$$T_B = \sum_{k=1}^{n} A_k^m \ (k = 1, \ \cdots, \ 10) \quad (1)$$

$$A_k^m = m \times u \times R_k (k = 1, \cdots, 10) \quad (2)$$

T_B total area of base camp

A_k^m area for functional space k when total m number of emergency workers

k identification of each functional space in base camp

- k = 1: space for accommodation
- k = 2: space for clinic
- k = 3: space for administration
- k = 4: space for shower room
- k = 5: space for toilet
- k = 6: space for recreation center
- k = 7: space for laundry room
- k = 8: space for dining and kitchen
- k = 9: space for staff
- k = 10: space for management

R_k ratio of functional space A_k^m to A_1^m, $R_k = 1$ when k = 1

m number of required emergency workers

u unit area for base camp per one emergency worker

2.2.2 Calculation method for a staging area

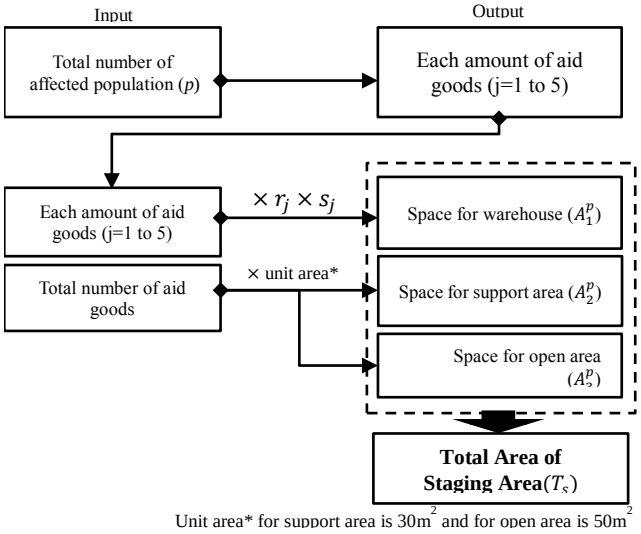

Unit area* for support area is 30m^2 and for open area is 50m^2

Figure 3: Calculation flow for a staging area

Calculation flow for size of staging area is calculated dbased on Figure3. In this study, the number of affected population is assumed defined as 10000, 30000, 50000, and 70000. Total area of a staging area consists of three parts which are warehouse, support area for workers, and open area for loading and unloading goods. Equation (4) explains required space for warehouse in order to store humanitarian aid goods Equation (5) is for support area with unit area of 30m^2 equation (6) explains open area for staging area.

$$T_s^p = A_1^p + A_2^p + A_3^p \quad (3)$$

$$A_1^p = \sum_{j=1}^{n} A_j^p \ (j = 1, \ \cdots, \ 5) = \sum_{j=1}^{n} r_j \ \times p \times s_j \ \ (j = 1, \ \cdots, \ 5) \quad (4)$$

$$A_2^p = \left(\sum_{j=1}^{n} r_j \ \times p \right) \times 30 \ (j = 1, \ \cdots, \ 5) \quad (5)$$

$$A_3^p = \left(\sum_{j=1}^{n} r_j \ \times p \right) \times 50 \ (j = 1, \ \cdots, \ 5) \quad (6)$$

T_S total area of staging area

A_1^p space for warehouse when total number of affected population are p

A_2^p space for support area when affected population are p

A_3^p space for open area when number of affected population are p

p total number of affected population

j identification for items needed for affected population

- j = 1: water
- j = 2: food
- j = 3: blanket
- j = 4: mandatory kit
- j = 5: temporary toilet

r_j required amount for item j per one person

s_j scale factor of item j from converting weight to area

2.3 Space planning

2.3.1 Adjacency matrix

Adjacency matrix is used in architectural planning in order to see relationship between each functional area in a building.[5] The adjacency diagram would let designers to identify the proximity requirements. This does not have definite answer for concluding the best answer and there may lay various approaches.

2.3.2 Bubble diagram and schematic plan

Architectural bubble diagrams are used to consider layout of functional areas in a floor plan. Bubble diagrams are to explore relationships among the sizes, adjacencies, and approximate shape of the spaces needed for various activities. A schematic plan is a revised version of bubble diagram before planning actual floor plans as in Figure 4.

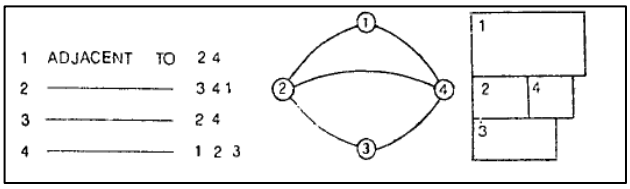

Figure 4: Graph representation in bubble diagram
Source: Adapted from Ruch (1978)[6]

3. Result

3.1 Base camp

3.1.1 Functional area estimation in a base camp

Approximate size of base camp area is calculated in Table 2. If 1000 workers would support humanitarian logistics in an airport in a base camp adapting a minimum unit area, accommodation area is approximately 9009.00m^2 and total area for base camp is assumed as 3ha.

Table 1: Base camp area estimation (Unit:m^2)

Emergency workers	1000	750	500	250	150	100
Accommodation	9009.0	6756.7	4504.5	2252.2	1351.3	900.9
Clinic	1126.1	844.5	563.0	281.5	168.9	112.6
Admin	1126.1	844.5	563.0	281.5	168.9	112.6
Recreation center	2252.2	1689.1	1126.1	563.0	337.8	225.2
Toilet	1407.6	1055.7	703.8	351.9	211.1	140.7
Shower	1407.6	1055.7	703.8	351.9	211.1	140.7
Laundry	563.0	422.2	281.5	140.7	84.4	56.3
Dining/Kitchen	12263.5	9197.6	6131.7	3065.8	1839.5	1226.3
Staff	563.0	422.2	281.5	140.7	84.4	56.3
Management	281.5	211.1	140.7	70.3	42.2	28.1
Total	30000	22500	15000	7500	4500	3000
Total(ha)	3	2.25	1.5	0.75	0.45	0.3

3.1.2 Space planning

Figure 5 shows immediate proximity and convenient proximity are assumed on base camp design from practical designs of State of Florida (2009). Immediate proximity means strongly recommended being located near each other, and convenient proximity means better to be located near each other.

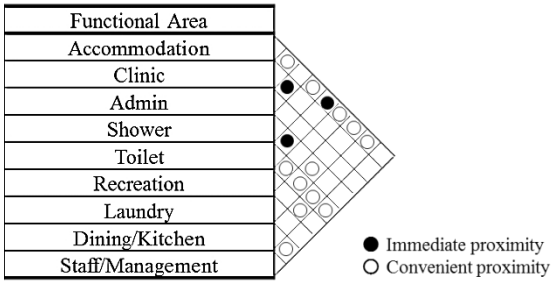

Figure 5: Adjacency matrix in a base camp

An initial bubble diagram and its adjusted figure with considered each functional area's relative size is in Fig.6. Staff area and management area are combined for simplicity in a diagram. It can be easily seen that 1 and 8 which are accommodation area and dining/kitchen area consist most of base camp gross area. The largest part within base camp is dining/kitchen area and accommodation area. (1: Accommodation, 2: Clinic, 3: Administration area, 4: Recreation center, 5: Toilet, 6: Shower, 7: Laundry, 8: Dining/Kitchen, 9: Staff/Management)

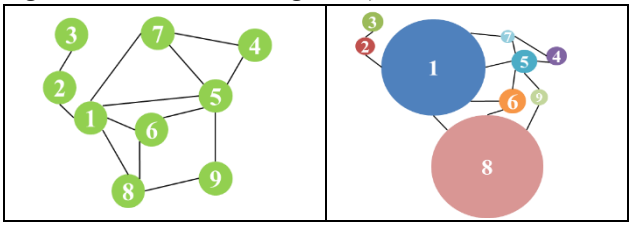

Figure 6: Bubble diagram for a base camp

3.2 Staging area

3.2.1 Staging area functional area estimation

Estimation for storage in staging area is indicated in Table 2. In order to support 10000 people, total sum of each area for goods required is assumed as 1074.15 m^2. In order to secure enough space, 120% of total sum of each area is regarded as 1288.98 m^2. Table 3 shows estimation for support area for workers in staging area. Total support area when assisting 10000 people is 4042.5 m^2. Table 4 shows estimation for open space in staging area. When supporting 10000 people, outdoor handling and staging is required as 4812.5m^2 and flexible use is as 4812.5 m^2 and parking space would be as 9625 m^2. Table 5 shows open area estimation. Total open space would be approximately 1.9ha when supporting 10000 people. Outdoor handling and staging area and flexible use are assumed to be the same size.

Table 2: Storage area estimation in a staging area (Unit:m^2)

Affected population	10000	30000	50000	70000
Water	342.3	1026.9	1711.5	2396.1
Food	396.9	1190.7	1984.5	2778.3
Blanket	133.2	399.6	666.0	932.4
Mandatory kit	111.0	333.0	555.0	777.0
Toilet	90.7	272.2	453.7	635.2
Storage area	1288.9	3866.9	6444.9	9022.8

Table 3: Support area estimation in a staging area (Unit:m^2)

Affected population	10000	30000	50000	70000
Workers	135	404	674	943
Accommodation	3234	9702	16170	22638
Office	202.1	606.3	1010.6	1414.8
Toilet/shower	202.1	606.3	1010.6	1414.8
Catering area	202.1	606.3	1010.6	1414.8
Common area	202.1	606.3	1010.6	1414.8
Support area	4042.5	12127.5	20212.5	28297.5

Table 4: Open area estimation in a staging area (Unit:m^2)

Affected population	10000	30000	50000	70000
Outdoor handling /staging	4812	14437	24062	33687
Flexible use	4812	14437	24062	33687
Parking space	9625	28875	48125	67375
Open area	19250	57750	96250	134750

The result from Table 7 suggests an approximate size of total staging area estimation combining Table 4, Table 5, and Table 6. In order to assist 10000 affected population, staging area is required as 2.45 ha within a humanitarian logistics base.

Table 5: Total area estimation of a staging area (Unit:m^2)

Affected population	10000	30000	50000	70000
Staging Area	24581	73744	122907	172070
Staging Area(ha)	2.45	7.37	12.29	17.2

3.2.2 Space planning

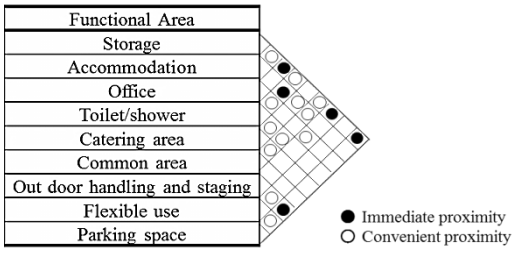

Figure 7: Adjacency matrix in staging area

The result of space planning are adjacency matrix and bubble diagram. Adjacency matrix is drawn in order to understand space relationships within a facitliy as in Figure

7. All functional areas in a staging area are located close to each other concerning proximity. Basic architectural planning concept is utilized in building adjacency matrix.

Figure 8 shows relative size of staging area and how each functional area is related to each other. Open area are correlated each other in order to assist smooth flow of aid goods. Parking space would take the position as the biggest part for staging area due to unexpected amount of vehicles and aid goods may clog in the area. (1: Storage, 2: Accommodation area, 3: Office, 4: Toilet/shower, 5: Catering area, 6: Common area, 7: Outdoor handling and staging, 8: Flexible use space, 9: Parking space)

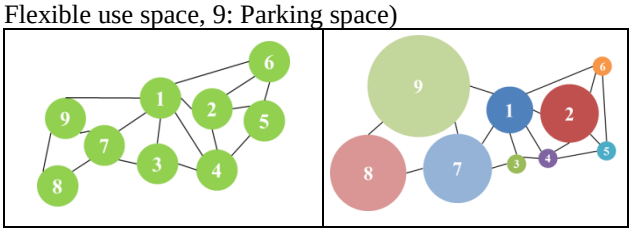

Figure 8: Bubble diagram for a staging area

4. Case Study

4.1 Scenario building

According to Tonankai disaster scenario by Cabinet office of Japan (2007), affected population and needed emergency workers in Shizuoka prefecture are 43,000 people and 17,000 people respectively. Shizuoka airport is assumed to cover between 25% and 30% of total required emergency workers and number of affected population. Current space constraint of a land area is assumed approximately as 16ha.

4.2 Space planning for Shizuoka airport

Fig.9 and Fig.10 shows space planning of a base camp and a staging area by the proposed methodology. Initial bubble diagrams are developed into a schematic plan. This process is iterative in a sense that it aims to locate as compact ac possible.

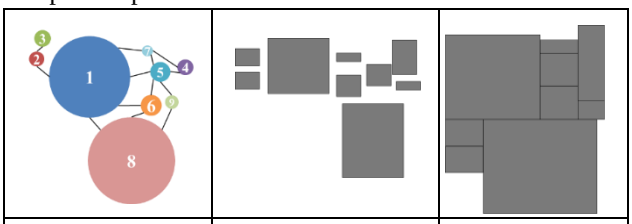

Bubble diagram	Rectangular formation	Schematic plan

Fiure.9: Base camp planning process

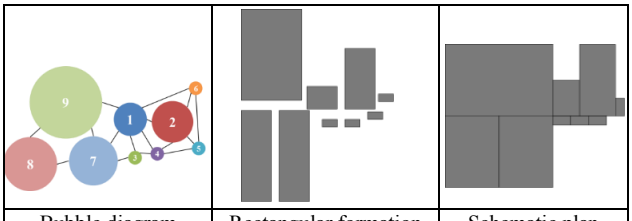

Bubble diagram	Rectangular formation	Schematic plan

Figure 10: Staging area planning process

Fig. 11 is a combined schematic plan as a humanitarian logistics base. This shows a layout for a humanitarian logistics base within current Shizuoka airport layout plan. It is estimated that gross land area of a base may be estimated around 16ha.

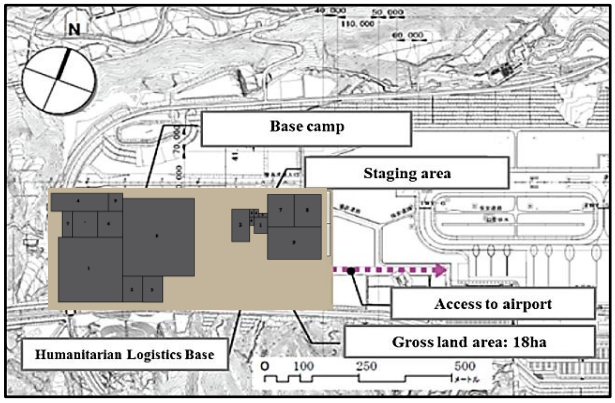

Figure 11: Layout plan for Shizuoka airport

4.3 Discussions

The result suggests an approximate size of a base camp and staging area. It also visualizes by following space planning as an output of a bubble diagram and a schematic plan. The case study of Shizuoka airport suggested that schematic plan may be larger than current size of each facility in Shizuoka airport since this study didn't consider space for aisles between goods in warehouses. The other reason is that hardware of architctural planning such as thickness of walls or other infrastructures allocations are not included. Following methodology of the study, staging area is comparatively smaller than the current plan. More consideration in revising relationship of the facilities inside of a humanitarian logistics base is recommended. The other considerations would be needed in determining how the size of a base can be determined.

5. Conclusions

This study proposed a design guideline for a humanitarian logistics base in an airport, and has presented its conclusion by integrating calculation model and architectural planning methodologies. This study is unique in a sense that it tackled an issue in border with architectural planning, humanitarian logistics and air transport studies. This research is an initiative research in airport as a humanitarian logistics base with various disciplines. This thesis investigated each facility space allocation and its inner space planning issues. Several future studies might focus on the following remaining issues such as mathematical model development concerning airport constraints and its coverage in region. Also, integration with urban planning perspective can be later developed in understanding relationship between the base and surrounded environment.

References

[1] Hanaoka, S., Indo, Y., Hirata, T., Todoroki, T., Aratani, T., and Osada, T. , "Lessons and Challenges of Airport Operation during a Disaster: Case Studies of Iwate Hanamaki Airport, Yamagata Airport, and Fukushima Airport during the Great East Japan Earthquake", *Journal of JSCE, Division F: Construction Engineering and Management*, In Press. 2013.

[2] Kapucu, N., Lawther, W., Pattison, S., "Logistics and staging areas in managing disasters and emergencies", *Journal of Homeland Security and Emergency Management*, Vol. 4, No. 2, pp.1-17, 2007.

[3] State of Florida, Division of Emergency Management Logistics Section, "State of Florida: State Unified Logistics Plan", 2009.

[4] MLIT, Nagoya Regional Disaster Prevention Network Working Group., "Simulation on Estimation Ideas of Case Studies", 2003.

[5] Demkin, J. The American Institute of Architects., "The Architect's Handbook of Professional Practice", 13th edition, 2001.

[6] Ruch, J., "Interactive Space Layout: A Graph Theoretical Approach", *Proceedings of the 15th conference on Design automation*, pp.152-157, 1978.

Study of the Effect of ICT on Antenatal Care in Remote Mountainous Region of Nepal

Student Number: 11M18083 Name: Kazuhiro KAMIYAMA Supervisor: Jun-ichi TAKADA

ネパール山岳地域での情報通信技術を用いた妊産婦の保健管理の効果に関する研究

神山　和大

本研究では，ネパールの山岳地域に住む妊産婦を対象に，ICT を活用することによって，母子医療保健知識を提供するプロジェクトを通して現地の村でアンケート・インタビュー調査を実施した．調査結果から，妊産婦がプロジェクトや Web アプリケーションに対して高い満足度を示していることがわかった．また, Web アプリケーションによって, 5 つの指標(食事・娯楽・家族との関係性・家事・休暇)のうち娯楽以外の 4 つの指標に対して妊婦の行動や彼女たちの家族の意識を改善することができたことが確認された.

1. INTRODUCTION

The reduction of maternal mortality has now become one of the leading global health agendas as emphasized in Millennium Development Goals (MDGs) 5. Approximately, 300000 women died worldwide due to complications related to pregnancy or childbirth in 2008[1]. The maternal mortality rate is particularly high in poor developing countries such as Nepal. In Nepal, maternal mortality rate is 170 per 100,000 whereas in the average of world maternal mortality rate is 66 per 100,000. Since this is the average rate of whole nation, the situation is more serious in the marginalized and poor community living in high altitude and remote rural areas of Nepal [2]. There are various reasons such as traditional customs, cultural barriers, lower literacy rates, as well as lack of infrastructure and qualified doctors [2]. It is known that antenatal care (ANC) is an important factor in reducing the maternal mortality. And information and communication technology (ICT) can be an effective tool to connect pregnant women to health services in remote areas.

2.RESEARCH BACKGROUNG

2.1 Mother and Child Protection Program implemented by E-Network Research and Development

The author is involved in Mother and Child Protection Program (MnCP) in Nepal. This study focuses on antenatal health care element of the Child Protection Program being implemented by E-Network Research and Development (ENRD) from 2011 December in 15 villages. ENRD is a non-profit and non-governmental organization in Nepal. Its goal is to empower and support rural community through the use of ICT. Figure 1 shows the schematic view of project. In this project, there are four primary stake holders; 1) the city hospital doctors in Kathmandu, 2) Female Community Health Volunteers (FCHV), 3) community health worker and 4) pregnant women in the villages. The secondary stake holders are Ministry of Health/Local government, Internet Society (ISOC) as the funding organization, ENRD as a project organization, and the families of pregnant women.

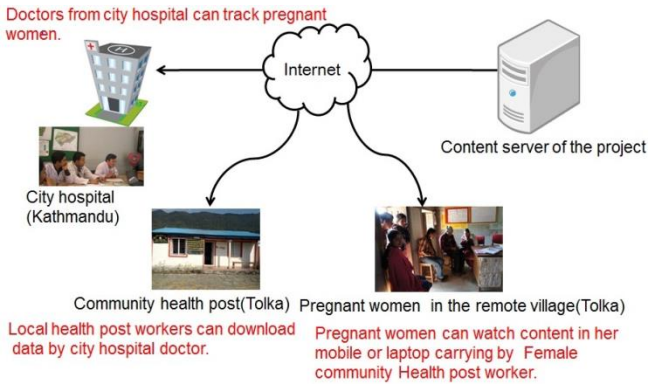

Figure1. Schematic view of project

The city doctors develop the education contents of antenatal care for pregnant women and make it available on the Internet by uploading them to the ENRD servers. Due to the Internet bandwidth constraints at the remote villages the contents are mainly texts and audio recordings, although few videos are also available.

The FCHV, nominated by individual villages, are trained by the project to handle laptop or tablet PC. They download the information onto a laptop or tablet and take it to the pregnant women's home. Moreover, pregnant women can register on the Web site of the project, which provides them with antenatal care information. As they login with her username and password they will start to get antenatal care related audio, video and text contents according to the stage of her pregnancy. Doctor and Health worker can also login to track and support pregnant women under their supervision. The main objective of this web application is to establish network among pregnant women, FCHV, health Post, and city hospital, and to monitor the situation of pregnant women.

In Nepal the internet penetration rate is just over 20.9% with majority of them using mobile internet and mainly, located in urban and city area [3]. However, Nepal Wireless Networking Project (NWP) led by ENRD has already networked health posts in more than 200 villages. All of the health posts have PC [4].

This project developed a Web application to provide pregnant women with antenatal care information. This project also enables the health posts in each village, local pregnant women, and the hospital in Kathmandu to constantly contact each other through the ENRD server.

2.2 Research Objectives

In this study, we focused to see how satisfied the pregnant women were after receiving the antenatal care information through the project. We used questionnaire and focus group methodology for data collection purpose.

The objective of research is as follows;

1) To investigate the attitude and behavior of pregnant women with regard to the maternal health in the project site
2) To study how the project (Child Protection Program) is important towards maternal health care in mountainous regions of Nepal
3) To present possible issues and the future direction of the project through the above discussion

2.3 Methodology

To know the effect of the project/Web application and the attitude and behavior of pregnant women in the remote villages after they received antenatal health care information through the use of Web application, this study conduct the questionnaire survey and interview survey in 6 villages (Tolka, Histan, Shikha, Keshabter, Nangi, Dadagau) .

The details of the questionnaire and interview survey are as follows;

1) Questionnaire survey
   - 5-scale evaluation of Web application
   - 5-scale evaluation of the project
   - Basic information of pregnant women
2) Interview survey (Individual, Focus group discussion)
   - The current situation of the project site (e.g., superstition in the villages)
   - Pregnant women's prior knowledge about antenatal health care before participating in the project

In this study, the research procedure is as follows;

1) Making the questionnaire which will enable us to evaluate the effect of the project.
2) Conducting a field survey in remote 6 villages of Nepal to solicit answers to these questionnaires from pregnant women.

2.4 Field survey

The field survey was carried out from 21st November 2012 to 1st December 2012, and from 22nd to 25th December 2012 in Nepal. The author participated in the project and observed the pregnant women in the remote Tolka, Nangi, Histan, Khibang, Dadagau and Shikha villages. In these villages the project is already being implemented and Internet connection is available. This study obtained information by means of questionnaire survey of all the 62 pregnant women who had participated in this project and received antenatal care information.

3.RESULT OF THE SURVEY

3.1 Result of the questionnaire (1)

Table 1. shows the 5-scale evaluation of the Web application. According to this table, Web application is highly regarded, especially, Web application improved the relation between pregnant women and doctor/TBA, and pregnant women preferred the Web application, compared to TV or FM Radio. Furthermore, by using this Web application pregnant women were able to better understand FCHV's advice. However, question 2, 3 shows relatively low score. It indicates this project cannot be an alternative to medical services.

Table 1. 5-scale evaluation of the Web application(N=60)

Questions	Result
	Mean value
1. This web application is better than FM radio and TV programs.	4.85
2. This web application can replace hospital service.	2.67
3. This web application can reduce the number of visit to doctor.	2.75
4. I trust this application.	4.70
5. I am confidence with my skill of handling computer and mobile to use this application.	4.45
6. This web application improves relation between me and health workers and/or doctors.	4.73
7. FCVH's advices are easy to understand.	4.82
8. Web contents are easy to understand.	4.69

3.2 Result of the questionnaire (2)

Table 2. shows the 5-scale evaluation of the project. In this table, we evaluated the 5 indicators (food, relation among family, household work, rest, entertainment), which was selected from the baseline survey. The baseline survey was conducted by project members from October 05- 25, 2011 in Nangi, Tolka, and Dadagau villages. According to this table, all indicators, except for "entertainment", got high scores. Particularly, it show that family members became more supportive and paid attention to pregnant women during pregnancy period and, helped with household work after participating the project. Moreover, table 2. also indicates that pregnant women got sufficient rest and improved their eating habit.

Table 2. 5-scale evaluation of the project (N=59)

Questions	Result
	Mean value
1. Have you established better relationship with your family?	4.77
2. Have you improved eating habit during pregnancy?	4.17
3. Have you shared the housework load with other family members?	4.48
4. Have you been respected your behavior and feelings from your family?	4.58
5. Have your family members become serious about pregnancy related issues?	4.52
6. Have you enjoyed entertainment, such as sightseeing, group dancing, picnic?	3.38
7. Have you taken rest sufficiently?	4.45

3.3 Qualitative analysis between baseline survey and questionnaire survey

Table 3. shows the qualitative analysis between baseline survey and questionnaire survey. Baseline survey has been already conducted by ENRD before the author participated in this project. According to this table, Food habit, household work, and amount of rest have changed after pregnant women received the knowledge of antenatal care through the project by using the Web application. This is evident from the high score of the Web application from Table 1.

Table3. Qualitative analysis of this study(N=62)

	Baseline survey	Result of this study
Indicators (Food, Rest, Entertainment, Relation, Household work)	● After pregnancy, they didn't change their food habit and household work ● Pregnant women didn't take sufficient rest due to the household work	● Changed their food habit and decreased the household work after pregnant women received information through the project ● Took sufficient rest during pregnancy
Web application	● TV and FM Radio primarily are used for entertainment and they gave lower priority to antenatal care broadcast	● Acquired antenatal care information through the use of Web application ● They believe the Web application is reliable, and they are satisfied with it

3.4 Result of interview survey

In parallel with conducting questionnaire survey, the author conducted the interview survey of pregnant women in the remote villages of Nepal. From the interview survey, there are two findings.

Firstly, superstition still exists in the remote villages. For example, few pregnant women believe that it is good to eat lots of food during pregnancy and that if they work hard during pregnancy it becomes easier to give birth to a baby. Few pregnant women believe that babies should sleep only as long as adults.

Secondly, pregnant women could have used the media as a means to get antenatal care information even before participating in the project, however they did not use the media such as TV and FM Radio to obtain the antenatal care information. Instead if the pregnant women had time to watch TV or listen to FM Radio, they spent their time only entertainment program. Therefore, most pregnant women have on snippets of knowledge about antenatal care because they did not watch TV and listen to FM Radio for related broadcasts.

Therefore, expected effects of the project are as follows: 1) improve the 5 indicators (food, relation among family, household work, rest, entertainment) by providing the antenatal care information; 2) weaken the influence of superstitious and wrong traditional beliefs regarding antenatal care.

4. DISCUSSION

4.1 Limitation of this study

In this study, the author tried to evaluate the impact of using ICT to provide antenatal care information to pregnant women through this project. However, it is difficult to clarify the impact of the project due to the fact that there are various restrictions such as, in the mountainous region of Nepal pregnant women cannot walk to the health post by themselves. This limits the number of times survey can be carried out and therefore data set. However, in this study we present possible issues and the future direction of the project through the above discussion by using socio-technical approach and Design Reality- Gap.

4.2 Socio-technical perspective

Many researchers (e.g. Checkland and Scholes 1990; Mumford 1995) support the socio-technical approach for information system projects. The socio-technical approach is theoretically based on the socio-technical theory (Emery and Trist 1960) which claims that "a technological system cannot be separated from the social system of those involved with it' (Emery and Trist 1960 cited in Checkland and Holwell 1998: 226). The suitability of the socio-technical approach for information and communication technology for development (ICT4D) projects can be justified (Heeks, 2008). In this project, the Web application aiming to lessen the gap between mountainous region and urban areas by providing pregnant women with the antenatal care information. Although, in this study, questionnaire survey shows that Web application is highly regarded among pregnant women, as many researchers (Madon 1994; Castells 2001; Heeks 2002b) mentioned, the social, economic and cultural environments determine the extent to which people can benefit from ICT. (Sein and Harindranath 2004). In this study, pregnant women were socially and geographically in a difficult position to get the benefit of ICT. Therefore, FCHV might have a vital role to play as an interface between the pregnant women and technology.

4.3 User participation

On the other hand, many researchers pointed out that user participation is important factor in order to make the ICT4D projects a success (Hickey and Mohan, 2004). Heeks (2008) state that one of the paradigm shifts from old ICT4D projects to the latest ICT4D projects is to treat local users as producers, not consumers. Therefore, in this project, pregnant women are required to participate actively to lighten the FCHV's work load. To providing opportunities to use Web application and to participate in this project can contribute not only to motivating them but also to making them confident. In other words, it is an empowerment of local users (i.e. pregnant women).

4.4 Design-Reality Gap

The importance of the socio-technical approach with user participation is clarified. However, one more problem is the gap between project design and reality. Unless the gap is minimized, it is quite difficult to realize project success. The ITPOSMO checklist (Heeks 1999a; 2006) is a useful tool to evaluate and measure the gaps from the point of the socio-technical perspective since it covers both technical and the other dimensions such as Information, Technology, Process, Objectives/Value,

Skills/Staffs, Management/Structure, Other resources (Time/money). Table 4. shows the Design-Reality Gap of this study. According to the table, under the factors of information, process and skill, FCHV were burdened with many tasks such as, they explain the Web application by bringing laptop/tablet to pregnant women's home. Furthermore, under the factors of technology and objective/value, the villages currently have serious problems such as, poor electric infrastructure and the Internet connection. These problems were not considered during project design.

Table4. Design-Reality Gap of this study

Factor	Design	Reality
Information	The project develops the Web application, which is made with the advice of doctors in Kathmandu, and then FCHV explain this application by visiting pregnant women's home.	In the survey, Web application had high score However, since most of pregnant women don't have laptop or tablet PC, FCHV have to explain the application to them.
Technology	Web application provides pregnant women with adequate antenatal care information anytime.	It is necessary to download the Web contents for offline use due to the poor electrical infrastructure and internet connection.
Process	As they login with her username and password pregnant women start to get antenatal care related audio, video and text contents according to stage of their pregnancy.	Even if FCHV explain the Web application to every pregnant women the same way, each pregnant women's understanding is different.
Objective/Value	To introduce localized ICT tools to the rural women, which will directly enhance the digital literacy and improve their behavior relating antenatal care information	Each village has different to the connectivity of the Internet and also each pregnant women's home has different the connectivity.
Skill /Stuff	FCHV were trained by the project on how to use the Web application and they in turn explain it to the pregnant women	The frequency of visiting pregnant women's home is different among each FCHV due to the geographical condition in the mountainous area.
Management/ Structure	The project recommend pregnant women to go to the health post in the village in order to communicate with the medical doctor via Internet.	Pregnant women cannot often go to the health post, because they have household work and it is difficult for them to walk in mountainous region

4.5 Problem identification

It should be noted that the Web application is used by FCHV, and not the pregnant women. Considering this fact, to fill these gaps, this study suggests two points. First, at the beginning of the project, the project paid attention to the quality of Web application and how to distribute the contents to each village. However, this analysis suggests the most important thing is how often FCHV can visit the pregnant women's home which is difficult in the mountainous region, and explain this application.

Second, as social-technical approach discussed, FCHV's burden have to be reduced and shared by the pregnant women through more active participation in the project. Actually, in this study, questionnaire survey shows that Web application is highly regarded among pregnant women. However, this means that pregnant women depends on FCHV for using the Web application and also come to bring it to their home. However, in terms of success of ICT4D project, users (pregnant women) participation can be one of the possible solutions to lessen the design-reality gaps.

5. CONCLUSION

In this study, antenatal care information provided through the Web application improved the attitude and behavior of pregnant women in the 4 indicators (food, relation among family, household work, rest) except for "entertainment" after they participated in the project.

Moreover, this study found that FCHV plays vital role to take ICT to pregnant women. Also through the analysis of the socio-technical approach and Design-reality Gap, FCHV, who introduced and explained how to use the web application, is found to be integral.

Therefore, to make the ICT4D project successful in the long term, user participation (pregnant women) might be very important.

REFERENCES

[1] World Health Organization,2012, *"World Health Statistics 2012"*, http://www.who.int/gho/publications/world_health_statistics/2012/en/, (Accessed on March 3, 2013).

[2]Padam Raj Bhatta, 2011, "*Nepal Demographic and Healthy Survey 2011*", Ministry of Health and Population [Nepal], United States Agency for International Development (USAID), New ERA, and Macro International Inc.

[3]Nepal Telecommunication Authority, 2012, "*Management Information System (MIS) report*", Nepal Telecommunication Authority, Kathmandu, Nepal.

[4]E-Network Research and Development (ENRD), 2012, "*Child Protection Application*", unpublished report, Kathmandu, Nepal

[5]Checkland, P. and Scholes, J., 1990," *Soft Systems Methodology in Action*", John Wiley & Sons, Chichester.

[6]Mumford, E., 1995, "*Effective Systems Design and Requirements Analysis: the ethics approach"*, MacMillan, New York.

[7]Emery, F.E. and Trist, E. L., 1960, "*Socio-technical system, in Management Science Models and Technique"s", Vol. 2*, Churchman, C. W. and Verhulst, M. (eds), Pergamon, Oxford.

[8]Checkland, P. and Holwell, S., 1998, *"Information, Systems and Information Systems: making sense of the field"*, John Wiley & Sons, Chichester.

[9]Heeks, R. B.,2008a, "*The ICT4D 2.0 Manifest"o*, Development InformaticsWorking, Paper Series, Paper No. 30, IDPM, University of Manchester.

[10]Madon, S.,1994, "*Designing information systems for development planning"* , Henley, Alfred Waller.

[11]Heeks, R. B. , 2002b, "*i-Development Not e-Development: Special Issue on ICTs and Development*" , *Journal of International Development*, vol.14, no.1, pp. 1-11.

[12]Sein, M. K. and Harindranath, G., 2004, "*Conceptualizing the ICT Artifact: Toward Understanding the Role of ICT in National Development*", The Information Society, vol. 20, no. 1, pp. 15 – 24.

[13]Hickey, S. and Mohan, G., 2004, "*Participation: From Tyranny to Transformation?"*, Zed Books, London.

[14]Heeks, R. B., 1999a, "*Reinventing Government in the Information Age"*, Routledge, London.

[15]Heeks, R. B. ,2006, "*Implementing and Managing eGovernment: An International Text"*, Sage, London.

Contribute of ICT Use to Promote Student-Centered approach in Primary Schools in Mongolia

Student Number: 11M18172 Name: Shotaro Yano Supervisor: Shinobu YAMAGUCHI, Jun-ichi TAKADA

モンゴルの小学校での「子ども中心の指導法」における ICT ツールの活用に関する分析

矢野　晶太郎

近年、モンゴルにおいて、教育の質の向上のために情報通信技術(ICT)の導入と従来の指導法から「子ども中心の指導法」への転換が促進されている。本研究においては、小学校で実際に利用されている各種 ICT ツールが「子ども中心の指導法」に有用であるか分析を行う。その結果、教員は ICT を授業で活用することに積極的であり、ICT ツールは「子ども中心の指導法」を促進させる上で有効なツールということが判明した。反面、機材の不足、ICT を使用して効果的な教材を作成するための知識や技術が課題となっていることが明らかとなった。

1. Background Information

In the early 1990s, Mongolia experienced decentralization and democratization of its government, along with a transition to a free market economy. The education sector also encountered problems such as a fall in the education budget, decreasing literacy rate, urban migration of rural teachers, and also inadequate infrastructure. As a result, the Mongolian government enacted several policies to address these issues described in Table.1.

In 2005 the New Education Standard was introduced to promote student-centered approach, a methodology to make students engaged more in their learning as opposed to a teacher-centered approach. By 2012, the Mongolian government amended the Education Law to encourage the sector to use ICT for further improvement of education quality. Furthermore in 2012, the Ministry of Education and Science (MES) developed "ICT in education policy".

Table 1 Policies related to education

New Education Law (1993, 2003)	Decentralized school management, more flexibility to manage the school curriculum.
New Educational Standard (2005)	Increase the schooling year from 10 years to 12 years, promote the use of student-Centered Approach
Mongolian Government Action Plan (2008-2012)	Improve the training system for teacher with the use of ICT and distance learning, increase the number of PCs in each school, Supply every teacher with a laptop, Connect the schools to the internet
Education Master Plan (2006-2015)	To integrate ICT in teaching and learning
Information and Communication Technology in Education Policy (2012-2016)	To increase the use of e-teaching, e-learning content in Mongolian language in primary and secondary education classrooms/teaching

(Source: created by author, 2012)

1.1 Student-centered approach

Kawaguchi indicated that student-centered approach was derived from Socratic method that teachers try to draw out the answers from learner [1]. Yucel defined that student-centered approach aims at training child according to its own nature, not depending on what adults want; in this way claiming that child will be more creative and freer [2]. The several institutes such as UNICEF, UNESCO and JICA pointed out the important factors of student-centered approach.

- *Leaning is not just about individual comprehension and skills acquisition; it is also about constructing knowledge with others (UNICEF)*
- *To enhance skills for using a wide range of interactive and leaner-centered teaching and leaning strategies that underpin the knowledge, critical thinking, values and citizenship objectives implicit in reorienting education towards sustainable development (UNESCO)*
- *Students take lesson themes as their own and find solutions on their own by using their mind and body, and through interacting with others (JICA)*

In Mongolia, student-centered approach has been introduced MES since 1990s. However the clear definitions of student-centered approach has not been shared in Mongolian context [3].

1.2 Scratch as a tool to creating teaching materials

Scratch is the programming learning software for children was developed by MIT media lab [4]. And in Mongolia, Scratch was introduced for creating teaching materials through educational project since 2011 [5] for the following features: 1) it is free and open source software, 2) Mongolian language can be used, 3) it includes many ready-made materials such illustration, pictures and sound, 4) original materials can be used and 5) it is easy to use.

The feasibility analysis was conducted in 2011 [6]. Teachers indicated that 1) scratch can attract students using animation, 2) scratch can enhance the students' group work and discussion. The result showed that Scratch has potential to support student-centered approach.

2. Objectives of Research

In the current Mongolian education sector, there are two approaches are considered important to improve quality of education. First, introducing ICT tools for managing the information and developing the teaching material can enhance school management and teaching. Second, introducing the student-centered approach to deliver effective lessons to 29 pupils in the classroom teaching [7].

However, definition of student-centered approach is not clearly shared among teachers. Also effectiveness of ICT tools on the student-centered approach has not been assessed. On this point of view, this research focus on two objectives as follow, 1) to identify the key-factors of student-centered approach on Mongolian context and 2) to illustrate how lessons using ICT tools contribute to promoting a student-centered approach in primary schools in Mongolia. The research was mainly conducted in Bayankhongor aimag, with additional information from and Songino Khair Khan district of Ulaanbaatar.

3. Research Methodology

The research consists of three components.

First is clarification of the definition of student-centered approach in Mongolian context. The study was conducted to identify the important factors of student-centered approach using both questionnaire and interview analysis. The professional staff of JICA identified historical information on history and definition of "student-centered approach". Then four professors of Mongolian State University of Education confirmed definition, practices and difficulties of student-centered approach. Further, potential key-factors of student-centered approach were extracted based on the results of these interviews and survey results. In addition, questionnaire was conducted to clarify the definition of student-centered approach among schools. In total 145 out of 204 questionnaire were retuned, yielding 71% response rate.

Second, in the analysis on the current state of use of ICT tools during the implementation of student-centered teaching. Various ICT tools (Computer, LCD Projector, Digital Camera, Video Player, Audio Player, TV, Radio, Power Point, Word, Excel, Scratch and Movie Maker) were evaluated for their usage, effectiveness, and issues through the questionnaire and focus group discussion. A total of 145 questionnaires ware collected (69 from Bayankhongor, 76 from Scongino Khairkhan district), yielding 81% response rate. Furthermore, the responses of Bayankhongor came from 25 out of 27 schools. Therefore results of questionnaire in Bayankhongor could represent of trend of Bayankhongor aimag.

In addition, 28 people in Bayankhongor and 29 people in Songino Khairkhan district participated to focus group discussion to observe the effectiveness of ICT tools, and discussed impression and issues in educational environment.

Third, in the analysis of the effectiveness of Scratch teaching materials through lesson reviews in 4 different primary schools on different regions. This study utilized the classroom observation to know how teacher implement student-centered teaching and the use of Scratch teaching materials through lesson assessment sheet. In total 29 teachers in Bayankhongor and 20 teachers in Ulaanbaatar observed lesson using Scratch.

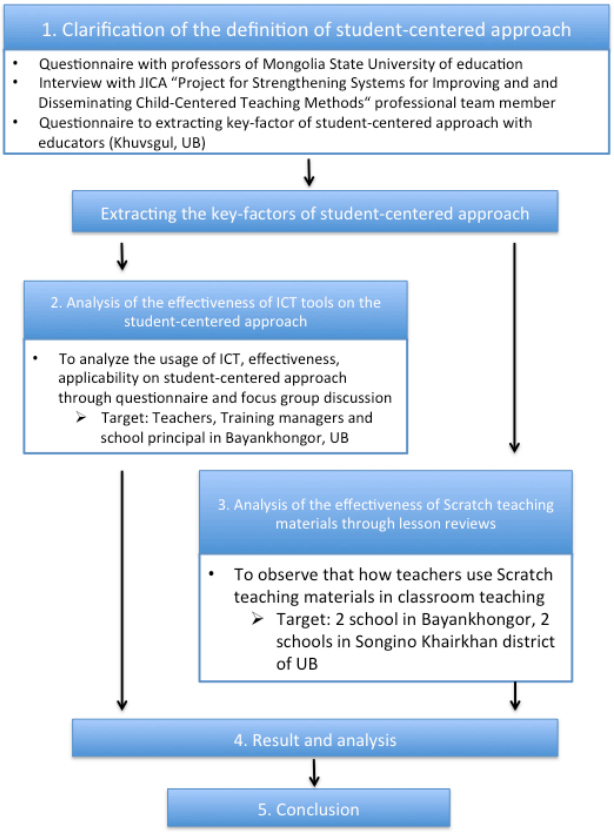

Fig. 1 Overview of research
(Source: created by author, 2013)

4. Findings

4.1 Student-centered approach in Mongolian primary education

Survey and interview results with Mongolian teachers corresponded to the prevailing definition of student-centered approach. It emphasized the importance of placing students as a core part of classroom teaching, through developing curriculum and activities suited for the group of students.

1) Student-centered approach in Mongolia emphasizes on students' creativity, self-learning abilities, problem-solving skills through interesting and innovative classroom activities

Teachers recognize the following three aspects the most important: 1) developing students' potential abilities; 2) activities centering students in classrooms; and 3) creating supportive environment to implement

student-centered learning. Among 12 factors to promote student-centered approach identified by Mongolian teachers, the top three factors are "developing students creativity", "developing self-learning', and "developing students' problem-solving skills". While these top there factors are ranking the highest, it does not mean these or any of the other factors are all required to implement the student-centered approach. Definition of Student-centered approach in Mongolia is in line with definition identified by the existing literatures, but it particularly focus on abilities of the students.

2) Teachers are expected to understand the needs for students by carefully reflecting, age, learning progress as well as level of understanding

According to survey result, to promote student-centered teaching, it is vital that teachers analyze the interest, problem-solving skills of the students, together with learning progress. Building onto the accumulated knowledge and understanding of the students is basis of effective student-centered approach.

3) By introducing student-centered approach, teachers are expected to be equipped with more knowledge and skills

To promote students' participation in classroom activities, as well as to increase motivation of the students, teachers need to learn various teaching methods and teaching skills. Teachers found the difficulty to shift from teacher-centered teaching to student-centered approach. Further, introducing more discussion, group activities, and students' presentation is time consuming and it is difficult to integrate these initiatives within the limited teaching hours. Lack of equipment and facilities also limit participatory activities using ICT tools.

4.2 Use of ICT tools and its effectiveness to promote student-centered approach

Teachers perceive the effectiveness of using ICT tools to promote student-centered approach. Multiple equipment and software are found effective and applicable in primary schools in Mongolia.

1) Teachers are motivated to use ICT tools and frequently use different tools to produce teaching materials

Survey result indicated that 84% of the respondents use computers more than once per week to produce teaching materials. Teachers use Power Point, Words, Excel and Scratch programs for material production, and they are equipped with enough skills to use variety of programs. Further, teachers use computers for self-learning at schools and willing to learn new technology.

2) Teachers consider that use of ICT tools support student-centered approach

Survey result indicated that multiple equipment and software are considered effective and applicable supporting tools to conduct student-centered approach. Concrete reasons include: 1) to attract students interest; 2) to promote students self-learning; 3) to save time (by avoiding writing information on blackboard); 4) to promote new way of information gathering; and 5) to explain difficult concept easy to understand (by using visual materials).

3) Teaching materials produced with software of visual effect was found particularly effective among teachers

Particularly, Power Point, Movie Maker, and Scratch, which enable to create visual materials were found effective to attract students interest, and thus, improved concentration during classroom teaching. According to interviews with teachers, photos, illustration and sounds make students to motivate to learn and participate in classroom activities. Scratch was a good example to keep students' concentration, and thus, was used for "motivating students to learn new subject", and "getting attention among students when important concept were introduced."

4) School leaders and community members expect teachers to use ICT tools into teaching

Reflecting high motivation of teachers to use ICT into teaching, schools provide technical support and ICT training for teachers. Survey result indicates that parents and other community members expect teachers to use computers and other ICT tools at schools.

5) Teachers believe that use of ICT tools to develop teaching materials improve teachers' creativity

The definition of student-centered approach generally focuses on students. However, the survey result illustrated that teachers feel that their skills and creativity have improved through experiences of using different ICT tools and developing various teaching materials. As New Education Standards require local government and schools to integrate local information and available materials, teachers try to be creative in developing own materials. This condition, along with introduction of new tools promoted teachers

to be "creative".

6) Lack of equipment is still an issue to further promote use of ICT

Lack of equipment and facilities also limit participatory activities using ICT tools. Currently, each school is equipped with at least two printers and one LCD projector [9], but this is considered not sufficient for the teachers to conduct classroom teaching using ICT. The condition is even worse where classes are conducted with 2 or 3 shift per day. Addition, at the one of the visited school, teacher couldn't use Scratch effectively due to the LCD projector's mechanical problem. The maintenance of the ICT equipment is also expected to fully utilize the ICT tools in education environment.

4.3 Effective use of Scratch to promote student-centered approach and issues

According to the results of questionnaire, focus group discussion and lesson review, Scratch is useful tool to enhance student-centered approach.

1) Scratch is useful for its visual effect and can be particularly used for introduction/motivation of class lessons

Lesson reviews in Bayankhongor revealed that teachers were creating teaching materials using Scratch with visual aids. Particularly, teachers used animation combining photos, illustrations and sounds, and such teaching materials was useful to get students' interest and to concentration. Teachers also found it useful to promote students" understanding of topics with visual effects. In lesson reviews, it was noticeable that teachers used Scratch for introduction (for attention getter) and identifying the problems.

2) Teaching materials produced by teachers using local materials would further interest students

Students enjoy teaching materials locally available. An advantage of Scratch is that teachers can incorporate own photos, illustrations and sounds to create unique teaching materials. During the lesson reviews, it was observed that students showed strong interest when teachers use familiar photos and information that students find close to, and thus, was promoting student-centered learning.

3) Further teacher training is necessary for the teachers to effectively utilize Scratch for teaching materials

Quality use of teaching materials with Scratch promotes students to be engaged into participatory activities, and thus promote student-centered learning. For many teachers, producing teaching materials with Scratch was new experiences, and thus, a series of training were found necessary, not only to improve skills to operate Scratch but also to incorporate it into curriculum.

5. Concluding remarks

This study identified specific definition of "students-centered teaching" in Mongolian context. Using such definition, the survey was developed and data was collected to illustrate how teachers utilize ICT tools effectively and in applicable manner in classroom teaching.

The study found, teachers have positive perception on the use of ICT tools into teaching and various ICT tools are effective to enhance student-centered approach. ICT use in teaching in current Mongolian primary schools has potential for further development.

This study illustrated the current condition of Bayankhongor case in Mongolia. These findings cannot explain the educational environment in entire Mongolia, but can be shared as useful information for educational sector for further development.

References

[1] Kawaguchi., (2012): Overview of Introducing "Student Centered Approach" – A case study of Malawi-

[2] Yucel, G.,(2009), The effect of Student Centered instructional approaches on student success, Department of Educational Sciences, Gazi University

[3] JICA.,(2005): モンゴル国子どもの発達を支援する指導法改善プロジェクト 実施協議報告書", 平成 18 年 10 月

[4] Scratch.,(2013): For Educators (about Scratch) ,[online], (available) http://scratch.mit.edu/educators/ , (accessed on July, 13 .2013)

[5] Yamguchi Laboratory, (2012): モンゴルにおける持続可能な教員研修のための ICT 教材開発,[online] http://www.yamaguchi.gsic.titech.ac.jp/research/monprintroduce/ (Accessed on July 10th)

[6] Shotaro, YANO, Seregelen Sukhbaatar, Shinobu, YAMAGUCHI.,(2012), Development of Teaching Material for Primary Schools in Mongolia : Lessons from Teachers' Feedback, 56th Annual Conference, Comparative and International Education Society Puerto Rico, April, 2012

[7] Ministry of Education Culture and Science, (2011): Statistical Abstract Education, Culture, Science and Technology, p.16

[8] ADB,(2012): 教育セクターにおける ICT 現状評価広告書, 2012

DATABASE OF METEOROLOGICAL URBAN GEOMETRIC PARAMETERS OF JAPAN AND ITS EXPANSION TO GLOBAL SCALE

Student Number: 11M18143 Name: Takuya MAKABE Supervisor: Manabu KANDA

気象解析のための全日本都市幾何データベースの構築と世界への拡張可能性

真壁 拓也

本論文では，日本全国の建物データを用いた気象シミュレーションのための都市幾何パラメータのデータベースを構築し，詳細な 3 次元都市幾何データベースを用いてその精度を検証した．また，詳細な建物データが未整備である都市へ同種のデータベースを拡張するための手法として，ほぼ全球的に整備され，無償で公開される衛星観測データのみを用いた都市幾何パラメータを推定する手法を提案し，その精度検証を行った．

1 Introduction

Numerous numerical simulations on urban meteorology have been conducted, and the land surface models employed have shown a great progress [1]. Thus, it is of importance that creating detailed geometry database of cities to conduct accurate numerical weather predictions. For example, Chen et al. [2] reports that incorporation of UCM (Urban Canopy Model) [3] to a meso-scale meteorological model WRF can improve reproducibility of the simulation. However, preparation of such database requires a great deal of effort. With a very small number of exceptions, detailed urban geometric database is not available in most of the cities in the world. In this study, we propose a method to estimate urban topography using satellite observational data, which is now open to public inspection. Along with that, database of urban geometric parameters in Japan are created using a detailed building data.

2 Database of Urban Geometric Parameters in Japan

2.1. Data used

The dataset of building heights is taken from a geographic information system (GIS), which is developed and distributed by ESRI Japan, Inc. The dataset contains the category, shape, location, and number of floors of buildings in Japan. Note that one-story buildings are not included in the dataset. On the basis of an assumption that height per floor is 3m, building heights are estimated by multiplying number of floors by 3m. To validate the accuracy of these parameters, a detailed building database, MAPCUBE, was employed. These data contain building height data with spatial resolution of 1 m. In this paper, the data in Tokyo Metropolis are used for the validation of the parameters calculated.

2.2. Calculation of Geometric Parameters

Using datasets mentioned in previous section, urban geometric parameters, including average building height H_{ave}, maximum building height H_{max}, standard deviation of building height σ_H, plane area index λ_p (ratio of area occupied by buildings to the total area), frontal area index λ_f (ratio of area of building walls that face a specific direction to the total area. In this paper, average value of λ_f for 8 different direction is used.), roughness length for momentum z_0, displacement height d, and sky-view factor SVF, are calculated for each 1 km^2 mesh in Japan. Displacement height d and roughness length for momentum z_0 were calculated based on equations proposed by Kanda et al. [4] And sky-view factor is calculated based on equations proposed by Kanda et al. [5]. The distribution of displacement height d is show in Figure 1. Higher values can be observed around major cities such as Tokyo, Osaka, and Nagoya.

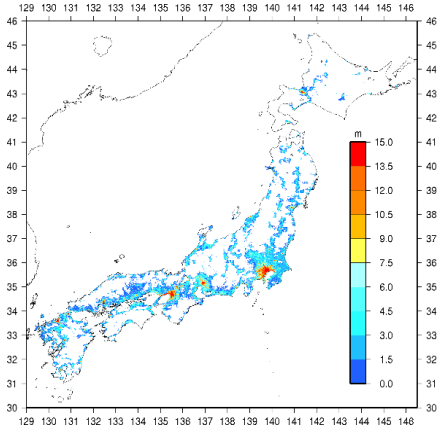

Fig. 1: Distribution of displacement height d across Japan (the color range is not consistent with the actual range)

2.3. Comparison to detailed building data

The calculated geometric parameters are validated by comparing to that based on detailed building height database MAPCUBE. For any parameters, the values from 2 different data sources show very high correlation. However, it is revealed that parameters calculated, except plane area index, tend to be smaller than that based on MAPCUBE (not shown). This might be due to the assumption that height for one floor is fixed to 3m for all kinds of buildings. For the consistency between parameters based on the 2 different data sources, height for one floor is changed according to building categories: 3m for low-rise dwelling houses, and 4m for the other buildings. The modified parameter, H_{ave}, and that from MAPCUBE is shown in Figure 2.

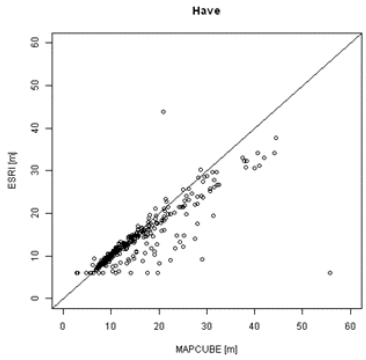

Fig. 2: Relation between average building height H_{ave} based on ESRI and MAPCUBE (for Tokyo Metropolis)

3 Estimation of Urban Geometric Parameters using Satellite Data

Constructing databases of urban geometric parameters requires accurate data of building shapes, which is very costly and are not available in most cities. Therefore, alternative method to substitute these data is of particular importance. In this chapter, urban geometry is estimated based on satellite digital elevation models (DEM), which are available almost anywhere on earth and open to public. Besides, building footprints are estimated by analyzing satellite visible imagery.

3.1. Estimation of Urban Geometric Parameters using Satellite DEM

3.1.1. Data Source

Two DEMs are used to estimate building height distribution. One is called ASTER GDEM2, which is generated from satellite imagery captured by The Advanced Spaceborne Thermal Emission and Reflection Radiometer (ASTER) instrument on-board the National Aeronautics and Space Administration (NASA)'s Terra spacecraft is employed. This DEM is prepared and distributed in cooperation with NASA and the Ministry of Economy, Trade and Industry of Japan [6]. The horizontal resolution of this DEM is 1 arc-second (approximately 30m), and its root-mean-square error (RMSE) in elevation is between ± 7 m in US and ± 15 m in other regions. [7] The other is called GMTED2010 (Global Multi-scale Terrain Elevation Data 2010), which is developed and distributed by the U.S. Geological Survey (USGS) and National Geospatial-Intelligence Agency (NGA). This DEM contains 3 different horizontal resolutions: 7.5 arc-seconds, 15 arc-seconds, and 30 arc-seconds [8]. In this paper, DEM with the resolution of 7.5 seconds is employed. At 7.5 arc-seconds, the RMSE range in elevation is between 26 and 30 m. In addition to terrain elevation, this DEM also has statistical based products, such as average elevation, maximum elevation, minimum elevation, and standard deviation of elevation calculated based on values of 3x3 pixels. Before analysis, horizontal resolutions of 2 DEMs are adjusted to 1 arc-second by bilinear interpolation.

3.1.2. Methodology

To estimate urban geometry, 3 different methods are examined. Procedures of each method are explained below.

a) CIM method:

First, divide the target DEM, ASTER GDEM2 into small areas. The shape of the small area is square, and 3 different sizes are examined: 3x3, 7x7, 11x11 pixels. Then, check if the value of the central pixel is the minimum in the area. If the value is the minimum, keep the value as the representative value of the area. Otherwise, retain null value as the representative value of the area. After this manipulation, pixels with values are concatenated by linear interpolation, and the outcome is regarded as terrain elevation without the infection of artificial objects. Finally, distribution of building height is estimated by subtracting the outcome from the target DEM before manipulation.

b) JM method:

Almost the same as the CIM method, but the central pixel of a small area is replaced by the minimum value of the area.

c) AmG method:

This method exploits one of the statistical based products of GMTED2010, that is, minimum value of each 3 x 3 pixels (GMTEDmin). Building height distribution is estimated by subtracting GMTEDmin from ASTER GDEM2. In this procedure, only the areas that are occupied by buildings are considered according to MAPCUBE.

3.1.3. Result

Figure 3 shows building height distribution estimated by AmG method. It is noteworthy that the higher buildings in the congested areas are captured. Figure 4 shows relation between estimated average building

heights based on the 3 different methods and that based on MAPCUBE. For the CIM and JM methods, regression line is proposed using estimated values larger than 5m. For the AmG method, the estimated values are seemed to be distributed on an exponential curve, so the regression curve is given in the exponential form. Among all the methods proposed, the AmG method shows the highest correlation between the values based on MAPCUBE.

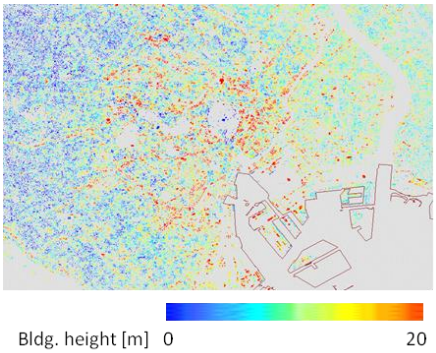

Fig. 3: Distribution of estimated building heights in Tokyo Metropolis. (AmG method)

3.2. Estimation of Building Footprints using Satellite Visible Imagery

3.2.1. Data Source

Satellite visible imagery is retrieved from Google Maps (https://maps.google.com). One image covers an area whose width is 45 arc-seconds in longitude and is 30 arc-seconds in latitude. This area corresponds approximately to 1km^2 in Japan. An image consists of 2340x1940 pixels with 0.5m/pixel in spatial resolution. Each pixel contains 3 bands: Red, Green, and Blue. (see Figure 5.)

3.2.2. Methodology

Supervised classification is conducted using a GIS software ArcGIS. The procedure conducted is described as follows: First, building rooftops, vegetation, and bare soil are extracted manually from images, and create training datasets with them. Then, multi-class supervised classification is conducted using the training datasets. Features in an image are classified to 3 different classes. Figure 6 shows one of the results. Here, 4 different training datasets are examined. After classification, road faces are excluded from the result using road face data contained in the ESRI data. The area of each class is calculated and plane area index is estimated.

Fig. 5: High-resolution satellite image used. Features for training are colored. (Retrieved from Google Maps)

Fig. 6: Result of supervised classification. (Purple: building rooftops, Green: vegetation, Orange: bare lands. Road faces are whitened using ESRI data)

3.2.3. Result

From the results of supervised classification, plane area index is estimated by the equation 6.

$$\lambda_{bldg} = A_{bldg}/A \qquad (6)$$

Where A_{bldg} is the area classified as building rooftops, while A is the total area that an image covers. Additionally, area of vegetation and bare land is

(a) (b) (c)

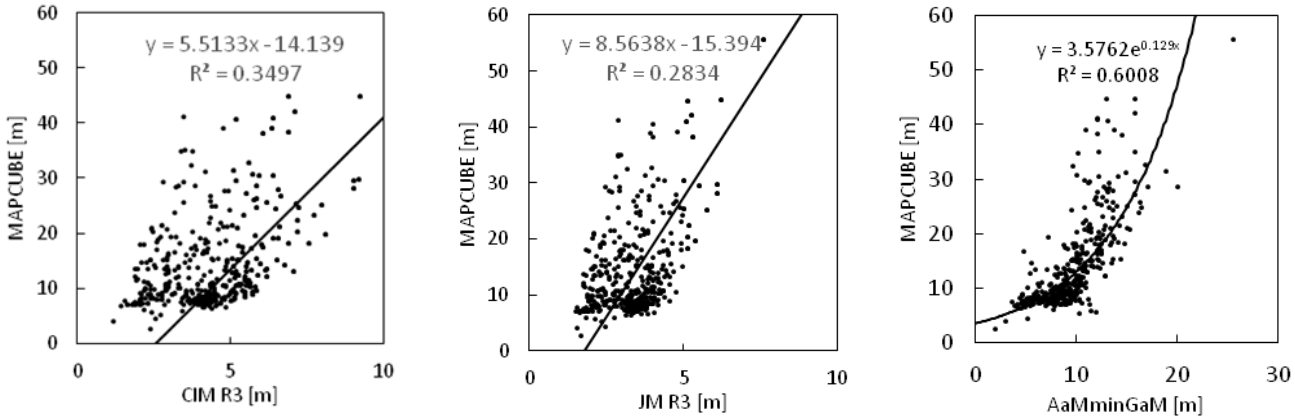

Fig. 4: Relationship between estimated average building heights and that based on MAPCUBE: (a) CIM method, (b) JM method, (c) AmG method.

estimated by the equation 7.

$$\lambda_{V+B} = (A_{veg} + A_{bare})/A \qquad (7)$$

Where A_{veg} is the area classified as vegetation, whereas A_{bare} is that for bare lands. Since appearances of vegetation and bare land are expected to have more homogeneous colors and textures than building rooftops, considering λ_{V+B} has a potential to estimate the real plane area index more accurately than λ_{bldg}. $1-\lambda_{V+B}$ is compared to plane area index based on MAPCUBE, because it can be regarded as the upper limit of the real plane area index λ_p of the area. Besides, it is observed that the classification results are very sensitive to the training datasets and differ depending on the training dataset given. Therefore, the average of results from 4 different training datasets is considered. As expected, estimation using λ_{V+B} showed higher correlation than that using λ_{bldg}. Results for λ_{bldg} and $1-\lambda_{V+B}$ are shown in Figure 7 and 8, respectively.

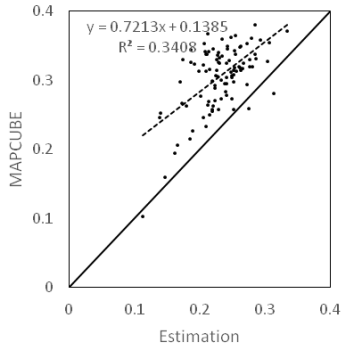

Fig. 7: Relationship between estimated plane area index λ_{bldg} and plane area index λ_{p} based on MAPCUBE.

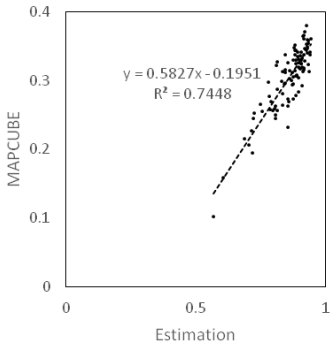

Fig. 8: Relationship between $1-\lambda_{V+B}$ and plane area index λ_{p} based on MAPCUBE.

4 Conclusion

A database of urban geometric parameters in Japan is constructed using a GIS with building data. Also, the methods for expanding the database to cities where detailed building dataset is not available are proposed. The results are summarized as follows:

(a) A database of urban geometric parameters is constructed using a detailed building data. The parameters are compared to that calculated based on a detailed 3D building data, and showed high correlation.

(b) Using DEMs generated from satellite observational data, methods to estimate urban geometry are proposed. And regression curves are proposed as well.

(c) By analyzing satellite visible imagery, building footprints in urban area is estimated.

Reference

[1] Kanda, M.: Progress in Urban Meteorology: A Review, *J. the Meteor. Soc. Of Japan*, 85B, pp.363-383, 2007.

[2] Chen, F., Kusaka, H. et al.: The Integrated WRF/Urban Modeling System: Development, Evaluation, and Applications to Urban Environmental Problems, *Int. J. Climatol.*, Vol. 31, pp.273-288, 2011.

[3] Kusaka, H., and Kimura, F.: Coupling a Single-layer Urban Canopy Model with a Simple Atmospheric Model: Impact on Urban Heat Islands Simulation for an Idealized case, *J. Meteor. Soc. Japan*, Vol. 82, pp.67-80, 2004.

[4] Kanda, M. et al.: A New Aerodynamic Parameterization for Real Urban Surfaces, *Bound. Layer Meteor.*, Vol. 148, pp.357-377, 2013.

[5] Kanda, M., Kawai, T. and Nakagawa, K.: A Simple Theoretical Radiation Scheme for Regular Building Arrays, *Bound. Layer Meteor.*, Vol. 114, pp.71-90, 2005.

[6] Abrams, M., "The Advanced Spaceborne Thermal Emission and Reflection Radiometer (ASTER): data products for the high spatial resolution imager on NASA's Terra platform", *International Journal of Remote Sensing*, Vol. 21, Issue 5, pp. 847-859, 2000.

[7] Hirano, A., Welch, R. Lang, H., "Mapping from ASTER stereo image data: DEM validation and accuracy assessment", *ISPRS Journal of Photogrammetry and Remote Sensing*, Vol. 57, Issue 5-6, pp. 356-370, 2003.

[8] U.S. Department of the Interior and U.S. Geological Survey: Global Multi-resolution Terrain Elevation Data 2010 Open-file report 2011-1073, 2011

LES ANALYSIS OF THE EFFECT OF VEGETATION ON FLOW FIELD IN URBAN AREA

Student Number: 12M18057　Name: Hiroyuki KATO　Supervisor: Manabu KANDA

街区風に及ぼす植生の影響に関する LES 解析

加藤寛之

本論文では，実都市の建物形状及び，植生配置を考慮した数値計算を行い，植生が都市の流れ場及び大気環境に与える影響について検討した．また，都市環境に効果的な植生配置条件の提案も行った．植生を考慮した場合，植生領域において突風率が減少することが定量的に示された．運動量輸送は建物の影響を受けやすく単純に植生割合に依存しないのに対し，スカラー輸送は空間に占める植生割合が直接的に影響することが明らかになった．

1. Introduction

Vegetation in urban area affect wind field, temperature, and scalar concentration field which are generated by complex arrayed buildings. These changes lead to various type of environmental problems like heat island phenomena, air pollution in urban area. Therefore, for urban planning in terms of the practical perspective such as disaster prevention and environmental improvement, it is important to investigate the impact of buildings and vegetation on urban atmospheric environment quantitatively and set an appropriate standard for vegetation arrangement.

Recently, real surface geometry data was developed and used as bottom boundary condition for numerical experiments instead of a horizontally-homogeneous building array. As a result, the flow-field was reproduced with a high degree of accuracy [1]. Also, the modeling of vegetation effect are studied so far to consider its effect into calculation model [2]. However, in these researches, horizontally-homogeneous plant canopy like forests was assumed, and there are few cases which focused on trees on streets and around buildings. Furthermore, large-eddy simulations which consider both real surface geometry and vegetation distribution were hardly done.

In this research, in order to clarify the effect of vegetation on flow-field in real urban areas, buildings and vegetation were incorporated as fluid resistances into large-eddy simulation model. In the consideration part, gust is estimated in terms of the practical perspective, and concentration field analysis was done by using passive scalar. To discuss the impact of vegetation quantitatively, bulk transfer coefficients for momentum and scalar were estimated, which relate to the process of turbulence transfer. Finally, the appropriate vegetation array were proposed.

2. Method

2.1 Basic equations

Parallelized large-eddy simulation model (PALM) was used. The equations used in this model are Navier-Stokes equations (eq.1), the continuity equation (eq.2), and the conservation equation for a passive scalar (eq.3).

$$\frac{\partial \overline{u_i}}{\partial t} + \overline{u_j}\frac{\partial \overline{u_j}}{\partial x_j} = -\frac{1}{\rho_0}\frac{\partial \bar{p}}{\partial x_i} + \varepsilon_{ij3} f \overline{u_j} + \frac{\overline{\theta^*}}{\theta} g \delta_{i3} - \frac{\partial}{\partial x_j}\left(\overline{u_i u_j} - \overline{u_i}\,\overline{u_j}\right) - c_d a U \overline{u_i} \quad (1)$$

$$\frac{\partial \overline{u_i}}{\partial x_i} = 0 \quad (2)$$

$$\frac{\partial \bar{\chi}}{\partial t} + \overline{u_j}\frac{\partial \bar{\chi}}{\partial x_j} = -\frac{\partial}{\partial x_j}\left(\overline{\chi u_j} - \bar{\chi}\,\overline{u_j}\right) - c_\chi a U (\bar{\chi} - \chi_c) \quad (3)$$

Each variable represents as follows; u_i is the velocity in the x_i-direction, p is pressure, ρ_0 is density, χ is scalar concentration, the upper bars denote filtered variables. The vegetation effect is introduced to momentum equations in the final term as external force, where c_d is the leaf drag coefficient, a is the leaf area density, U is the instantaneous local wind speed which is defined as $U = (\bar{u}^2 + \bar{v}^2 + \bar{w}^2)^{\frac{1}{2}}$. In this research, Coriolis force, Buoyancy force, and scalar exchange between leaves and atmosphere are neglected.

2.2 SGS model

SGS flux of momentum and scalar are presented as follows,

$$\left(\overline{u_i u_j} - \overline{u_i}\,\overline{u_j}\right) = -K_m\left(\frac{\partial \overline{u_i}}{\partial x_j} + \frac{\partial \overline{u_j}}{\partial x_i}\right) + \delta_{ij}\frac{2}{3}\bar{e} \quad (4)$$

$$\left(\overline{\chi u_j} - \bar{\chi}\,\overline{u_j}\right) = -K_\chi \frac{\partial \bar{\chi}}{\partial x_j}, \quad (5)$$

where $\bar{e}$ is the SGS kinetic energy. K_m and K_χ are the SGS eddy diffusivities for momentum and scalar respectively, and modeled by using Deardorff's SGS model as follows,

$$K_m = C_M \Lambda \sqrt{\bar{e}} \quad (6)$$

$$K_\chi = -\left(1 + 2\frac{\Lambda}{\Delta}\right)\frac{\partial \bar{\chi}}{\partial x_j}, \quad (7)$$

Λ is the SGS length scale and given by :

$$\Lambda = \min(0.7 \cdot z, \Delta), \quad (8)$$

where Δ is the grid scale, $\Delta = (\Delta x \Delta y \Delta z)^{1/3}$.

3. Simulation settings

3.1 Calculation conditions

Numerical settings of the simulations are shown in Table1. Since the simulations assume thermally neutral stratification, heat flux from the ground and building surfaces are zero. Cyclic boundary conditions were used for both horizontal boundaries, and volume flow was conserved at each time step. 3-dimensional urban surface geometry is reproduced by using MAPCUBE which includes two-dimensional building height information obtained from aerial survey. Passive scalar were supplied from the ground surface constantly.

Table1 Calculation conditions

Domain size	1000m×1000m×600m
Grid size	2m×2m×2m
Initial wind velocity	6.0 m s^{-1}
Boundary condition (x,y)	Cyclic
Boundary condition (Top)	Slip
Boundary condition (Bottom)	No-slip
Calculation time	18000 sec

3.2 Vegetation data

Spatial distribution of vegetated area was obtained from the satellite image of Google by using Feature Analyst for Arc GIS which can derive vegetation area precisely. It is assumed that the height of tree is set a constant value of 15 m, and leaves exist above 3m where fluid feels a resistance. Drag coefficient and leaf area index are 0.2, 0.3 m^2m^{-3} respectively.

3.3 Calculation area

Four different areas were chosen in Tokyo. Shinjuku is a skyscraper, Shibuya is a commercial area, Denenchofu is a residential area, and Roppongi is also a commercial area and has a high-rise building. The example of distribution of vegetation and building height are shown in Fig1, and geometric parameters of each areas are shown in Table2. Three different

simulations were conducted for each area by changing the amount of vegetation as follow; (a) no vegetation exist (Noveg), (b) real vegetation distribution were considered (Real), (c) all ground is covered by vegetation (Fill).

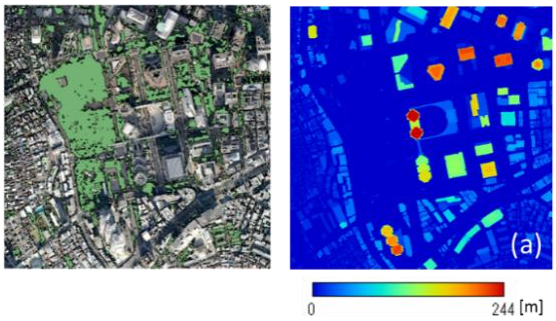

Fig1 Left: vegetation distribution
Right: building height map

Table2 Surface geometric parameters

	Shinjuku	Shibuya	Denenchofu	Roppongi
λ_p	0.30	0.38	0.34	0.34
λ_f	0.59	0.62	0.25	0.43
H_{ave}	52.64	28.31	7.72	23.53
H_{max}	244	188	42	256
σ_H	60.28	21.10	4.03	34.47

4. Result & Discussion

4.1 Turbulent statistics

The effect of vegetation on the streamwise velocity and Reynolds stress were examined. It is found that horizontally-averaged streamwise velocity decreases near the ground due to vegetation for all areas. In Denenchofu, mean streamwise velocity becomes lower at entire level of the numerical domain. However, the decline of mean streamwise velocity in the other areas is enclosed at close to the ground. The magnitude of peak Reynolds stress increases with an introduction of vegetation in most cases since vegetation acts as larger aerodynamic drag on fluid.

4.2 Gust analysis

Gust is the strong wind which blows locally and instantaneously. It is quantified as U_{max}/u_* in this research, where U_{max} is the maximum wind speed of the last 30 minutes of calculation, and u_* is the friction velocity. Left of Fig2 is the Probability density function of each vegetation case in Shinjuku. With introduction of vegetation, occurrence of strong gust decreases and the gust factor becomes less than 4 in all areas of case 'Fill'. Right of Fig2 is the contour map near surface, which shows the difference between the gust factor of 'Real' and that of 'Noveg'. An introduction of vegetation decreased gust factor in most area at close to the ground, however, those increased in some areas; such as main street with no trees and open area behind buildings.

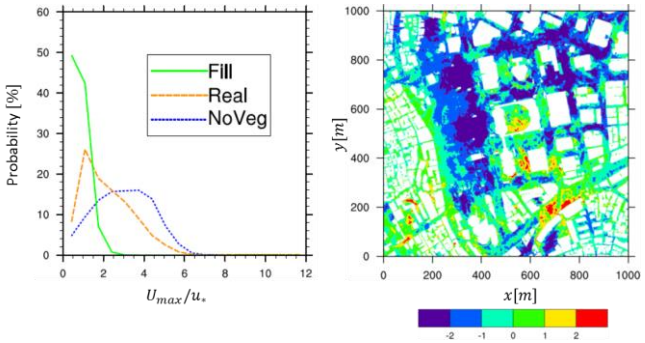

Fig2 Left: Probability density function of gust factor
Right: Gust factor difference between 'Real' - 'Noveg'

4.3 Scalar concentration field

Fig3 shows the scalar concentration map in Shinjuku. Scalar concentration increased at the area where the vegetation covered. This is because vegetation suppressed the turbulent mixing between in and above the vegetation canopy and scalar, which is released from the ground, is kept near the ground. Therefore, horizontally-averaged scalar concentration is correlated to vegetation ratio (Fig4).

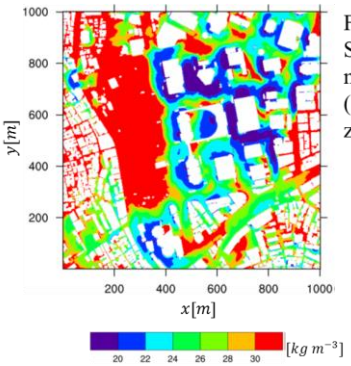

Fig3
Scalar concentration map
('Real', Shinjuku, z=2m)

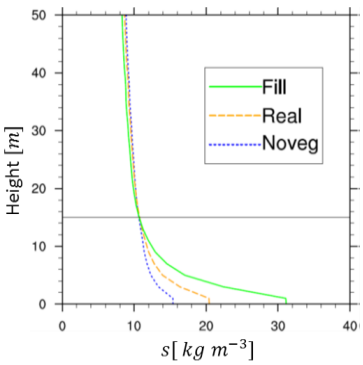

Fig4
scalar concentration profile near surface (Shinjuku)

4.4 Bulk transfer coefficient

Fig5 shows the effect of vegetation on the bulk transfer coefficients for momentum. Vertical axis is the value derived by predicted aerodynamic parameters, and Horizontal axis is that derived by results of LES. There are some biases, however, it can be said that the prediction equation is sufficient to estimate the urban aerodynamic parameters. Generally, vegetation has small impact on these coefficients for momentum. In Shibuya and Shinjuku, the coefficients are smallest in 'Real'. It means that transportation of momentum doesn't depend on vegetation ratio directly. Fig6 shows the relation between the bulk transfer coefficients for scalar and vegetation ratio. With increasing in vegetation ratio, coefficients for scalar decrease and the variation become smaller. Therefore, transportation of scalar depends on the vegetation ratio directly.

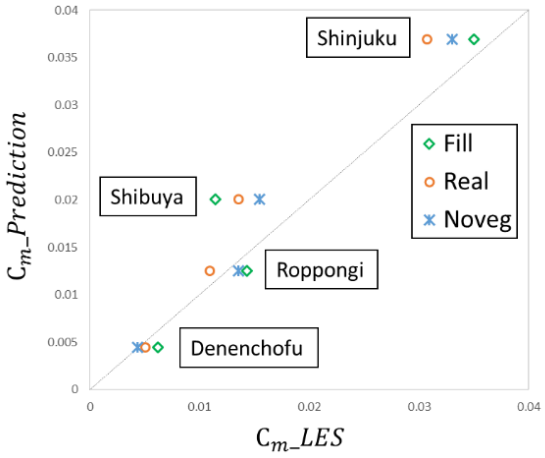

Fig5 Prediction versus LES results

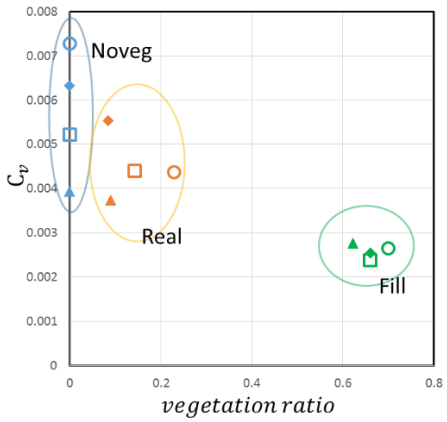

Fig6 Bulk transfer coefficients for scalar versus vegetation ratio
(○:Shinjuku □:Roppongi △:Shibuya ◇:Denen)

5. Conclusion

The effect of vegetation on flow-field in real urban areas is examined in terms of gust, scalar concentration, and momentum and scalar transports.

The occurrence of gust and the magnitude of gust factor can be reduced and scalar concentration increased with the introduction of vegetation. Scalar transport depends on the vegetation ratio, while momentum transport depends on the surface geometry predominantly.

References

[1] Kanda, M., Inagaki, A., Miyamoto, T, Gryschka, M, Raasch, S. (2013) : A New Aerodynamic Parametrization for Real Urban Surfaces, Boundary-Layer Meteorology, Vol48, pp. 357-377.

[2] Watanabe, T. (2004) : Large-eddy simulation of coherent turbulence structures associated with scalar ramps over plant canopies, Boundary-Layer Meteorology, Vol112, pp.307-341.

[3] Kanda, M., Moriizumi, T. (2009) : Momentum and heat transfer over urban-likes surfaces , Boundary-Layer Meteorology, Vol131, pp385-401.

[4] Letzel, MO., Krane, M., Raasch, S. (2008) : High resolution urban large-eddy simulation studies from street canyon to neighborhood scale, Atmospheric Environment, Vol42, pp.8770-8784.

Research on Stochastic Typhoon Model in Low Latitudes of Northwest Pacific Ocean

Student Number: 12M18063 Name: Sarii KAWAI Supervisor: Hiroshi TAKAGI

北西太平洋低緯度海域を対象とした確率的台風モデルに関する基礎的研究

河合 彩里伊

将来的な台風発生の予期・予防は防災上重要な課題である．日本を含む北西太平洋中緯度海域に着目した確率的台風モデルはこれまでにも幾つか提案されているが，フィリピンやベトナムなど低緯度海域に焦点を当てたモデルは提案されていない．本研究では1951年から2012年の台風経路データに基づき，北西太平洋における台風の発生特性や強度特性を分析し，低緯度海域における台風発生位置を確率的に予測するモンテカルロ法に基づく確率的台風発生モデルを作成した．過去の発生頻度および空間的な広がりと比較した結果，概ね妥当な結果を与えることが分かった．

1. Introduction

In the last few years, strong tropical cyclones have unexpectedly occurred in lower-latitudes where used to be almost free from tropical cyclones, such as Typhoon Haiyan in 2013, Typhoon Bopha in 2012 and Severe Tropical Storm Washi in 2011. These tropical storms have caused a lot of casualties and damaged properties due to land slide, flooding and storm surge. The damage due to tropical cyclones can be exacerbated particularly in lower-latitudes due to lack of people's awareness for tropical cyclones. Thus, assessing occurrence of these lower-latitude tropical cyclones is essentially important for achieving disaster risk reduction.

Many studies on the development of stochastic typhoon model for the mid-latitude areas of northwest Pacific Ocean have been carried out to date, particularly focusing on the typhoons making landfall in Japan. However the studies focusing on lower-latitudes of northwest Pacific Ocean encompassing such as the Philippines and Vietnam have not been established so far yet. Thus, a stochastic typhoon model focusing on lower-latitudes needs to be developed to predict the future possibilities of lower-latitude tropical cyclones.

Typhoon track data (called Best Track Data) between 1951 and 2012 provided by JMA is used in the present research, and the total number of tropical cyclones in the best track data is 1,619. Though it covers more than 60years, it may be insufficient to predict the future occurrence of unexpected severe tropical cyclones in lower-latitudes as the data does not necessarily contain historical large typhoons which may only occur once every 100 years or further smaller chances. In case the data available is limited, a stochastic model is often utilized in predicting future possibility of severe disasters. Thus the authors try to develop the stochastic model which is able to generate future possible devastating tropical cyclones.

2. Analysis and extraction of tropical cyclone data

To establish the stochastic typhoon model which is able to deal with typhoons traveling in lower latitudes, historical tropical cyclones occurred in such areas first needs to be separated from the entire paths in Northwest Pacific Ocean.

2.1 Analysis of tropical cyclone data

The Best Track Data between 1951 and 2012 in northwest Pacific Ocean were examined to understand general trends of tropical cyclones in terms of tropical cyclone genesis, annual frequency and travel direction.

(i) Tropical cyclone genesis

The map showing the locations of tropical cyclone genesis of a total of 1,619 tropical cyclones between 1951 and 2012 is shown in Fig.1. The point of tropical cyclone genesis indicates the location at which tropical depression became a tropical storm of which wind speeds exceed 17 m/s.

As Fig.1 shows, some of tropical cyclones passed through the lower-latitudes, contrary to the fact that the Coriolis force can be too small to generate the whirlpool of the tropical cyclone. This kind of unexpected tropical cyclone path can occur partly because 1) a tropical depression which is generated at middle latitude goes southward and developed into tropical storm at lower latitude or 2) sea surface temperature has been rising by the global warming. However, the behavior of tropical cyclone is essentially complex phenomenon with many uncertainties which are predominated by stochastic natures. Regarding climate change effects, it is confirmed that sea surface temperature rose by 0.45℃ for this 100 years. However the relationship between the global warming and the annual number of tropical cyclones is not clear scientifically.

(ii) Tropical cyclone path

The traveling paths of the total of 1,619 tropical cyclones are shown in Fig.1.

According to the Fig.1, there appear to be two distinctive patterns, namely (1) tropical cyclones traveling westward nearly in parallel to the equator, and (2) tropical cyclones traveling westward and turn their courses to northeastward with the influence of westerlies blowing around N30°. To develop a stochastic typhoon model for predicting the future occurrence of lower-latitude tropical cyclone, cyclones which primarily travel westward and affect damage to lower latitudes need to be distinguished from others.

(iii) Traveling angle

Distribution of angles between the locations where tropical cyclones are generated and disappeared is shown in Fig.2. Angle 0° shows tropical cyclones traveling in an eastward direction, 90° in a northward, and 180° in a westward respectively.

According to the Fig.2, there exist two types of distributions, (a) angle from 0 to around 125 and (b) angle from around 125 to 360. Tropical cyclones traveling to northeast are considered to be included in (a) and tropical cyclones traveling to west from east are considered to be included in (b). Thus (b) needs to be extracted from others to develop stochastic typhoon model focusing on lower-latitudes.

(iv) Latitude where tropical cyclones disappeared

Distribution of latitudes where tropical cyclones disappeared is shown in Fig.3.

According to the Fig.3, there exist two distinctive patterns of distributions, (c) latitude from N 0° to around N 28° and (d) latitude from around N 28° to N 50° . Tropical cyclones traveling westward from east are considered to be included in the group of (c). Tropical cyclones traveling northeastward are considered to be classified in (d). Thus (c) needs to be extracted from others to develop stochastic typhoon model focusing on lower-latitudes.

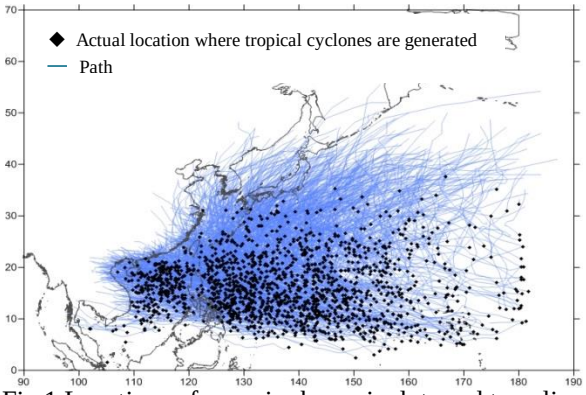

Fig.1 Locations of genesis shown in dots and traveling paths of tropical cyclones between 1951 and 2012.

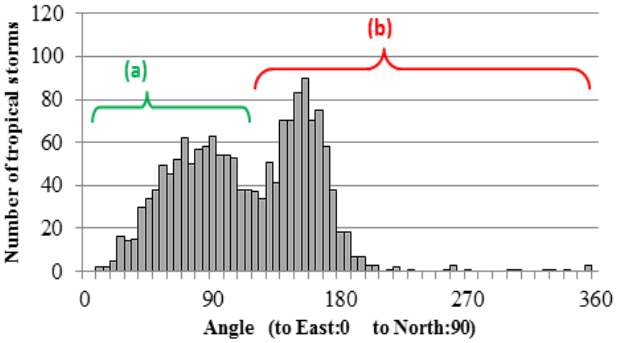

Fig.2 Azimuth from original locations to locations disappeared

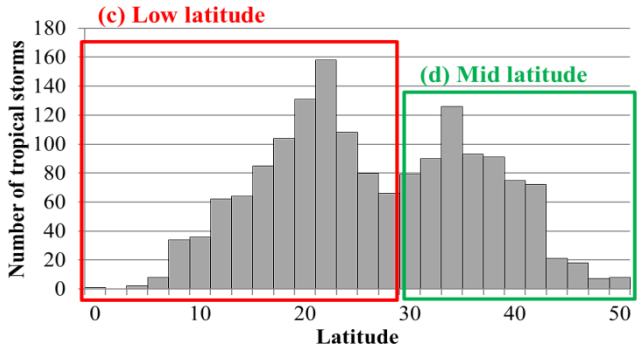

Fig.3 Latitudes where tropical cyclones disappeared

2.2 Extraction of tropical cyclone data

Historical tropical cyclone data mainly influencing on lower-latitudes are extracted in reference to two separation methods mentioned in the previous section, namely (iii) traveling angle and (iv) latitude where tropical cyclones disappeared.

2.2.1 Extraction with angle

Tropical cyclones traveling northeastward can be eliminated with the angle between the locations where tropical cyclones occurred and disappeared as mentioned in chapter 2.1 (iii). To extract tropical cyclones which were classified as (b); angle from around 125 to 360, composition of two gauss functions is applied to represent the distribution of traveling angles. The coefficients of the gauss function were decided as shown in Eq.1 and 2, adjusting the correlation between the proposed function and actual angles to be a maximum value. Fig.4 shows two gauss functions and composed value.

$$g(x) = 0.07 \cdot exp\left(\frac{-(x-82)^2}{2 \cdot 32^2}\right) \quad \cdots\cdots\cdots\cdots \text{(Eq. 1)}$$

$$g(x) = 0.091 \cdot exp\left(\frac{-(x-155)^2}{2 \cdot 16^2}\right) \quad \cdots\cdots\cdots\cdots \text{(Eq. 2)}$$

A total number of 654 tropical cyclones are classified as (b) and applied with Eq.2 to be eliminated from the original set of tropical cyclones which includes the total of 1,619 tropical cyclones observed between 1951 and 2012.

However, the extraction with angle seems not to be enough to thoroughly separate tropical cyclone data in lower latitudes because some tropical cyclones still appear in middle latitudes.

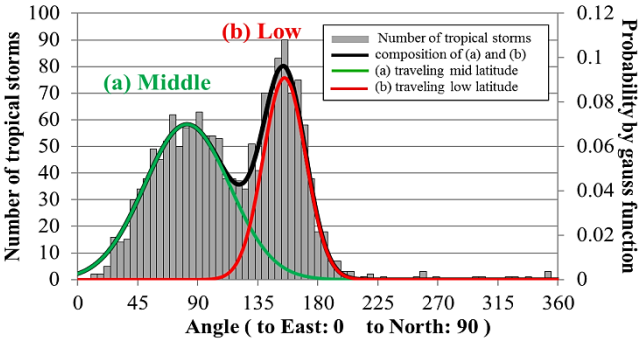

Fig.4 Gauss functions of angles

2.2.2 Extraction with latitude

With still unwilling tropical cyclone paths as described in the previous section, the revision of the extraction method is further required to improve the accuracy of stochastic typhoon model.

To extract tropical cyclones which were classified as (c), tropical cyclone data whose latitude where they finally disappeared in the middle latitudes (higher than N 30°) was also eliminated.

A total number of 607 tropical cyclones classified as (b) and (c) were finally extracted from the original data, and they are shown in Fig.5. It can be confirmed that

extracted 607 tropical cyclones mostly move within the lower-latitude band.

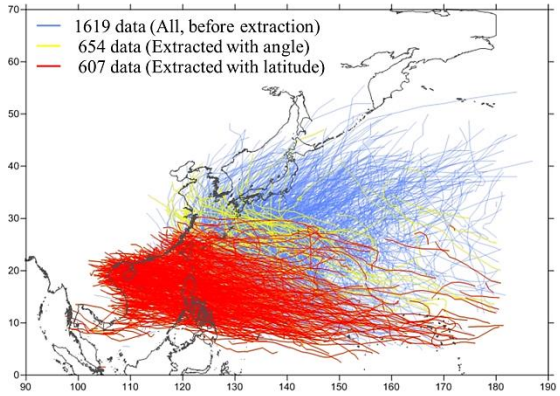

Fig.5 Extraction of tropical cyclone data

3. Development of stochastic typhoon model

To predict the future occurrence of lower-latitude tropical cyclones, a stochastic typhoon model especially focusing on lower-latitudes needs to be developed on the basis of a long-term historical typhoon records.

Parameters on tropical cyclones derived in chapter 2 are used to develop the stochastic typhoon model in chapter 3. The calculation performs the iterative calculation based on a Monte-Carlo method that changes a random number and estimates a probability of typhoon occurrence at given location. Stochastic typhoon model which estimates the location where tropical cyclones will be generated has been developed in this study, so programing a model about tropical cyclones' path and strength makes this model upgraded.

3.1 Monte Carlo method

Numerical simulation by the Monte Carlo method uses random numbers which have been produced many times according to a given probability distribution function. Therefore, the probability distribution has to express actual phenomenon precisely and random numbers has to be produced so that probability distribution is reflected correctly.

Multiplication and division method is adopted to generate uniform random number u_i, as Eq.3, 4 and 5. In Eq.3, $\mathrm{mod}(ax_n, \mathrm{m})$ is the surplus that m divides ax_n.

$$x_{n+1} = mod(ax_n, m) \quad (n = 1,2,\cdots) \quad \cdots\cdots\cdots (\mathrm{Eq.3})$$

$$x_0 = b \quad \cdots\cdots\cdots\cdots\cdots\cdots\cdots\cdots\cdots\cdots (\mathrm{Eq.4})$$

$$u_i = x_i/m \quad (i = 0,1,2,\cdots) \quad \cdots\cdots\cdots\cdots\cdots\cdots (\mathrm{Eq.5})$$

Using $u_j$calculated above, Box-Muller method is adopted to generate random numbers; Y which reflect normal or log-normal distributions as Eq.6 and 7. M is mean value and SD is standard deviation.

$$X = \sqrt{-2logU}\, cos(2\pi V) \quad \cdots\cdots\cdots\cdots\cdots (\mathrm{Eq.6})$$

$$Y = SD * X + M \quad \cdots\cdots\cdots\cdots\cdots\cdots\cdots\cdots (\mathrm{Eq.7})$$

3.2 Calculation process

The flow of the proposed stochastic typhoon model is shown in Fig.6. The number of repetition number N was decided as 1000 in this study, after examining stability of the calculation results for many settings with different N values.

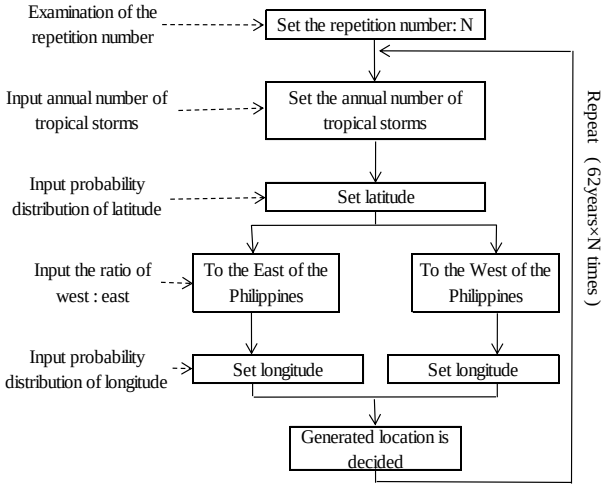

Fig.6 Flowchart of proposed stochastic typhoon model

3.3 Proposed model

3.3.1 Probability distribution function of each parameter

To develop a stochastic typhoon model, probability distribution which can reasonably represent the extracted 607 tropical cyclone data is needed to be assumed. Normal distribution or lognormal distribution was applied for probability distributions for this purpose. However, it was found that two associated parameters of mean and standard deviation without adjustments many produce inconsistent results at a specific part of the areas (e.g. unrealistic tropical cyclone generation in Eurasian Continent). Thus, the authors introduce adjustment coefficients for modifying the mean and standard deviation to fit the probability distribution with the actual distribution.

(I) Annual number of the tropical cyclones

Lognormal distribution is applied to represent annual number of tropical cyclones with increasing the mean vale by 4.8 % and decreasing the standard deviation by 20.8 % from these unadjusted values.

It should be noticed that in Fig.7 a peak of the annual frequency of tropical cyclones appears at the number of 5 which is the smallest number among all the numbers of frequency in the range between 5and 21. However, it appears that the curve would be unexpectedly biased towards smaller side if such small number is included in determining the distribution. Though it may not correct scientifically, the frequency of 5 in Fig.7 was intentionally eliminated as the frequency of tropical cyclones genesis should not be underestimated from a viewpoint of the disaster prevention.

(II) Latitude where tropical cyclones are generated

Normal distribution is simply applied to represent latitudes where tropical cyclones are generated without any modifications for parameters.

(III) Longitude where tropical cyclones are generated

Tropical cyclone cannot be generated on the Philippines' land. Therefore, the tropical cyclones generated around E 120° need to be removed, and consequently the distributions in terms of longitude would be prepared for both in the east side and west side. When a distribution is applied without considering the Philippines' land, tropical cyclones are generated on the Philippines' land unrealistically. Tropical cyclone data needs to be divided into the east side and west side of the Philippines and applied to probability distribution for each. West side is to the west of E 122° , and east side is to the east of E 122° . According to the tropical cyclone data for these 62 years, the ratio of the tropical cyclone generation between west side and east sides is 0.277: 0.723. Thus when the calculated random numbers (which would be within the range between 0 and 1) indicate less than 0.277, the distribution of west side is applied to calculate the longitude at which tropical cyclone occurs.

Normal distribution is applied to the calculation of the west side's longitude, with increasing the mean by 0.16 % and decreasing the standard deviation by 8.01 % than the actual data to modify the width narrower. On the other hand, lognormal distribution is applied to the calculation of the west side's longitude, with decreasing the mean by 1.2 % to slightly shift the distribution towards west and decreasing the standard deviation by 3.13 % than the actual data.

To decrease the expected number of tropical cyclones' generation around E 120° , tropical cyclone data to the west of E 124° is used to examine probability distribution of longitude about the west side and tropical cyclone data to the east of E 124° is used to examine probability distribution of longitude about the east side. As the result of composing these two distributions, the expected number of tropical cyclones which were generated on the Philippines' land could be decreased. Actual data of longitude and two types of distributions are shown in Fig.8.

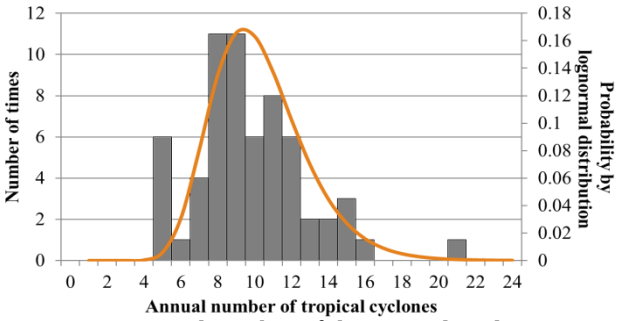

Fig.7 Annual number of the tropical cyclones

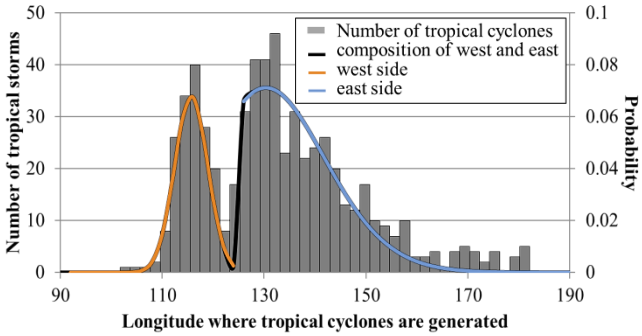

Fig.8 Distribution of longitude where tropical cyclones are generated

3.3.2 Results of simulation

As the result of stochastic typhoon model, expected number of tropical cyclones in every 2° ×2° grid and actual location where tropical cyclones are generated are shown in Fig.9.

Correlation of calculation results and actual data on annual numbers of tropical cyclones and location where they are generated is higher than 0.87. And the results of the generation frequency and the spatial distribution show a proper result with the model.

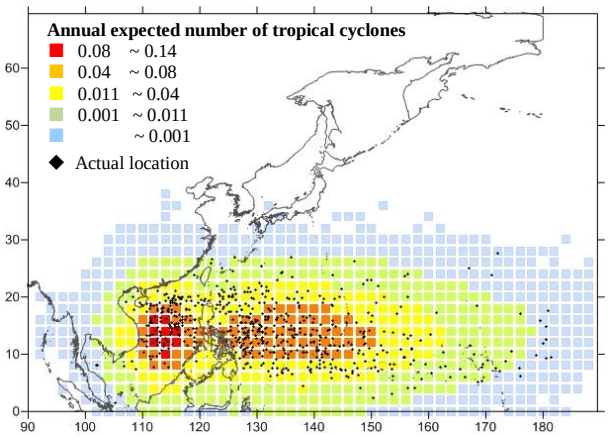

Fig.9 result of stochastic typhoon model

4. Conclusion

In this research, 1) tropical cyclones in Northwest Pacific Ocean between 1951 and 2012 were examined to identify characteristics of tropical cyclone genesis location and frequency using the Best Track Data of JMA. 2) Tropical cyclones which move westward were extracted in reference to both the traveling angles from the origin and the latitudes where they disappeared. 3) Stochastic typhoon model which is able to predict the occurrence of future possible significant tropical cyclones was developed based on Monte Carlo method.

5. References

[1] Jonas Rumpf, Helga Weindl, Peter Hoppe, Ernst Rauch, Vilker Schmidt, "Stochastic modeling of tropical cyclone tracks", 2007

[2] Hiroyasu KAWAI and Noriaki HASHIMOTO, "Evaluation of Occurrence Probability Distribution of Extreme Storm Surges Using Stochastic Typhoon Model", technical note of the port and airport research institute No.1122, 2006

[3] Tomohiro YASUDA, Kei ANDO, Nobuhito MORI and Hajime MASE, "Prediction and Stochastic Modeling of Future Typhoon Characteristics based on AGCM Projections under Global Warming Scenario", 2010

[4] 國富將嗣, "高潮と高波の同時生起確率特性に関する研究", pp.43-80, 2005

COMPOSTING BY INOCULATION OF FUNGUS THAT DEGRADES ANTIMICROBIAL COMPOUNDS PRESENT IN THE COMPOST RAW MATERIAL PRETREATED USING SUB-CRITICAL WATER

Student Number: 12M18034　Name: Akiko OINUMA　Supervisor: Kiyohiko NAKASAKI

亜臨界水処理した生ごみ中に含まれる阻害物質の分解菌の単離および単離菌の接種によるコンポスト化

生沼　晶子

近年、有機性廃棄物を資源化する前処理として亜臨界水が注目されており、コンポスト化の前処理としても期待された。本研究では、食品残渣の亜臨界水処理により微生物活性を阻害するフルフラール類が生成されるのでそのままではコンポスト化できないが、新たに発見したフルフラール類を分解する糸状菌を接種することにより可能になること、また食品残渣を 160℃の亜臨界水で前処理するとコンポスト化 10 日間で 186%以上の GI を達成し、高速コンポスト化が可能であることを確かめた。

1 Introduction

Composting is one of the methods for treating organic waste. Among waste materials, organic fractions such as food waste originating from households, restaurants, and food processing factories can be reclaimed as compost for agricultural use [1].

Development of an accelerated composting method has been expected to treat a large amount of food wastes rapidly. In recent years, food wastes has been treated by sub-critical water based on an assumption that the breaking up of the food waste by the pretreatment using sub-critical water would make the food wastes more easy to be degraded by the microorganisms. However, the generation of 5-hydroxy methyl furfural (5-HMF) and 2-furfural (Furfural) during the sub-critical water pretreatment has been pointed out. Both the 5-HMF and furfural are known to have the inhibitory effect on the microbial activity and the efficacy of the sub-critical water pretreatment came to be doubted. In this study, we investigated the effect of the sub-critical water pretreatment of the food waste on the performance of the composting using the treated food waste as raw material.

2　Material & Methods

2.1　Organic matter decomposition rate and the generation of 5-HMF and furfural

The rabbit food and rice were mixed at a ratio of 4:1 to prepare the representative model of food waste. 4 kinds of organic acids are characteristic of food waste: acetic acid, propionic acid, butyric acid, and lactic acid [2]. These were all added to the reaction mixture to achieve adjusted concentrations of 2.90, 3.02, 2.43, and 12.45 g/kg-ds for acetic acid, propionic acid, butyric acid, and lactic acid, respectively. The food waste and sawdust were mixed at a ratio of 10:9 and then, the total 20g-ws of the reaction mixture was treated by sub-critical water for 30 min at 160, 180, 200, 220, and 240ºC. After the treatment, the organic matter decomposition rate was calculated from ash contents of the reaction mixture before and after treatment (1). The concentrations of 5-HMF and furfural in the samples were determined by high performance liquid chromatography (HPLC).

$$\text{Organic matter decomposition rate}(\%) = \left(1 - \frac{100 - \mathrm{Ash}^{t}}{100 - \mathrm{Ash}^{0}} \times \frac{\mathrm{Ash}^{0}}{\mathrm{Ash}^{t}}\right) \times 100 \quad (1)$$

Ash^{0}：Ash content before treatment (%)
Ash^{t}： Ash content after treatment (%)

2.2 Composting of food waste after sub-critical water pretreatment and isolation of fungus decomposing the 5-HMF and furfural

Food wastes and sawdust were mixed at a ratio of 2:1 on wet weight basis and the mixture was treated by sub-critical water at 180°C for 30 min to prepare the treated raw material. The treated raw material was mixed with a commercial seeding material at a ratio of 19:1 on dry weight basis and then, the moisture content and the pH were adjusted to 50% and 5.0. At the start of composting, approximately 3000 g of the raw compost mixture was put into the reactor, diameter: 300 mm and depth: 400 mm (Fig. 1). Two types of seeding materials, Compost product A and B were used for the Run A1 and B1, respectively. Temperature was controlled at 30°C until the third day

and then, raised to 60°C at a constant rate of 2.5 °C h^{-1}, and the 60°C was maintained until the tenth day. The composting runs were carried out for 10 days. At the time of turning, approximately15 g of compost was withdrawn from the reactor at every day. The degradation of organic matter was monitored by measuring CO_2 evolution rate, expressed in moles of CO_2 evolved per unit of dry solid compost material weight per day. In addition, a fungus was isolated from third day sample in Run A1 and identified by determining the base sequence of the ITS1, 5.8S, ITS2 gene in the genome of isolated fungi.

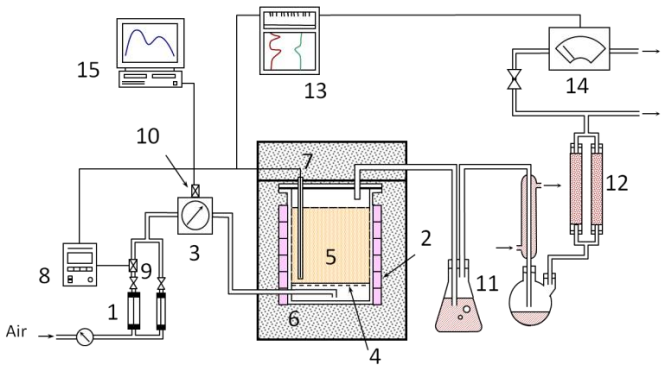

1. Flow meter
2. Ribbon heater
3. Gas meter
4. Perforated plate
5. Reactor
6. Styrofoam insulator
7. Thermocouple
8. Temp. controller
9. Solenoid valve
10. Pulse transmitter
11. Ammonia trap
12. Silicagel adsorber
13. Recorder
14. CO_2 analyzer
15. Micro-computer

Fig. 1 Schematic diagram of the composting system.

2.3 Decomposition of 5-HMF, furfural by the isolated fungus in the liquid culture

PD liquid medium was added with 5-HMF and furfural to the final concentrations of 7g/L and 0.4g/L, respectively. The prepared medium with and without isolated fungus was Run A2 and B2. The FA13 was stored in a -80°C freezer and precultured twice in potato dextrose liquid medium at 30°C while shaking to prepare the inoculum. Upon inoculation, the concentration of FA13 was adjusted to 10^5 CFU/ml of the raw compost mixture. Run B2 was the control without inoculation of FA13.

2.4 Degradation of 5-HMF and furfural in the after sub-critical water-pretreated food waste using the isolated fungus

The compost raw material (same as 2.2) was mixed with a commercial seeding material of compost product B in a ratio of 19:1 on dry weight basis and then, the moisture content and the pH were adjusted to 50% and 5.0, respectively. The compost row material with and without the isolated fungus was Run A3 and B3. At the start of composting, approximately 12 g of the raw compost mixture was put into the reactor (Fig. 2). The temperature was controlled similarly as described at 2.1. Two composting runs, i. e., Run A3 and B3 were carried out for 10 days. Changes in the concentration of the 5-HMF and furfural in the composting runs were determined by HPLC.

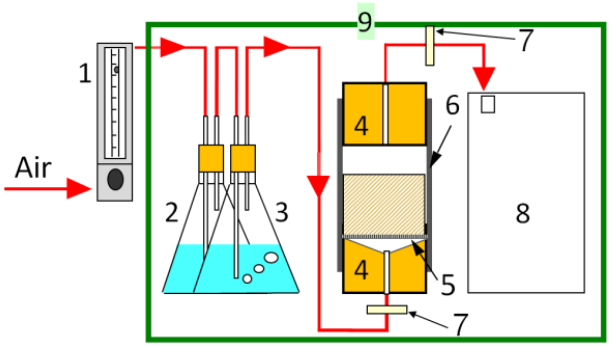

1. Flow meter
2. CO_2 trap
3. Bubbler
4. Rubber plug
5. Stainless screen
6. Pylex glass
7. Membrane filter
8. Tedlar bag
9. Incubator

Fig. 2 Schematic diagram of the composting system.

2.5 Composting of food wastes treated by sub-critical water with different heating conditions

The same mixture same as 2.1 was prepared and then, treated by sub-critical water for 30 min at 160°C (Run B4), 200°C (Run C4), 240°C (Run D4). In addition, Run A4 was carried out with the row mixture. The mixtures prepared were mixed with seeding material of compost products at a ratio of 19:1 to prepare the compost raw materials. The moisture content and pH of the compost raw materials were adjusted to 50% and 5.0, respectively. At the start of composting, approximately 10 g of each compost raw material was put into the mini reactor. The temperature was controlled at 30°C until the fifth day and then, raised to 60°C at a constant rate of 2.5 °C h^{-1}, and the 60°C was maintained until the tenth day. On the fifth day of composting, The moisture content and pH was adjusted to 50% and 8.0. The composting runs were carried out for 10 days. The conversion of carbon at a given compost time was defined as a molar ratio of carbon loss (as CO_2) to the total carbon present in the rabbit food and rice of raw compost material. Germination index (2) were calculated for zero and tenth day compost sample of A4, B4, C4, and D4 to evaluate the matulity [3].

$$\text{Germination index} = \frac{(\%\ \text{seed germination}) \times (\%\ \text{Shoot length})}{100\%} \quad (2)$$

3 Results & Discussion

3.1 Degree of organic matter decomposition and the generation of 5-HMF and furfural

Percentage of organic matter decomposition was 6.3, 16.1, 26.1, 37.6, and 56.1% in 160, 180, 200, 220, and 240 ºC, respectively. The case of 240 ºC was the highest organic decomposition rate in 160-240 ºC. In addition, the concentration of 5-HMF was 1.32, 5.30, 3.05, 0.50, and 1.10 and furfural was 1.15, 4.67, 3.21, 1.14, and 0.06 in 160, 180, 200, 220, and 240 ºC, respectively. Concentration of 5-HMF and furfural in 180 ºC were the highest in 160-240 ºC.

3.2 Composting of food waste after sub-critical water pretreatment and isolation of fungus decomposing the 5-HMF and furfural

The courses of the concentrations of 5-HMF and furfural during the composting were shown in Fig. 3. The concentration of 5-HMF was decreased from 8mg/g-ds to 3mg/g-ds and the concentration of furfural was decreased to below the detection limit until third day in Run A1. On the other hand, the concentration 5-HMF was remained 3.1mg/g-ds on tenth day and furfural was decreased to below the detection limit until eighth day in Run B1. Fungi increased to $10^{5.6}$ CFU/g-ds on third day in Run A1, and, any microorganisms didn't increase on third day in Run B1 (data not shown). CO_2 evolution rate increased on third day in Run A1 (Fig. 4). On the other hand, CO_2 evolution rate was low until ninth day in Run B1. It was suggested that the fungi decomposed the organic materials include inhibitor and the CO_2 evolution rate increased on third day. The fungus was isolated and identified as *Paecilomyces* sp. (Fig. 5). The fungus was named strain FA13.

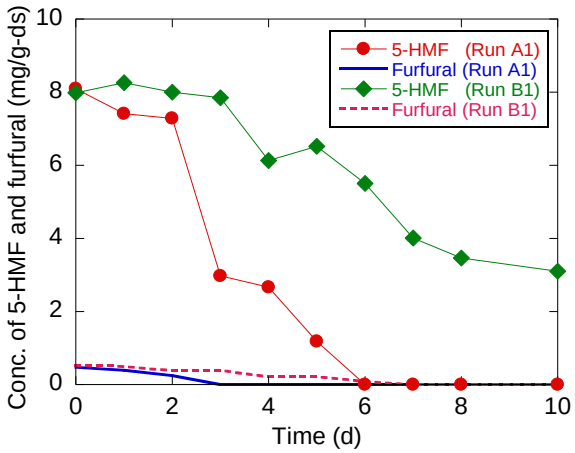

Fig. 3 The courses of concentration of 5-HMF and furfural during the composting for Run A1 and B1.

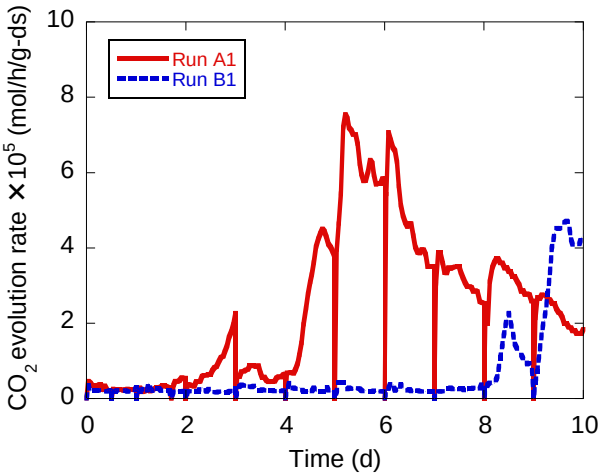

Fig. 4 The courses of CO_2 evolution rate during the composting for Run A1 and B1.

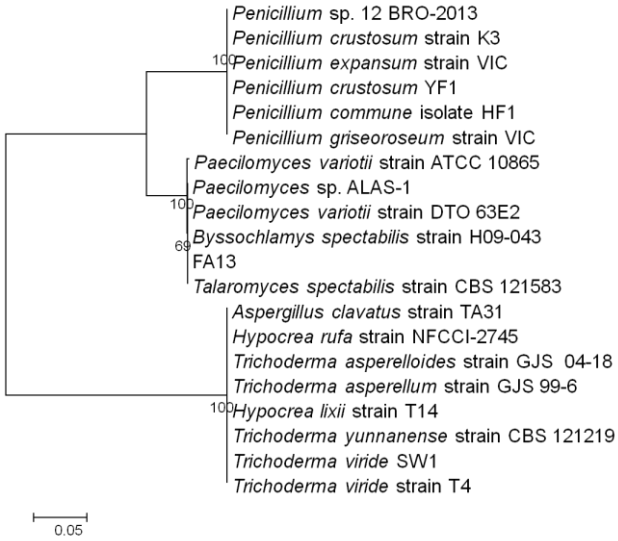

Fig. 5 Phylogenetic tree for the strain FA13

3.3Decomposition efficiency of 5-HMF, furfural by FA13

The concentration of inhibitors was measured under both conditions (Fig. 6). The concentration of 5-HMF decreased 85% after 72 hours and the concentration of furfural decreased to below the detection limit after 48 hours in Run A2. On the other hand, the concentration of both inhibitor didn't decrease in Run B2. Therefore, decomposition efficiency of 5-HMF, furfural by FA13 became clear.

3.4 Composting of food waste by sub-critical water pretreatment with FA13

The marked production of CO_2 was observed in Run A3 in contrast to the case of Run B3 though both runs were conducted under the same experimental conditions and it was confirmed that the organic matter was degraded vigorously in Run A3 (Fig. 7).

Fig. 7 compares the concentration of 5-HMF and furfural in Run A3 and B3. The concentration of 5-HMF on day 0 was 8.0mg/g-ds and it decreased to below the detection limit on third day in Run A3, which demonstrated that the strain FA13 had the 5-HMF degradation ability.

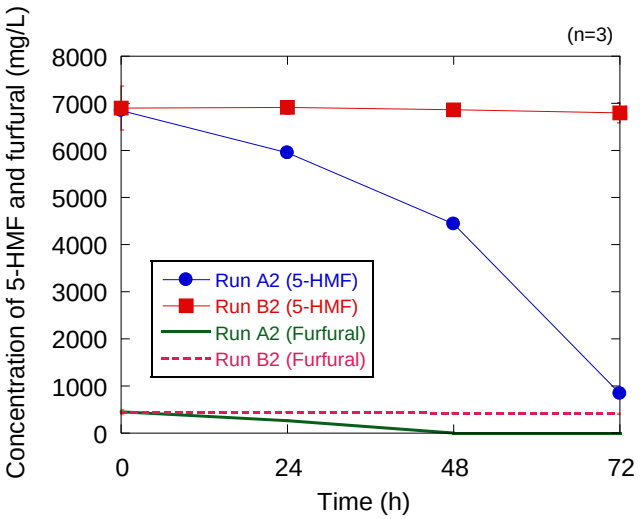

Fig. 6 The courses of concentration of 5-HMF and furfural for Run A2 and B2.

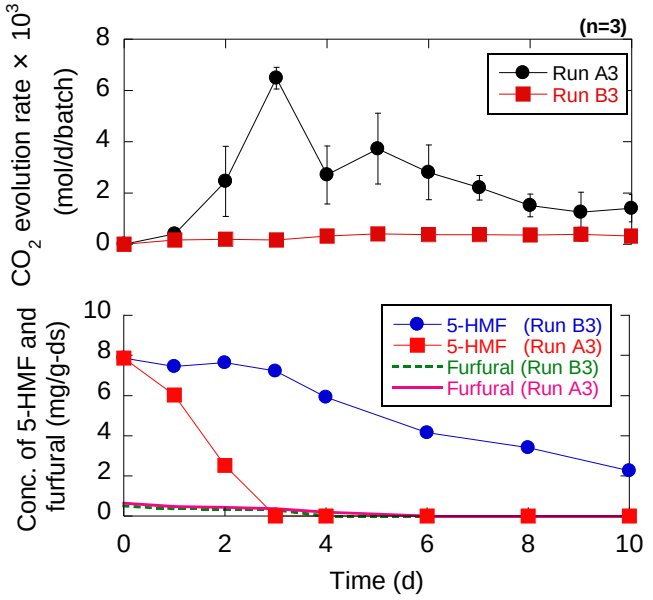

Fig. 7 The courses of CO_2 evolution rate and concentration of 5-HMF and furfural during the composting for Run A3, B3.

3.5 Composting of representative model of model food waste by sub-critical water pretreatment of different heating condition with FA13

Conversion of carbon during composting was measured as depicted in Fig. 8. The higher the heat pretreatment, higher the conversion of C became on day 0. On the other hand, Run A4 was 50%, B4 was 37%, C4 was 32%, D4 was 38% on day 10 and Run A4 was the highest value among 4 experimental runs. It suggest that a parts of organic matter was changed into decomposing persistent matter for microorganisms by sub-critical pretreatment. It was reported that the GI for very mature, mature and immature sample were >90, 80-90% and <80%, respectively. The GI was 0% in Run B4, C4 and D4 on day 0. On the other hand, GI was 25.2% in Run A4, 194% in Run B4, 319% in Run C4 and 186% in Run D4 on day 10. It suggested that the food waste with sub-critical water pretreatment became mature compost without containing the germination and growth inhibitor.

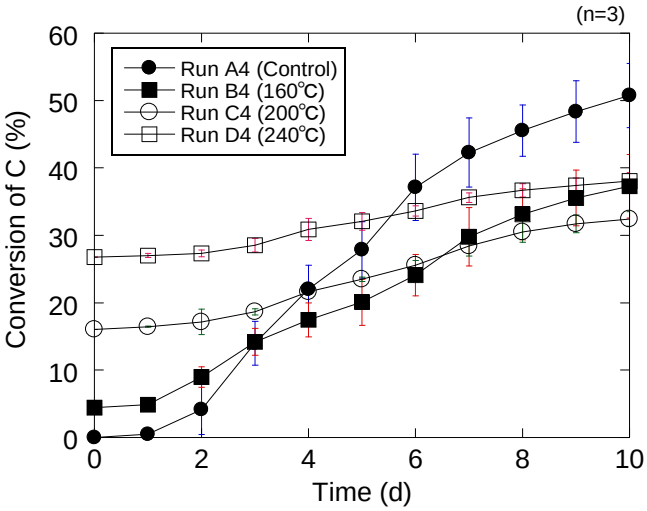

Fig. 8 The courses of conversion of C during the composting for Run A4, B4, C4 and D4.

4 Conclusions

In this study, it can be achieved the composting of food waste with sub-critical water pretreatment by inoculation of FA13. Food waste with sub-critical water pretreatment became mature compost without containing the germination and growth inhibitor for shorter periods of composting than food waste without sub-critical water pretreatment.

References

[1] Nakasaki, K., Araya, S., Mimoto, H., Inoculation of Pichia kudriavzevii RB1 degrades the organic acids present in raw compost material and accelerates composting. Bioresour. Technol. (2013)

[2] Sundberg, C., Franke-Whittle, I., Kauppi, S., Yu, D., Romantschuk, M., Insam, H., Jönsson, H. Characterisation of source-separated household waste intended for composting. Bioresour. Technol. 102, 2859-2867. (2011)

[3] Kanazawa, S., 肥効の高い堆厩肥の製造と新しい腐熟度検定法. Soil and Microorganism. 56, 1, 45-54. (2002)

The isolation and utilization of thermopilic lactic bacterium strain TP1 in the biorefinery

Student Number: 12M18212　Name: Yimeng Xu　Supervisor: Kiyohiko Nakasaki

バイオリファナリーにおける好熱性乳酸菌 TP1 株の単離および利用

徐　芸萌

本研究では、耐熱性乳酸菌の単離と、単離した好熱性乳酸菌を用いたバイオマスからの乳酸生産を試みた。耐熱性乳酸菌として TP1 株を単離することができ、同定の結果 *Bacillus smithii* strain NRS-173 と 99%の相同性を有することがわかった。TP1 株によるグルコースからの乳酸生成速度を常温乳酸菌 LA1 株と比較したところ、TP1 株の方が大きい生成速度を示した。また、バイオマスとしてマイクロウェーブ処理したタケ、未処理のアナアオサとチガイソを使用し、TP1 株を用いて乳酸生成について検討したところ、チガイソが最も乳酸生成に適することが確かめられた。

1 Introduction

Biorefinery, production of bulk chemicals and fuels from biomass, has attracted attention in recent years. Lactic acid is used as raw material of biodegradable plastic, and the development of the process for an efficient lactic acid production from inedible biomass has long been required. Thus, many studies have been performed on the production of lactic acid from inedible biomass, such as lignocellulosic biomass [1], paper sludge [2], and other wastes [3-4].

In order to produce lactic acid from biomass, the enzymatic hydrolysis of polysaccharide in biomass to produce fermentable sugar and fermentation of the sugar by lactic acid bacterium to produce lactic acid are combined. In addition, the efficient enzymatic hydrolysis of polysaccharide in biomass requires a pretreatment to make enzyme more accessible to polysaccharide. The pretreatment of biomass using acid, alkali, or organic solvent [5]enhances the efficiency of the enzymatic hydrolysis of polysaccharide, but chemical reagent such as acid, alkali, and organic solvent has a negative effect on the environment. Therefore, hydrothermal treatment is recognized as a promising pretreatment method.

Microwave treatment is a hydrothermal treatment, and microwave irradiation heats water in this treatment. In this study, bamboo, one of the lignocellulosic biomass, sea lettuce, one of the green seaweed, and chigaiso, one of the brown seaweeds, were used as inedible biomass, and microwave treatment was used as the pretreatment of these biomass to enhance the efficiency of enzymatic hydrolysis of glucans which are polysaccharides composed of glucose.

Generally, chemical reaction proceeds more rapidly under higher temperature condition. Therefore, it is considered that lactic acid can be produced more rapidly at high temperature condition. In this study, it was aimed to isolate a thermophilic lactic acid bacterium and to produce lactic acid from biomass under high temperature condition using newly isolated microorganism.

2 Materials & Methods

2.1 Biomass, enzyme, and lactic acid bacterium

Bamboo, sea lettuce (*Ulva pertusa* Kjellman), and chigaiso (*Alaria crassifolia* Kjellman) (Fig.1) were used as biomass for lactic acid production. Moso bamboo obtained in Shizuoka prefecture was used as bamboo, and pulverized into fine powder that has an approximately 50 μm of average particle size by using a grinder (PA-C, Marudai Co.). Sea lettuce and Chigaiso were harvested in Hokkaido prefecture. These seaweeds were washed using tap water, and dried in the sun for 5 h. Dried seaweeds were powdered using a mill (ZM-100, Retsch GmbH) to less than 0.5mm in diameter before use. The glucans contents of bamboo, sea lettuce and chigaiso were approximately 45.0%, 22.0%, and 24.5%, respectively, on a dry weight basis. In addition, mannnitol was also contained as a fermentable sugar in chigaiso with the content of 7%.

Meicerase (CEPB-5394, Meiji Seika Kaisya Ltd.), derived from *Trichoderma viride* was used as enzyme for the hydrolysis of glucans in biomass.

Lactobacillus paracasei LA1 (strain LA1), isolated from a wastewater sludge, was used as lactic acid bacterium.

Bamboo (Fine powder)

Sea Lettuce

Chigaiso

Fig.1 The pictures of the biomass used in this study.

2.2 Isolation and identification of a themophilic lactic acid bacterium

Seaweed compost of 1g in 9 mL of sterilized water was homogenized and the suspension was serially diluted with sterilized water. The diluted suspension was spread onto GC agar medium and the agar plate was incubated at 60ºC. GC agar medium contained insolubile CaCO3 and generation of lactic acid bacteria will dissolve CaCO3. Therefore the formation of a clear zone around the colony of lactic acid bacteria was expected. For the identification of the isolated bacteria, DNA extraction, PCR amplification and DNA sequencing of 16s rRNA gene fragment were carried out.

2.3 Lactic acid production from glucose

Production of lactic acid from glucose using the isolated thermophilic lactic acid bacterium and strain LA1 were carried out. The thermophilic lactic acid bacterium was inoculated to GC liquid medium and cultivated at 60ºC 150rpm for 48h. The cultivation of the strain LA1 was the same with that of isolated bacterium except that the temperature was 30ºC instead of 60ºC. During the cultivation, samples were taken and concentrations of glucose, lactic acid, acetic acid were measured by HPLC.

2.4 Enzymatic hydrolysis of biomass with and without microwave treatment

One gram of biomass was put into a microwave reactor with 10 mL of distilled water. The reactor was irradiated by microwave (Wave magic, EYELA), and heated. The heating temperature conditions were 180, 190, and 200ºC. The enzymatic hydrolysis of biomass with and without microwave treatment was carried out to investigate the effect of microwave treatment for enzymatic hydrolysis. Each biomass was added to 0.1 M citric acid buffer solution (pH 5.5). The mixture was sterilized by autoclaving at 121ºC for 20 min. Filter sterilized Meicelase solution was then added to the mixture. The concentrations of biomass and Meicelase were adjusted to 20 and 1 g/L, respectively. Enzymatic hydrolysis was conducted at 35ºC for 96 h. The concentration of glucose after hydrolysis was determined using HPLC.

2.5 Lactic acid production from biomass using isolated bacterium

In order to produce lactic acid from biomass, lactic acid fermentation was carried. Bamboo treated by microwave at 190ºC for 30 min was washed using distilled water and then used for lactic acid production. Sea lettuce and chigaiso without microwave treatment were used for lactic acid production.

Enzymatic hydrolysis of biomass was conducted as described in 2.4 except that hydrolysis temperature and the concentration of biomass were changed to 50ºC and 60 g/L, respectively. After hydrolysis, Bacto peptone and yeast extract were added to the hydrolysate so that the concentrations of Bacto peptone and yeast extract attained 5 and 10 g/L, respectively. The precultured isolated lactic acid bacterium was then inoculated, and fermentation was conducted at 60ºC for 36 h.

The concentrations of fermentable sugars and lactic acid, acetic acid were determined using HPLC, and the cell density of isolated bacterium was also determined using the dilution plating method.

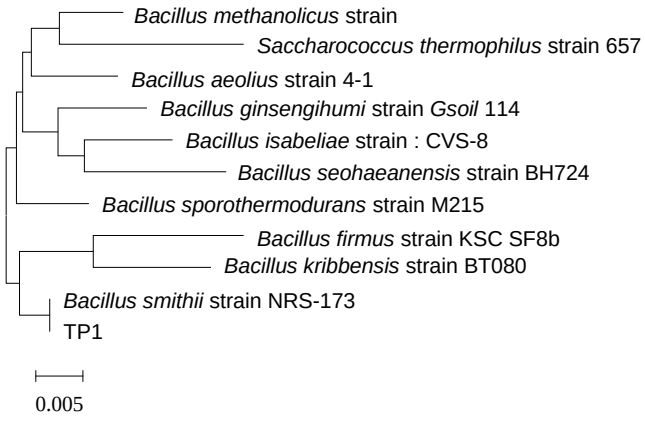

Fig. 2 The phylogenetic tree of strain TP1 base on gene sequences.

3 Results & Discussion

3.1 Identification of isolated thermophilic lactic acid bacterium

The thermophilic lactic acid bacterium, strain TP1, was successful isolated from seaweed compost. Fig. 2 shows the phylogenetic tree of strain TP1 constructed based on the 16s rRNA gene sequence. Strain TP1 showed 99% of similarity with the gene sequences of *Bacillus smithii* strain NRS-173.

3.2 The productivity comparison between isolated bacterium and strain LA1

Fig. 3 and Fig. 4 show the courses of concentration of glucose, lactic acid and acetic acid during the cultivation of the strain TP1 and strain LA1 respectively. It was ascertained that the lactic acid was produced by strain TP1. Most of the glucose was consumed by strain TP1 in 6h and 8.07 g/L of lactic acid was produced. On the other hand, there remain some glucose in the culture of strain LA1 after 6h and 6.77g/L of lactic acid was produced. The productivity of lactic acid by strain TP1 and LA1 in 6h were 1.34g/L/h and 1.13g/L/h, respectively. The productivity of strain TP1 was higher than strain LA1 though the difference was not much significant as we expected.

After 6h of cultivation, the increase in the acetic acid concentration was observed with the decrease of the lactic acid concentration. Therefore, it was also revealed that the longer cultivation time than 6h reduced the productivity of lactic acid because of the conversion of lactic acid to the acetic acid by TP1. On the other hand, acetic acid producing ability of TP1 was indicated. Therefore, by shortening the fermentation time, lactic acid can be produced and by extending the fermentation time, acetic acid can be produced. Since acetic acid is also produced in the biorefinery production of acetic acid in addition to the lactic acid using the strain TP1 was expected.

3.3 Effect of microwave treatment on the enzymatic hydrolysis of biomass

The concentration of glucose produced by enzymatic hydrolysis of biomass treated by microwave at different temperatures for 30 min is compared to that of untreated biomass in Fig. 5. The concentrations of glucose produced from untreated bamboo, bamboo treated at 180, 190, and 200ºC were 1.5, 2.6, 4.7, and 4.8 g/L, respectively, and microwave treatment enhanced the efficiency of enzymatic hydrolysis of bamboo. Since the concentrations of glucose produced from bamboo treated at 190 and 200ºC were similar, we used bamboo treated at 190ºC as substrate for the production of lactic acid. The conversion of glucans and oligosaccharides was calculated as 52.2% in the case of bamboo treated at 190ºC.

The concentrations of glucose produced from seaweeds treated by microwave at all temperature were lower than those from untreated seaweed. In addition, glucans and oligosaccharides contained in seaweeds were considerably hydrolysed without pretreatments, such as microwave treatment, and 58.0% and 94.2% of glucans and oligosaccharides conversions were achieved in the cases of sea lettuce and chigaiso, respectively.

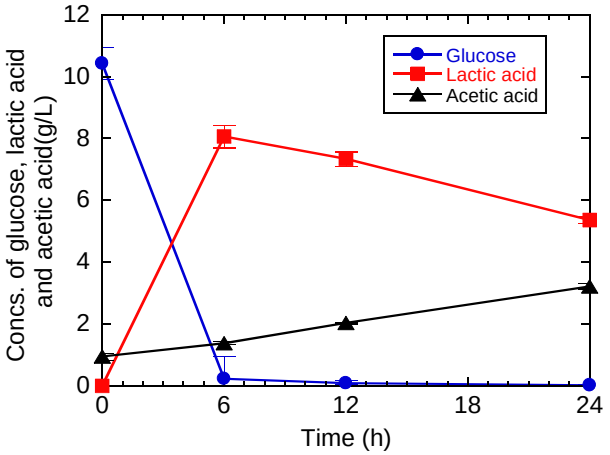

Fig. 3 The courses of concentrations of glucose, lactic acid and acetic acid by strain TP1 cultivation (n=3).

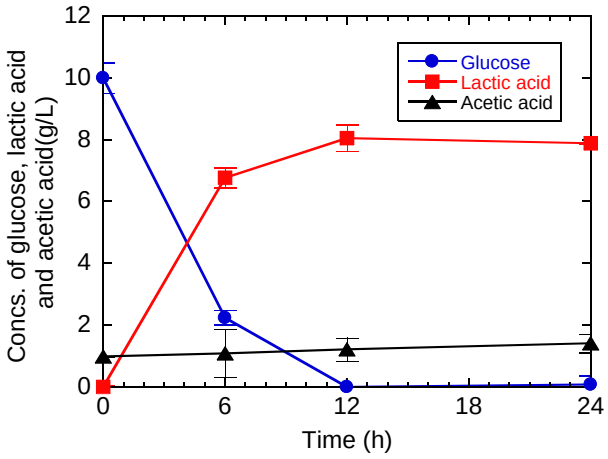

Fig. 4 The courses of concentrations of glucose, lactic acid and acetic acid by strain LA1 cultivation (n=3).

Therefore, untreated sea lettuce and chigaiso were used as substrates for the production of lactic acid.

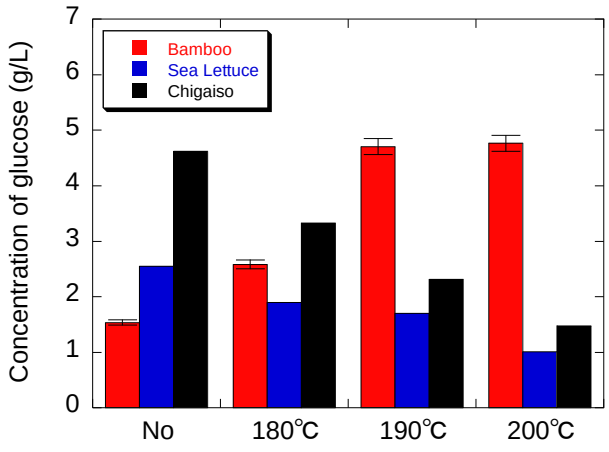

Fig. 5 Comparison of the concentration of glucose produced by enzymatic hydrolysis of biomass treated by microwave at different temperatures for 30 min and that of untreated biomass (n=3).

3.4 Lactic acid production from biomass

The concentrations of lactic acid and acetic acid produced from biomass using strain TP1 are shown in Fig. 6. After 6 hours cultivation, glucose was almost consumed and the lactic acid concentration attained 6.8g/L in the fermentation of microwave treated bamboo. The productivity of lactic acid from treated bamboo after 6h cultivation was 1.13g/L/h. In addition, it was confirmed that 4.1 g/L of acetic acid could be produced after 24h cultivation.

In the fermentation of sealettuce、5.4g/L of Lactic acid after 6h and 4.1 g/L of acetic acid after 24h cultivation were attained while 9.0 g/L of lactic acid after 12h and 8.0g/L of acetic acid after 48h was

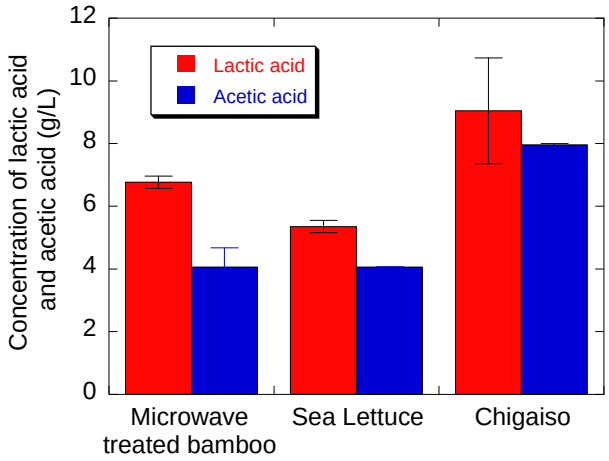

Fig. 6 The concentration of lactic acid and acetic acid produced from biomass using strain TP1(n=3).

produce in the fermentation of chigaiso. Higher concentration of lactic acid and acetic acid could be produced from chigaiso compared to those from sea lettuce and treated bamboo, and it was considered that chigaiso was more suitable for the fermentation using strain TP1.

4 Conclusions

In this study, thermophilic lactic acid bacterium *Bacillus smithii*, strain TP1 was successfully isolated. It was demonstrated that the productivity of lactic acid from glucose by strain TP1 was higher than that by the strain LA1. In addition to the lactic acid, the acetic acid also can be produced using strain TP1 by controlling the fermentation time. Microwave treatment facilitated the enzymatic hydrolysis of bamboo and high lactic acid productivity by strain TP1 from treated bamboo could be demonstrated. Both the lactic acid and acetic acid could be produced form the sea lettuce and chigaiso, and fermentation of chigaiso showed more efficient productivity than that of sealettuce.

References

[1] Garde A, Jonsson G, Schmidt AS, Ahring BK. Lactic acid production from wheat straw hemicellulose hydrolysate by Lactobacillus pentosus and Lactobacillus brevis.Bioresour Technol 2002;81:217–223.

[2] Nakasaki K., Adachi T. Effects of Intermittent Addition of Cellulase for Production of L-lactic acid from Wastewater sludge by Simultaneous Saccharification and Fermentation. Biotechnol bioengineering 2003; 82:263-270.

[3] Ohkouchi Y, Inoue Y. Direct production of L-(+)-lactic acid from starch and food wastes using Lactobacillus manihotivorans LMG18011. Bioresour Technol 2006; 97:1554-1562.

[4] Chan-Blanco Y, Bonilla-Leiva AR, Velazquez AC. Using banana to generate lactic acid through batch process fermentation.Appl Microbiol Biotechnol 2003;63:1

[5] Sun Y, Cheng J. Hydrolysis of lignocellulosic materials for ethanol production: a review. Bioresource Technol. 2002;83:1-11

MULTIPLE PERSPECTIVES OF THE ONE LAPTOP PER CHILD INITIATIVE: THE CASE OF MONGOLIA

Student Number: 11M51175 Name: John AUXILLOS Supervisors: Shinobu YAMAGUCHI & Jun-ichi TAKADA

This study employs a multi-phased pragmatic mixed-methods research that investigates the impact of the One Laptop Per Child (OLPC) initiative introduced in Mongolian in 2008. The OLPC is a non-profit organization founded by Nicholas Negroponte in 2005 to empower the world's underserved children, following the constructivist learning theory, through purposely built low-cost and rugged laptops filled with educational software. In Mongolia, 46 schools were given a total of 12,100 OLPC XO1 laptops and this research analyzes both quantitative and qualitative data collected between December 2011 and May 2013 from the stakeholders. The findings indicate that children develop differently and the impact also proliferated to the community. While these findings are not generalizable, it builds a case for further research.

1. Introduction

Over three decades ago, Seymor Papert, a protégée of a Swiss development psychologist named Jean Piaget, suggested that "it is possible to design computers so that learning to communicate with them can be a natural process" and when computers are designed suitably, it was envisioned that learning to communicate with it, as suggested by the constructionist learning theory, will change how learning takes place. (Papert, 1980, p. 6). In 1980, Papert and Nicholas Negroponte conducted an experiment in Dakar, Senegal and found that children they encountered would learn how to use the computer similar to middle-class Americans (Negroponte, 1996). These ideas and experiments lead to the launch of the One Laptop Per Child (OLPC) initiative in 2005 with a goal of designing, manufacturing, and distributing laptops with a target price of 100 USD for children between the ages of 6 to 12 in underserved areas in the world.

The OLPC is a non-profit organization and its vision is also embodied in its name. Thoughtful design of laptops is believed to create learning opportunities for children. What they envisioned is not that of a teacher in a classroom teaching, but rather children exploring and building a mental model of ideas and knowledge using a laptop. Around the world, there are 54 countries with OLPC deployments to date (One Laptop Per Child, 2011)

In Mongolia, the OLPC initiative was introduced by two MIT students, Enkhmunkh Zurgaanjin and Jan Jungclaus. By late 2007, a Memorandum of Understanding was made between OLPC and the Mongolian government to introduce the laptop to children in the rural area and in Ulaanbaatar City (Embassy of Mongolia, 2007). A total of 12,100 OLPC XO1 laptops were distributed throughout the country to 46 schools.

The objective of this research is twofold. The first is to document and understand the impact of the OLPC XO1 laptops distributed in Mongolia since 2008 on the children and other stakeholders. The second is to conduct this research using a pragmatic mixed methods approach, a methodological exercise, to be able to illicit breadth and depth in understanding the context of the stakeholders of the project.

2. Literature Review

There is widespread belief that there is a need to do research on ICT in education as "it is generally believed that ICTs can empower teachers and learners, promote change and foster the development of 21st century skills, but data to support these beliefs are still limited." (Trucano, 2005, p. 5)

In the studies conducted over the past decade, impact of the use of computers and its software on student learning achievement scores has not been found (Angrist, 2002; Institute of Education Sciences, 2007). Specifically, in a two-year randomized evaluation of the Computer for Education project in Columbia published in 2009, there was little impact on math and Spanish test scores (Barrera-Osorio & Linden). In a large-scale randomized evaluation of the OLPC program in Peru after 15 months of implementation in 319 primary schools found no evidence of effect on test scores in Math and Language (Cristia, Ibarrarán, Cueto, & Santiago, 2012).

There are various opinions about the OLPC project in current literature. James (2010) questions the need for the one laptop per child ratio that the OLPC adopted, especially in the context of improving education in developing countries. Mitra's project in India (2006) found evidence that groups of children using a computer can have positive results. In Uruguay, Hourcade (2008) found that in spite of problems with infrastructure, hardware, and software problems, there was a positive impact on children, the school, and the town, with children specifically increasing their interest in reading and writing. In Peru, researchers found that cognitive abilities may increase through using the programs on the laptop and it was reflected in slight increases measured by Raven's Matrices (Cristia, Ibarrarán, Cueto, & Santiago, 2012). In Nepal, researchers claim that OLPC allowed teachers to fully integrate ICT-based instruction since students can continue learning outside the classroom (Bhatta, 2008).

Literature about the OLPC in Mongolia is limited. No journal articles have been published thus far on this country deployment. Therefore this study serves to contribute towards understanding the OLPC deployment in the Mongolian context. It furthers the current literature by conducting a study with the use of multiple perspectives.

3. Methodology

3.1. Mixed-Methods

Mixed-methods was chosen because of three reasons: First, the research problem of this study is a complex one that seeks to understand the relationship of a piece of technology, the people who use it, and also in the context of the community they are in. The second reason is the limited information available for the study, which is a reality in developing countries. The third is the lack of a standard methodology for fully assessing the impact of computers on children (Trucano, 2005).

This study was conducted between December 2011 and May 2013 including six field visits to Mongolia. Both quantitative and qualitative data collection techniques were used to gather different perspectives. It involved three phases.

3.1.1. Phase 1

The first phase focused on establishing a base of knowledge in the case of Mongolia and seeks to answer: 1. What is the context the OLPC was introduced in Mongolia? 2. What is the extent of the project implementation? 3. What are the available information about the OLPC initiative in Mongolia? 4. What are the opportunities and challenges the OLPC initiative are facing in Mongolia?

Interviews and focus group discussions were conducted with two members of the OLPC Project Management Unit in Mongolia, 10 teachers, 4 training managers, and 7 methodologists. A questionnaire was also distributed to all 46 OLPC schools where 34 schools responded. This covered the following five aspects: 1) the background of the school, 2) infrastructure available at the school, 3) OLPC distribution information, 4) status of the hardware, and 5) the views of the initiative.

3.1.2. Phase 2

The second phase was a quasi-experimental study conducted with the use of two instruments. It intends to understand the impact of the OLPC measured by student learning achievement scores and a computer attitude measure. Data was collected from 2000 students in November 2012 from 14 schools, where half were control schools. Of the 7 pairs of schools, 3 pairs were from the capital city, and one pair of schools was then selected from the northern, southern, eastern, and western regions. Schools were paired on the basis of location and advise from the local education specialists.

The first instrument was the Mongolian National Assessment of Primary Education Mathematics and Reading for 5th graders, a student learning achievement instrument developed, piloted, and administered in 2008 under the World Bank Rural Education and Development project. Among 7 paired schools, 3 pairs, one pair from Khovd province and two pairs from Ulaanbaatar City, were selected for the analysis with a total of 489 valid samples. The mathematics test included questions relating to numeracy, algebra, geometry, and probability while the reading test covered topics on language use, meaning, grammar, and an essay section. To analyze the data, the following OLS (ordinary least squares) model was used to estimate the effect of the OLPC XO1 laptops on math score (1) and reading score (2), controlling for relevant factors:

$$\begin{aligned} math.score = {} & \beta_0 + \beta_1 case.category \\ & + \beta_2 socioeconomic.index \\ & + \beta_3 student.sex + \beta_4 stq02.0 \\ & + \beta_5 stq14.0 + \beta_6 stq16.0 \\ & + \beta_7 stq20.0 \\ & + \beta_8 student.class.ratio \\ & + error \end{aligned} \quad (1)$$

$$\begin{aligned} reading.score = {} & \beta_0 + \beta_1 case.category \\ & + \beta_2 socioeconomic.index \\ & + \beta_3 student.sex + \beta_4 stq02.0 \\ & + \beta_5 stq14.0 + \beta_6 stq16.0 \\ & + \beta_7 stq20.0 \\ & + \beta_8 student.class.ratio \\ & + error \end{aligned} \quad (2)$$

where *math.score* and *reading.score* represents the outcome variable, and *case.category* is a dummy variable for treatment assignment status. Control variables include *socioeconomic.index* an 18-point scale measuring available materials at home and school. Other variables included are, *student.sex* (a dummy variable), the number of family members (*stq02.0*), the daily hours a student spends on homework (*stq14.0*), the daily hours a student spends on house chores (*stq16.0*), the daily hours a student spends watching TV (*stq20.0*), and the total number of Grade 5 students divided by the number of Grade 5 classes in a school (*student.class.ratio)*. Finally, *error* is the error term. The coefficient β_1 is the parameter of interest and corresponds to an estimate of the average treatment effect. β_2 to β_8 are the coefficients of the control variables.

The second instrument was the Computer Attitude Measure for Young Students (CAMYS), a tool to measure children's' disposition towards computers. The CAMYS scale is presented as a 5-point Likert scale (5 - strongly agree to 1 - strongly disagree) that consists of twelve questions divided into three groups: 1) perceived ease of use; 2) affect towards computer; and 3) perceived usefulness. Independent samples t-test was used to compare the average CAMYS scores of 7 paired schools with a total of 1596 valid samples.

3.1.3. Phase 3

The third phase is a confirmation of the data collected in the first two phases with the use of case studies. The research questions of this phase are as follows:

1) What are the similar experiences of using the OLPC in the different schools?
2) What are the similar issues of concern of the different OLPC schools?
3) What are the similar observed impacts of the OLPC across schools and different stakeholders of the project?

4) What are the unique practices of specific OLPC schools that can lead to better implementation of the initiative?

Interviews and focus group discussions were conducted with a total of 15 children, 22 teachers, 2 parents, 5 school administrators, and 2 methodologists from Tsast-Altai, a school in Khovd province, School #52 in the center of Ulaanbaatar city, and School #12 in the periphery of Ulaanbaatar city.

4. Findings

4.1. Findings from Phase 1

The OLPC initiative introduced in 2008 is the largest ICT in Education project for Mongolia. With 12,100 laptops distributed to 46 schools, this was primarily a rural project as 57% (26) schools that participated were rural schools and 61% (7494) of laptops were distributed to rural schools. Electricity was available for 89% (41) of the participating schools. Internet was available for 59% (27) schools but this does not indicate whether students themselves can access the internet on their laptops. As a matter of national policy, the OLPC XO1 laptops distributed are the property of the state and parents must sign a tripartite contract with their child's teacher and the school that binds parents to any costs incurred when the laptop needs to be repaired due to damages arising from their child's usage or loss. The OLPC initiative and responsibility was handed to the Ministry of Education and Science, who formed a Project Management Unit (PMU) to oversee the program. Gaps were found on the understanding of the project objectives from the different levels of the stakeholders. The OLPC vision was to empower children by providing them with learning opportunities through the XO1 laptop. The state understood the project as enabling access to education. Teachers understood project as giving children the opportunity to be exposed to ICT. At this moment, the future of the OLPC initiative in Mongolia is uncertain as indicated by the PMU.

4.2. Findings from Phase 2

The result of the OLS Regression on the Mongolian National Assessment of Primary Education Mathematics and Reading is as follows:

$$\begin{aligned} math.score = {} & 23.03 + 2.37 case.category \\ & - 0.02 socioeconomic.index \\ & - 1.46 student.sex \\ & - 0.19 stq02.0 - 0.27 stq14.0 \\ & - 0.04 stq16.0 + 0.95 stq20.0 \\ & + 0.02 student.class.ratio \\ & + error \end{aligned} \quad (3)$$

The math results is $R^2 = 0.050, F(8,480) = 3.17, p < 0.01$. The variable of interest was $case.category = 2.37$ and is statistically significant at the 99% level. This indicates that a student with an OLPC computer can score an average of 2.37 points higher for a 44-point math learning achievement test. In addition, two significant control variables, namely, student sex and the daily hours a student watches TV, suggest the followings: 1) female students would score 1.46 points higher on average; and 2) students who spend longer hours watching TV would score 0.95 points higher.

$$\begin{aligned} reading.score = {} & 24.76 + 3.42 case.category \\ & - 0.01 socioeconomic.index \\ & - 2.16 student.sex \\ & - 0.24 stq02.0 + 0.12 stq14.0 \\ & + 0.30 stq16.0 + 1.29 stq20.0 \\ & + 0.04 student.class.ratio \\ & + error \end{aligned} \quad (4)$$

The reading results is $R^2 = 0.065, F(8,480) = 4.187, p < 0.001$. Variable of interest is $case.category = 3.42$ and is statistically significant at the 99% level, indicating that a student with an OLPC computer can score an average of 3.42 points higher for a 52-point reading learning achievement test. Similar to the math results, two significant control variables, student sex and the daily hours a student watches TV, suggest the following analysis: 1) female students would score 2.16 points higher on average; and 2) students who spend longer hours watching TV would score 1.29 points higher.

Independent-samples t-tests were conducted to compare mean computer disposition as measured by the CAMYS instrument in OLPC and non-OLPC schools. It was found that rural schools (Darkhan-Uul, Dornogobi, Khovd, and Sukhbaatar) all exhibited statistical differences in the average computer disposition of 5th grade students, whereas urban schools (UB Bayangol and UB Khaanuul) exhibited similar average computer disposition. UB Songingnokhairhain is the exception to the urban schools group since and is likely because of its location at the periphery of the capital city.

4.3. Findings from Phase 3

Schools that were visited indicated that children are able to develop a variety of skills as a result of the OLPC program. Stakeholders have also indicated that the OLPC has a positive benefit to teachers, parents, and the community such as increasing teachers and parents' ICT skills. In one school a parent indicated that because of the program, they are now willing and able to invest in buying their own computer and also support repair costs of broken laptops.

5. Discussion

As a result of the interviews and focus group discussions with the different stakeholders, several trends have emerged that can solicit further investigation. 1) The OLPC lead a bottom-up adoption of ICT. 2) Teachers worked together to teach themselves ICT. 3) Teachers believe there is a positive impact on children's' development. 4) Teachers were able to find a means of maximizing the utility of the XO1 laptops. 5) The design of the XO1 laptop is a deterrent to theft. 6) There was a positive acceptance of

the OLPC initiative. 7) There are possible negative repercussions.

As there is also no coherent national policy on how the XO should be integrated into the curriculum, every school had its own policy and a variation of its implementation. It was observed that the integration of the OLPC XO1 into the school curriculum was influenced by Teacher's motivation, school administrator leadership, and methodologist leadership.

In terms of the impact of the OLPC initiative in Mongolia, student learning achievement scores indicate positive results. However, the low R^2 indicates other factors to predict test scores are not present in the model, and thus further investigation is required. On the qualitative side, there are many interesting findings from the teachers that should be used as areas to further validate in future studies. The stakeholders who took part in this study strongly believe in the positive effect of the OLPC program. The positive effects, which include communication skills and creativity, are not measurable by student learning achievement tests.

6. Conclusion

Seymour Papert's idea of designing computers so that learning to communicate with it as a natural process that facilitated learning drove the creation of One Laptop Per Child initiative. Mongolia is one of 54 countries around the world with OLPC XO1 laptops deployed with the hopes to improve education.

This research studied the impact of the OLPC initiative in Mongolia from multiple perspectives, looking at learning achievement scores, computer attitude measures, perspectives of children and the different stakeholders.

The implementation of the OLPC initiative in Mongolia started with a PMU overseeing the entire deployment but later moved towards a model where the school would be the center with its own policies and sources of support for the program. Each school had a different implementation because of a variety of factors such as school's leadership, access to resources, proximity to UB, support of the community, and teacher's ability to implement.

Student learning achievement scores indicate that students with an OLPC computer can score higher for both math and reading. While it is indicated that there are some gains, these cannot be generalized for the entire case of Mongolia as it did not pass some of the rigors of randomized control tests. Computer attitude measure on paired schools found rural schools all exhibited statistical differences in the average computer disposition of 5th grade students, whereas urban schools, with the exception of the one located at the periphery, exhibited similar average computer disposition.

Interviews and focus group discussions with 68 stakeholders found that the OLPC was a positive experience for children, teachers, parents, and the community. The different stakeholders believe that children have learned computer literacy and typing skills, and it is also able to foster creativity, communication, and independence.

On the other hand, the study also found there are multiple challenges that teachers, parents, and school administrators face, in planning and implementing OLPC initiatives at school level, including financial implications for the parents.

This research concludes that there is an impact in several areas but it is not generalizable in entire Mongolia, and thus, needs to be further studied.

References

[1] Angrist, J., & Lavy, V. (2002). *New Evidence on Classroom Computers and Pupil Learning*. The Economic Journal, 1–32.

[2] Barrera-Osorio, F., & Linden, L. L. (2009). *The Use and Misuse of Computers in Education*. Policy Research Working Paper, 1–43.

[3] Bhatta, S. D. (2008). *Tackling the problems of quality and disparity in Nepal's school education: The OLPC model*. Studies in Nepali History and Society, 11(1), 00–00.

[4] Cristia, J., Ibarrarán, P., Cueto, S., & Santiago, A. (2012). *Technology and Child Development: Evidence from the One Laptop Per Child Program*. IZA Discussion Paper Series, (No. 6401), 1–43.

[5] Hourcade, J. P., Beitler, D., Cormenzana, F., & Flores, P. (2008). *Early OLPC Experiences in a Rural Uruguayan School*. CHI Proceedings, 2503–2512.

[6] Institute of Education Sciences, Dynarski, M., Agodini, R., Heaviside, S., Novak, T., Campuzano, L., et al. (2007). *Effectiveness of Reading and Mathematics Software Products (No. 2007-4005)*. U.S. Department of Education.

[7] James, J. (2010). *New Technology in Developing Countries: A Critique of the One-Laptop-Per-Child Program*. Social Science Computer Review, 28(3), 381–390. doi:10.1177/0894439309346398

[8] Mitra, S. (2006). *The Hole in the Wall*. New York.

[9] Negroponte, N. (1996). *Being Digital*. Vintage Books.

[10] One Laptop Per Child. (2011, October). *One Laptop Per Child Deployments*. Retrieved January 22, 2014, from http://www.laptop.org/en/children/countries/

[11] Papert, S. (1980). *Mindstorms: Children, computers, and powerful ideas*. Basic Books, Inc.

[12] Embassy of Mongolia, Washington, D.C.. (2007) *President N. Enkhbayar's Official Visit to the United States.* Retrieved July 17, 2013, from http://www.mongolianembassy.us/mongolia_and_usa/mongolian_presidents_visit_to_us.php

[13] Trucano, M. (2005). *Knowledge Maps: ICT in Education*. Washington, DC: infoDev / The World Bank.

[14] Trucano, M. (2013). *Mobile learning and textbooks of the future, e-reading and edtech policies: Trends in Technology Use in Education in Developing Countries.* The World Bank.

DEA Evaluation of Agriculture and Industry Water Use Efficiencies in China

Student Number: 12M18198 Name: Lu Gao Supervisor: Naoya Abe

包絡分析法を用いた中国における農業用水と工業用水の利用効率性評価

Water shortage is becoming one of the most crucial issues in China because of the rapid increasing water demand for economic development. In order to propose an appropriate policy, we mainly need to work on the two problems: first finding in the evident how much the value of agricultural and industrial water use efficiencies are in each target region and second identifying the factors affecting agricultural and industrial water use efficiencies. The data envelopment analysis (DEA) is adopted to measure the agriculture and industry water use efficiencies. We also identify the dominant factors affecting water use efficiencies by the Tobit model.

1. Introduction

Water shortage has become a crucial issue in China because of the rapidly growing population. At present, 61.3% of water is used for agriculture, which accounts for only 8.9% of GDP, and China's water use efficiency is lower than that of developed countries(3). Because industrial output has increasingly become much more profitable than agricultural output, water resources are being transferred to industry, which affects agricultural production. For this reason, increasing water use efficiency is an important issue for China.

In order to solve this problem, the Chinese government has initiated a number of projects, such as transferring water from agriculture to industry in water-saving irrigation in Ningxia and Inner Mongolia since 2003. In this study, Ningxia, Inner Mongolia, and Gansu provinces are selected to evaluate whether water transfer projects affect water use efficiency in each region. Data envelopment analysis (DEA) is adopted to measure the agriculture and industry water use efficiencies. We also identify the dominant factors affecting water use efficiencies by the Tobit model.

2. Methodology

2.1. Data Envelopment Analysis

2.1.1. Conventional DEA Model

We adopt DEA to analyze water use efficiency. This approach is used to measure the relative efficiency of homogenous units called decision making unit (DMU). The efficiency of each DMU is the ratio of the sum of weighted outputs to the sum of weighted inputs; this value is never greater than 1. If the efficiency is 1, it means that the DMU is efficient; otherwise, it is inefficient.

The input-oriented model of the Charnes, Cooper, and Rhodes (CCR) model was chosen in this study. We use fractional programming (FP), as shown in equations 1–4, to obtain values for the input weights (v_i , i=1,2,…,m) and output weights (μ_r , j=1,2,…,m) of DMU_k to obtain the maximum efficiency of DMU_k ($\max \theta_k$)(9).

$$\underset{(v,\mu)}{Max}\ \theta_k = \frac{\mu_1 y_{1k} + \mu_2 y_{2k} + \cdots + \mu_s y_{sk}}{v_1 x_{1k} + v_2 x_{2k} + \cdots + v_m x_{mk}} \quad (1)$$

$$\text{Subject to} \frac{\mu_1 y_{1j} + \mu_2 y_{2j} + \cdots + \mu_s y_{sj}}{v_1 x_{1j} + v_2 x_{2j} + \cdots + v_m x_{mj}} \le 1 (j = 1,2,\ldots n) \quad (2)$$

$$v_1, v_2, \cdots, v_m \ge 0 \quad (3)$$

$$\mu_1, \mu_2, \cdots, \mu_s \ge 0 \quad (4)$$

The (v^*, μ^*) obtained as an optimal solution for FP results in a set of optimal weights for DMU_k. v_i^* is the optimal weight of the input item i and μ_r^* is the optimal weight of the output item j. The ratio scale is evaluated by

$$\theta_k^* = \frac{\sum_{r=1}^{s} \mu_r^* y_{rk}}{\sum_{i=1}^{m} v_i^* x_{ik}} \quad (5)$$

The DEA defines three different forms of efficiency: technical efficiency (TE), pure technical efficiency (PTE), and scale efficiency (SE). Table 1 explains the three efficiencies.

Table 1. DEA efficiencies and their explanations

Concept	Explanation	Detail
PTE	The conversion of physical inputs into outputs relative to the best practice	For the current technical level, the inputs are completely utilized.
SE	For a given level of output, inputs are chosen to minimize the cost of production	Indicats whether the scale of production is overlarge or small
TE	The conbination of pure technical and scale efficiency.	Is technically efficient if it is both technically pure and scale efficient.

2.1.2 SE–DEA

The conventional DEA model leaves all efficient units with a unity score and thus does not allow the ranking of the efficient units themselves. An extended DEA model provides a procedure for ranking them by comparing the units under evaluation with a linear combination of other units in the sample. The unit obtained in this case an efficiency score above 1. The score reflects the radial distance from the DMU under

evaluation to the production frontier estimated with the DMU excluded from the sample.

The model is identical to the conventional BBC model except that the unit evaluation is not included in the reference set. [5] The programming problem equation is given by

$$\begin{cases} \min E_j - \delta e' s^- - \delta e' s^+ \\ \text{s.t.} \quad E_j X_j = \sum_{\substack{k=1 \\ k \neq j}}^{m} z_k X_k + s^+, \\ Y_j = \sum_{\substack{k=1 \\ k \neq j}}^{s} z_k Y_k - s^-, \\ z, \quad s^+, \quad s^- \geq 0 \end{cases} \tag{6}$$

where X_j is an m-dimensional input vector, Y_j is an s-dimensional output vector for the jth unit, E_j is a scalar defining the share of the jth DMU input vector within the reference technology, Z is an intensity vector in which z_k denotes the intensity of the kth unit, δ is a non-Archimedian infinitesimal, and e' is the row vector (1,…,1) of the appropriate dimension.

Once the efficient frontier is determined, inefficient DMUs can improve their performance to reach the efficient frontier by either increasing their current output levels or decreasing their current input levels. However, both desirable (good) and undesirable (bad) factors may be present. For example, if inefficiency exists in production processes where final products are manufactured with a production of wastes and pollutants, the outputs of waste and pollutants are undesirable and should be reduced to improve performance. This paper will use the data translation invariance property of the DEA to improve performance. [1][2][6]

2.2. Tobit Model

After the evaluation of water use efficiency, the next step is to determine the influence factors. Some similar studies[4] use a Tobit model to estimate a second-stage relation between the efficiency related influential factors, which is expressed by equations 7 and 8.

$$\theta_k^* = Z\beta + \varepsilon \tag{7}$$

$$\theta_k = \begin{cases} \vartheta_k^* & if \quad 0 < \vartheta_k^* < 1 \\ 0 & if \quad \vartheta_k^* < 0 \\ 1 & if \quad \vartheta_k^* > 1 \end{cases} \tag{8}$$

where θ_k^* is the DEA efficiency score of DMU_k for water use as a dependent variable and Z is a vector of the independent variable. β is the vector and ε is the error term vector.[10]

3. Data Collection

3.1. Scope of Study

In this study, 31 areas in Ningxia (5 areas), Inner Mongolia (12 areas), and Gansu (14 areas) were used to calculate the DMU for each area (Figure 1).

In China, Ningxia and Gansu have the third- and fifth-smallest GDP by province, respectively, and Inner Mongolia has the fifteenth-largest GDP. These three provinces have more people work in agriculture than in any other industry. In each of these three provinces, more than 74% of water is used for agriculture; in Ningxia, over 90% of water is used for agriculture, which comprises only 11% of the GDP[2].

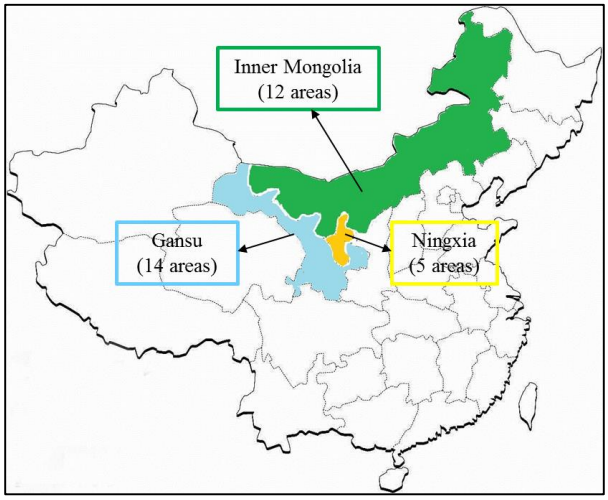

Figure 1. Map of China

3.2. Input and Output for the DEA Model

For the purpose of agricultural water use efficiency analysis, the input is the volume of agricultural water taken from water resources, and the output includes the gross output value of agriculture, forestry, animal husbandry, fishery, and the net income of rural households. For industry water use efficiency analysis, the input is the volume of industrial water taken from water resources, and the output is aggregated into two categories: industry value-added and wastewater discharged by industry.

3.3. Determinant Factors for the Tobit Model

The Tobit model is adopted to identify the determinant factors. Following the previous literature and theories associated with water use efficiency, the main elements that affect water use efficiency are given in Tables 2 and 3.

Table 2. Explanation of the involved variables (Agricultural water use efficiency)

	Variable name	Variable definition	Unit
Natural System	Water Endowment	Water resource capacity per capita	m^3/person
	Natural Conditions	Precipitation	100 million c.m.
Social System	Economy Level	Ln (GDP per capita)	Yuan/ Person
	Industrial Structure	Primary Industry/GDP	%
	Policy	Water right trade	0 or 1
	Market Openness	Foreign trade	100 million dollars

Table 3. Explanation of the involved variables (Industry water use efficiency)

	Variable name	Variable definition	Unit
Natural System	Water Endowment	Water resource capacity per capita	m^3/person
Social System	Economy Level	Ln (GDP per capita)	Yuan/ Person
	Industrial Structure	Secondary Industry/GDP	%
	Water Price	Industrial use water fee	Yuan/c.m.
	Fixed Asset Investment	Urban faxed asset investment	100 million yuan
	Policy	Water right trade	0 or 1
	Market Openness	Foreign trade	100 million dollars

4. Results

4.1 Water Use Efficiency

The DEA model is estimated using the model program Deap 2.1 under the assumption of variable returns to scale (VRS). The agricultural water use technical efficiency (TE) values in the target areas during 2008–2011 are relatively low as a whole, with average annual values of 0.284, 0.342, 0.353, and 0.272, respectively. In all of the target area, Jiayuguan and Gannan were at DEA-efficient levels for most years. However, most areas were DEA-inefficient during the research period. The average annual TE, PTE, and SE values of agricultural water use for each province are summarized in Figure 2. The results show that PTE has more influence on TE in Ningxia and Gansu, whereas SE has more influence on TE in Inner Mongolia. Based on the input-orientated DEA, the results show that there is water overabundance in the agricultural production of Ningxia and Gansu. In contrast, the agricultural production scale is overlarge in Inner Mongolia.

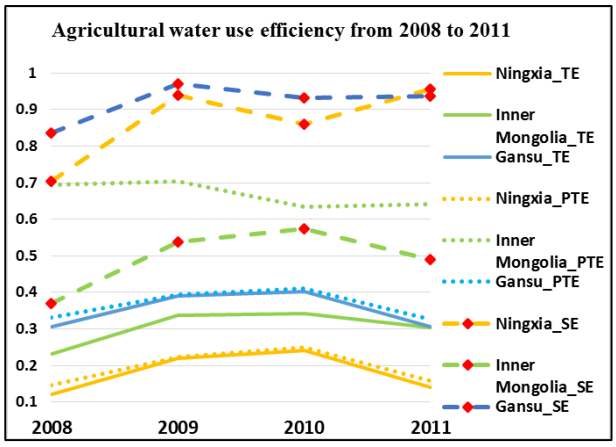

Figure 2. Agricultural water use efficiency in each province (TE, PTE, and SE)

The average annual industry water use efficiency values for 2008–2011 are 0.298, 0.479, 0.453, and 0.259 respectively. The results show that industry water use TE values in the target areas during the research period are relatively low on the whole. Gannan is at a DEA-efficient level for most years. Guyuan, Baotuou, Erdos, and Qingyang reached the DEA efficiency level for one year during the research period. However, most areas were DEA-inefficient during the research period. The average annual TE, PTE, and SE values of industry water use for each province are summarized in Figure 3. As the results show, PTE has more influence than SE on TE in Ningxia, Inner Mongolia, and Gansu. This means that water resources were used extravagantly in all provinces.

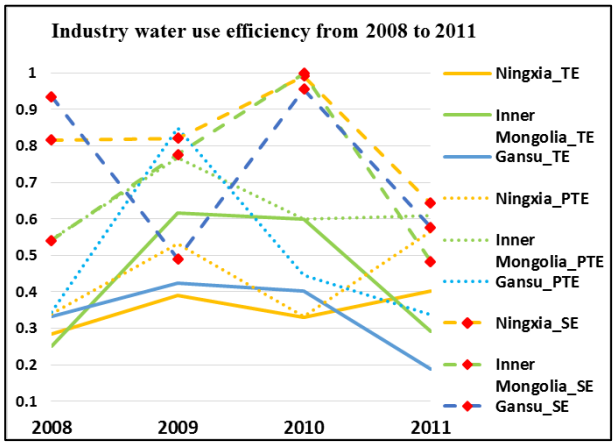

Figure 3. Industry water use efficiency in each province (TE, PTE, and SE).

4.2 Determinant Factor Results

The Tobit model is estimated using the model program Stata 12 for 31 areas. The estimated results for the six models showed incomplete consistency (Table 4).

Table 4. Agricultural Tobit model results

Independent variable	Model 1	Model 2	Model 3	Model 4	Model 5	Model 6
Economy Level	-0.0765*				-0.0966	-0.0687
Industrial Structure		0.0024			-0.0127*	-0.0118*
Market Openness			-0.0600**		-0.1021**	-0.0976**
Policy				-0.2715***		-0.1251
Water Endowment	-0.0684	-0.0594	-0.0909*	-0.0578	-0.0939*	-0.0911*
Natural Conditions	0.0007**	0.0006**	0.0009***	0.0006**	0.0011***	0.0011***
Constant	1.4458**	0.5613*	1.3047***	0.6480**	2.9663**	2.6255**

Note: (1)Robust estimates are used to eliminate data heteroscedasticity.
(2)*indicates a 99% significance level, ** a 95% significance level, * a 90% significance level.**

The results show that the natural conditions

variable—that is, rainfall—was significant and positively influenced agricultural water use efficiency in the six models. Generally, natural conditions greatly affected agricultural production. The market openness variable showed a significantly negative influence on agricultural water use efficiency in models 3, 5, and 6. The negative coefficients imply that the export benefits exceed the production cost, which motivates people to use more water. According to conventional views, economic development level significantly influences water use efficiency. In this paper, this conclusion is called into question by the estimated results for models 5 and 6. In these models, the EL was not significant. Perhaps the better economy did not bring advanced technology of agriculture production. The test significance of the variable policy also was inconsistent between models 4 and 6. For the society–economy system, the regression result of policy was significant (model 4). Because water right transfers may make it possible for farmers to compensate for their losses, farmers may lose the motivation to improve water use efficiency.

As shown in Table 5, the estimated coefficients of the 11 models showed inconsistency.

Table 5. Industry Tobit model results

Independent variable	M1	M2	M3	M4	M5	M6	M7	M8	M9	M10	M11
Economy Level	0.04								0.012	0.012	0.017
Fixed Asset Investment		0.07					0.122*	0.13**	0.003*	0.049	0.051
Industrial Structure			6E-04					0.003	-0.05	6E-04	6E-04
Market Openness				-0.01			-0.04*	-0.05	0.128	-0.04	-0.04
Price					0.123*					0.109	0.109
Policy						0.068					-0.03
Water Endowment	0.01	0	0.009	0.006	-0	0.012	-0.01	0.005	0.006	-0.01	-0.01
Constant	0.02	0.07	0.401	0.499	0.41**	0.402	0.206	0.102	0.009	0.385	0.345

Note: (1)Robust estimates are used to eliminate data heteroscedasticity. (2)*indicates a 99% significance level, ** a 95% significance level, * a 90% significance level.**

The estimated coefficients of the economic development level, fixed asset investment, and water price were positive. The estimated coefficient of industry structure was positive except for model 9. The variable market openness was the opposite. The estimated policy coefficient did not show identity between models 6 and 11. The estimated coefficients of water endowment were inconsistent in all the models. Among the variables, the estimated coefficients of water price and market openness were significant at the 10% significance level in model 5 and model 7, respectively. The water price mechanism definitely affected water use efficiency. In addition, a more market openness will lead to stronger competition production. Furthermore, urban fixed asset investment significantly influenced industry water use efficiency in models 7–9. The increase of investment in fixed assets indicates that advanced equipment and facilities are employed to utilize water for production.

5. Conclusions and Suggestions

This study showed that agricultural and industrial water use in the study area fail to reach overall technical efficiency levels, as both agricultural and industrial water use efficiency were at relatively low levels. PTE has a more significant impact on TE than SE does. For the determinants of agricultural water use efficiency, economic development level, agricultural industry structure, policy, and water endowment significantly influenced agricultural water use efficiency in some models. In addition, market openness and natural conditions were consistently significant. For the determinants of industrial water use efficiency, urban fixed asset investment, market openness and water price significantly influenced industrial water use efficiency. In order to improve water use efficiency, this study proposes the following policy recommendations. 1. Develop modern agriculture: utilize advanced agricultural technology, adopt drop irrigation, and develop agri-corporations. 2. Use advanced water-saving equipment and facilities and improve water use technology. 3. Improve the water price mechanism.

References

1. Agha IQBAL ALI, Lawrence M.SEIFORD, 1990, Translation Invariance in Data Envelopment Analysis, Operations Research Letters, 11, pp. 403–405.
2. Lawrence M. Seiford, Joe Zhu, 2002, Modeling undesirable factors in efficiency evaluation, European Journal of Operational Research, 142, pp. 16–20.
3. National Bureau of Statistics of China. (2011). CHINA STATISTICAL YEARBOOK. **12**(17), Beijing INFO Press.
4. Onishi A, Sato Y, Shi F, Han J, Morisugi M, Watanabe T, Fukushima, Y. 2009. Evaluation of Regional Difference of Agricultural Water Use Efficiency in China. J. Japan Soc. Hydrol. and Water Resour., 22(5), 356–371.
5. Per Andersen , Niels Christian Petersen,1993, A Procedure for Ranking Efficient Units in Data Envelopment Analysis, Management Science,39(10),pp:1261-1264.
6. Rolf Fare, Shawna Grosskopf, 2004, Modeling undesirable factors in efficiency evaluation: Comment, 157, pp. 242–245
7. Stihn Speelman, Marijke D'Haese, Jeroen Buysse, Luc D'Haese. A measure for the efficiency of water use and its determinants, a case study of small-scale irrigation schemes in North-West Province, South Africa. Agricultural Systems, 2008, 98:31–39.
8. T. Yaghi, A. Arslan, F. Naoum, 2013, Cucumber (Cucumis sativus, L.) water use efficiency (WUE) under plastic mulch and drip irrigation [J], Agricultural Water Management, 128, pp. 149–157.
9. William W. Cooper, Lawrence M. Seiford, Kaoru Tone, 2007, Data Envelopment Analysis, Springer, NY, p. xix.
10. Wooldridge, Jeffrey. 2002. Econometric Analysis of Cross Section and Panel Data. Cambridge: MIT Press.

ESTIMATING DIRECT AND INDIRECT CO_2 EMISSIONS OF AUTOMOTIVE MANUFACTURING SUPPLY CHAIN IN CHINA

Student Number: 12M18229 Name: Yun GU Supervisor: Shinya HANAOKA

中国における自動車産業サプライチェーンの直接・間接CO_2排出量の将来推定

谷 蘊

本研究では、中国の自動車メーカーの生産・輸送・使用段階における乗用車一台当たりの直接・間接CO_2排出量を、サプライチェーン全体を考慮して算出した。サプライヤーへのインタビュー調査により輸送機関や調達情報を確認し、現状の排出量を推計した。次に排出量削減シナリオを設定して推計したところ、使用段階の排出量が最も大きく、低公害車の普及や燃費改良が有効なことを明らかにした。また、石炭発電量の削減や鉄道輸送普及により、生産と輸送段階の排出量が同時に削減できることを示した。

1. Introduction

CO_2 emission reduction is one of the biggest issues in the world. Eighty percent of world's CO_2 emission comes from energy and heat, transportation and industry sector. Fossil fuel combustion generates a high emission in the world. China has been the largest CO_2 emission country since 2010. The role of CO_2 reduction in China, which relies on thermal power generation, has become more important. An automotive manufacturing, in particular, emits a large amount of CO_2 on its supply chain, as shown in Table 1.

Table1. Automotive manufacturing and CO_2 emissions

Step	Content	Emission sector
Production of parts and complete vehicles	Energy and electricity	Fossil fuel combustion
Transportation of parts and complete vehicles	Delivery from supplier to manufacture and from manufacture to dealer	Gasoline or other fuels
Use of vehicles	Run a car	Gasoline or other fuel
End-of-life vehicles	Recycle and dispose	Fossil fuel combustion

Automotive manufacturing occupies an important position in China manufacturing industry. The production and sales of automobile became number one in the world in 2009. However, the retain volume per thousand people in China is still 71, about half of the average retain volume per thousand people compared with developed countries. Purchasing power as well as demand for vehicles will increase along with an increase in economic growth and population number. Automobile sales will therefore increase significantly in China. It is certain that this would negatively affect the environment due to more CO_2 emissions from the manufacturing process.

According to Greenhouse Gas (GHG) protocol many companies and organizations have taken action in calculating and reporting GHG emissions while there are few Chinese companies that do so. Chinese companies are reluctant to announce their information to the public, which makes it difficult for third party to collect and calculate related data on GHG emissions. In addition, Chinese companies have been asked to share their GHG emissions information by foreign companies.

Looking at automotive manufacturing in China, more than 120 automobile companies and 2000 automobile part factories have been established in recent years. However, the merging and acquisitions of manufacturers with each other or with foreign manufacturers brings difficulty in getting the accurate data. Along with the problems of imitation of foreign car design and securities, several manufacturers shut down or transfer their website and even have their name changed. Many researches on estimation of CO_2 emissions in supply chain were conducted by using input-output table which can only make an average estimation, for example, an average estimation of all parts production in production phase. With the urgency of knowing the emissions of automotive manufacturing in China, and making a more accurate result, the research objectives are set as the followings:

1) To calculate the CO_2 emissions from automotive manufacturing in China based on the supply chain of both direct and indirect emissions.

2) To make CO_2 emissions reduction scenarios based on the present situation in China, and clarify the most efficiency way of reducing CO_2 emissions by comparing scenarios and current results.

2. Estimation Method

2-1. Study Boundary

According to GHG protocol, scopes of emission are defined into three categories. Combine the situation of automotive manufacturing, the boundary of this research is:

1) Direct CO_2 emissions – Direct emissions are generated from electricity, steam or heat in equipment that is owned by assembly plant when producing complete vehicles.

2) Indirect CO_2 emissions – Indirect emissions are generated from consumption of purchased electricity, natural gas, steam or heat that is not owned by assembly plant. For example, emissions from suppliers by producing parts. Relevant emissions from delivery of parts and complete vehicles, the use of vehicles and dispose stage are also considered as indirect emissions.

By considering locations and transportation modes of suppliers, the emission estimation might be more accurate.

2-2. Data

To estimate the direct CO_2 emissions, we need input energy data of complete vehicles production phase.

To estimate indirect CO_2 emissions, we need the data of electricity used in assembly plants, and energy used in suppliers during making parts in production phase. Data on total travelling distance and mode of transport (road, rail, maritime etc.) should be collected in transportation phase. In addition, data of total distance traveled by a vehicle also need to be considered in indirect emissions.

By comparing all automobile companies in China, Shanghai Automotive Industry Corporation (SAIC) has the largest share of production and sales, especially its branch company, Shanghai Volkswagen Automotive Co. (SVW). Considering the complex environment of automobile companies in China, one vehicle model (Lavida) is chosen as a representative in the research target considering data availability. Further, due to data unavailability, Life Cycle Assessment Society of Japan (JLCA) database (Japanese vehicle data) was used instead of Chinese database in production phase and transportation phase.

Table2. Comparison of Lavida and JLCA database model

Type	4 door sedan	4 door sedan
Weight[kg]	1265	1037
Displacement[cc]	1598	1500

There is no supplier list of SVW in manufacturing Lavida. By collecting supplier from reference materials, checking each part of suppliers producing and considering the distance of suppliers to assembly plant, a brief supplier list has been made. To ensure the accuracy of list, telephone interviews were directly done by asking suppliers' provider and method of delivery. After ensuring location of suppliers, distances between suppliers and assembly plant were measured by considering road traffic situation.

Dealers are found in the website of SVW. It shows number of dealers in each province in China. However, it was not clear whether the dealers deliver directly from assembly plant or not. By interviewing dealers directly, the method they use in transportation was then identified. For land transportation, Google map was used in distance measurement, while in railway and maritime part, distance information between each station was found in their official websites.

In use phase, the official fuel consumption is much smaller than the actual voting in the website. When considering reality, the bigger value is chosen for the research.

2-3. Methodology

2-3-1. Production Phase

Emissions from suppliers and emissions from assembly plant can be calculated based on Equation (1) and (2).

$$E_p = \sum_n g_n f \quad (1)$$

$$E_a = gf \quad (2)$$

Where: E_p and E_a is CO_2 emissions from suppliers and assembly plant on production process, respectively, g_n and g are electricity use ratio in China. f is emission factor. n is the number of supplier.

2-3-2. Transportation Phase

Calculation of this part is divided into road transportation and railway/maritime transportation. Road transportation is calculated by improved tonnage method while railway and maritime transportation are calculated by tonnage method. These calculations are made by estimation tool of the Policy Research Institute for Land, Infrastructure, Transport and Tourism (PRILIT). This tool was established under Ministry of Land, Infrastructure, Transport and Tourism (MLIT) of Japan. Equations are followings.

Road transportation for parts:

$$E_i = \frac{W_i \times d_{ij} \times C \times H \times F \times {}^{44}/_{12}}{u} \quad (3)$$

Land transportation for complete vehicles:

$$E_c = \frac{W \times d_{kl} \times C \times H \times F \times {}^{44}/_{12}}{q} \quad (4)$$

Railway and maritime transportation for complete vehicles:

$$E_R = \frac{W \times d_{rn} \times F_R}{q} \quad (5)$$

$$E_M = \frac{W \times d_{lm} \times F_M}{q} \quad (6)$$

Where: E_i and E_c are CO_2 emissions from truck by suppliers and assembly plant. E_R and E_M are CO_2 emissions from railway and maritime by assembly plant deliver to dealers. d is distance. W_i and W are the weight of parts and one complete vehicle. C is fuel use ratio basic unit. H is heat generation per unit. F is emission coefficient. F_R and F_M are emission factors. u and q are number of unit and number of complete vehicles.

Since there are all 876 dealers considered in this research, emissions of complete vehicles transportation phase from assembly plant to dealers can be calculated as follows:

$$E_D = \sum \frac{(E_M + E_C) \times S}{876} \text{ or } E_D = \sum \frac{(E_R + E_C) \times S}{876} \text{ or } E_D = \sum \frac{E_C \times S}{876} \quad (7)$$

Where: E_D is CO_2 emissions from assembly plant to dealers on transportation process. S is number of dealers in each province.

2-3-3. Use Phase

Equation in use phase is as follow.

$$E_u = \frac{d}{e} \times f' \quad (8)$$

Where: E_u is CO_2 emissions in use phase. d is average distance of one vehicle until life end. e is fuel consumption. f' is emission factor by gasoline.

3. Results

3-1. Present Emissions

From the interviews of suppliers and dealers, it is found out that road transportation is the most fundamental and dominating transportation mode. This is because of its low cost and availability of door to door service. Even though distance is more than 500km from assembly plant,

they prefer to use trailers than railway or shipping. Results of CO_2 emissions on supply chain of one vehicle in this research are shown in Table3. Use phase has the highest emissions among all stages. It shows urgency in reducing emissions on use phase.

Table 3 Current CO_2 emissions (t- CO_2/vehicle)

Production		Transportation			
Parts	Complete vehicle	Parts	Complete vehicle	Use	Total
0.2788	0.6361	0.0076	0.8807		
0.92		0.89		49.92	51.73

3-2. Scenario Building

From the results above and the equations in calculation, there are some factors that might affect CO_2 emissions. Besides fixed factors like distance and weight, other factors such as emission factors of electricity and fuel consumption might change results of emissions. In addition, results also rely on transportation modes because the emission factors are different. Therefore, several scenarios are considered, as shown in Figure 1.

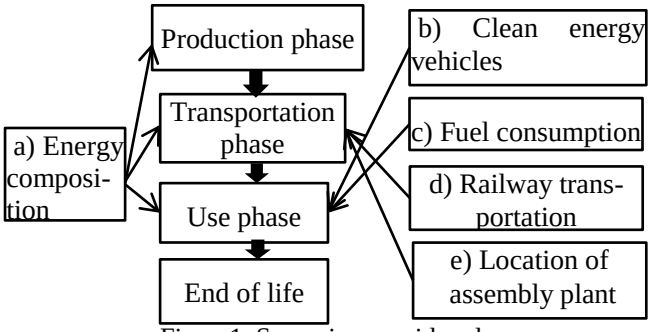

Figure1. Scenarios considered

i. Environmental Protection Scenario

a) Energy composition

This scenario is based on changes in emission factor of electricity generation. Emission factor of electricity generation in China plays an important role in production, transportation and use phase. For example, reduction of coal in energy consumption can make emission factor of electricity become much lower. Under the policy on expanding the use of natural gas, this scenario is considered as a) in Figure 1. In order to make comparison, electricity generation scenarios made by Low Carbon Asia research project are used in this research to estimate emissions in 2050 of both business as usual and mitigation results.

b) Clean energy vehicles

Another way of protecting environment is the popularization of a new energy car. This shows b) Clean energy vehicles in Figure 1. By 2020 mild hybrid & full hybrid cars are estimated to have more than 50% share of total sales of passenger vehicles in China.

d) Railway transportation

In transportation phase, the use ratio of trailers is currently high in complete vehicle transportation according to interviews. Currently there are no relevant laws and regulations to guide utilization of trailers. Dealers are used to overload the trailers. However, since freight railway infrastructure development is expected to increase in the future, the use ratio of railway is expected to increase too. This refers to d) Railway transportation in Figure1. Because of the emission factor of railway is much lower than truck and trailer, the reduction of CO_2 emissions could be forecasted. In this scenario, we set transportation mode as railway in the case when transportation distance is larger than 300km.

a) Energy composition × d) Railway transportation

Furthermore, a combination of energy composition and railway transportation can be considered as one of the scenarios (point a)×d) in Figure 1). This can not only effect transportation phase, but also production phase of CO_2 emissions.

ii. Technical Improvement Scenario

c) Fuel consumption

SVW aims to reduce their fuel consumption on vehicles to 0.049L/km, while the current fuel consumption of Lavida is 0.09L/km. Infrastructures and traffic situations affect fuel consumption in reality. In this scenario, we use official fuel consumption in calculation without thinking of real traffic situations. This refers to c) Fuel consumption in Figure1.

iii. West Development Scenario

e) Location of assembly plant × d) Railway transportation

Due to high cost of labor, market saturation and environmental degradation, more companies move to the mid-west China for development. Chinese government provides preferential policies in taxation to attract more companies to develop west side of China. In fact, SVW has made a new assembly plant in Xinjiang located in west of China to expand production.

Based on the consideration of the local resources, market share, as well as cost of labor, Yunnan province is chosen in this scenario as a new assembly plant. In addition, the railway connect Yunnan to Singapore is expected to be built in 2030; it will be more convenient for complete vehicles export through Yunnan. By considering the current location and situation of dealers, we can suppose that the new assembly plant will be built in Yunnan in 2020. Under the high use ratio of railway on transportation, CO_2 emissions might change in this case, which shows in Figure1 e)×d).

3-3. Results of Scenario Analysis

The results of scenarios are shown in Figure 2.

i-a) In this scenario, by changing the a) Energy composition, all stages of supply chain will be affected.

From the results, we can find that by changing the electricity generation, emission from the use phase is reduced significantly. Natural gas fuel emits fewer emissions than gasoline. Emission reduction on production phase is higher than on transportation phase, which shows energy composition plays significant role in production phase.

i-b) In this scenario, fuel consumption in use phase is changed from gasoline to fuel used by hybrid car.

More than half of the emissions will be reduced by using hybrid car instead of current passenger vehicle. Although the result only changed in use phase, it shows that it is important to generalize clean energy vehicles in China in order to reduce CO_2 emissions in automotive manufacturing.

i-d) By using railway on complete vehicles delivery, the CO_2 emission on transportation phase can be reduced significantly. Although the total emission is still high, the expansion railway transportation can still be considered meaningful.

i-a)×d) Combine changes on energy composition, and transportation mode to railway.

Reductions of emission on transportation phase are now higher than on production phase. This means that using railway on transportation is more significant compared to only changing the energy composition on transportation stage. In general, emission reduction of a) is larger than d), because use phase still has a biggest emissions on whole supply chain.

ii-c) The aim of this scenario is to reduce CO_2 emissions in use phase by reducing the fuel consumption. We assume that there is no change in production and transportation phase.

In use phase, the reduction is almost half of current emissions. The scenario shows changes in use phase has very effective result in CO_2 emissions reduction.

iii-e)×d) In this scenario, we consider that the location of the assembly plant is moved to Yunnan. Therefore, the transportation distance will also be changed. To make some assumptions on this scenario: firstly, the distance of dealers to assembly plant is between each railway station of provinces city; secondly, the method of transportation is by railway only; finally, the scenario only on transportation stage.

From this result, it is clear that by transferring the assembly plant to West China and by using railway as transportation, CO_2 emissions will be reduced.

Because of lack of data, on this scenario there are a lot of assumptions. In order to get more accurate result, the data need be reconsidered.

4. Conclusions and Discussions

This research calculated CO_2 emissions on automotive supply chain of one vehicle by considering locations of each supplier. This method may estimate more accurate results than input-output table. By identifying the suppliers, companies can get accurate emission data, and also can quickly take actions when problems happened with the suppliers.

By calculating the direct and indirect CO_2 emissions on supply chain of automotive manufacturing in China, we found out that the emission in use phase is much larger than any other two phases, takes about 96% share of CO_2 emissions in all phases. About 80% of real suppliers are used in this research due to data limitation. However, even if all suppliers are identified and utilized in calculation, the emissions from production and transportation phases still cannot reach the emissions as high as in use phase.

Furthermore, by comparing with Japanese vehicles, the emission in use phase in Chinese case is more than 7 times larger of Japanese case. There are two reasons considered: (1) the vehicle total travel distance is 2.5 times more than Japanese one, and (2) the fuel consumption of Chinese vehicle is 3.2 times more than Japanese one. However, of all life cycle, use phase has the greatest emission share of both countries' automotive manufacturing.

From both the current results and scenario analysis, we can identify that the more efficient way to reduce CO_2 emissions is by reducing the use phase emissions. By changing the mode in transportation phase can also lead to an emission reduction, even though the reduction is relatively small. Compared to changing energy composition, popularization of clean energy car is considered more effective in reducing CO_2 emission. However, the emissions will not be much reduced in case that the energy composition is not changed because clean energy cars use electricity as fuel.

Moreover, the traffic congestion situation should also be considered in this issue, since the CO_2 emissions are very much dependent on the fuel consumption of vehicle speed in the use phase. Without reasonable urban planning and vehicle purchase policy, the CO_2 emission reduction will not be completely effective.

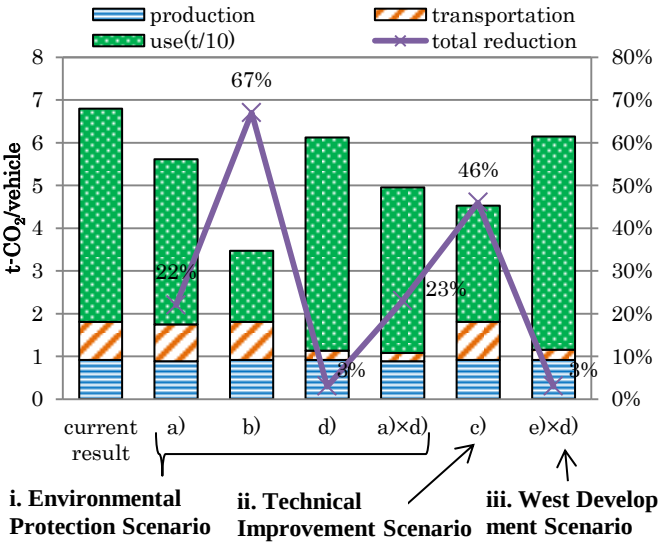

Figure2. Results of comparisons of scenarios
(For ease of comparison among the stages, to set unit of use as t/10)

References

[1] 国土交通政策研究所：物流から生じる CO_2 排出量に関する手引き，国土交通政策研究第 105 号，2012.

[2] Wang Shoubing el al.: Life cycle inventory of a China Car, Journal of Fudan University (Natural Science), 45(3), 2006.(in Chinese)

[3] 林寧他：産業連関表を用いた中国における経済発展と二酸化炭素排出に関する研究，Journal of Life Cycle Assessment, Japan, 6(4), 2010.

[4] 湯進：中国自動車産業のキャッチアップ工業化，専修大学社会科学年報第 45 号，pp.109-127, 2011.

[5] 李景明他 :中国新能源資源潜力及前景展望，天然气工业，28(1), pp.149-153, 2008.

[6] 丹治和男：中国におけるアフターマーケットの動向，Roland Berger Strategy Consultants, Vol.10, 2003.

CLARIFICATION OF AGRICULTURAL PRODUCTS SUPPLY CHAIN STRUCTURE, INCLUDING TRASPORTATION MODE CHOICE IN VIETNAM

Student Number: 12M18235 Name: Van Hung CHU Supervisor: Shinya HANAOKA

ベトナムにおける輸送機関選択を含めた農産物サプライチェーン構造の実態解明

チューバンフン

本研究は、ベトナムの主要農作物である米とそれを用いた加工食品を対象に、輸送機関選択を含めたサプライチェーン構造の実態を現地調査により解明することを目的とする。農家、集荷業者、代理店等の各アクター間の輸送量シェア、輸送機関分担率を算出し、距離別輸送機関分担率の違い、生産地と消費地で利用する輸送機関の違いを明らかにした。また、現状のサプライチェーンには多くのアクターが存在するという問題点とその原因を指摘した。

1 Introduction

Vietnam is a developing country and its economy is highly dependent on agriculture. 48.4% of total employees are engaged in agriculture, forestry and fishery in 2011[1]. Rice plays an important role in the economy of Vietnam because of the production volume (i.e. the largest among agricultural products) and workers (i.e. production, transportation, sales and the other sectors of rice).

Market size of processed food has been expanding at 17% annual rate in recent years [2]. In Vietnam, both traditional retail stores and modern retail stores (i.e. convenience stores, supermarkets, and hypermarkets) do exist. A number of modern retail stores are growing 23.7% annually while traditional retail stores increase slowly at rate 1.9%.

The processed food market has been growing because of change of economic development and lifestyle (i.e. working women, awareness of health and safety). The level of expectation of consumer becomes higher, so sales method should be changed. To meet the high requirements of consumers, large retailers demand high quality of products from suppliers. As a result, it requires a comprehensive innovation in the supply chain to meet these high requirements of consumers. Supply chain of agricultural products are said to be underdeveloped and need strategies to improve the supply chain. Many motorcycles that have low carrying capacity are used for transportation of agricultural products. It is also necessary to clarify which mode of transportation should be used for transportation between actors. Besides, processed food needs to be considered as important actors in the supply chain of agricultural products because it creates high value-added even higher than agricultural products produced.

So far, there are many research related to agricultural products of Vietnam, but the researches which clarify the structure of supply chain are still very few. Phan, et al.[3] came up with a solution to replace co-operatives in the supply chain by a company to complete supply chain for a safe vegetables area at Tuy Loan- Da Nang, but this research did only at the introduction to what kind of actors should exist in the supply chain. Quantitative analysis did not show transportation volume share in the supply chain. Vo, et al.[4] drew up the rice supply chain in the Mekong River Delta. This research only showed transportation volume share between each actor, but there was no information about modal share between each pair of actors in supply chain. This research also did not consider processed food as important actor.

The objective of this study is to clarify the real situation of supply chain structure, including the modal share of agricultural products and processed foods in Vietnam. In specific, 1) Clarify actual situation of supply chain, especially focus on rice and consider processed food as important actor. 2) Estimate transportation share and modal share between each actor in supply chain. 3) Identify problems of supply chain structure.

2 Formulations

To clarify the supply chain of agriculture products, this study uses two formulations below.

2-1 Calculation of transportation volume share between each actor

Figure1: Description of origin and destination

Assumed that i is origin actor, j is destination actor, and k is origin actor of actor i, N is number of actors existing in the supply chain, therefore $i,j,k = \{1,2,..i,..,j...N\}$. Products transported in supply chain, in this case, are rice and processed food from rice such as liquor or dried noodle.

r_{ij} is the transportation volume share of products transported from origin actor i to destination actor j in total weight of products transported in supply chain. r_{ij} is calculated by equation (1) below.

$$r_{ij} = \left(\frac{q_{ij}}{q_{i1}+q_{i2}+\cdots+q_{iN}}\right) r_i \qquad (1)$$

Here, $q_{i1}, q_{i2}, \ldots, q_{iN}$ is the weight (unit: kg) of products transported from origin actor i to destination actor $1,2 \ldots j,..N$.

$r_i$is total of transportation volume share of products transported from another actors $\{1,2, \ldots k\}$ to actor i be calculated as:

$$r_i = r_{1i} + r_{2i} + \cdots + r_{ki} = \sum_{k=1}^{N} r_{ki} \qquad (2)$$

The constraint condition here will be:

$$q_{ij} = 0, if, i \geq j \quad (3)$$

$$and, \quad r_1 = 1 \quad (4)$$

Equation (3) means that in supply chain, the products will be transported from an origin actor to a destination actor and not be able to conversely transport from destination actor to origin actor.

In supply chain, total of transportation volume share of products transported from another actor $\{1,2,\dots k\}$ to actor i will be equal to total of transportation volume share of products transported from actor i to another actor $\{1,2,\dots k\}$. Therefore, equation (4) means that total of transportation volume share of products transported from actor 1 to another actor will be equal 100%.

S_i is the sample size obtained from survey in the case of products transported from origin i to destination actor j, h is one of samples, $h = \{1,2,\dots . S_i\}$.

Then, $q_{ij} = \sum_{h=1}^{S_i} q_{ihj}$ (5)

Therefore:

$$r_{ij} = \frac{\sum_{h=1}^{S_i} q_{ihj}}{\sum_{j=1}^{N} q_{ij}} \sum_{k=1}^{N} r_{ki} \quad (6)$$

2-2 Calculation of modal share between each actor

p_{ijm} is modal share of transportation mode m used to transport products from origin actor i to destination actor j, p_{ijm} will be calculated as the equation (7) below:

$$p_{ijm} = \frac{q_{ijm}}{q_{ij}} \quad (7)$$

q_{ijm} is the weight (unit: kg) of products transported from origin actor i to destination actor j by mode m,

$$q_{ijm} = \sum_{h=1}^{S_i} q_{ihjm} \quad (8)$$

Therefore:

$$p_{ijm} = \frac{\sum_{h=1}^{S_i} q_{ihjm}}{q_{ij}} \quad (9)$$

3 Field survey

Red River Delta including rice-producing area (Kim Son district of Ninh Binh Province and 3 District of Nam Dinh Province) and rice consuming region (Capital Hanoi, Nam Dinh City, Ninh Binh City) were chosen to be the places for field survey.

Figure 2: Location of field survey

All actors are required to answer the questions asked in the questionnaire. Important questions are 1) what kind of vehicle have you used? 2) How much was volume of product transported to another actor? And 3) how far of distance of products transported in one shipment?

The total number of respondent is 470 and total of sample size obtained in survey is 1056. Actually, one respondent in interview can give one or more sample.

4 Results

4-1 Structure of supply chain

After conducted field surveys, we divided the number of actors existing in the supply chain and the number of transport modes used to be 16 and 24 respectively.

Names of the actors are summarized in the Table 1. Actors i), ii), iii), iv), v) located in producing area while actors vi), viii), ix), xii) located in consuming area. Actors vii), x), xi), xiii), xiv) located in both producing area and consuming area.

Table1: The name of the actors

Name of actors, (number of respondents), (sample size)	
i) Farm	ix) Regional agency, (12), (33)
ii) House of farmer, (213), (489)	x) Bottling plants, (0), (0)
iii) Collector, (22), (39)	xi) Distributor of processed food, (1), (2)
iv) Agency, (66), (136)	xii) Super market, (3), (6)
v) General agency, (35), (101)	xiii) Traditional store, grocery store, (23), (39)
vi) Wholesaler, Polishing factory (3), (13)	xiv) Consumer in Red River Delta (individual consumer, hotel, restaurant, karaoke, army, school)
vii) Processed food household (liquor, dried noodle), (85), (171)	xv) Whole Vietnam except Red River Delta
viii) Distributor of rice, (7), (27)	xvi) Export

Names of transportation modes are summarized in the Table 2. The transportation distance of motorcycle and three wheels motorcycle is longer than the other short trip modes (i. e. (b), (d), (k), (p), (q), (r), (s), (t), (u), (x)). The volume transported by three wheel motorcycle in one shipment is larger than that transported by the motorcycle in Figure 3. All trucks are overloaded (i.e. (e), (f), (g), (h), (i)). For example, (e) 0.5 ton truck is designed to transport 500 kg of goods, but in fact it is used to transport nearly 2,000 kg of rice. Bus is used to transport rice and processed food in the distance from 20km to 1700km in Figure 3.

By using data obtained from the field survey, this study can clarify the supply chain structure of rice and processed food (liquors, dry noodles) made from rice in the Red River Delta, and is able to calculate amount of transportation share between each actors.

The transportation volume share and structure of supply chain are drawn as the Figure 7. The result is

Table 2: The name of transportation modes

(a) Motorcycle	(m) Bus
(b) Mode of combining box and two wheel motorcycle	(n) Railway
(c) Three wheel motorcycle	(o) Coastal shipping (vessels)
(d) Cong nong	(p) Bicycle
(e) 0.5 ton truck	(q) Mode of combining shelf and bicycle
(f) 1 ton truck	(r) Cyclo, trishaw
(g) 1.25 ton truck	(s) Put on head
(h) 3.5 ton truck	(t) Put on shoulder
(i) 8 ton truck	(u) Human rickshaw
(j) Trailer	(v) Taxi
(k) River shipping (boats)	(w) Animals (horse, buffalo)

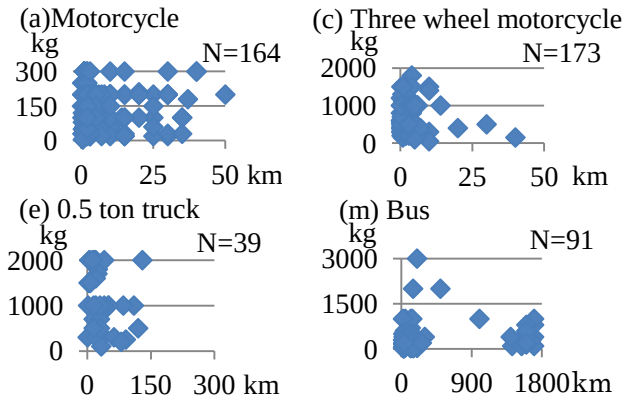

Figure 3: Dispersion diagram of transportation distance and transportation volume of (a), (c), (e) (m) in one shipment

that 100% of total volume of rice products are transported from actor i) to actor ii) after harvesting, 15.62% of total volume of rice products are used to make processed food such as liquor, dried noodle, only 2.23% of volume of rice are sold through supermarket. While 50.93% of total of rice and processed food such as liquor and dried noodle is sold through actor xiii). 62.96 % of total volume of rice and processed food are consuming by actor xiv), 32.04 % of total volume of rice and processed food are sold to actor xv), only 5% of total volume of rice are exported directly from actor v) and vi).

4-2 Modal share between each actor

This study calculates modal share between each actor in the supply chain, also shows the difference of modal share between short and long transport distance in the supply chain as shown in Figure 4. In short distance transport, motorcycle is mainly used. In long distance transport, uses of motorcycle are also found. Transportation by bus also exists for long distance transport because it is more convenient and cheaper than truck or train when transporting in small volume only as shown in Figure 4. Owner of bus put bags of dry rice or bags of dried noodles, cans of liquor under

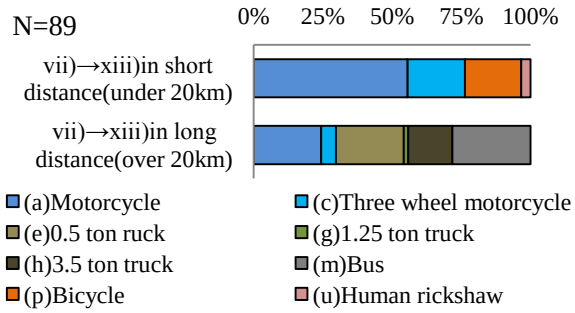

Figure 4: Different of modal share between short and long transport distance of vii)→xiii)

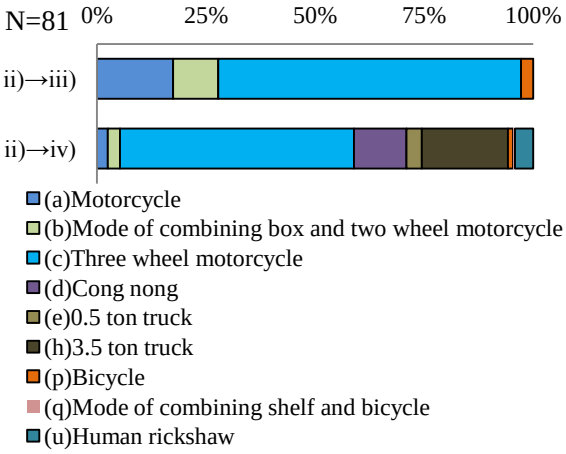

Figure 5: Modal share in producing area

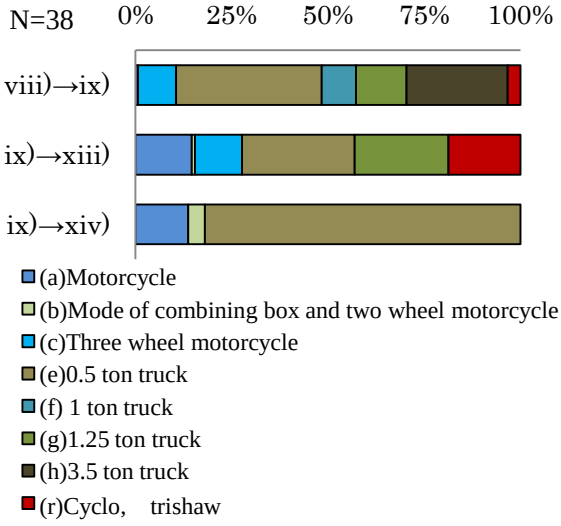

Figure 6: Modal share in consuming area

the footrests of passenger seat, space in the bus, or under the bus where using to put luggage.

In producing area, main transport mode is not truck. The main transport modes are motorcycle and three wheel motorcycle because of some reasons (i.e. a lot of motorcycles are available; farmers do not sell much in one time; roads from the house to farmer are narrow; the using of homemade transportation modes, such as mode (b), are not prohibited etc.) in Figure 5.

In consuming areas, 0.5 ton truck and motorcycle are mainly used as shown in Figure 6. The reason is because roads in the capital Hanoi or other cities are narrow, and drivers want to avoid traffic congestion.

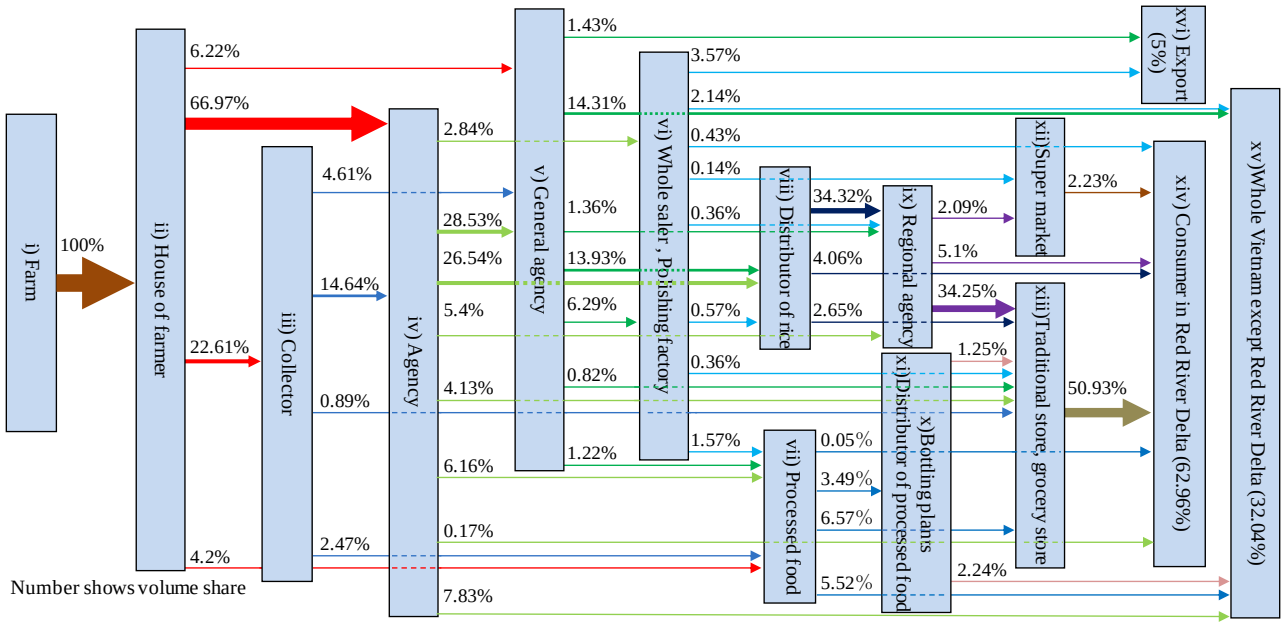

Figure 7: Structure of supply chain of rice, processed food from rice (liquor, dried noodle) in Red River Delta

4-3 Identify problems

There are three reasons why many actors exist in supply chain. First, it is easy to participate in the supply chain (i.e. Free market, rice is producing in whole Vietnam). Second, consumer mainly buy rice from traditional stores (sold by traditional stores is 50.93% and supermarket is 2.23%), most consumers do not consider value-added of rice, so actor iii) Collector who cannot make value-added still exsits. Third, it is difficult for an actor to make his own distribution and marketing network; and lack of distribution network (ex. Yamato or Sagawa in Japan) because, except for actor vi) and actor xii), all actors can be managed with only few employees from 1 to 5 persons, so many actors need to play as a distributor in supply chain now.

Both iv) Agency and v) General agency existing in supply chain are one of special characteristics of Vietnam because of first reason and third reason written above.

5 Conclusions

After clarification of the rice supply chain in the Red River Delta area, it is found out that there are a lot of transportation modes used between each actor. Actors mainly use motorcycle, three wheel motorcycle and homemade mode in producing area, while actors mainly use motorcycle and 0.5 ton truck in consuming area. In long distance, actors still use motorcycle and bus for transportation.

At present, existing problem in supply chain is that there are too many actors. This problem leads to drop in quality and loss in quantity of rice because repackaging at each actor, which make supply chain become inefficient. Moreover, profits of famer become very few because after agricultural products were produced by farmer, they have to go through many intermediaries before reaching consumer.

In future, when consumers mainly buy products through modern retail store (i.e. supermarket) collectors do not need to exist in supply chain. In this case, collectors mean iii) and other actors such as iv), v), viii), ix) shown in Figure 7.

Until now, there are a lot of cooperatives existing in Vietnam, but most of them only cooperates in upstream of supply chain, only have relationship with farmer as supplier of irrigation services, plant protection and agricultural materials such as fertilizers, pesticides (Pham Vinh Dien[5]). Therefore, we propose to re-eatablish cooperative to replace the role of intermediary actor such as actor iv), v), and vi) located in producing area. This cooperative can play the role as actor wholesaler, polishing factory and have enough ability to make high quality of rice to sold directly for supermaket or retailer (such as actor xii), xiii) at consuming area.

References

[1] General Statistics Office of Vietnam: http://www.gso.gov.vn/default_en.aspx?tabid=466&idmid=3.

[2] The food market environment research in Thailand, Vietnam, Myanmar, Daiwa Institute of Research report, 2012 (in Japanese).

[3] Phan Thi Nhu Hoa, et all.: Completing supply chain for a main safe vegetables area at Tuy Loan- Da Nang, Collections of Report of student scientific research Conference 8th at Danang University, 2012 (in Vietnamese).

[4] Vo Thi Thanh Loc, et all,: Part1: Value chain analysis of rice product in the Mekong Delta, Science journal, 19a, 96-108, 2011 (in Vietnamese).

[5] Phan Vinh Dien: The current situation and development solution of agriculture cooperative of our country today, Southern Center for Support and Development of Cooperative, Small and Medium Enterprise, (in Vietnamese).

Visual Object Categorization by Background Removal with Depth Image

Students Number: 12M18175 Name: Joowon KIM Supervisor: Yukihiko YAMASHITA

深度画像によって背景情報を除去する画像分類

金 柱源

近年，スマートフォンの普及により爆発的に増加したデジタル画像は，日付や場所などの情報を含んでおり，その情報によって自動的に整理されている。しかし，その画像内の物体やシーンの情報に基づく現在の自動的な整理手法にはまだ性能が低いという問題がある。そのため，自動的に画像内の物体を認識して分類する手法の高性能化が要求されている。画像分類では，画像を局所特徴量を用いて分類する Bag-of-Keypoints 法が提案され，広く利用されている。しかしながら，この手法は画像全体から特徴を抽出するため，背景情報の影響を受けやすいという問題がある。そこで，本研究では深度画像により背景を除去する手法，そして階層型データベースの構築手法を提案し，計算機実験によって提案手法の有効性を検討する。

1 Introduction

In recent years, the digital image revolution in the World Wide Web facilitates the storage of large collections of digital images. Especially, the proliferation of digital imaging sensors in smartphones has increased the number of images exponentially. These images of various scenes include an important information such as datetime, place and the type of camera. However, this information is not enough to manage a huge number of images. Thus, this exponential growth of the digital images has generated a compelling need for innovative techniques to retrieve and categorize images from large data to use education, the artificial intelligence and the medical field.

For visual object categorization, many kinds of methods were proposed from 1960. Among many methods, Bag-of-Keypoints (BoK) [1] that expresses an image by a histogram has been applied widely because of the computation efficiency and time. However, this method has limitations that image lost its size and the histogram can be influenced by the background information. Thus, I focus the research on the background removal and the construction of hierarchical database based on the size and the shape to improve the categorization time and precision.

The rest of this paper is organized as follows. Section 2 presents the Bag-of-Keypoints method and its disadvantages. Section 3 presents the proposed method and Section 4 presents experimental results and discussions. Finally, I conclude this paper in Section 5.

2 Bag-of-Keypoints

Recent advances in image processing techniques have given rise to extract such robust and invariant features from images. Among many techniques, Scale Invariant Feature Transform (SIFT) [2] has been applied to the visual object categorization because of the robustness to changes in scale, rotation, and illumination. Usually, a large number, hundreds or thousands, of features are extracted from each image by computing the intensity pattern using SIFT. However, the visual object categorization method with all SIFT features has a disadvantage on computational complexity and time.

The Bag-of-Keypoints method is similar to Bag of Words (BoW) in the text retrieval. First, each keypoint is extracted by a vector descriptor such as SIFT and described as a high dimensional vector. The calculated descriptors are vector-quantized by the k-means clustering. Then, all of the descriptors are assigned to the nearest cluster. Finally, an image is represented by a bag of these keypoints expressed by a histogram so that images are categorized by a classifier.

However, this method has two disadvantages. In the Bag-of-Keypoints model, an image is considered as a set of keypoints besides loss of size and shape. However, the characteristics such as size and shape are very important informations of the object. Therefore, it is necessary to use not only keypoint descriptors but also other characteristics to improve the precision of categorization. Also, in this method, the keypoints are extracted in a whole image so that the background information is contained in the histogram. The information of background decreases the precision. In recent years, the RGB-D camera such as Kinect that can get not only 2D location but also depth has been started to use in our daily life so that it will propagate rapidly in the future. The background can be removed easily if the depth between the object and the camera is known. Therefore, to overcome the limitation, I propose a background removal method by using depth images and a construction method of a hierarchical database. In background removal stage, the histogram of depth values is used for background removal and the RANSAC method is used for ground removal. Also, in the database construction stage, the size and the number of keypoints are used.

3 Overview of Proposed Method

In general, for background removal, color-based image segmentation techniques are often used. However, it is very difficult to extract the exact region of an object. Therefore, I propose to use a depth image for background removal. A depth image has an image channel that contains information about the distance between the object and the viewpoint. It is obtained by infrared sensors of a RGB-D camera. Usually, an image consists of background, object, and ground. Each region has different characteristics. In the background region, the depth values are larger than those of the object or the ground and the most of depth values have similar values. Besides, in the ground region, the ground is a plane and the depth values are increased continuously from bottom to up in an image. Thus, I extract the object region by 2 steps: background removal and ground removal. First, the histogram of depth values is used for background removal. The depth value is increased sharply on the boundary between an object and an background in a depth image. It means that the depth values between the object and the background do not exist. Thus, the histogram is divided into two regions so that the background can be removed by removing the region of high depth values in the histogram. Also, the region of 0 depth values is removed.

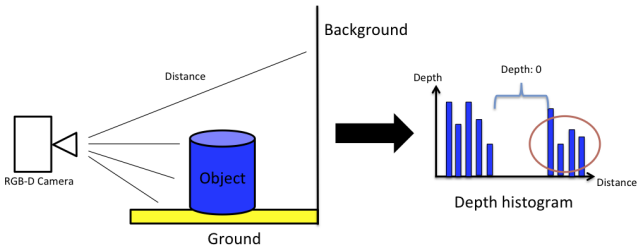

Figure 1: Background removal

Second, I propose to use the constrained RANdom SAmple Consensus (RANSAC) [3] method for ground removal. RANSAC that was proposed by Fischer is an iterative method to estimate a statistical model from a set of data which include outliers. In general, ground is a plane and an object is on the ground in many images so that the ground is considered as an inlier for plane fitting in an depth image. However, objects have many shapes so that an object is considered as an outlier. The process of ground removal is as follows. First, three columns are selected randomly from the depth image. Second, the depth values are analyzed by bottom up approach in the selected three columns. The two points are selected when the depth value of the below pixel is smaller than that of the upper pixel and one point is selected when the depth value of the below pixel is larger than that of the upper pixel. Then, the plane is estimated by these three points. To find the best plane, the same process is repeated. By this method, the object region is extracted.

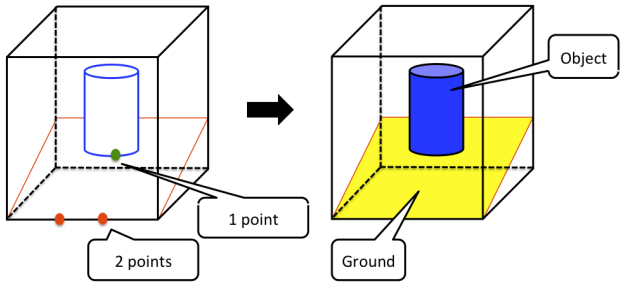

Figure 2: Ground removal

For the construction of a hierarchical database, I use the size of an object and the number of keypoints. The size is an important characteristic to categorize the images based on objects. The size of an object is computed by counting pixels in the object region. However, the size depends on the distance between the object and the camera. Thus, some objects are downsized if the object is closed to the camera and some are upsized if the object is far from the camera. Also, the number of keypoints can be used as a characteristic for categorization. We can expect that the object which has a large number of keypoints is a complex object and the object which has a small number of keypoints is a simple object. Therefore, I build a three layer hierarchical database of the training images by using the size and the number of keypoints. The third layer consists of the original data. The second layer consists of the three clustered image groups based on the size of an object. The first layer consists of the nine clustered image groups based on the number of keypoints.

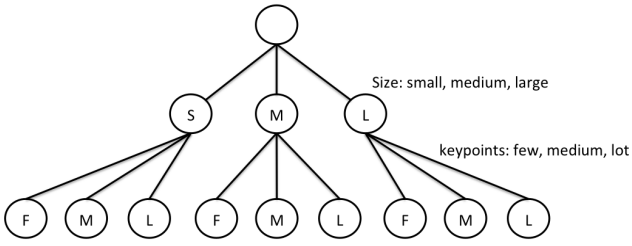

Figure 3: Hierarchical database

The precess of the proposed method is as follows:

1. Remove the background of each training image based on its depth image.
2. Detect and make descriptors of keypoints in the object region.
3. Generate visual vocabularies by applying the vector quantization.

4. Assign all descriptors to a set of visual vocabularies which is called as codebook.
5. Construct a resulting histogram on an individual training image, which counts the number of descriptors assigned to each vocabulary and treat the histogram as a feature vector.
6. Build hierarchical database by the size and the number of keypoints.
7. Construct a resulting histogram of an unknown image based on the same codebook.
8. Evaluate the similarities between the query and training images.

4 Experimental Result

To evaluate the proposed method, a large image collection for the visual object categorization task by depth images is used [4]. The experimental data set consists of 20 kinds of objects, the total number of images are 18,511. Before the learning process, 9,904 images are selected as a training set. To compare the categorization time and precision, I set the seven different numbers of visual vocabularies as 10, 30, 50, 100, 200, 300, and 500. After the construction of visual vocabularies, all images in the training set are represented by histograms. For a quantitative evaluation of the categorization results, another 8,607 images are selected as a test set and the nearest neighbor method is used for categorization. The distances that are used for the nearest neighbor are euclidean distance, manhattan distance, correlation, chi-square, intersection, and Bhattacharyya distance. The categorization time is used to evaluate the construction of hierarchical database.

Figure 4 shows the results of the background removal by using a depth image. It is observed from Figure 4 that for the image that consists of a background, an object, and a ground, its object region can be extracted clearly. However, for the image that consists of a turntable and an object, its object region cannot be extracted. Also, for the images such as a soda can and a water bottle which have reflective surfaces, the exact region of an object cannot be extracted because of the 0 depth value.

Figure 5 shows the categorization time by performing the proposed method and the original method to show the actual improvement on seven different numbers of visual vocabularies. The categorization time is the average of six trials. It is clear from Figure 4 that the categorization time of the proposed method is about 5 times faster comparing to that of the original method. This result shows that constructing a hierarchical database is an effective method to speed up the categorization.

Figure 4: Examples of background removal

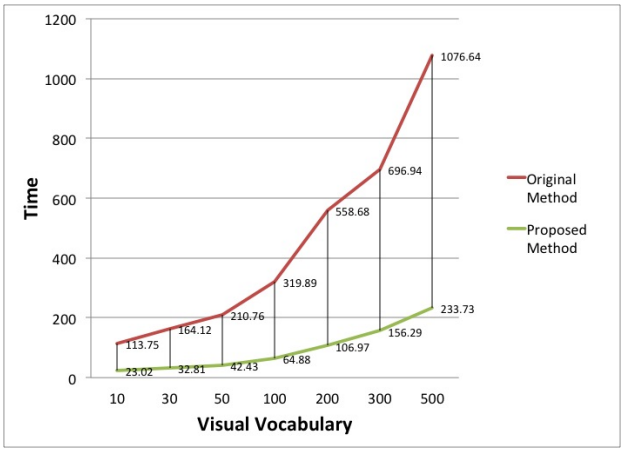

Figure 5: Categorization time

Figure 6 shows the precision of categorization on seven different numbers of visual vocabularies by using six kinds of distances. It is observed that the precision of the proposed method is increased comparing to that of the original method. This result shows that the background removal method and the hierarchical database based on the size and the number of keypoints improve the precision. Also, it is clear from Figure 6 that the precision of categorization by using manhattan distance and intersection is better comparing to that by using other distances. It is the reason that the influence of outliers in the histogram becomes larger when the distance is raised to the second power.

Table 1 shows the precision of categorization in each object when the number of visual vocabularies is 300 and the distance for the nearest neighbor is intersection. It is clear from Table 1 that the objects such as

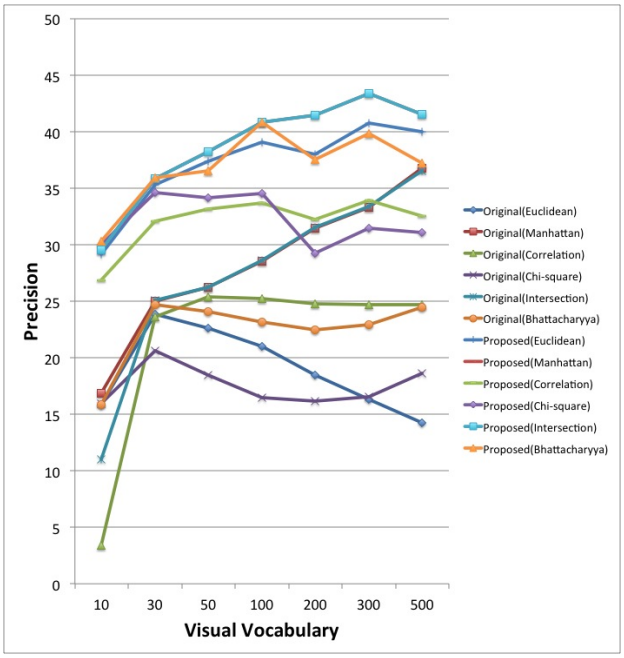

Figure 6: Precision of categorization

cap and cereal box have good precisions in the proposed method. By analyzing the sizes of objects, it is observed that the two kinds of objects have distinctive characteristics. They are larger than other kinds of objects. Thus they are clustered into the same group by constructing the hierarchical database based on the size so that the precisions are increased sharply. Also, it is observed that the precisions of objects of which background regions are removed clearly are increased but the precisions of balls and calculators are still low. It is the reason that those objects are too small and have various shapes.

From those results, it is not necessary to evaluate all training images. We can speed up and improve the precision by evaluating between a query image and selected images.

5 Conclusions

I have investigated the visual object categorization by background removal and a hierarchical database. In this approach, the background and the ground region are removed at the preprocessing stage. An keypoint is detected and described by the SIFT descriptor. Based on the construction of visual vocabularies, an image is represented by a histogram. The proposed method evaluates the similarities/correlations between hierarchical training data and a query image. The query image is categorized by the nearest neighbor method. Experimental results showed that the proposed method improved the categorization time and the precision of categorization. However, the results are not enough to apply to a practical use. It would be necessary to improve the precision in more than 50% for a practical use.

Table 1: Categorization rate on each object

	Original method	Proposed method
Object	Precision	Precision
apple	79.13%	77.56%
ball	4.23%	6.55%
banana	41.22%	31.08%
bowl	16.01%	25.29%
calculator	26.99%	0.00%
cap	62.70%	89.29%
cereal box	55.46%	78.18%
coffee mug	23.09%	40.97%
flashlight	0.00%	0.00%
food bag	58.00%	0.8%
food box	9.88%	20.50%
food can	38.70%	67.87%
greens	41.22 %	30.07%
instant noodles	28.12%	72.98%
keyboard	92.13%	71.76%
kleenex	80.88%	43.34%
notebook	42.37%	30.84%
soda can	20.67%	31.01%
toothpaste	25.46%	56.52%
water bottle	13.16%	80.78%

For future works, I plan to research on a better Hierarchical database for training data to speed up the categorization time and improve the precision. Also, I plan to study on a better visual object categorization method by using many kinds of characteristics.

References

[1] G.Csurka, C. Bray, C. Dance, and L. Fan.: Visual categorization with bags of keypoints, ECCV Workshop on Statistical Learning in Computer Vision, pp.1-22 (2004).

[2] Lowe, D. G.: Object recognition from local scale- invariant features, IEEE International Journal of Computer Vision, 60, 2, pp. 91-110 (2004).

[3] Martin A. Fischler and Robert C. Bolles.: Random Sample Consensus: A Paradigm for Model Fitting with Applications to Image Analysis and Automated Cartography. Comm. of the ACM, pp.381-395 (1981).

[4] RGB-D Object Dataset: http://www.cs.washington.edu/rgbd-dataset/dataset/rgbd-dataset/

Control Method of Boost Switching Regulator for Generators with Voltage Variation

Student Number:12M18117　　Name: Yoshito HONDA　　Supervisor: Kunio TAKAHASHI

周期的に電圧が変動する電源を入力とした昇圧スイッチングレギュレータの制御手法

本多 慶人

変動のある電源を入力とし昇圧スイッチングレギュレータを用いてエネルギーを蓄積する際に、最大出力点追従を用いない制御手法を検討している。電源を直流電源と変動と見立てた交流電源に置き換え、等価回路モデルを用いてエネルギー蓄積効率を解析的に導出した。等価回路モデルの限界により解析解を用いることのできない範囲では数値的にエネルギー効率と各パラメータの関係を明らかにした。導出したエネルギー効率をもとに昇圧スイッチングレギュレータの制御手法を提案した。

1. Introduction

Energy harvesting has become a popular research topic as a technology of scavenging energy. The energy sources are vibration, sunlight, wind, water flow, and so on. The characteristics of harvested energy from these energy sources are small or unstable to use directly. In order to use the energy sources as a power sources, Maximum Power Point Tracking (MPPT) methods using a convertor is researched [1][2][3]. Maximum Power Point (MPP) is a point on i-v characteristics at which the harvested energy is maximized. MPPT is the technique for searching and tracking the variation of MPP by the power source's voltage variation. Tanaka optimized a boost switching regulator for energy harvesting analytically considering MPPT [4]. Fig.1 is a schematic illustration of the relation of the sampling period of MPPT T_{MPPT}, the switching period of the regulator T_{S} and the period of power source's voltage variation T_{P}. Considering the applicability of MPPT, when T_{P} is enough longer than T_{MPPT}, MPPT is effective. However, when T_{P} is comparable or shorter than T_{MPPT}, MPPT is not adoptable. In this study, for suggesting a control method of the boost switching regulator for the power source with the voltage variation without MPPT, the energy efficiency of the boost switching regulator is obtained by analytically and by numerically. When T_{P} is comparable or shorter than T_{S}, the switching regulator cannot be used. So, in this study, T_{P} is assumed enough longer than T_{S}.

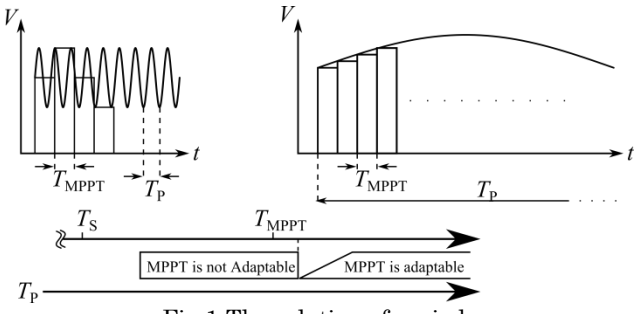

Fig.1 The relation of periods

2. Theoretical approach

2.1 Equivalent circuit of switching regulator circuit

Fig.2 shows a switching regulator circuit. To make an equivalent circuit of the switching regulator, some assumptions are introduced. A power source which has voltage variation is assumed as a DC voltage source and an AC voltage source which have a constant internal resistance and linear I-V characteristics like fig.3. The waveform of output voltage of power source is shown in fig.3 (b). It is assumed that the period of AC voltage source is enough longer than the switching period of the regulator. A capacitor is used as the storage device. The capacitor has large capacitance so that the capacitor's voltage can be assumed to constant voltage in several switching. In other part of the switching regulator, the circuit which is used in [4] is used. Then the equivalent circuit is shown in fig.4. Followings are parameters in the equivalent circuit and the model of power source.

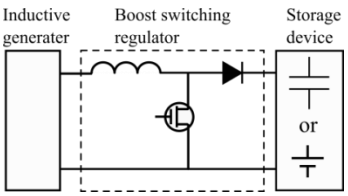

Fig.2 The switching regulator circuit

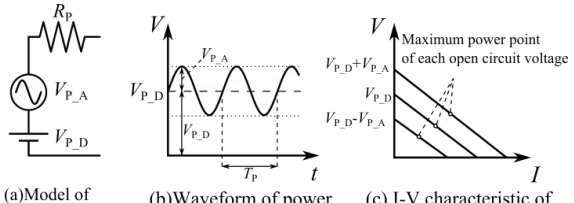

Fig.3 The model of the power source

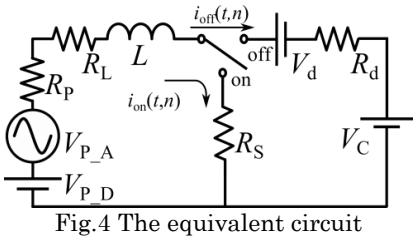

Fig.4 The equivalent circuit

V_{P_D} : Average voltage of power source

V_{P_A} : Amplitude of power source's variation

R_P : Internal resistance of power source

T_P : Period of power source's variation

L : Inductance

R_L : Internal resistance of inductor

V_d : Forward voltage of diode

R_d : Internal resistance of diode

R_S : Internal resistance of FET

V_C : Voltage of capacitor

V_{CD} : $V_C + V_d$

$i_{on}(t,n)$: Current when switch is on

$i_{off}(t,n)$: Current when switch is off

T_{on} : Time span when switch is on

T_{off} : Time span when switch is off

The open circuit voltage of power source is defined as $V_{in} = V_{P\_D} + V_{P\_A}\sin\omega t$ where ω is the angular rate of the voltage variation and is defined as $\omega = 2\pi/T_P$. n is the number of switching times. In order to get an effect of voltage variation, the voltage variation ratio is defined as $\tilde{V} = V_{P\_A}/V_{P\_D}$. The switching period of the regulator is defined as $T_S = T_{on} + T_{off}$. The duty ratio of the regulator is defined as $d = T_{on}/T_S$. The gain of the regulator is defined as $\tilde{g} = V_{CD}/V_{P\_D}$. The equivalent circuit has a low pass filter consisted of the inductor and the resistance. In this study, the cutoff frequency is enough longer than the switching frequency and the frequency of the power source's variation.

In order to use the equivalent circuit, to know the applicable condition of the equivalent circuit is needed. In the equivalent circuit, the diode in the regulator is replaced with the forward voltage and the resistance. In the regulator, the reverse current from the storage device cannot exist by the rectifying effect of the diode. However, the reverse current can exist in the analytical solution of the current of the equivalent circuit. When the reverse current exists, the equivalent circuit does not fit the real phenomenon of the regulator. In this study, the condition in which the reverse current does not exist is named the applicable condition of the equivalent circuit. In the applicable condition of the equivalent circuit, the energy efficiency is maximized by analytically. Out of the applicable condition of the equivalent circuit, the energy efficiency is maximized by numerically.

2.2 Obtain the energy efficiency analytically

In order to obtain the energy efficiency analytically, the analytical solution of current is obtained. Considering each current of the regulator, the Kirchhoff's voltage laws are written as

$$L\frac{di_{on}(t,n)}{dt} + R_{on}i_{on}(t,n) = V_{P\_D} + V_{P\_A}\sin(\omega t) \quad (1),$$

$$L\frac{di_{off}(t,n)}{dt} + R_{off}i_{off}(t,n) = V_{P\_D} + V_{P\_A}\sin(\omega t) - V_{CD} \quad (2).$$

where $R_{on} = R_P + R_L + R_S$, $R_{off} = R_P + R_L + R_d$ .From eq.(1) and eq.(2), the current of the regulator $i_{on}(t,n)$, $i_{off}(t,n)$ is derived as

$$i_{on}(t,n) = \frac{(B-A)\left(1-e^{-(1-d)\tilde{T}}\right)}{1-e^{-\tilde{T}}}e^{-\frac{R}{L}(t-nT_S)} + A + C\sin(\omega t+\phi) \quad (3),$$

$$i_{off}(t,n) = \frac{(A-B)\left(1-e^{-d\tilde{T}}\right)}{1-e^{-\tilde{T}}}e^{-\frac{R}{L}(t-nT_S-dT_S)} + B + C\sin(\omega t+\phi) \quad (4),$$

where $\tilde{T} = RT_S/L$, $A = V_{P\_D}/R$, $B = (V_{P\_D} - V_{CD})/R$, $C = V_{P\_A}/\sqrt{R^2 + (\omega L)^2}$. The internal resistance of the power source is assumed enough large to be assumed that $R_{on} \approx R_{off} = R$. The energy which stored in the capacitor during one cycle of the power source's variation is derived from eq. (4). The energy efficiency of one cycle is defined as the stored energy during one cycle per the ideal energy which is harvested at the maximum power point during one cycle. The energy efficiency is derived as

$$\eta_{cycle} = \frac{1}{1+\frac{1}{2}\tilde{V}}\frac{R_P V_S}{RV_{CD}}\left\{\begin{array}{r}\dfrac{\tilde{g}^2\left(1-e^{-d\tilde{T}}\right)\left(1-e^{-(1-d)\tilde{T}}\right)}{\tilde{T}\left(1-e^{-\tilde{T}}\right)} \\ +(1-d)\tilde{g}(2-\tilde{g})\end{array}\right\} \quad (5).$$

Considering the parameters in eq. (5), it is clear that the period of the power source's variation has no effect for the energy efficiency when the period of voltage variation is enough longer than the switching period. In eq. (5), only the duty ratio is the controllable parameter. The optimum duty ratio is defined as a duty ratio which maximizes the energy efficiency. The optimum duty ratio which is analytically approximated is obtained as

$$d_{opt} = 1 + \frac{1}{\tilde{T}}\ln\left(\left(\frac{1}{2}-\frac{1}{\tilde{g}}\right)\left(1-e^{-\tilde{T}}\right) + \sqrt{\left(\frac{1}{2}-\frac{1}{\tilde{g}}\right)^2\left(1-e^{-\tilde{T}}\right)^2 + e^{-\tilde{T}}}\right) \quad (6).$$

2.3 Applicable condition of the equivalent circuit

Before deriving the energy efficiency numerically, it should be clear the relation of the applicable condition of the equivalent circuit and the voltage variation ratio. In the applicable condition of the equivalent circuit, the analytical solution of the current should be positive. From a condition in which eq.(4) is positive, the relation of the applicable condition of the equivalent circuit and the voltage variation ratio is obtained as

$$\frac{\sqrt{R^2 + (\omega L)^2}}{R}\left(1 - \frac{\tilde{g}\left(1-e^{-(1-d)\tilde{T}}\right)}{2\left(1-e^{-\tilde{T}}\right)}\right) \geq \tilde{V} \quad (7).$$

Considering that the analytically approximated duty ratio is used, eq.(7) can be described as a function of $\tilde{g}$ and $\tilde{T}$ because the optimum duty ratio is a function of $\tilde{g}$ and $\tilde{T}$. Then, eq.(7) is plotted in fig.5. The area under each line is the

applicable condition of the equivalent circuit. In the applicable condition of the equivalent circuit, the analytical approximated optimum duty ratio is the same as the optimum duty ratio. The range of voltage variation has a convergence value and the convergence value is less than 0.5 in each case.

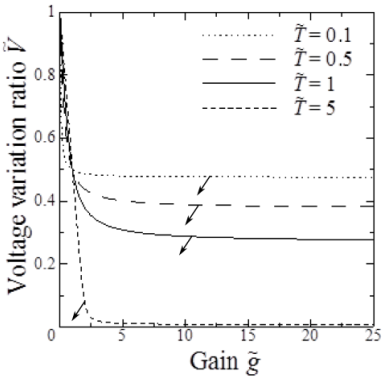

Fig.5 The relation of the voltage variation ratio and the gain which meets the limitation of equivalent circuit

2.4 Obtain the energy efficiency analytically

Out of the applicable condition of the equivalent circuit, the energy efficiency is obtained by numerical integration. In the calculation, the analytical solution of $i_{\mathrm{off}}(t,n)$ is used as the value of current when $i_{\mathrm{off}}(t,n)$ is positive. The value of current is assumed 0 when $i_{\mathrm{off}}(t,n)$ is negative. Fig.6 shows, the relation of the energy efficiency and the duty ratio when $\tilde{V}=1$. In fig.6, the solid line is the energy efficiency obtained numerically and the dash line is the energy efficiency obtained analytically. From fig.6, it is clear that the numerical energy efficiency is larger than the analytical energy efficiency and that the numerical energy efficiency is maximized by a duty ratio which is different from the analytically approximated optimum duty ratio out of the applicable condition of the equivalent circuit. When the voltage variation ratio is 1, the maximum energy efficiency is 20% larger than the energy efficiency using the analytical approximated duty ratio.

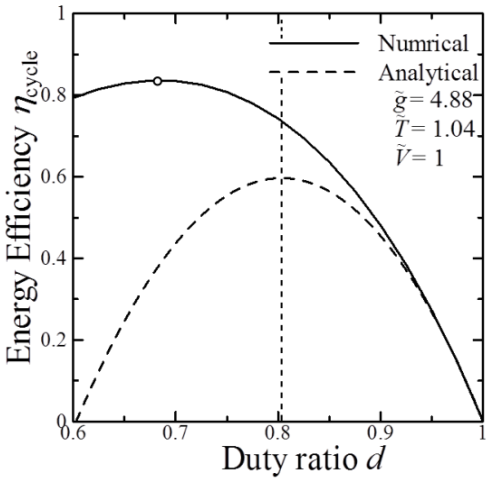

Fig.6 The relation of duty ratio and the energy efficiency

In order to visualize the relation of the voltage variation ratio and the energy efficiency using the optimum duty ratio, fig.7 is plotted. The energy efficiency used the optimum duty ratio and the energy efficiency used the optimum duty ratio can be compared in fig.7. The energy efficiency using the optimum duty ratio is larger than the energy efficiency using the analytical approximated duty ratio. However, it needs more complex calculation to obtain the optimum duty ratio than to obtain the analytical approximated duty ratio. From Fig.7, the difference of the energy is about 10%. So, both using the optimum duty ratio and using the analytical approximated duty ratio should be considered as the control method.

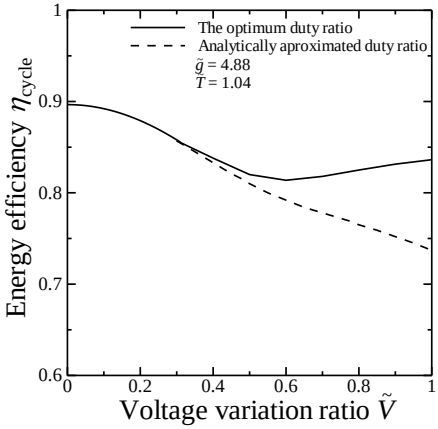

Fig.7 The relation of the energy efficiency and the voltage variation ratio when the optimum duty ratio is used

3. Experimental setup and result

In order to validate the energy efficiency which obtained by the theoretical approach, the energy efficiency is obtained by measuring the capacitor's voltage. In the experimental setup, a DC voltage source of MATSUSADA PL-36-2.2 and an AC voltage source of KENWOOD FG-273A which has an internal resistance $R_{\mathrm{P}}=48[\Omega]$ are used as the power source with linear I-V characteristics. $L=470[\mu\mathrm{H}]$ and $R_{\mathrm{L}}=0.21[\Omega]$ of Panasonic ELC18B471L is used as the inductor. $R_{\mathrm{S}}=78[\mathrm{m}\Omega]$ of TISHIBA TPC6006-H is used as the FET. $V_{\mathrm{d}}=0.32[\mathrm{V}]$ and $R_{\mathrm{d}}=0.20[\Omega]$ at 100[mA] of forward current flow of TOSHIBA CMS16 is used as the diode. $C=219[\mathrm{mF}]$ of BHC ALS3-224NP040 is used as the storage device. The capacitor's voltage is measured 6.95[V] to 7.05[V]. In this range, the relation of the energy efficiency and the duty ratio does not change in the theoretical approach. The experimental setup is shown in fig.8.

In the first experiment, the relation of the energy efficiency and the duty ratio with respect to the voltage variation ratio which obtained numerically is validated. The result is shown in fig.9. In fig.9, the experimental points fitted the relation obtained numerically well. However, the difference

between the theoretical energy efficiency and the experimental result increases with decreasing the duty ratio. The causes of the difference are supposed that the numerical error from the assumption occurred or that the effect of the inductor of the regulator is not estimated well in the numerical calculation.

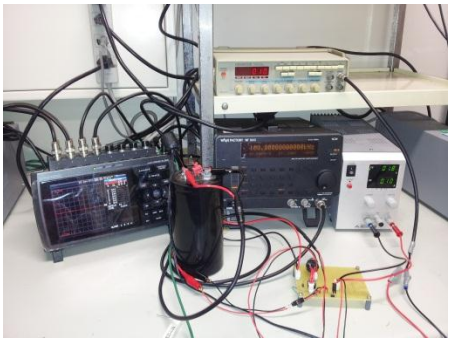

Fig.8 The experimental setup

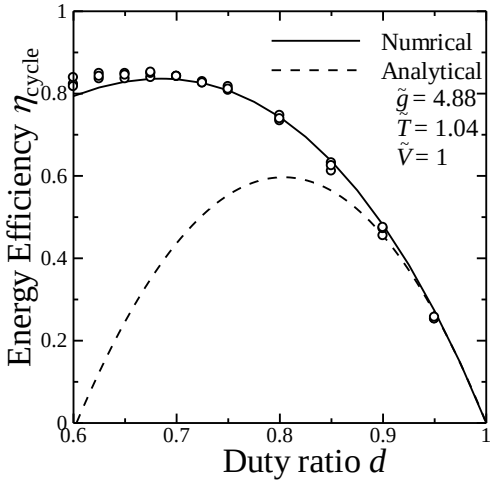

Fig.9 The Experimental result about the relation between the duty ratio and the energy efficiency

In the second experiment, the relation of the energy efficiency and the voltage variation ratio with respect to the optimum duty ratio and the maximized duty ratio is validated. From fig.10, the experimental points fitted the modified curve well. From experimental results, it is considered that the relation obtained in the theoretical approach have applicability.

4. Discussion

From the theoretical approach and experiment, the obtained energy efficiency is validated. Then the control method of the duty ratio of the boost switching regulator is discussed. When the voltage variation ration is in the applicable condition of the equivalent circuit, the duty ratio should be controlled by using eq.(6) because the optimum duty ratio is the same as the analytical approximated duty ratio. When the voltage variation ratio is out of the applicable condition of the equivalent circuit, the optimum duty ratio or the analytical approximated duty ratio should be chosen depend on the needs. When the high energy

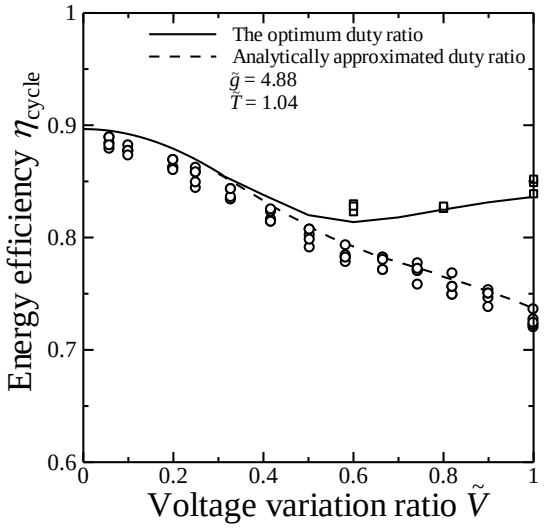

Fig.10 The experimental result about the voltage variation ratio and the energy efficiency with respect to the optimum duty ratio

efficiency is needed, the optimum duty ratio should be chosen and calculated according to the gain. When the simple control is needed, the analytical approximated duty ratio should be chosen.

5. Conclusions

In this paper, the control method of the boost switching regulator without MPPT is suggested by discussing the effect of voltage variation of power source for the energy efficiency. In the theoretical approach, the energy efficiency and the analytical approximated duty ratio are obtained by using the analytical solution of equivalent circuit's current. In the condition in which the analytical solution cannot be used, the energy efficiency and the optimum duty ratio are obtained by the numerical integration. In the experiment, the relation of the energy efficiency and each parameter are validated. In the result, the control method of the duty ratio of the boost switching regulator is suggested by considering the energy efficiency obtained by the analytical approximated duty ratio and the energy efficiency obtained by the optimum duty ratio.

References

[1] R. Dayal, K. Modepalli and L. Parsa, "A New Optimum Power Control Scheme for Low-Power Energy Harvesting Systems," IEEE Trans. Ind. Applications, vol. 49, no. 6, Nov.-Dec. 2013

[2] G. Joseph, C. Foreman and M. L. Mclntyre, "A Variable Duty Cycle Maximum Power Pint Tracking Algorithm for Wind Energy Conversion System," *IEEE Power Electronica and Machines in Wind Applications,* 2012

[3] R. Asami, "Prototype of boost converter for energy harvesting with automatic Maximum power Point searching," Bachelor's thesis of Tokyo Institute of technology, 2013

[4] M. Tanaka, P. Hemthavy and K. Takahashi, "Optimization of control parameters of a boost converter for energy harvesting", Journal of Physics: Conference Series, vol. 379, no. 1, 2012

Temperature Distribution Change by Point Contact Current

Student Number: 12M18130 Name: Kazuki WAKABAYASHI Supervisor: Kunio TAKAHASHI

点接触部における通電による温度分布変化

若林一貴

本論文では、点接触部における通電による温度分布変化を理論的に検討している。点接触とは二物体間の微小領域における平面接触を指す。温度分布が定常である系の固体内部の電流密度分布が過渡状態場合にも適用可能であることを示し、電流密度分布が接触部端部に持つ特異点の扱いに注意をしながら、温度分布変化を求めている。その結果、温度は接触部中央付近で最も高くなる。また温度と温度変化率を接触面電位と接触径を変えることで制御可能であることが示唆されている。

1. Introduction

Temperature distribution change by point contact point is significant for the design of processes and devices, for example, the resistance welding, the mechanical relay, etc.

Kohlrausch[1] obtained relationship between temperature and voltage inside the body under the steady condition in which temperature distribution does not change. Greenwood[2] obtained current density distribution under the same condition as Kohlrausch used. Both researches did not discuss temperature distribution for non-steady condition. Kubono[3] did FEM thermal analysis for non-steady condition by using current density distribution obtained by Greenwood with the assumption that the current density distribution is available for the non-steady condition. The result of the thermal analysis could differ according to the way to deal with the singular point, however the way to deal with the singular point has not clearly discussed.

In this study, current density distribution obtained by Greenwood is proved to be available for non-steady condition and temperature distribution change by point contact current is theoretically investigated.

2. Derivation of current density distribution

2.1 Model and assumptions

Semi-infinite asymmetry body with point contact is introduced as shown Fig.1. The finite current is passed from the outside to a semi-infinite body. The dark part represents the contact area. V_c[V] is the potential at the contact area; a[m] is the contact radius; I[A] is the total current introduced to the body. The boundary condition at the contact area is much reasonable if the difference of resistivity of two materials is larger and if the geometrical symmetric property of the two materials is higher. The followings are assumed to prove current density distribution obtained by Greenwood is available for the model; the contact area is circle, magnetic effects are ignored, the potential equals zero at infinity far from the contact area, and the electric resistivity ρ[Ω m] is constant. Even though the resistivity changes with temperature, the order of the result doesn't change. Note there is no assumption of steady state.

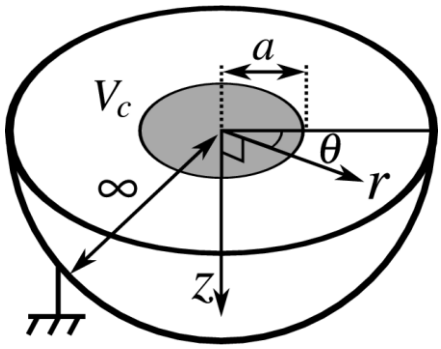

Fig. 1 Schematic illustration of the model

2.2 Derivation of the current density distribution

Basic equation which current density distribution must satisfy is Gauss' law without charge $\mathrm{div}\,\boldsymbol{E} = 0$ and Ohm's law $\boldsymbol{E} = \rho \boldsymbol{i}$. By combining them, Eq. 1 is obtained.

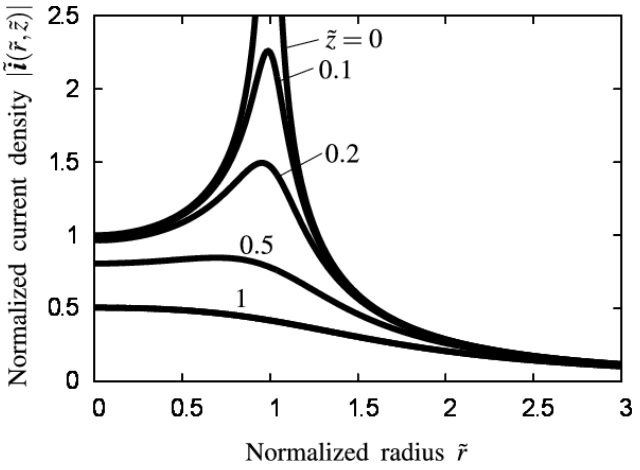

Fig. 2 Normalized current density

$$\mathrm{div}\,\boldsymbol{i} = 0 \tag{1}$$

Current density distribution must satisfy Eq.1 and boundary condition described in the model and assumptions. Greenwood showed current density distribution as shown Eq. 2 in the ellipsoidal coordinate system.

$$\boldsymbol{i} = \left(\frac{2V_c}{\pi a \rho}\frac{1}{\sqrt{(1+\xi^2)(\xi^2+\eta^2)}}, 0, 0\right) \tag{2}$$

where $r = a\sqrt{(1+\xi^2)(1-\eta^2)}$, $z = a\xi\eta$, $\xi \in [0,\infty), \eta \in [-1,1]$. Since the component ξ of the divergence in the ellipsoidal coordinate system is shown as Eq.3, Eq. 2 satisfies Eq.1.

$$\frac{1}{a(\xi^2+\eta^2)}\frac{\partial}{\partial\xi}\left(\sqrt{(1+\xi^2)(\xi^2+\eta^2)}\right) \tag{3}$$

Potential distribution derived from Eq.2 based on $\boldsymbol{E} = -\mathrm{grad}V$ is shown as Eq.4.

$$V(\xi) = \frac{2V_c}{\pi}\tan^{-1}\left(\frac{1}{\xi}\right) \tag{4}$$

Eq.4 satisfies the boundary conditions. Therefore, Eq.2 is the analytic solution of the current density distribution in this model. Fig.2 shows the result of Eq.2. Note the current density distribution has the singular point at the edge of the contact area.

3. Derivation of temperature distribution change

3.1 Model and assumptions

Additional assumptions are introduced for thermal analysis: specific heat C [J/K kg], thermal conductivity κ[W/m K] and density ρ_d[kg/ m^3] are constant, the loss of heat from the surface is ignored, and the latent heat and phase transition are ignored.

3.2 Derivation of the temperature distribution change

The heat conduction equation is shown as Eq. 5.

$$\frac{\partial T(\boldsymbol{r},t)}{\partial t} = D\Delta T(\boldsymbol{r}.t) \tag{5}$$

where $D(=\kappa/C\rho_d)$ is thermal diffusivity and Δ is Laplace operator. The solution of Eq. 5 for the impulse heat input $d\delta Q$ [J] $(t=t')$ at $\boldsymbol{r}=\boldsymbol{r}'$ is obtained as Eq.6.

$$d\delta T(\boldsymbol{r},\boldsymbol{r}',t,t') = \frac{d\delta Q}{C\rho_d}\frac{1}{\left(4\pi D(t-t')\right)^{3/2}}\exp\left(-\frac{|\boldsymbol{r}-\boldsymbol{r}'|^2}{4D(t-t')}\right) \tag{6}$$

where d represents variation of space and δ represents variation of time. Temperature distribution change $T(\boldsymbol{r},t)$ when there is heat distribution is obtained as Eq. 7 by integrating Eq. 6 over the space v' and heat input period $0 \le t \le t_{\mathrm{in}}$.

$$d\delta T(\boldsymbol{r},t,t_{\mathrm{in}}) = T_0 + \int_0^{t_{\mathrm{in}}}\iiint_{v'}\frac{d\delta Q(r',t')}{C\rho_d}\left(4\pi D(t-t')\right)^{-3/2}\exp\left(-\frac{|\boldsymbol{r}-\boldsymbol{r}'|^2}{4D(t-t')}\right) \tag{7}$$

where T_0 [K] is the initial temperature. Heat is generated by current inside the body in this case. The heat distribution is obtained as Eq. 8 by the Ohm's law.

$$d\delta Q(\boldsymbol{r}) = \rho|\boldsymbol{i}(\boldsymbol{r})|^2 dv\delta t \tag{8}$$

Since $\mathrm{d}v = a^3(\xi^2+\eta^2)d\xi d\eta d\theta$ in the ellipsoidal coordinate system, $d\delta Q(\boldsymbol{r})$ is obtained as Eq. 9 by Eq. 2, 8.

$$d\delta Q(\boldsymbol{r}) = \frac{4{V_c}^2 a}{\pi^2\rho}\frac{1}{1+\xi^2}d\xi d\eta d\theta\delta t \tag{9}$$

Note that the heat distribution has finite value everywhere in the body while the current density distribution has the singular point. Temperature distribution change by point contact current is obtained in an integration form as Eq.10 by substituting Eq. 9 for Eq. 7.

$$\tilde{T}(\tilde{\boldsymbol{r}},\tilde{t},\tilde{t}_{\mathrm{in}}) = (4\pi)^{-\frac{3}{2}} \int_0^{\tilde{t}_{\mathrm{in}}} \iiint_{v'} \frac{1}{1+\xi^2}\frac{1}{(\tilde{t}-\tilde{t}')^{\frac{3}{2}}} \exp\left(-\frac{|\tilde{\boldsymbol{r}}-\tilde{\boldsymbol{r}}'|^2}{4(\tilde{t}-\tilde{t}')}\right) d\xi d\eta d\theta \delta\tilde{t} \quad (10)$$

where parameters whose have dimension of length and time are normalized as $\tilde{\boldsymbol{r}} = \boldsymbol{r}/a$ and $\tilde{t} = t/(a^2/D)$, and temperature is normalized as Eq. 11.

$$\tilde{T} = (T - T_0)/\frac{4{V_c}^2}{\kappa\rho\pi^2} \quad (11)$$

The form of Eq. 10 suggests that FEM thermal analysis can be done appropriately by modifying the coordinate system of the simulation to the ellipsoidal coordinate system.

4. Results and discussion

4.1 Temperature distribution change and the temperature change rates

Fig. 3, 4 shows the temperature distribution change at the surface. Fig. 3 takes normalized time as the horizontal axis and Fig. 4 takes normalized radius.
As shown in Fig.3,4, The result shows the vicinity of the origin has the highest temperature and temperature gradually decreases with the distance from the origin while temperature distribution, conventionally , has an edge at the peripheral of the contact area. The difference is due to the treatment of the singular point. This result suggests that when the melting happens by passing current at the point contact, materials around the origin melts and spreads to the periphery part.Temperature heating rate and cooling rate are introduced as Eq. 12,13.

$$\alpha_h = \frac{dT}{dt} \quad (1)$$

$$\alpha_c = -\frac{dT}{dt} \quad (2)$$

Both temperature change rates are with respect to time normalized as Eq. 14.

$$\tilde{\alpha} = \alpha/\frac{4{V_c}^2}{C\rho_d\rho a^2\pi^2} \quad (3)$$

Fig.5,6 shows Eq. 12,13 normalized as Eq. 14. Fig. 5 shows that the heating rate is higher around origin than far parts. The heating rate only at the origin has non-zero value $\tilde{\alpha}_h = 1$ and at other parts equal zero. Fig.6 shows that the cooling rate at the origin is always positive. It means the temperature at the origin immediately decreases after current passage stops. Some parts have negative value of the cooling rate in certain period after current passage stops. It means temperature increases for the period there even though current passage stops.

4.2 Possibility of the control of the temperature and temperature change rate with respect to time

Temperature is normalized as Eq.11 and temperature change rate with respect to time is normalized as Eq. 14. Temperature depends on potential at the contact area but not on contact radius while temperature change rate depends on contact radius. The dependencies suggest controllability of the maximum temperature and temperature change rate by varying potential at the contact area and contact radius.

5. Conclusion

Temperature distribution change by point contact current is theoretically investigated. The current density distribution obtained by Greenwood is proved that it is the analytic solution of the current density distribution for this non-steady state model under the assumptions: magnetic effects are ignored and the electric resistivity ρ[Ω m] is constant. The current density has a singular point at the peripheral parts of the contact area and the singular point is clearly treated by introducing the ellipsoidal coordinate system. The temperature distribution change is obtained under the assumptions: specific heat C[J/K kg], thermal conductivity κ[W/m K] and density ρ_d[kg/ m^3] are constant, the loss of heat from the surface is ignored, and the latent heat and phase transition are ignored.
Temperature distributes higher around the origin and gradually decreases with the distance from the origin while temperature distribution, conventionally, has an edge at the peripheral of the contact area. The difference is due to the treatment of the singular point. This result suggests that when the melting happens by passing current at the point contact, materials around the origin melts and spreads to the periphery part. Temperature change rate with respect to time is obtained which would be useful for quenching.
Temperature depends on potential at the contact area

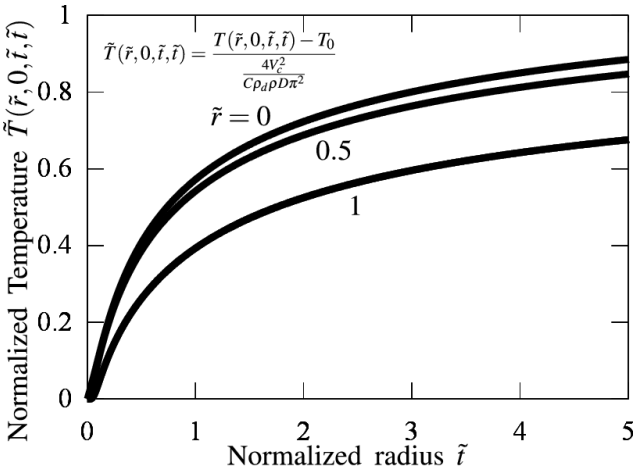

Fig. 3 Normalized temperature change at the surface.

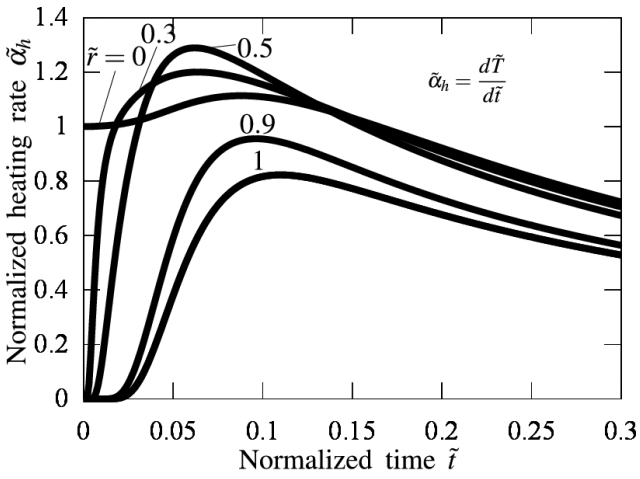

Fig. 5 Normalized heating rate at the surface

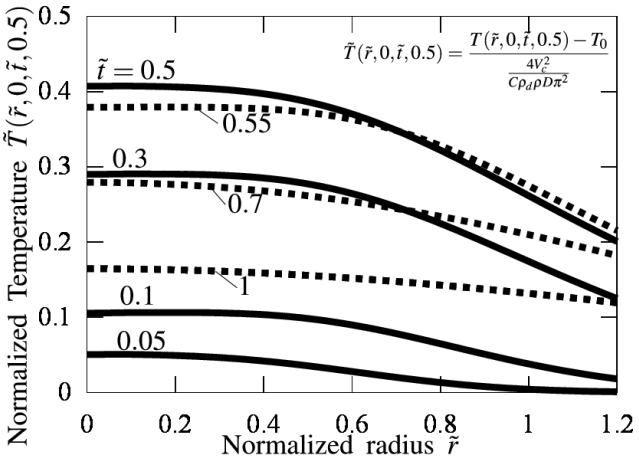

Fig. 4 Normalized temperature distribution change at the surface ($t_{\text{in}} = 0.5$). Solid lines represent the temperature distribution while current is passed and dotted lines represent the temperature distribution after current passage ends.

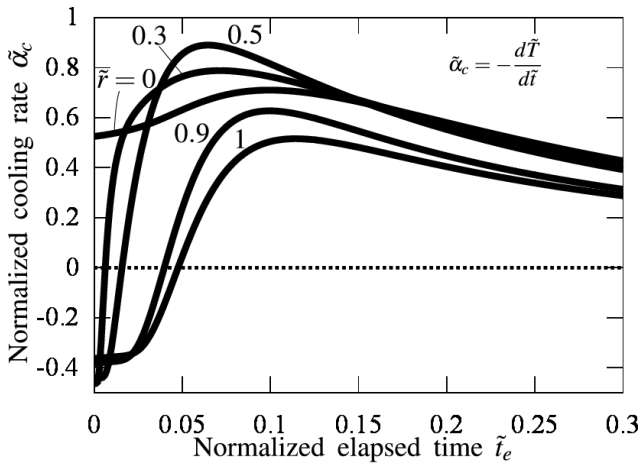

Fig. 6 Normalized cooling rate at the surface. The horizontal axis is the normalized elapsed time $t_e = t - t_{\text{in}}$.

but not on contact radius while temperature change rate with respect to time depends on contact radius. The dependencies suggest controllability of the maximum temperature and temperature change rate by varying potential at the contact area and contact radius.

Reference

[1] F. Kohlraush, Ueber den stationaren Temperaturzustand eines elektrisch geheizten Leiters, Ann alen der Physik, pp132-158, Issue.1, Vol.306(1900).

[2] J. A. Greenwood and J. B. P. Williamson, Electrical conduction in solids II. Theory of temperature-dependent conductors, Proceedings of the Royal Society of London. Series A, Mathematical and Physical, pp13-31,no.1244, Vol.246(1958).

[3] Takayoshi KUBONO, Temperature Distribution in the Constriction Region of Electrical Contacts Carrying the DC-current, The transactions of the Institute of Electrical Engineers of Japan.A, pp47-53, no.6, Vol.104(1985)

Effect of Curing Conditions and Reinforcing Bars Arrangement on the Corrosion of Steel in Concrete Mixed with Seawater

Student ID: 12M18270 Name: Zoulkanel MOUSSA GARBA-SAY Supervisor: Nobuaki OTSUKI

海水練りコンクリート中鉄筋の腐食における養生方法および鉄筋配置の影響に関する研究

ムッサ　ガルバ　サーイ，ズルカネル

本研究では海水練り鉄筋コンクリートにおいて養生方法と部材高さが物質透過性に及ぼす影響と、鉄筋配置が腐食挙動に及ぼす影響を検討し、構造物の寿命を定量的に評価した。その結果、海水で養生を行った場合塩化物拡散と中性化速度が小さくなる。また、大きな供試体においても上部より下部のほうが塩化物拡散と酸素透過性が小さいことがわかった。一方、海水の場合は腐食開始が早いので伏期間が短くなるが、腐食速度あまり大きな差が認められなかった。結論としては海水中に養生すると潜伏期が長くなった。高さの影響に関しては上部より下部の方が 1.5～3 倍寿命が長く、小さい供試体に比べても上部の方が短い寿命だった。

1. Introduction

Fresh water scarcity represents one of the major crises on 21st century. According to World Meteorological Organization, by 2025 about 2/3 of the world will not have access to enough fresh water. So it seems important to save fresh water, by promoting seawater usage. On the other hand, in the concrete industry some studies on seawater usage in concrete demonstrated that it could be possible to use seawater for RC material, if appropriate material is used [1]. But those studies did not consider real construction factors such as curing and rebars arrangement.

Therefore the objective of this study is to investigate the effects of curing condition, size of members and rebars disposition on corrosion behavior of steel in concrete mixed with seawater. To attain this objective, sub-objectives have been set as follows.

- To Determine the effects of curing and height of specimen on material properties such as chloride diffusivity, carbonation rate and oxygen permeability.
- To elucidate the effects of height and direction of rebars on corrosion behavior.
- To quantitatively estimate the lifetime of concrete mixed with seawater under marine and carbonation environment.

2. Experimental procedure

Two types of specimens mixed and cured with tap water and seawater, OPC (Ordinary Portland Cement) and BFS (Blast Furnace Slag cement: 0, 40 and 70%) as binder were fabricated; water/binder ratio was 0.5

The first type is plain concrete specimen for analyzing the effects of curing on Cl diffusivity and carbonation rate. The second type is reinforced concrete used for investigating height effects on Cl diffusivity and oxygen diffusivity, and effects of rebars direction on steel corrosion under accelerated marine and carbonation environment (Fig 1). The concrete cover was 4cm for all rebars. Curing patterns are summarized in table 1; for the second type, only burlap curing was conducted.

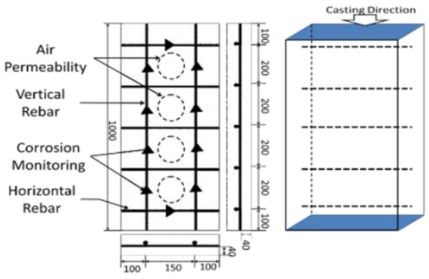

Fig. 1 Outline of Pv series specimen

Table 1 details of curing method	
Curing method	Curing code
No curing	**N/C**
7days Tap water curing	**TW 7d**
3 days Seawater curing	**SW 3d**
7days Seawater curing	**SW 7d**
12 days Seawater curing	**SW 12d**
7days Sealing	**Sealing**

2.1. Chloride diffusivity test

After curing the specimens were submerged into salt water (3% NaCl) for 9months, or Alternate Dry and Wet (ADW) test (3%NaCl, 50℃) for 6 months. After testing, chloride content was analyzed by method conforming to JSCE-G 573-2003 standard. From the value of total chloride by depth, chloride diffusivity coefficient (D_{ap}) was determined by using Fick's law of diffusion (Eq.1).

$$C(x,t) = C_0\left(1 - \mathrm{erf}\left(\frac{x/2}{\sqrt{(D_{ap} \times t)}}\right)\right) \qquad (1)$$

In which: D_{ap}(cm^2/year), Co(=13kg/m^3): Surface Chloride content, C(x,t): Chloride concentration at position (x) and time (t), erf: Error function

As shown in figure 4, for same curing method, seawater mix cases had lower chloride diffusivity coefficient; this could be due to lower gradient of concentration. Also due to the fineness of particle and chloride binding ability, BFS cases had lower diffusivity. On the other hand, D_{ap} increased with height; and this is principally because of density variation along the height (Fig. 2.1 and 2.2).

2.2. Carbonation test

The specimens were exposed into carbonation chamber (10% CO_2, 20 ℃), and carbonation depth was measured after 1, 4 and 12 months by Phenolphthalein method. The carbonation rate was calculated by √(t) method (Eq. 2).

$$X = (0.742 - 0.224\log C)A\sqrt{C/0.07} \cdot t \qquad (2)$$

Where: A(mm/√t): carbonation rate coefficient X(mm): carbonation depth, t: exposure time, C: CO_2

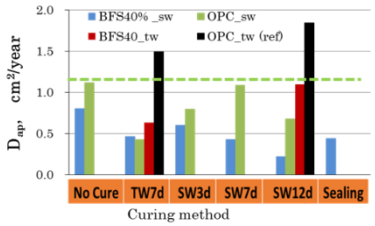

Fig. 2.1 Cl diffusivity coefficient with curing

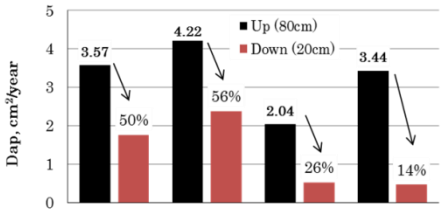

Fig. 2.2 Effect of height on Cl diffusivity

concentration in carbonation chamber, 0.07= indoor CO_2 concentration.

As result, BFS concrete showed higher rate of carbonation than OPC; because of lower pH value in BFS. However, for concrete mixed or cured with seawater the carbonation rate was lower or almost same as normal concrete (Fig. 3). From these results, it can also be confirmed that the rate of carbonation decreases with moisture supply. Thus 12days seawater curing had the lowest value; 1.0 for OPC and 2.3 mm/√(year) in case of BFS.

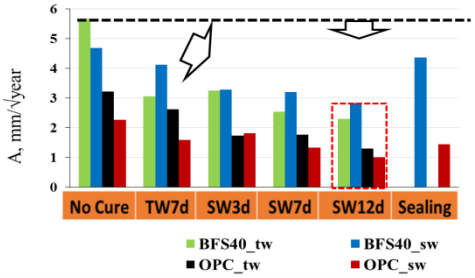

Fig. 3 Effect of curing on carbonation rate

2.3. Oxygen permeability

Oxygen permeability (J_O) was estimated from cathodic polarization curve measured on RC specimens subjected to ADW test.

$$J_O = \frac{dQ}{dt} = -\frac{i_{lim}}{nF} \qquad (3)$$

Where, I_{lim}(A/cm^2): Limit current density, n(=4): numbers of electrons in cathodic reaction, F(96500C/mol): coulomb number.

O_2 permeability was higher at upper layers, but there was no significant difference between mixing water (fig. 4). However, when mixed with BFS J_O became far lower than concrete mixed with OPC; because of reduction ability of oxygen by BFS

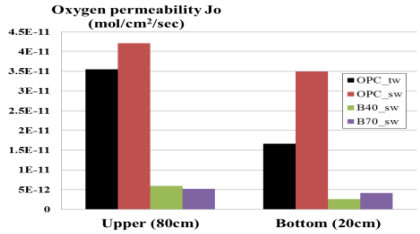

Fig. 4 Effect of height on oxygen permeability

2.4. Corrosion phenomena in marine condition

Corrosion of steel was investigated by conducting Alternate Dry and Wet (ADW) test into 4%NaCl water. Polarization resistance $R_{ct}(\Omega)$ was measured by AC impedance method, and the microcell corrosion current density$I_{corr}(\mu A/cm^2)$ was estimated (Eq. 4).

$$I_{corr} = \frac{K}{R_{ct} \times S} \qquad (4)$$

Where: S (cm^2): steel surface area, K(=0.0209 V): Stern-Geary constant.

Also macrocell current was estimated analytically, and then total corrosion rate was calculated from microcell and macrocell current.

As results, the corrosion rate of horizontal rebars was almost same as horizontal ones. And because of small bleeding rate, there was no significant difference between upper and bottom layer. On the other hand upper layers were anodic and bottom were cathodic (Fig 5.1~5.3)

2.5. Estimation of Lifetime

The lifetime of concrete was estimated on the basis of material properties defined. It is divided into initiation and propagation period, as shown in the conceptual graph (fig. 6). Investigations were done under few assumptions: corrosion threshold Cl content= 5.5 for OPC and 3.5kg/m^3 for BFS; concrete cover=7cm for marine and 5cm for carbonation condition. Propagation period was estimated by determining the critical amount of rust to induce cracks by an approximation method proposed by Yokozeki et al.

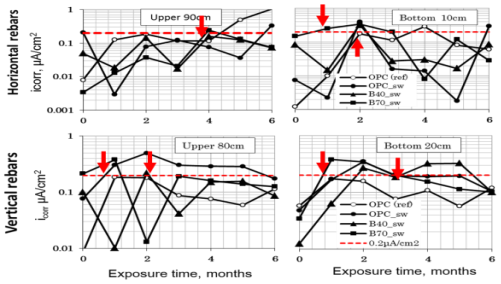

Fig. 5.1 time dependent change of i_{corr}

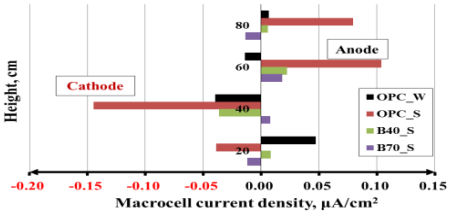

Fig. 5.2 Macrocell corrosion behavior

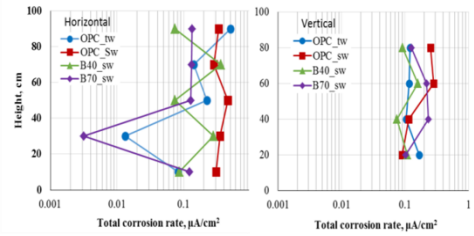

Fig. 5.3 Total corrosion rate with Height

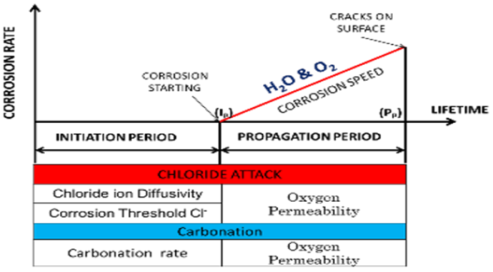

Fig. 6 Concept of Lifetime

2.5.1. Initiation and propagation period

In marine condition, mixed and cured with seawater had shorter initiation period, due to initial Cl content (fig.7). But this can be elongated by conducting longer curing into seawater. On the other hand, initiation and propagation periods were both longer at bottom compared to upper layers. And for propagation, BFS case showed longer duration than OPC.

Under carbonation, the initiation period was inversely

proportional to carbonation rate (Fig. 3). As result, 12 days seawater curing had longest initiation period equals to 2500 years (Fig. 7.2). Almost all specimens had more than 75 years which was long enough; thus under carbonation the propagation period was not estimated.

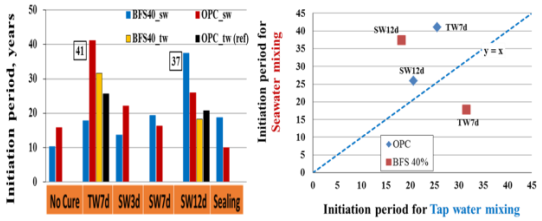

Fig. 7.1 Initiation period under marine conditions

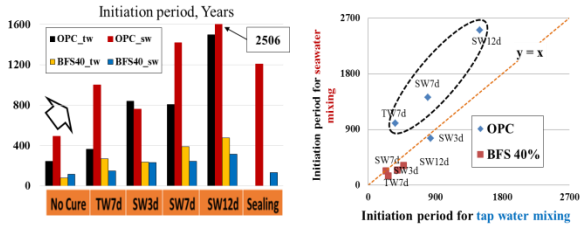

Fig. 7.2 Initiation period under carbonation conditions

Fig. 7 Effect of curing on initiation period

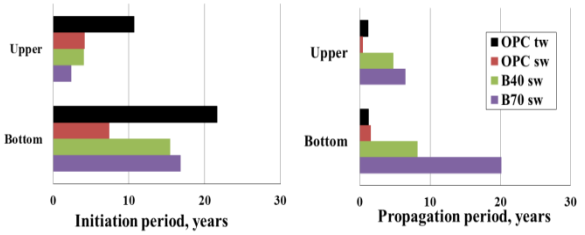

Fig. 8 Effect of height on initiation and propagation period (marine conditions)

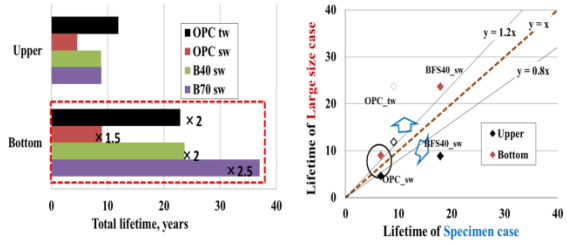

Fig. 9 Total lifetime of concrete

2.5.2. Total lifetime

In marine conditions, the total lifetime was 1.5~3 times longer at bottom layers compared to upper layer, because of higher density. In addition, the upper layers had shorter lifetime than small size concrete specimen (Fig. 9). It could also be confirmed that BFS mixed with seawater may have longer or almost same lifetime as normal OPC concrete mixed with tap water.

3. Conclusions

Effects of curing, height and rebars direction on corrosion of steel in seawater mixed concrete have been investigated, and the conclusions are as following.

1. Cl diffusivity and carbonation rate became lower when concrete was cured with seawater; and so 12days seawater curing was more effective.
   In large specimens bottom layers had lower Cl and O_2 diffusivity, because of higher density than upper layer.
2. Corrosion of steel in concrete mixed with seawater begins faster than tap water case, because of initial chloride. However rebars arrangement did not affect much the corrosion rate.
3. Initiation period of seawater mixed concrete was shorter than tap water case. But when cured into seawater, longer initiation period can be obtained; so in marine conditions, initiation period of BFS 40% mixed with seawater and cured for 12days in seawater was about 40years.
4. Total lifetime at bottom layer was 1.5~3 times longer than upper layer which was almost same as specimen case.

References

[1] N. Otsuki et al., "Possibility of Seawater as Mixing Water in Concrete", Journal of Civil Engineering and Architecture, V6, No.10 serial 59, 2012.

[2] H. Ohara, "Lifetime Estimation of Seawater mixed Concrete in Marine and Carbonation Environment", Feb. 2013.

[3] M.A. Baccay et al., "Influence of Bleeding on Minute Properties and Steel Corrosion in Concrete", JACT, Vol.2, No.2, 2004.

A Study about Influential Factors on Corrosion Behavior of Paint-coated Steel in Submerged Zone

Student Number: 12M18152 Name: Kenji WADA Supervisor: Nobuaki OTSUKI

干満帯直下における塗装鋼板腐食への影響因子の検討

和田賢治

海洋環境下に存在する塗装された鋼構造物においては、干満帯直下部（干潮位のすぐ下）における塗膜の欠陥を起点とした腐食が問題となっている。本研究では干満帯直下における欠陥を有する塗装鋼材の腐食劣化機構解明に取り組み，とくに塗料種類と塗料膜厚、複合環境による影響が腐食挙動に与える影響について明らかにした。

1. Introduction

At offshore steel structure in marine environment, paint coating is often appllied to protect structure from corrosion. However, in submerged zone sometimes severe corrosion occurs due to paint defect by impact of floating object.

In exisiting structure, various kind of paint coating is used. However, ability of paint coating as corrosion inhibitor is not clear. Also environment seems to have influence and another important issue.

From the above background, objective of my study is “To investigate influential factors on corrosion behavior of Paint-coated Steel in Submerged Zone”. The objectives are divided into three followings objectives:

Purpose 1: Investigate influence of paint type on corrosion behavior of paint coated steel in submerged zone quantitatively in actual environment.

Purpose 2: Investigate deterioration process and influence of paint thickness on corrosion behavior of paint coated steel with defect in submerged zone using accelerated test.

Purpose 3: Investigate influence of multiple environments on corrosion mechanism of paint coated steel with defect in submerged zone with exposure test.

2. Investigation of Influence of Paint Type on Corrosion Behavior of Paint Coated Steel in Submerged Zone in Actual Environment

(1) Outline of exposure test

- **Specimens:** Steel pipe with various paints (**Fig. 1**). Paints are divided into four groups as shown in Table 1: (a) Polyethylene paint, (b) Epoxy paint, (c) Glass flaked paint and (d) Vinyl paint.
- **Exposure Site:** Taira Bay in Miyako’s island for 20 years.
- **Measuring Method:** Following items were measured.

（ｉ）Appearance was observed

Table 1: List of paint coating

Group	Paint Type	Thickness (μm)
(a) Polyethylene	Polyethylene	3000
(b) Epoxy	Tar Epoxy	800
	Inorganic Zinc / Tar Epoxy A	475
	Inorganic Zinc / Tar Epoxy B	475
	Inorganic Zinc / Tar Epoxy C	325
	Inorganic Zinc / Pure Epoxy A	325
	Inorganic Zinc / Pure Epoxy B	325
	Inorganic Zinc / Pure Epoxy C	350
	Inorganic Zinc / Pure Epoxy D	325
	Inorganic Zinc / Pure Epoxy	325
(c) Glass flaked	Organic Zinc / Glass Flaked Epoxy	1520
	Glass Flaked Polyester A	1500
	Glass Flaked Polyester B	750
	Glass Flaked Epoxy	1500
	Glass Flaked Polyester C	1000
(d) Vinyl	Thick Vinyl Film A	325
	Thick Vinyl Film B	375

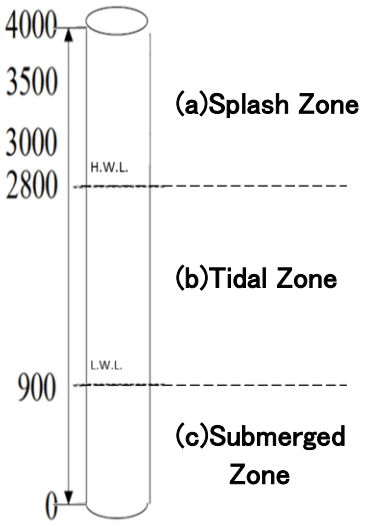

Fig. 1: Paint Coated Steel Pipe

Table 2: Comparison of Paint Ability as Corrosion Inhibitor

	(a) Polyethylene 3000μm	(b) Epoxy 325~800μm	(c) Glass Flaked 750~1500μm	(d) Vinyl 325~375μm
Appearance (after 20 years Exposure) (Corrosion Area%)	◎  (0%)	△  Corrosion (1.5%)	△※ 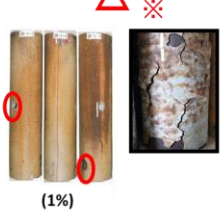 (1%)	×  (33%)
Adhesion Test (after 20 years Exposure)	None (Peeling Test)	○ High Adhesive	× Low Adhesive	× Low Adhesive
Drop-weight Impact Test (before Exposure)	◎ No Peeling	△ Peeling Occur	× Peeling Widely Occur	△ Peeling Occur

※In some case, paint was peeled widely off from steel and corrosion occurred under the paint

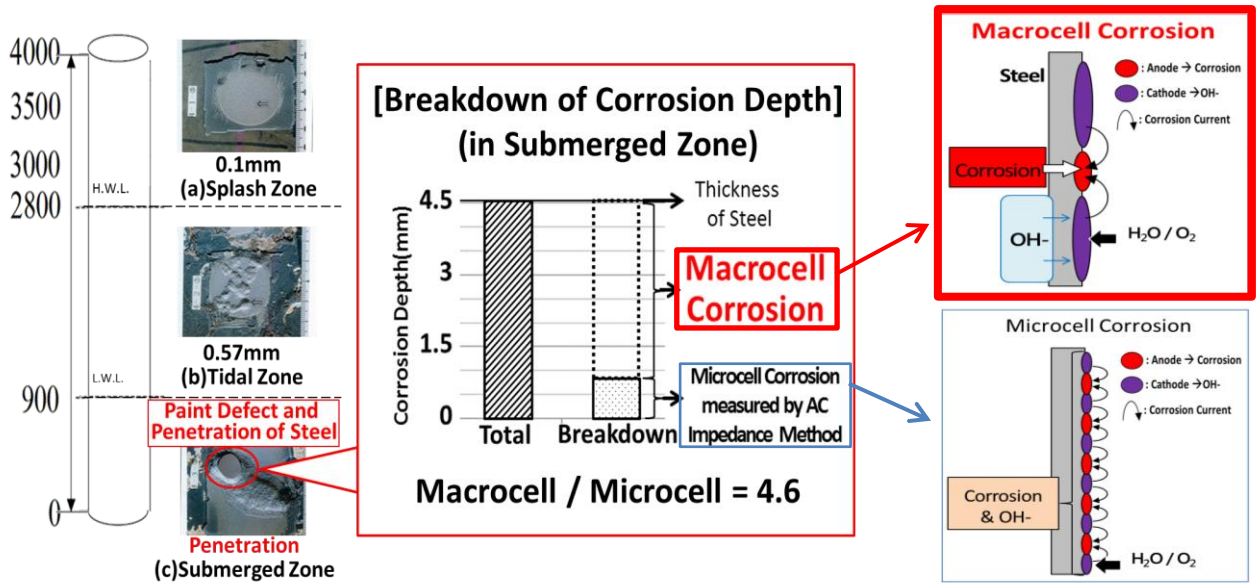

Fig. 2: Corrosion Depth at Each Environment and Skematic Model of Macrocell Corrosoin (Tar + Zinc)

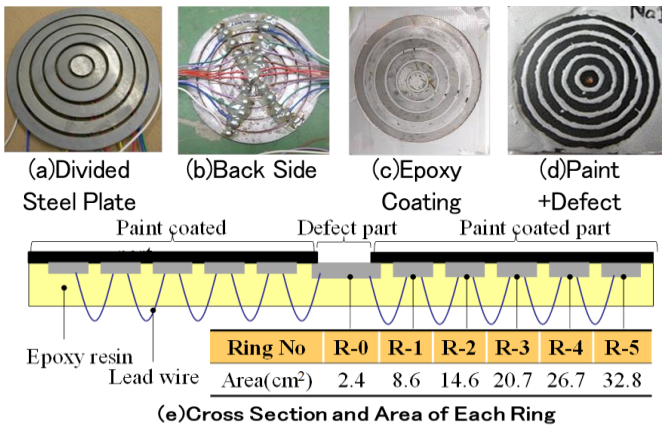

Fig. 3: Paint Coated Divided Steel with Defect

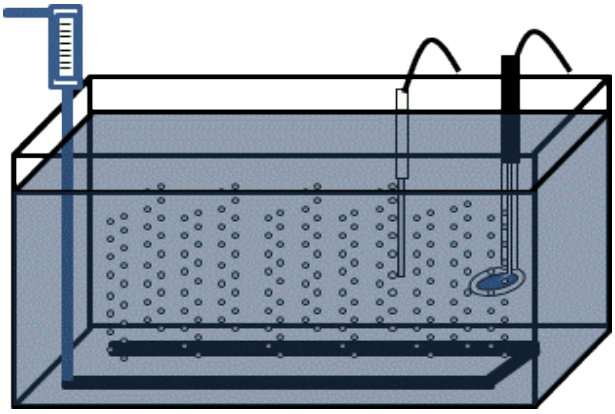

Fig. 4: Acceleration Test

(ⅱ)**Drop-weight impact test** reveals resistance for impact by checking how much area is peeled by impact.

(ⅲ) **Adhesion test** reveals how much power is needed to peel paint coating off from steel pipe.

(ⅳ) **AC impedance method** can get paint resistance and polarization resistance with bode plot. With polarization resistance, microcell current density was calculated as Stern-Geary constant (In this study, 0.0209V) divided by Polarization resistance.

(2) Result of exposure test

- **Paint type:** As Table 2 shows, polyethylene paint keeps sounds. On the other hand, specimens with vinyl or glass flaked paint are heavily corroded. In case of tar epoxy, more research is necessary as well as the influence of paint thickness. (→ discuss in next chapter)
- **Corrosion in Submerged Zone: Fig. 2** shows close outlook of deteriorated part of specimen with tar epoxy with zinc paint at each environment.

In submerged zone, severe corrosion was observed and corrosion made penetration.

Compared with the value of total corrosion depth in submerged zone, value of corrosion depth by microcell corrosion in submerged zone obtained from AC impedance method is much smaller. This graph suggests macrocell corrosion had contribution of penetration of steel pipe.

3. Investigation of Deterioration Process of Tar Epoxy and Influence of Paint Thickness on Corrosion Behavior of Paint Coated Steel with Defect in Submerged Zone Using Acceleration Test

(1) Outline of acceleration test

- **Specimens:** Divided steel plate which consists of 6 divided parts as shown in **Fig. 3 (a)** is prepared. Lead wire is attached by soldering on the backside of each part as shown in **Fig.3 (b)**. Location of each part is fixed by gray epoxy coating as shown in **Fig. 3 (c)**. Then, tar epoxy is spraied on the top side with 80, 100, 150, 300μm thickness and defect (φ10mm) is installed at the center as shown in **Fig. 3(d)**.

Center circulated steel was called "R-0". Other steel plates were called "R-1" to "R-5" from inside. The area of each steel plate is as shown in **Fig. 3(e)**. By connecting lead wire, the divided steel plates were considered as one circulated plate.

- **Accelerated test:** Accelerated corrosion test was

Fig. 5: Outlook (Tar Epoxy)

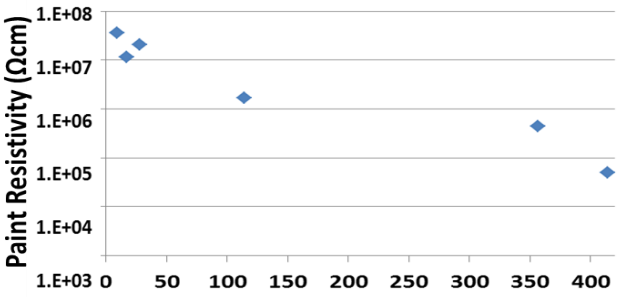

Fig. 6: Change in Paint Resistivity (Tar Epoxy/ R2)

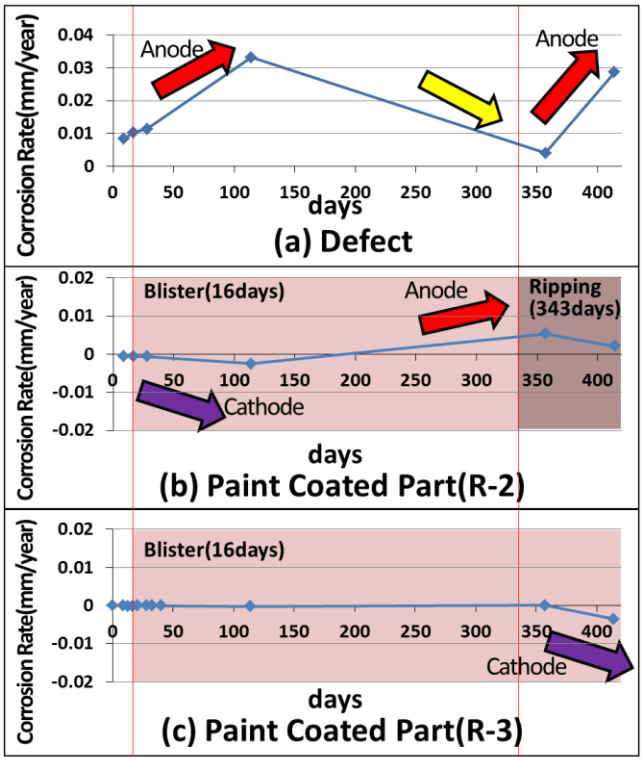

Fig. 7: Change in Macrocell Corrosion Rate at Each Part (Tar Epoxy)

conducted. This test was proposed by JSCE simulating under low water level (**Fig. 4**). Test specimens were submerged to NaCl solution (3.0w.t. %, 50˚C). 2 l/min air was pumped.

- **Measuring method:**
  (ⅰ)Appearance
  (ⅱ)AC impedance method
  (ⅲ)Ammeter is used to measure macrocell current by connecting between each ring.

(2) Result of acceleration test

- **Deterioration Process: Fig. 5** shows change in appearance of a specimen with tar epoxy. Blister occurs at 16 days and ripping occurs at 343 days. Comparing appearance with change in paint resistivity shown in **Fig. 6** it can be said that paint resistivity dropped especially when blister and ripping occurs.
  Macrocell corrosion along with deterioration is shown in **Fig. 7**. From this result, it can be said that when blister occurred at paint coated part, cathodic reaction got larger and anodic reaction (corrosion rate) at defect also got larger. Then when ripping occurred at paint coated part, cathodic area got anode and anodic reaction (corrosion rate) at defect got smaller.
- **Influence of Paint Thickness:** Days until blister occurs seems in proportion to the paint thickness in case of more than specific paint thickness (**Fig. 8**), considering diffusion of oxygen.

4. Investigation of Influence of Multiple Environment on Corrosion Behavior of Paint Coated Steel with Defect in Submerged Zone with Exposure Test

(1) Outline of Exposure Test

- **Specimens: Fig. 9** shows specimens**.** At the back of the steel, lead wire is soldered and was covered with epoxy resin. At the surface, phthalic resin with a thickness of 150μm was sprayed. At element in submerged zone, defect is installed. In addition, ends of the steel were coated with clear epoxy. When specimens immersed, lead wire between steel elements connected.
- **Exposure environment:** Artificial sea water tank in Port and Airport Research Institute, located in the Yokosuka, Kanagawa Prefecture is used for exposure site.

(2) Result of Exposure Test

Fig. 10 shows change in appearance at submerged zone. From these results, corroded area in case of multiple environments is wider than area in case of single environment. **Fig. 11** shows macrocell corrosion rate at each area. At first, large macrocell corrosion occurs at submerged zone at defect point with large cathodic area at paint coated part. Then blister occurs at tidal zone and cathodic reaction get larger and anodic reaction at defect in submerged zone also become larger. Finally blister in tidal zone are ripped and then macrocell corrosion within tidal zone where newly ripped area as anode and other blistered or sound area as cathode occurs.

Considering above all, wider corroded area in submerged zone in case of multiple environment seems due to the macrocell corrosion between submerged zone with anode and tidal zone with cathode.

5. Conclusions

Purpose 1: (1)Severe macrocell corrosion occurs in submerged zone.

・It is proved what kind of paint can keep steel sound in long term.

Purpose 2: (1)As for corrosion of paint coated steel with defect,

(1)-1 when paint blistered, macrocell corrosion at defect get larger.

(2)-2 when paint ripped, macrocell corrosion at defect get smaller.

(3) Term of incubation stage seems in proportion to the paint thickness in case of more than specific paint thickness.

Purpose 3: As for multiple environments, in submerged zone, heavy macrocell corrosion occurs with tidal zone as cathode.

Reference 1) PWRI, Joint research report about durability of marine steel structures – Research result until exposing 20years

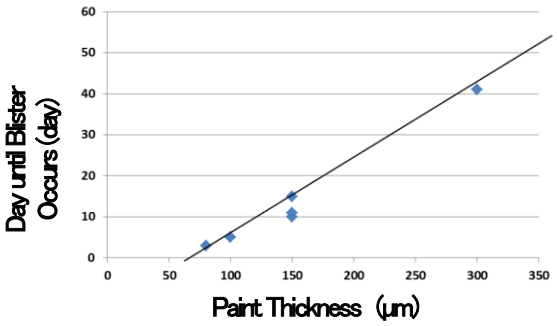

Fig. 8: Days until Blister Occurs in Each Paint Thickness (Tar Epoxy)

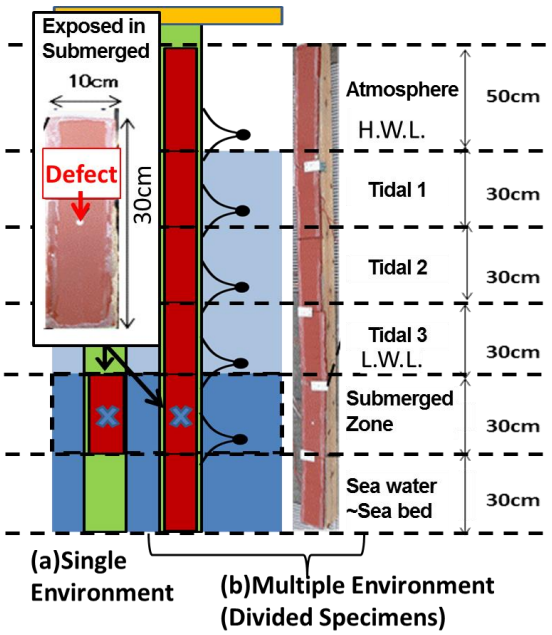

Fig. 9: Specimens for Single and Multiple Environments (Phthalic Resin 150μm)

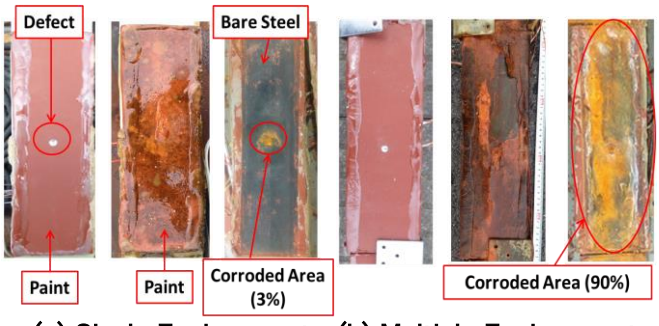

Fig. 10: Change in Appearance (Phthalic Resin 150μm)

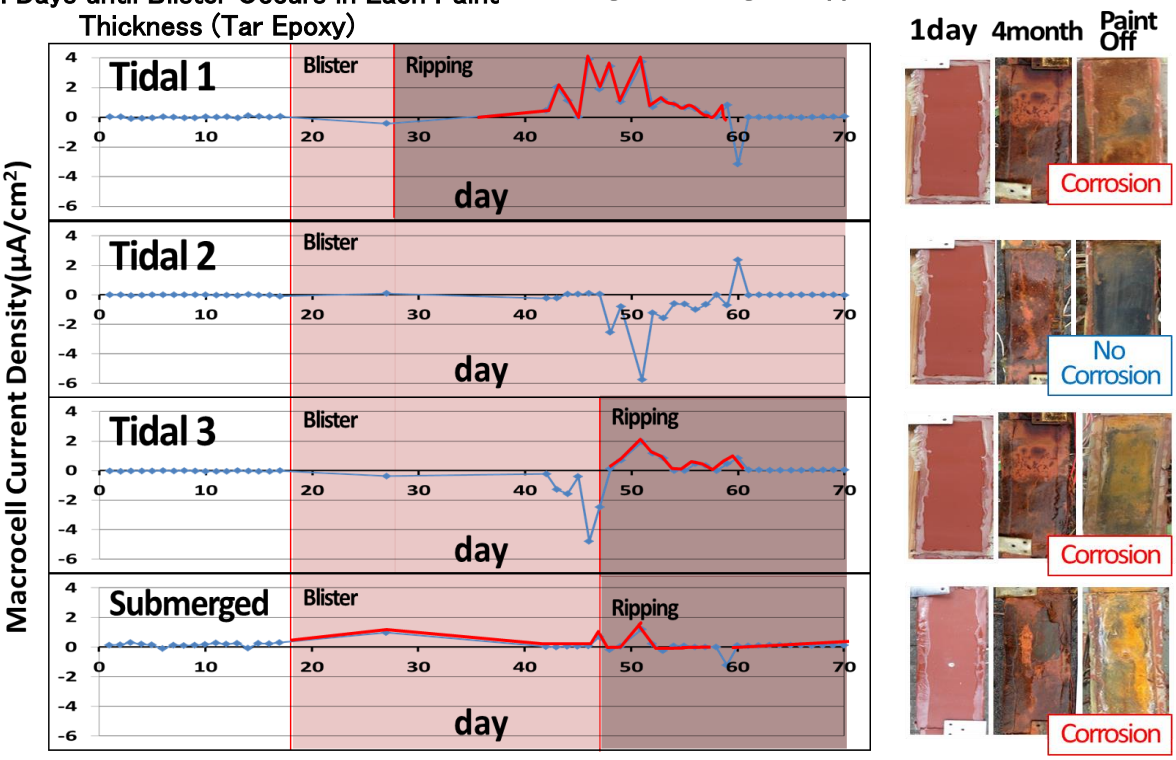

Fig. 11: Change in Macrocell Corrosion Rate in Each Area (Phthalic Resin 150μm)

Effect of shear pin arrangement to a critical width of undercut slope aligned with a bedding plane

Student Number: 12M18070 Name: Shuhei KITAKATA Supervisor: Thirapong Pipatpongsa

層理面に沿う斜面法尻での限界掘削幅に及ぼす抑止杭の配置の影響

北方 秀平

In the previous research, the undercut method developed from physical and theoretical models has been successfully applied to the Mae Moh open-pit lignite mine of Thailand. Due to the weakening basal support after backfilling process, shear pin reinforcement is required in the subsequent excavation. In this study, the effect of shear pin arrangement and its failure mechanism was studied using a series of physical model of moist silica sand No.6. A bedding plane was modeled by Teflon sheet and shear pins were modeled by bolts and wires. Particle image velocimetry and high-speed video camera were used to capture slope movement and triggering mechanisms of instability. The study reveals that the number and stiffness of shear pin, location of installment, interval span and size of shear pin have effects on a critical width of undercut slope.

1 Introduction

Prediction of the maximum stable undercut width under which the slope does not collapse for mining purpose was developed in the past research (Khosravi, 2012; Pipatpongsa et al., 2012&2013, Leelasukseree et al., 2012). The actual engineering application of the developed theory was immediately tested by Electricity Generating Authority of Thailand (EGAT) at Area 4.1 of the Mae Moh open-pit mine in the north of Thailand. The current undercut slope was found stable after mining the lignite; however, it is necessary to fill the current pit and cut the neighboring slope in the subsequent procedure. This subsequent mining will cause the factor of safety less than one; therefore, EGAT has installed an array of shear pins to reinforce the slope. In order to evaluate the reliable factor of safety for undercut slope reinforced by shear pins, failure mechanisms studied by physical models are required to before starting the actual excavation. In this study, we aim to investigate the effect of shear pin arrangement, location and number of pins on a critical width of undercut slope, failure modes as well as failure speed in order to apply to the site.

2 Theoretical review

We employ the theory of arching effect to estimate the stable width of excavation (Khosravi, 2012).

$$B_f = k\frac{1}{(sin\alpha - tan\phi_i cos\alpha - \frac{c_i}{\gamma T})}\frac{\sigma_c}{\gamma} \qquad (1)$$

In this equation, T is a thickness of slope, α is an angle of slope, ϕ_i is an interface friction angle, c_i is an interface adhesion, γ is a bulk unit weight, σ_c is an unconfined compressive strength, B_f is a failure width and k is defined as an arching coefficient (k_0 = 0: no arching, k_1 = cosϕ: strip arch with soil slip, k_2 = 1: segmented arch with stable scarp, $k_3 = 4/\pi$: circular arch with slope buckling).

3 Experiments

Physical model was made of moist silica sand No.6 with bulk density of 1,395 kg/m^3 and water content of 10%. This model was composed of two parts, the base parts and the slope parts. The base part was 1.3×0.4 m^2 and the slope part was 1.3×0.8 m^2 with thickness 0.06m. The slope angle was 40°. Both were placed on 10 mm-thick acrylic plates. The acrylic plate of the slope part was covered with a 2 mm thick Teflon sheet in order to provide a low friction interface. Typical 1G model of slope is shown in Fig 1.

The list of material parameters is shown at Table 1 following Khosravi et al 2012. According to Khosravi et al 2012, water content 10% and bulk unit weight 13.68 kN/m^3 is suitable to achieve slope failure results within a width of the model. Unconfined compressive strength σ_c of moist silica sand no.6, interface adhesion c_i between Teflon plate and moist silica sand no.6, interface friction angle ϕ_i between Teflon plate and moist silica sand no.6 was obtained from the past laboratory tests (Khosravi, 2012).

In the present study, shear pins were additionally installed using either the screw bolts ($\emptyset = 4$ mm) or steel wires ($\emptyset = 0.28$ mm). The arrangement of shear pins is shown in Table 2 where the span of shear pins means the interval between shear pin and shear pin and the position of shear pins means the location measured from the toe of slope along the bedding plane where shear pins are fixed. A digital camera was set to monitor movement every 5 seconds for PIV analysis and a high speed camera was set at 2000 frame per second to capture triggering mechanisms. The method of undercut followed Khosravi (2012). The base part of the model was cut with a 0.05 m slice until the failure of slope. Subsequent excavations were continued up to a total failure. The undercut widths of the first failure, second failure or more are summarized in Table 2. For example, Fig. 2 shows the first failure of undercut slope with 3 screw bolts.

Table 1 Material parameters

Water content of moist silica sand no.6	w	10%
Bulk unit weight of moist silica sand no.6 (ρ = 1395 kg/m^3)	γ	13.68 kN/m^3
Unconfined compressive strength of moist silica sand no.6	σ_c	1.59 kPa
Interface adhesion between Teflon plate and moist silica sand no.6	c_i	0.1 kPa
Interface friction angle between Teflon plate and moist silica sand no.6	ϕ_i	18.5°
Thickness of slope made of moist silica sand no.6	T	0.06 m

Table 2 Arrangement of shear pins and failure width

Test number	1	2	3	4	5	6	7	8	9
Model of shear pins	No			Bolts (Ø=4mm)				Wires (Ø=0.28mm)	
Number of shear pins	0	0	0	1	3	1	3	22	12
Span of shear pins (m)					0.1		0.1	0.01	0.02
Position of shear pins (m)				0.12		0.24		0.12	0.12
Failure undercut width 1(m)	0.45	0.45	0.525	0.60	0.65	0.52	0.40	0.40	0.425
Failure undercut width 2(m)	0.525	0.525	0.55	0.625	0.78	0.57	0.52	0.45	0.575
Failure undercut width 3(m)			0.60			0.70	0.70		

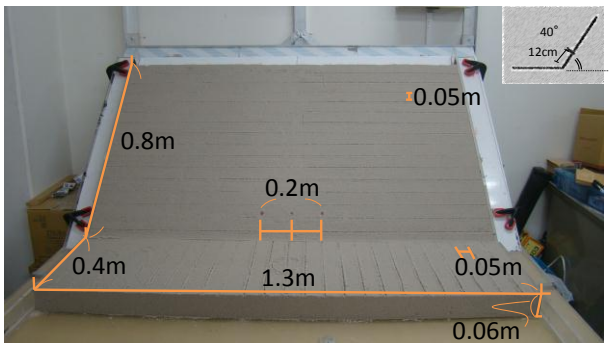

Fig.1 Model of slope with 3 screw bolts

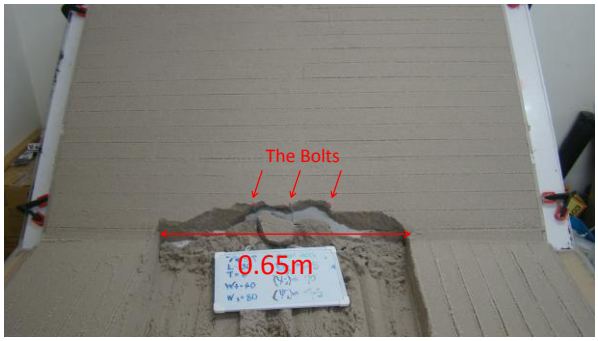

Fig.2 Failure of undercut slope with 3 screw bolts

4 Results and discussion

4.1 Critical excavation width

In Table 2, the first and total failure widths of Test 4 and Test 5 (with bolts) were significantly greater than those with no reinforcement tests (Test 1–3), indicating the effect of shear pins installed at the position 0.12 m on the failure width in relationship with a number of pins. Though the subsequent failure widths were higher, the first failure width for Test 6 and Test 7 where bolts were installed at the position 0.24 m were not significantly greater than those of no reinforcement (Test 1–3), indicating that the location of shear pins has an effect on the failure width. The closer the location of shear pins to the toe of slope, the higher the reinforcement takes effective. However, if the shear pins are installed excessively close to the excavated pit, local failure along the interval of shear pins could occur.

$$\frac{\sin(\alpha-\phi_i)}{cos\phi_i}-\frac{c_i}{\gamma T}=k\frac{\sigma_c}{\gamma B_f} \quad (2)$$

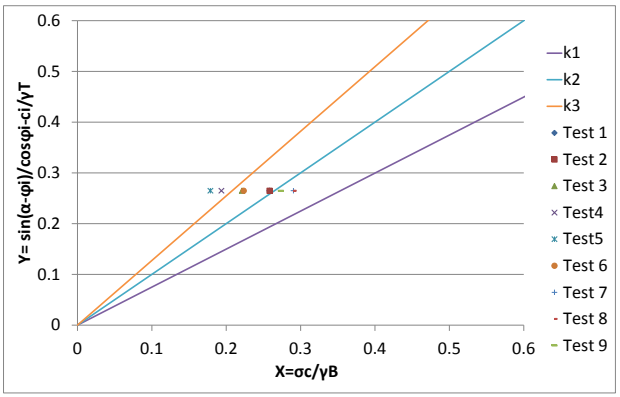

Fig. 3 Relationship between experimental results and theoretical predicitons

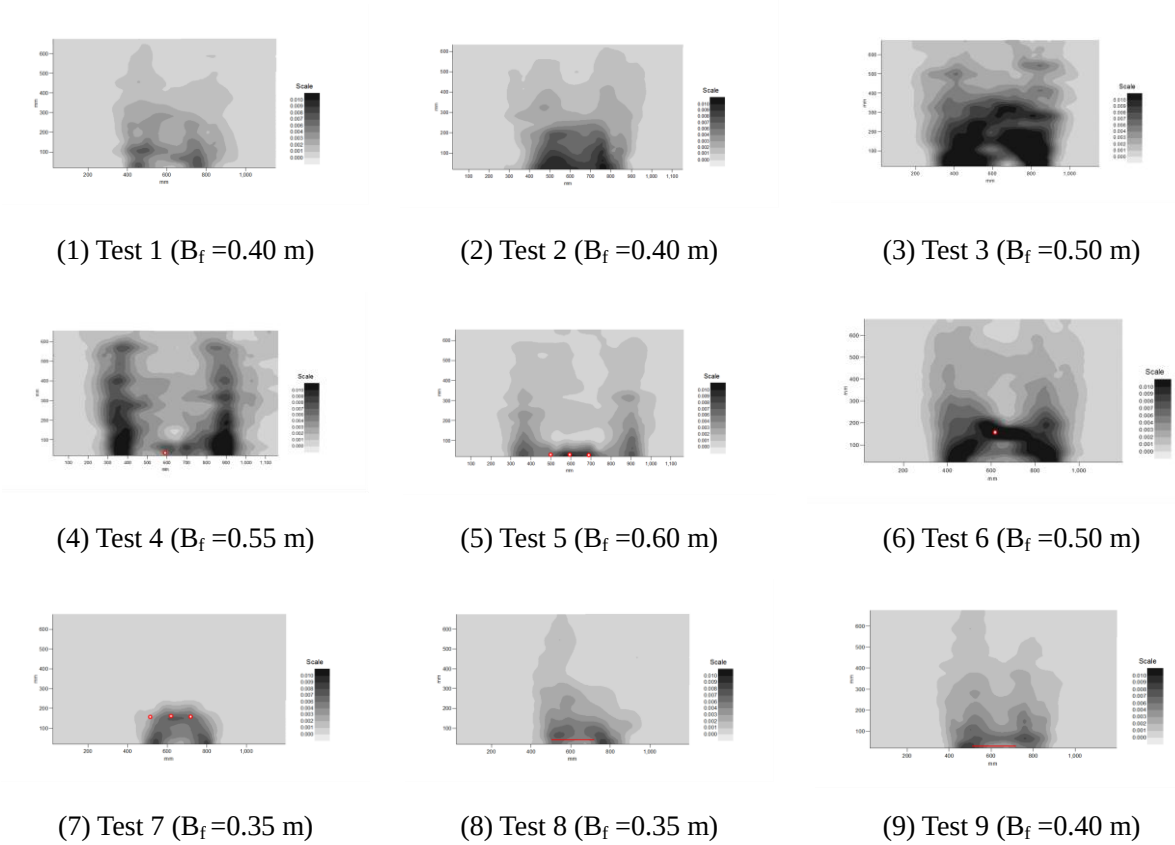

(1) Test 1 (B_f =0.40 m) (2) Test 2 (B_f =0.40 m) (3) Test 3 (B_f =0.50 m)

(4) Test 4 (B_f =0.55 m) (5) Test 5 (B_f =0.60 m) (6) Test 6 (B_f =0.50 m)

(7) Test 7 (B_f =0.35 m) (8) Test 8 (B_f =0.35 m) (9) Test 9 (B_f =0.40 m)

Fig. 4 Contours of deviatoric strain observed in Test 1–9

The test using wires (Test 8 and Test 9) revealed that the first and second failure width were not higher than those of no reinforcement (Test 1–3). Therefore, flexible type of pin might not be sufficiently effective in reinforcement than rigid type. In other words, stiffness of shear pins has an effect on the failure width. However, discontinuous plane developed along wires during compaction process would weaken the stability of slope instead of low stiffness of shear pins.

The presentation of Eq.1 can be alternatively expressed in Eq.2 and exhibited in Fig.3 by referring the right-hand side and the left-hand side of Eq.2 to the X-axis and the Y-axis, respectively. Most experimental data are appeared between boundary of k_2 (arch) and k_3 (buckling) except those of Test 4 and Test 5; thus, reinforcement by shear pins at suitable location takes effect with a wider critical width observed at the first failure than the limit predicted by the theory for slopes without reinforcement.

4.2 PIV analysis

To analyze the surface movement when the slope was excavated, the photos taken from digital camera were analyzed using PIV techniques (White & Take, 2002). Displacement vectors and contours of deviatoric strain of slope part were analyzed with careful consideration of physical coordinates. The contours of deviatoric strain at a stage just before failure (first failure) for Test 1–9 are summarized in Fig.4 where B_f means the undercut width of each test.

Arching involves in an ability of lateral load transmission due to relative displacement where yielding part transfers load to unyielding part. Partial movements due to sliding along the bedding plane caused by gravitational loading cause an intense deviatoric strain. According to Fig.4, arch action can be observed in all tests because yielding and unyielding parts are clearly appeared. The lower intensity of deviatoric strain above the bolts installed at the position 0.12 m measured from the toe of slope as shown in Fig. 4(4)–(5) can be interpreted as effects of reinforcement when compares to those of no reinforcement (Test 1–3). Once the position of bolts were shifted higher to 0.24 m measured from the toe (Test 6–7), the lower intensity of deviatoric strain is also observed as shown in Fig. 4(6)–(7); however, the intensity of deviatoric strain under the bolts was as high as those of no reinforcement with susceptible forming of arch failure. Therefore, the bolts can significantly decrease the movement above them, but cannot sustain movements under them. This fact implies that the bolts should be installed within the height of the crown of arch failure as observed in those with no reinforcement. Flexible type (wires) showed no effect of reinforcement. For each test, the center line of the captured area was chosen to obtain the incremental displacement with respect to width of excavation as shown in Fig.5. It was observed that incremental displacement at the central line of all tests except Test 7 considerably increased before failure.

Table 3 Failure mode of total collapse and time interval

Test No.	1	2	3	4	5	6	7	8	9
Buckling	○	×	×	○	×	×	○	○	○
Time interval	3.3 s	-	5.9 s	1.5 s	3.2 s	4.9 s	1.9 s	2.1 s	-

Note: "-" indicates observation by high-speed camera was not successful

4.3 Failure mechanisms

Progressive failures every 0.1 second time interval exhibited in Fig. 6 were selected from VDO stream of high-speed camera set at speed 2000 frame/second. Table 2 summarizes results observed by high-speed camera. Failure modes of total collapse were not obviously different between slopes with and without reinforcement. Hence, shear pins might not be able to change the final mode of failure, but could take effect only on the initial stage. Generally, time interval of collapse under buckling mode was shorter. Upheaval buckling occurs at the abutments of slope; thus, reinforcement at the central portion of slope would be an ineffective measure against buckling while counter-weight backfill would be an effective measure. Buckling failure happened in subsequent failure; therefore, it is depended on the geometry of scrap left after the previous failure, not shear pins.

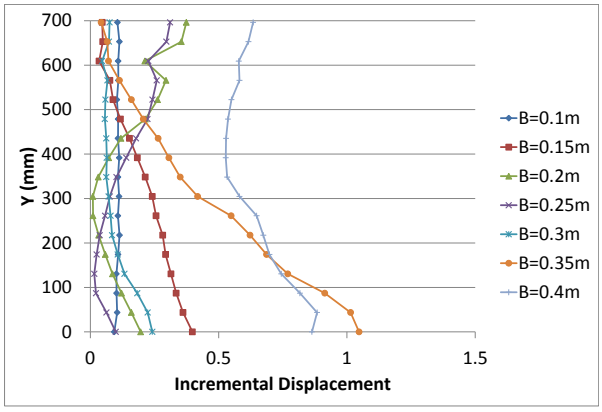

Fig. 5 Changes between incremental displacements vs width of excavation B along the center line of Test 1

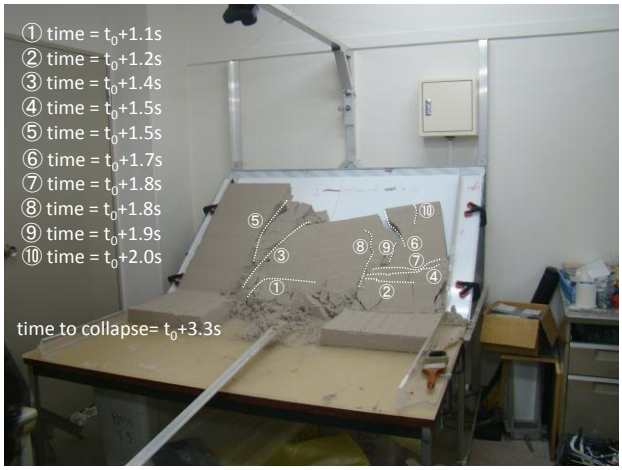

Fig. 6 Progressive failure occurred before a total collapse in the second failure of Test 1

5 Conclusions

Based on a series of 1G physical model conducted in this study, main conclusions are summarized below.

5.1 Despite local failure due to detachment along the interval of shear pins was observed, experimental results confirmed that movements of slope above shear pins for rigid type (bolts) were decreased.

5.2 Rigid-type shear pins located near the scrap gave a better performance in reinforcement; therefore, reinforcement by shear pins installed within a boundary of arch failure is effective. Still, total failure observed in slope with/without shear pins did not change significantly; thus, shear pins could be effective only in the initial stage because shear pins could not change a final model of failure.

5.3 Interpretation of movements of slope with respect to undercut width observed in physical models might be useful to monitoring scheme of actual sites. Incremental movements behave in both increment and decrement during excavation due to readjustment process of load transmission, but will dramatically increase when approaching to the failure.

Reference

[1] M.H Khosravi (2012), Arching effect in geomaterials with applications to retaining walls and undercut slopes, Department of International Development Engineering, Graduate School of Science and Engineering, Tokyo Institute of Technology, PhD Dissertation.

[2] T. Pipatpongsa, M.H. Khosravi, D. Stathas, C. Leelasukseree and J. Takemura (2012), Cohesive arch action in laterally confined block of moist sand placing on an inclined Bedding plane, 7th Asian Rock Mechanics Symposium, pp.1378-1387.

[3] C. Leelasukseree, T. Pipatpongsa, M.H. Khosravi and N. Mavong (2012), Stresses and a failure mode from physical and numerical models of undercut slope lying on inclined bedding plane, 7th Asian Rock Mechanics Symposium, pp.1295-1304.

[4] T. Pipatpongsa, M.H. Khosravi and J. Takemura (2013), Physical modeling of arch action in undercut slopes with actual engineering practice to Mae Moh open-pit mine of Thailand, 18th International Conference on Soil Mechanics and Geotechnical Engineering, Vol.1, pp.943-946

[5] White, D. J. & Take, W. A. (2002) GeoPIV: Particle image velocity (PIV) software for use in geotechnical testing. Cambridge University Engineering Department.

ACTIVE ARCH ACTION DUE TO INTERFACE FRICTION IN A RIGID RETAINING WALL

Student Number: 12M18241 Name: Lin TANG Supervisor: Thirapong PIPATPONGSA

剛体壁の界面摩擦による主働的アーチ効果の観察

唐 麟

Abstract: In the previous study, lateral pressure distribution on the rigid retaining wall under translation mode has been derived using the arch action theory and validated by a 1g physical model. This study extends the previous work in order to validate the theory using different interface friction of the retaining wall with/without a surcharge load applied on the surface of backfill. Pressure distribution along a retaining wall was measured by a set of precise miniature pressure cells and backfill movement was observed by particle image velocimetry. Sandpaper used in the previous study was replaced by Teflon sheet. Surcharge using bearing balls was additionally considered. Reliability of pressure gauges under both loading and unloading processes was discussed. Despite difficulties in controlling a uniform density of Silica sand No.8, the experimental results sufficiently confirm the developed arch action theory.

1. Introduction

Retaining walls have the function to prevent soil or slope falling, meanwhile sustain lateral earth pressure from retained materials or backfilled soils. The estimation of active earth pressures acting on retaining walls is important in geotechnical design. Normally, civil engineers have calculated the active earth pressure against rigid walls using either Coulomb (1776)'s or Rankine (1857)'s classical theory. Both theories assume that the distribution of active earth pressure exerted against the wall is triangular. However, many experiment results show that the distribution of active earth pressure on a wall is non-linear and depends on the mode of wall movement, which is different from the assumption made by Coulomb and Rankine. The non-linearity of the active earth pressure distribution results from arching effects in backfill due to roughness of the retaining wall.

Arching, as the word suggests, is a stress redistribution by which stress is transferred laterally around a region of the soil mass, which then becomes to lower stress. This research focuses on earth pressure acting on rigid retaining wall under active translation mode. A series of retaining wall experiments with/without a uniform surcharge were conducted to validate the developed active earth pressure theory which considers the arching effect. In addition, the measured earth pressures were compared with the previous testing results which were conducted in fully rough condition of retaining wall in order to understand the influence of interface friction on the profile of earth pressure distribution.

2. Theoretical Background

2.1 Lateral earth pressure at-rest

In soil mechanics, lateral earth pressure at-rest for the horizontally inclined subsoil is generally calculated by Jaky (1948)'s theory as follows.

$$\sigma_h = K_0 \gamma H \ , \quad K_0 = 1 - \sin\phi \qquad (1), (2)$$

Where K_0 is a coefficient of lateral earth pressure at-rest, ϕ is an internal friction angle of subsoil, γ is unit weight, and H is a depth of subsoil.

2.2 Active arch action in retaining wall

Arching effect has been considered in the analysis of active earth pressure exerting on a retaining wall by various studies. Khosravi et al. (2013) proposed a formulation to describe the active earth pressure behind a retaining wall under active translation mode by integrating the two-dimensional equilibrium conditions

with an assumption on a uniform distribution of vertical pressure in a planar active wedge. The interface friction between the wall and the backfill is mobilized while the active wedge is separated from the stagnant backfill along the slip line with a critical angle determined from Coulomb or Rankine's theory.

According to Khosravi et al. (2013), the magnitude of active lateral earth pressure σ_h at a depth h of a retaining wall with backfill height H and a uniform surcharge Q is expressed by Eq.(3).

$$\sigma_h(h) = K_w \left(\begin{array}{l} \dfrac{\gamma H}{1-n}\left(\left(1-\dfrac{h}{H}\right)^n - \left(1-\dfrac{h}{H}\right)\right) \\ +Q\left(1-\dfrac{h}{H}\right)^n \end{array} \right) \quad (3)$$

$$K_w = \frac{1-\cos(\omega-\phi_w)\sin\phi}{1+\cos(\omega-\phi_w)\sin\phi}, \quad \omega = \sin^{-1}\left(\frac{\sin\phi_w}{\sin\phi}\right) \quad (4), (5)$$

$$n = \mu_w K_w \cot\alpha, \ \mu_w = \tan\phi_w, \quad \alpha = \frac{\pi}{4} - \frac{\phi}{2} \quad (6), (7), (8)$$

where K_w is a ratio of horizontal to vertical soil stress at the wall, μ_w is the wall friction, γ is the bulk unit weight of backfill, α is a critical angle of active wedge, ϕ is an angle of shearing resistance of backfill, ϕ_w is an interface friction angle between the backfill and the wall.

3. Preliminary Laboratory Element Tests

3.1 Validation of pressure cells in Silica sand

In retaining wall experiment, "bin effect" and "cell action" must be taken into account when conducting a small-scale 1G model. Bin effect or silo effect is caused by arch action in the soil mass stored in the bin. If the dimension of the bin is too narrow, pressure distribution will not be linear along the depth direction. In contrast, local arching in the surrounding soil next to the pressure cell face may cause cell action which leads to over/under registration of the cell.

Validations of the pressure cells in dry Silica sand No.8 and No.6 in a chamber were conducted in order to evaluate the silo effect and unloading responses which will have significant influence on the interpretation of experiments. Air pluviation method (Fig. 1) was used in sample preparing. In loading process, the sample was prepared 50 mm step by step, while in unloading process, the sand was removed 25 mm step by step. The average values of measured pressures against calculated hydrostatic pressures were plotted in Fig. 2.

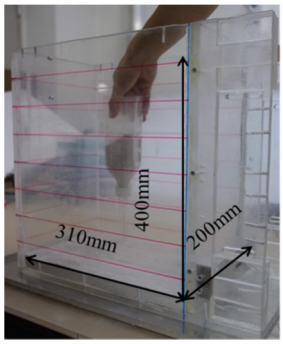

Fig. 1 Sample preparation by air pluviation method poured at constant height 100 mm in an acrylic container

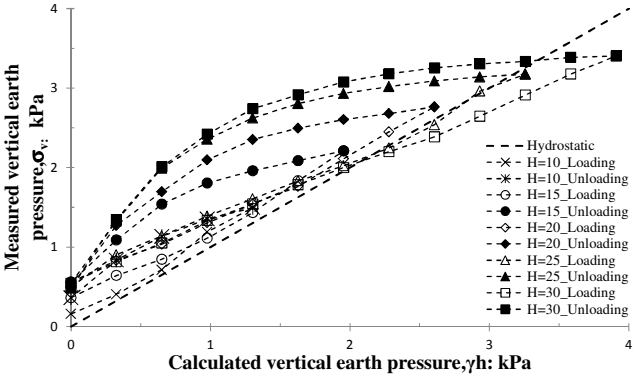

Fig. 2 Validation of pressure cells using Silica sand No.8 in unloading process

Table 1 Basic properties of dry Silica sand No.8

Specific gravity	2.637
Maximum grain size	0.250 mm
Medium grain size (D_{50})	0.090 mm
Uniformity coefficient (U_c)	3.05
Minimum density	1.153 g/cm^3
Maximum density	1.554 g/cm^3

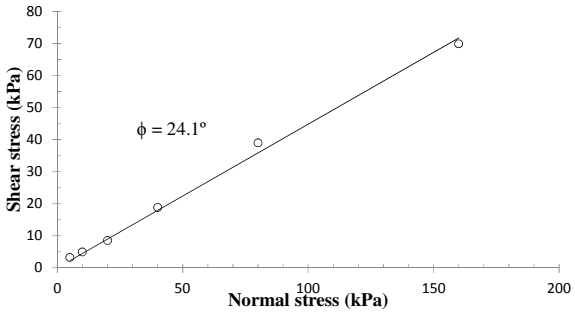

Fig. 3 Direct shear test on dry Silica sand No.8 with interface friction between Teflon sheet

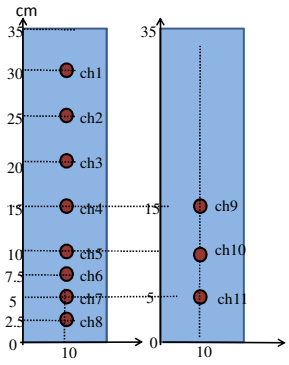

Fig. 4 Configuration of pressure cells (left is retaining wall side, right is the opposite side)

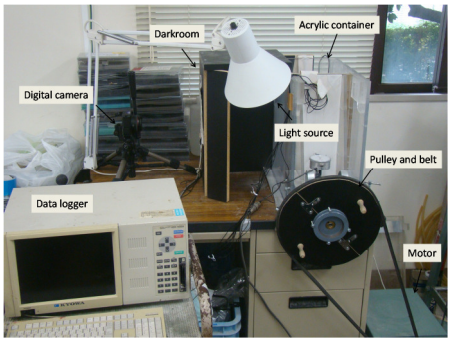

Fig. 5 A general view of the experimental setup

The hysteretic nature of the calibration curve was drawn to compare the variation of coefficient of calibration under both loading and unloading processes. In general, pressure cells show linear behavior in loading process, but show non-linear behavior in unloading process. For physical model of retaining wall, using Silica sand No.8 would better reduce "bin effect" and "cell action" than silica sand No.6 even at the almost same density.

3.2 Physical profile of Silica sand No.8

The basic physical properties of Silica sand No.8 is listed in Table 1. Direct shear test was conducted with a shear rate of 0.22 mm/min to obtain the interface friction angle between Silica sand No.8 and Teflon sheet, which is shown in Fig. 3.

4. Retaining wall experiments with/without surcharge

4.1 Instruments and experimental setup

Totally 11 miniature pressure cells (Fig. 4) were embedded flush to the surface of retaining wall and the opposite wall covered by Teflon sheet. Pressure cell in big size was placed on the bottom of acrylic container to measure vertical stress. A retaining wall retained the backfill soil inside an acrylic container as shown in Fig. 5. A strong screw passed through a fixed rigid frame and connected the wall to a pulley. Rotation of the pulley and screw made the wall able to slide horizontally. The speed of wall movement was controlled by an electric motor. During experiment, digital camera in front of the transparent side of acrylic container will take photos for PIV analysis. A lamp was used to provide light source when digital camera working. A darkroom was in the middle of PIV camera and acrylic container to minimize the unwanted reflections on the screen.

4.2 Retaining wall experiments without surcharge

Backfilled soil was produced by filling sand to the container using air pluviation method pouring from a funnel. By keeping the pouring height constant at 100 mm above the sand level during the process of preparation, a uniform density of sand in the container was reached. Data logger recorded earth pressures every second from the initial condition in which sand was deposited in acrylic container, to the active condition when the wall is gently moved outward. The electric motor rotated and pulled the wall to move horizontally at a constant speed of 0.005 mm/sec. Digital camera was set in time interval about 20 seconds to take images for every 0.1 mm of wall movement. Conditions of 4 actual retaining wall experiments without surcharge were listed in Table 2.

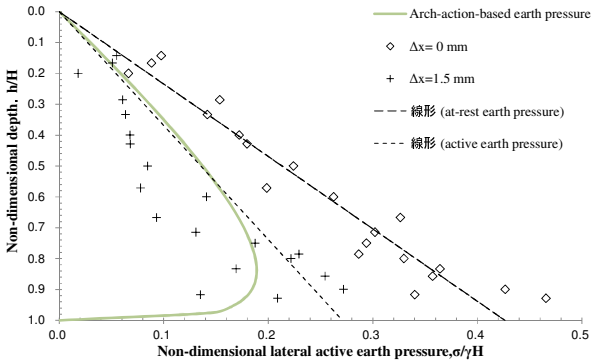

Fig. 6 Changes of lateral earth pressure from at-rest to active conditions along the depth in normalized scale

Table 2 Retaining wall experiments without surcharge

Test	Height of wall H (mm)	Amount of pressure cell	Bulk density ρ (kg/m^3)	Relative density D_r (%)
9	300	7	1242	28
10	350	8	1224	22
11	200	6	1206	17
15	250	5	1219	21

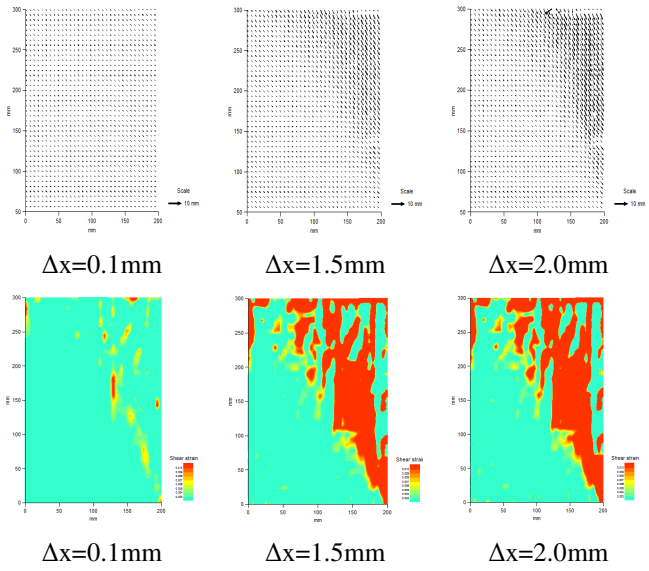

Fig. 7 Vector displacement and contours of shear strain analyzed in Test 9, 10, 11 and 15

When retaining wall started to move, the magnitudes of earth pressure decreases gradually. This decrement continues until "active wall movement" (Δx_a), referring to the state when the measurements on every pressure cells reach nearly constant values and do not change much despite further wall movement. Average of Δx_a in every test is around 1.75 mm. Changes of lateral earth pressure is plotted in Fig. 6, where at-rest pressure shows a good agreement with Jaky's semi-empirical equation. At the active wall movement of 1.5 mm, pressure of the upper portions of the wall is slightly less than the theoretical prediction by Eq.(3).

Vector displacement and contours of shear strain were plotted in a range of panel 200 mm × 300 mm as shown in Figs. 7, each of which showed vector displacement and shear strain contour for Δx = 0.1, 1.5 and 2.0 mm using a common scales. There are no significant change once Δx reaches to Δx_a=1.5 mm which is a value of active wall movement determined from pressure cells.

4.3 Retaining wall experiments with surcharge

Experiments were conducted by following the same procedure of retaining wall experiment without surcharge. What the difference is surcharge was loaded after finishing sand ground preparation. Bearing ball with a diameter of 12.68 mm was used as surcharge and loaded on the surface of sand ground in 3 times with a total weight 6 kg. Another 4 tests with height of backfill 350, 300, 250 and 200 mm were conducted. In the initial state, at-rest earth pressure shifts from Jaky's theoretical pressure due to surcharge. When retaining wall moved 2 mm outward, active earth pressure decreased but with no agreement with the distribution of arch-action based earth pressure, which means there was low influence from arching between Teflon sheet and retaining wall.

5. Conclusions

The observed lateral pressure acting on Teflon sheet did not indicate a strong arch action like what achieved in the previous study using sandpaper; therefore, the experimental results satisfied with arch-action based theory indicating that the smoother the surface, the closer the profile of lateral active earth pressure approaches to Rankine's active earth pressure. Both vector displacement and shear strain contour obtained from PIV analysis showed a clear distinction between stationary and failure zones. Active wall movement observed by pressure cells agreed with that observed by PIV with the same value independent of depth of backfilled sand and surcharge. Therefore, the same pattern of pressure change can be confirmed by both lateral earth pressure analysis and PIV analysis.

References

1) M.H. Khosravi, T. Pipatpongsa and J. Takemura (2013), Experimental analysis of earth pressure against rigid retaining walls under translation mode, Géotechnique, Vol. 63(2), pp.1020-1028.

2) J. Jaky, (1948), Earth pressure in silos, 2nd ICSMFE, pp. 103-107.

Fe-TiO_2-MWCNT Composite Photocatalyst for Degradation of Methylene Blue

Student Number: 12M18206　Name: Hao ZUO　Supervisor: Hirofumi HINODE

Fe-TiO_2-MWCNT 複合触媒によるメチレンブルーの分解

左　皓

本研究の対象中国では、重化学工業を中心とした高度経済成長期に入ってからの大量生産、大量消費、大量廃棄という自然の浄化力を上回る社会活動の流れの中で、種々の環境汚染問題が発生してきた。特に、繊維生産による染料の廃水は毒性が高く、生物による分解の可能性も比較的低いため、すでに生態系に深刻な環境被害をもたらしている。この現状を踏まえて、本研究では、鉄ドープ酸化チタンと多層カーボンナノチューブ(MWCNT)を複合した新しい複合触媒 Fe-TiO_2-MWCNT を開発することを目的としている。

1. Introduction

Recently, the rapid growth of industries leads to the expansion of environmental problems in China. One of the main environmental problems is water pollution from sources such as industries, agricultures, and households, which contain contaminants such as organic and inorganic compounds [1]. In particular, textile wastewater is well-known for its high variability of composition with intense colors, fluctuating pH values, high chemical oxygen demand (COD) and relatively low biodegradability with large amount of suspended solids and dissolved salts. These effluents deteriorate the aesthetics of receiving water body and pose significant threat to the surrounding ecosystem and human health. Textile industry wastewater is usually treated using conventional physical methods such as adsorption or biological technologies. Sludge formation and large number of aromatic rings present in organic dye compounds may cause conventional biological treatment methods to be ineffective for their mineralization. Moreover, adsorption may be effective for decolorization but the process only involves a phase transfer of pollutants which subsequently requires additional treatment or disposal [2].

Recently, the new approach proposed for textile wastewater treatment is an application of photocatalyst through advanced oxidation process (AOPs). Titanium dioxide (TiO_2) is one of the most efficient photocatalyst due to its high stability, chemical inertness, non-toxicity, and low cost. Yet, efficient application of solar irradiation for the photocatalysis is restricted due to the limitation of TiO_2 than can only be activated under UV light due to its wide band gap of 3.2 eV [3]. To increase the efficiency of TiO_2 by extending the activity into the visible light range, TiO_2 can be modified by doping with transition metal and modified by CNT.

In this research, the photodegradation of methylene blue (MB), as a representative of organic dye compounds due to its ubiquitous presence in factory wastewater, under visible light irradiation using the composite of Fe-TiO_2 and multi-walled carbon nanotube (MWCNT) photocatalyst will be investigated.

2. Experimental

2.1. Cutting of MWCNT

As used MWCNT synthesized by chemical vapor deposition (CVD) method contains many catalysts [4], the raw MWCNT was put into 300 ml of concentrated HCl under magnetic agitation for 5 h followed by filtration to eliminate these catalysts. The cutting experiments were carried out as follows: 250

mg of pretreated MWCNT was suspended in 300 ml of concentrated H_2SO_4 under magnetic agitation for 30 min at room temperature then added by 180 ml of concentrated HNO_3. Then the mixture was heated at 60℃ for 6 h. The cut MWCNT was collected using glass fiber filter paper and washed with deionized water until the pH value reach neutral.

2.2. Preparation of Fe-TiO_2-MWCNT

Fe-TiO_2-MWCNT was prepared by a modified sol-gel method using titanium tetraisopropoxide (TTIP) as the Ti-precursor. Iron nitrate ($Fe(NO_3)_3 \cdot 9H_2O$) was used as the metal precursor. 18.6 mL of TTIP was hydrolyzed using 35.8 mL of glacial acetic acid at around 0℃. To this solution, Iron nitrate solutions (395 mL) with appropriate amount of Fe of 0.25 mol%, 0.5 mol% and 1.0 mol% were added drop wise under vigorous stirring for 1 h, subsequently the solution was ultrasonicated for 30 min and continued the stirring for another 5 h until a clear pale yellow solution was formed. Simultaneously, amount of cut MWCNT of 10wt. %, 20wt. % and 30wt. % were mixed with 20 ml ethanol and ultrasonicated for 30 min. Subsequently, these parts were put into the previous pale yellow solution and ultrasonicated for another 30 min. After this period, the solutions were placed in an oven maintained at a temperature of 70℃ for 12 h for aging process. The gels were then dried at 100℃ and subsequently the catalysts were crushed into fine powder and calcined at 500℃. For comparison, undoped TiO_2, Fe-TiO_2 and TiO_2-MWCNT composites were also synthesized using the same route.

2.3. Characterization of photocatalysts

Crystal structure and crystallite size of the photocatalysts were determined by X-ray diffraction spectroscopy (XRD). Morphology and particle size were investigated by transmission electron microscopy (TEM) and scanning electron microscopy (SEM). Elemental composition of the catalysts was analyzed by energy dispersive X-ray spectroscopy (EDS). The Brunauer Emmett and Teller (BET) adsorption-desorption of nitrogen gas at the temperature of liquid nitrogen to measure specific surface area was performed on autosorb-1MP-Quantachrome. Quantitative analysis of photocatalysts was done using Inductively Coupled Plasma-Atomic Emission Spectrometry (ICP-AES).

2.4. Photodegradation Experiments

The photocatalytic set-up is showed in Fig. 1. The experiments were carried out in a glass photochemical reactor. The reactor was equipped with a UV and visible light lamp (100 W, 312-577 nm) located axially and held in a quartz immersion, equipped with a UV-cut film which allows only visible light (400-577 nm) to pass. The UV photodegradation experiments were carried out without the UV-cut film and the visible light photodegradation experiments were carried out by applying the UV-cut film on the lamp. For each run, 0.35 g of photocatalyst was dispersed in 700 mL of methylene blue solution with an initial concentration of 20 mg/L. Before irradiation, the MB solution with photocatalyst was stirred in a dark condition for 1 h to establish an adsorption-desorption equilibrium.

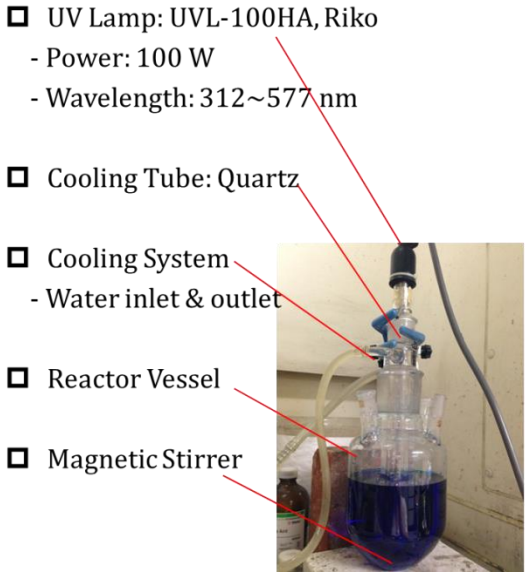

Fig. 1 Photocatalytic set-up

3. Results and discussion

3.1. BET and XRD Characterization

Table 1 shows the results of BET and XRD of each Fe doped TiO_2. It indicated that there were some positive effects of Fe doped TiO_2. Fe doped TiO_2 had higher specific surface area and smaller crystal size. And Fe^{3+} also acted as electron traps to decrease in electron-hole recombination.

Table. 1 BET and XRD results

Photocatalyst	BET Specific Surface Area (m^2/g)	XRD Crystal Size (nm)	Crystal Phase
Degussa P25	47.28	21.3	Anatase&Rutile
Undoped TiO_2	70.54	16.1	Anatase
0.25mol% Fe-TiO_2	78.96	14.3	Anatase
0.5mol% Fe-TiO_2	82.59	14.6	Anatase
1.0mol% Fe-TiO_2	73.95	14.8	Anatase

The XRD patterns showed that TiO_2 present in the photocatalysts were anatase and no characteristic peaks indicating Fe phases or its oxides were observed in the patterns.

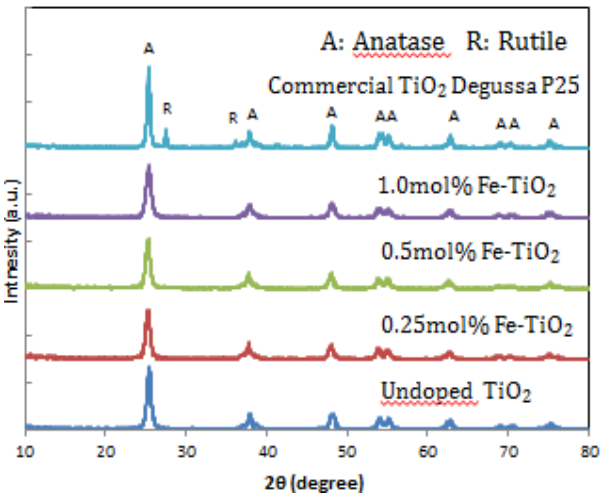

Fig. 2 XRD patterns of Fe-TiO_2

The effect of doping on the crystallinity of anatase TiO_2 was confirmed after further analyzing the XRD data for the lattice parameters a and c of anatase (a tetragonal crystal) using the h, k, l and d values. Plotting the % Fe doping against the unit cell parameters, it indicates re-arrangement of atoms in the crystal of anatase structure by substitution of metal dopants, most probably because Fe being an element with smaller atomic radius, in the TiO_2 structure. The lattice parameters decreased and eventually stabilized in the event that maximum dopant loading is reached as shown in Figure 4 and 5. The maximum dopant loadings to affect the lattice parameters were 0.5% and 0.5% for *a* and *c*, respectively.

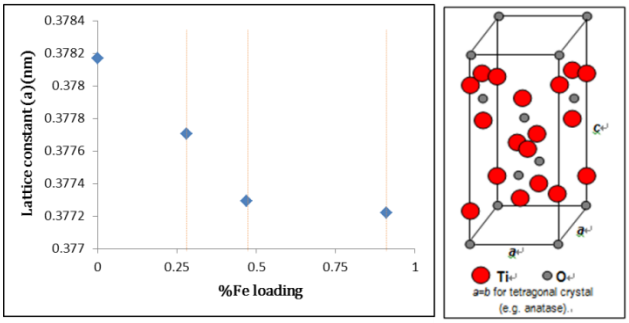

Fig. 3 Left: Plot of effect of Fe-doping on unit cell parameter *a* of anatase TiO_2. Right: Structure of anatase TiO_2 crystal.

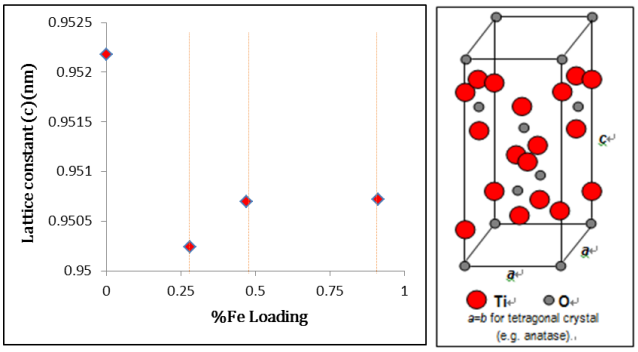

Fig. 4 Left: Plot of effect of Fe-doping on unit cell parameter *c* of anatase TiO_2. Right: Structure of anatase TiO_2 crystal.

3.2. Photodegradation of MB

Figure 5 shows the results of photodegradation of MB using Fe doped TiO_2 under UV-visible light irradiation. Commercial TiO_2 degussa P25 showed better photoactivity, which can degrade 20 ppm of MB completely within 120 min. Undoped TiO_2 degraded 20 ppm of MB completely within 300 min. 0.5mol% Fe- TiO_2 degraded 71.7% of MB within 300 min under UV-visible light irradiation.

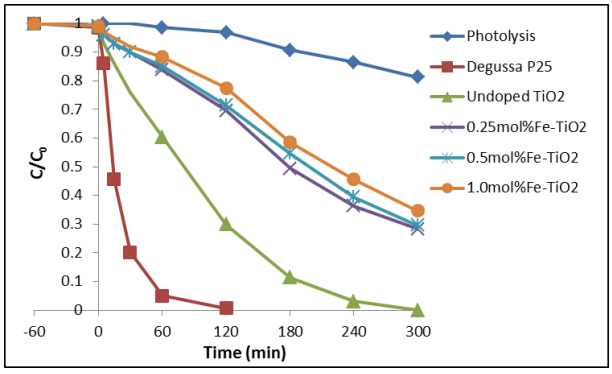

Fig. 5 MB degradation under UV-visible light irradiation using Fe-TiO_2

Figure 6 shows the results of photodegradation of MB using Fe doped TiO_2 under visible light irradiation. 0.5 mol% Fe-TiO_2 degraded 38.6% of 20 ppm of MB within 300 min, which showed a better photoactivity than undoped TiO_2 under visible light irradiation.

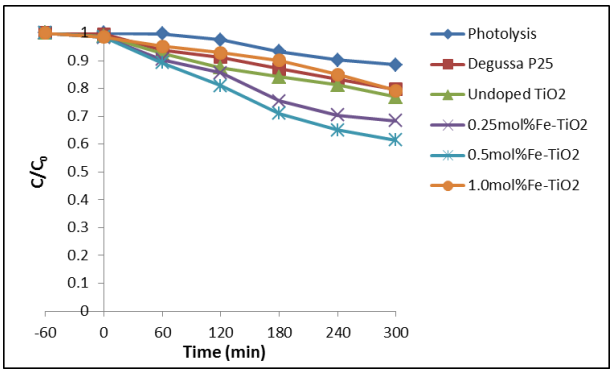

Fig. 6 MB degradation under visible light irradiation using Fe-TiO_2

Figure 7 shows the results of photodegradation of MB using composite photocatalyst under UV-visible light irradiation. 0.5mol% Fe-TiO_2-20 wt.% MWCNT degraded 74.7% of 20 ppm of MB within 300 min under UV-visible light irradiation.

Figure 8 shows the results of photodegradation of MB using composite photocatalyst under visible light irradiation. 0.5mol% Fe-TiO_2-20 wt.% MWCNT degraded 42.6% of 20 ppm of MB within 300 min under visible light irradiation.

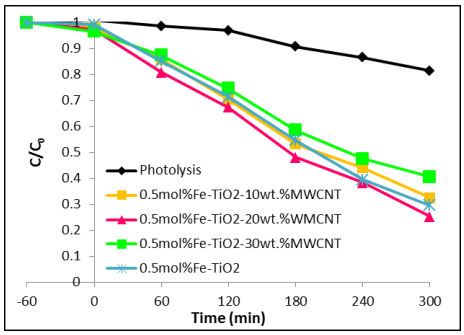

Fig. 7 MB degradation under UV-visible light irradiation using Fe-TiO_2-MWCNT

The results indicate that the presence of MWCNT slightly enhances the photocatalytic activity.

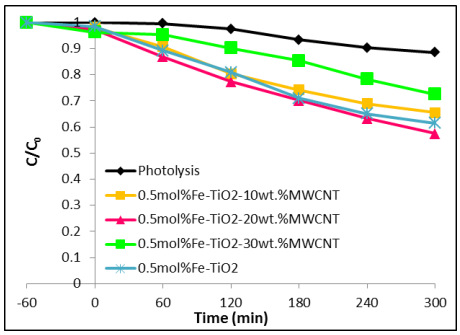

Fig. 8 MB degradation under visible light irradiation using Fe-TiO_2-MWCNT

4. Conclusion

Fe-TiO_2-MWCNT composite photocatalyst was synthesized by a modified sol-gel method. The new catalyst was more effective than Fe-TiO_2 under visible light irradiation for methylene blue treatment by the synergetic effect between Fe-TiO_2 and MWCNT.

Reference

[1] Paruchai Pongwan et al. / ENGENEERING JOURNAL, Volume 16 Issue 3

[2] Yean Ling Pang et al. / Applied Catalysis B: Environmental 129 (2013) 473-481

[3] Shaari N et al. / JOURNAL OF RARE EARTH, Vol. 30, No. 7, July 2012, P. 651

[4] P.X. Hou et al. / Carbon 40 (2002) 81

Selective Catalytic Reduction of Nitrogen Oxides with Propene over Metal Oxides mixed with $(Ti,Zr)_2O_4$ Catalyst

Student Number: 12M18181 Name: Dongil KIM Supervisor: Hirofumi HINODE

C_3H_6 を還元剤とした機械的混合法による(Mo,W)-$(Ti,Zr)_2O_4$ 複合触媒の NO の選択還元

金 東一（キム ドンイル）

本研究では、排ガス内に混在する炭化水素のプロペンを還元剤とした NO の選択還元（HC-SCR）を目的とした触媒の開発を行った。担体として$(Ti,Zr)_2O_4$を用い、Mo と W を用いて含侵法と機械的混合法によって調製した複合触媒の活性及び特性の変化について検討した。これらの複合触媒の中で機械的混合法によって調製された 30%MoO_3+$(Ti,Zr)_2O_4$触媒が 450℃で最大活性を示し、約 78%の NO 分解が達成できた。また、最大活性を示した触媒の実用面を考慮した水の影響や再利用性について述べる。

1 Introduction

Nitrogen oxides (NO, NO_2 and N_2O) are major sources of atmospheric environmental problems such as photochemical smog, acid rain, ozone depletion and greenhouse effects. Furthermore, presence of nitrogen oxides in the atmosphere can cause problems to human health. Most of the NO_x comes from automobiles (48.5%) and power plants (46.2%) using fossil fuels [1].

Nowadays, three-way catalysts (TWC) are generally used to reduce NO_x in automobiles. This method can reduce NO_x with high efficiency at specific air to fuel (A/F) ratio. However, the development of lean-burn engines that have higher fuel economy and cleaner emissions requires catalyst for NO_x reduction that can function also at higher A/F ratio which cannot be achieved using TWC only. One potential method to reduce NO_x in exhaust gas is by selective catalytic reduction of NO using hydrocarbon as reducing agent (HC-SCR of NO) [2]. Among several applicable methods, HC-SCR contained in the exhaust is currently the most studied technology for NO_x reduction.

Previous study showed that TiO_2 supported Mo catalyst was effective in NH_3-SCR of NO [3]. Compared with impregnated catalyst, manually mixed MoO_3+TiO_2 catalyst showed more activity for the selective catalytic reduction of NO by NH_3[4]. Similar with MoO_3, WO_3 can improve mechanical strength of the catalyst by acting as chemical and structural promoters thus enlarging the temperature window of the SCR reaction.

The main reactions taking place during SCR process are the following:

$$2NO+O_2 \rightarrow 2NO_2 \quad (1)$$

$$3NO+3NO_2+C_3H_6 \rightarrow 3N_2+3CO_2+3H_2O \quad (2)$$

Another study reported that $(Ti,Zr)_2O_4$ composite used as support material exhibited higher catalytic activity towards HC-SCR of NO when compared to bare TiO_2 [5]. Also $(Ti,Zr)_2O_4$ is known of its high BET surface area and high mechanical strength, and is widely used in many reactions as catalyst[6].

Therefore, in this study, the catalytic activities of $(Ti,Zr)_2O_4$ supported Mo and W catalysts was studied. Mo supported catalyst was prepared by two different methods, impregnation (IM) and manual mixing (MM). W supported catalysts were prepared by MM method. $(Mo\text{-}W)_xO_y$+$(Ti,Zr)_2O_4$ metal combined catalysts were also investigated for comparison of the catalytic activity. They were investigated for HC-SCR of NO_x using propene as reducing agent[7-9].

2 Experimental

2.1 Materials

$(Ti,Zr)_2O_4$ catalyst was prepared by co-precipitation method using $Zr(NO_3)_2.2H_2O$ (Wako) and $[(CH_3)_2CHO]_4Ti$ (Wako) as precursors with the same molar ratio for Ti and Zr [4]. First, $Zr(NO_3)_2.2H_2O$ was dissolved in 35 ml of deionized water with continuous stirring and the pH was controlled by addition of HNO_3 (pH=0.5-1.0). Then $[(CH_3)_2CHO]_4Ti$ was added to the solution and the pH was changed by addition of NH_3 solution (pH=9-11). The resulting mixture was filtered, dried at 100℃ for 8 h and calcined at 550℃ in air for 4 h.

In the case of IM method, $(NH_4)_6Mo_7O_{24}.4H_2O$ (Wako) was dissolved in 50 ml of deionized water and mixed with $(Ti,Zr)_2O_4$. Then the mixture was stirred at room temperature for 12 h and dried at 80℃ for 12 h. The catalyst prepared by IM method was designated as $Mo/(Ti,Zr)_2O_4$.

In the MM method, Mo precursor used in IM method was calcined first at 400℃ prior to mixing with $(Ti,Zr)_2O_4$ prepared earlier. The mixing was carried out by hand using mortar and pestle with a little amount of ethanol. WO_3 was used for preparing MM W supported catalysts.

$(NH_4)_6H_2W_{12}O_{40}.xH_2O$ was used as W precursor for preparing metal combined catalyst. Both W and Mo precursor dissolved in deionized water at the same time, and catalyst were prepared by sol-gel method.

All prepared catalysts were calcined at 550℃ in air for 4 h. Finally, the catalysts were crushed and sieved to 0.71-1.00 mm [4]. The catalyst prepared by MM method was designated $MoO_3+(Ti,Zr)_2O_4$, $WO_3+(Ti,Zr)_2O_4$, $(W,Mo)_xO_y+(Ti,Zr)_2O_4$.

2.2 Catalytic Activity Test

The SCR activity experiments were carried out in a fixed-bed flow reactor. The reactant gas was composed of 1500 ppm NO, 10% O_2, 1500 ppm C_3H_6 and He as a balance gas. 0.8~1.4 g catalyst was used with a corresponding space velocity of 13000 h^{-1} and a total gas flow rate of about 4 mL/s. The temperature was changed stepwise from 150℃ to 550℃.

NO and NO_2 concentration were analyzed by NO_x analyzer (Shimadzu, NOA-7000). N_2O, CO_2 and CO were analyzed by gas chromatograph (GL Science, GC-323w for N_2O; GL Science, GC-390 for CO_2 and CO). The catalysts were characterized by TG-DTA, XRD, N_2 adsorption (Autosorb 1MP/TSU, BET analysis) and SEM-EDS.

3 Results and Discussion

3.1 Catalytic Activity

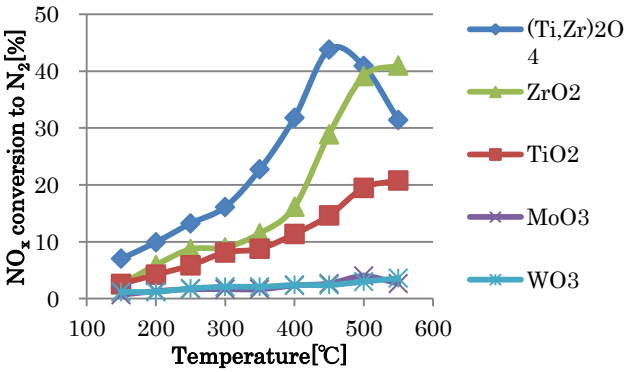

Fig.1 Catalytic activity of bare catalysts for the reduction of NO_x conversion to N_2 using C_3H_6 as a reductant

Fig.1 shows the conversion of NO to N_2 over TiO_2, ZrO_2, MoO_3, $(Ti,Zr)_2O_4$ catalysts. $(Ti,Zr)_2O_4$ catalyst shows the highest activity at 450℃ among all the catalysts followed by ZrO_2 and TiO_2 while MoO_3 and WO_3 showed the lowest conversion to N_2.

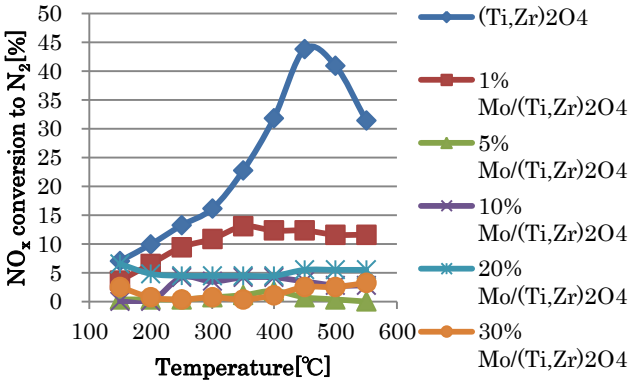

Fig.2 Catalytic activity of $Mo/(Ti,Zr)_2O_4$ IM method catalyst for the reaction of NO_x to N_2 using C_3H_6 as a reductant

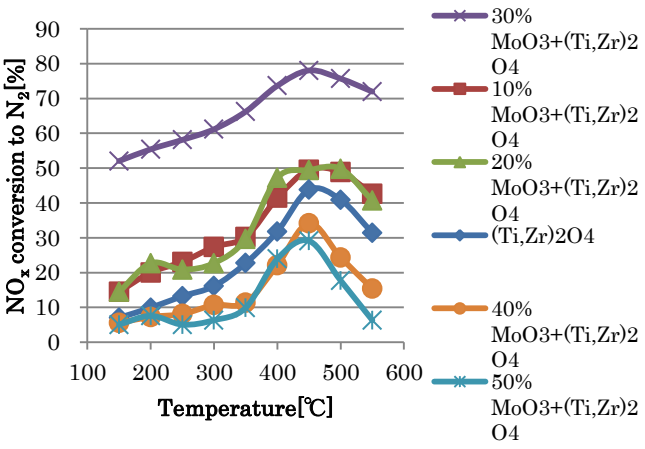

Fig.3 Catalytic activity of $MoO_3+(Ti,Zr)_2O_4$ IM method catalyst for the reaction of NO_x to N_2 using C_3H_6 as a reductant

Fig.2 shows the conversion of NO to N_2 over $Mo/(Ti,Zr)_2O_4$ catalyst by IM method with Mo loading levels from 0-30 wt.%. Metal loaded catalyst showed lower catalytic activity than unloaded $(Ti,Zr)_2O_4$ catalyst. It is possible that the addition of Mo metal on the $(Ti,Zr)_2O_4$ support by IM method reduced the exposed surface of $(Ti,Zr)_2O_4$ available for reaction thus reducing its catalytic activity [3].

Fig.3 shows the conversion of NO to N_2 over $MoO_3+(Ti,Zr)_2O_4$ catalysts by MM method with Mo loading levels from 0-50 wt.%. Catalyst with 30% MoO_3 showed the highest catalytic conversion at 450℃ followed by 10% and 20%. However, further increase of Mo loading to 50% showed a decrease in activity as compared to the bare $(Ti,Zr)_2O_4$ catalyst.

Fig.4 shows the conversion of NO to NO_2 and the conversion of C_3H_6 to CO_2 using the $(Ti,Zr)_2O_4$ and 30%

MM method MoO_3+$(Ti,Zr)_2O_4$ catalysts. Addition of 30%Mo by MM method increased the conversion of C_3H_6 to CO_2 while decreasing the conversion of NO to NO_2. This suggested that addition of Mo improved the selectivity of NO reduction to N_2 as shown in Fig.3.

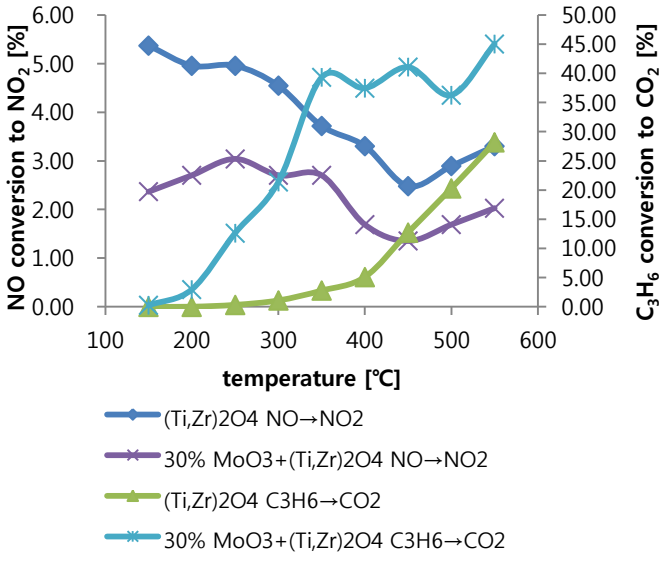

Fig.4 Catalytic activity of $(Ti,Zr)_2O_4$, 30%MoO_3+$(Ti,Zr)_2O_4$ catalyst for the conversion of NO to NO_2 and C_3H_6 to CO_2 using C_3H_6 as a reductant

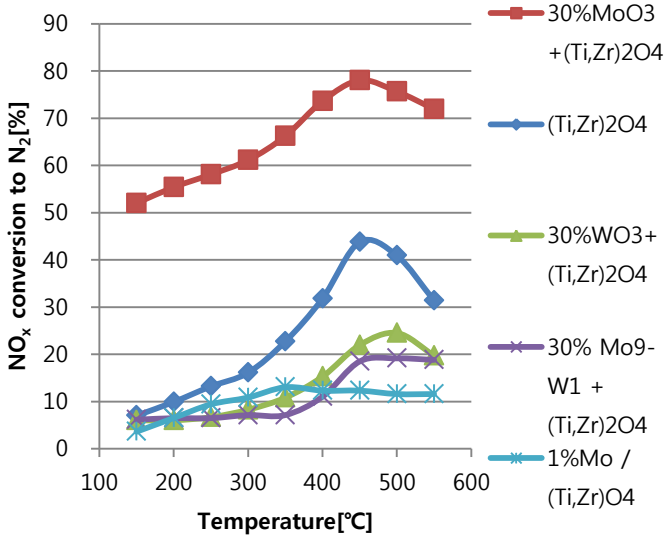

Fig.5 Catalytic activity of various kind of Mo, W MM $(Ti,Zr)_2O_4$ catalyst for the conversion of NO_x to NO_2 and C_3H_6 to CO_2 using C_3H_6 as a reductant

This time, 30%MoO_3+$(Ti,Zr)_2O_4$ catalyst showed highest catalytic activity than other metal supported $(Ti,Zr)_2O_4$ combined catalyst. Fig.5 gives us an overview of catalytic activity changes and comparison of each catalysts conversion property. WO_3 shifted bare $(Ti,Zr)_2O_4$ catalysts' optimal temperature to a higher value. There was no synergetic effect from Mo with W in which the result of $(Mo,W)_xO_y$+$(Ti,Zr)_2O_4$ catalyst showed lower NO_x reducing ability than MoO_3+$(Ti,Zr)_2O_4$ and WO_3+$(Ti,Zr)_2O_4$.

It was reported by Ch. Fountzoula et al.[3] that addition of MoO_3 to bare catalysts improves its mechanical strength through chemical and structural promotion which enlarges the temperature window of the SCR reaction. The synergistic effects could also be observed in the result of this study by comparing MoO_3 and $(Ti,Zr)_2O_4$.

3.2 Catalyst Characterization

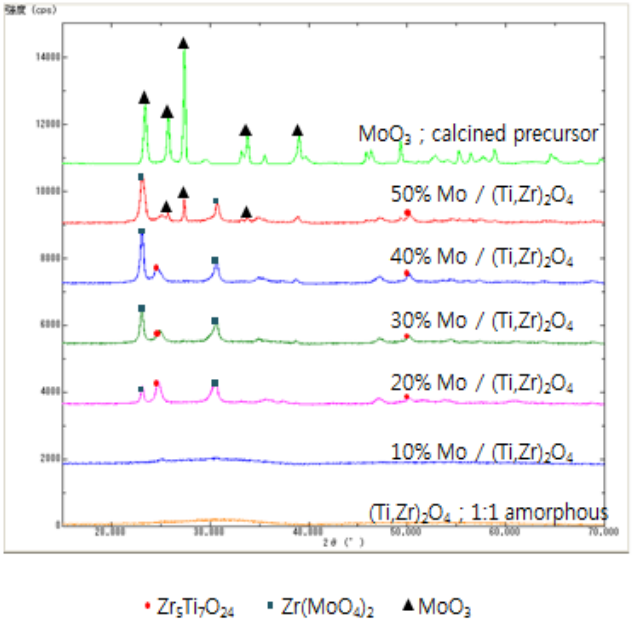

Fig.6 XRD patterns of Mo supported $(Ti,Zr)_2O_4$ catalyst prepared by IM method.

Fig.6 showed that formation of binary-type oxides such as $Zr_5Ti_7O_{24}$ and $Zr(MoO_4)_2$ on the surface deactivated the NO_x reduction performance.

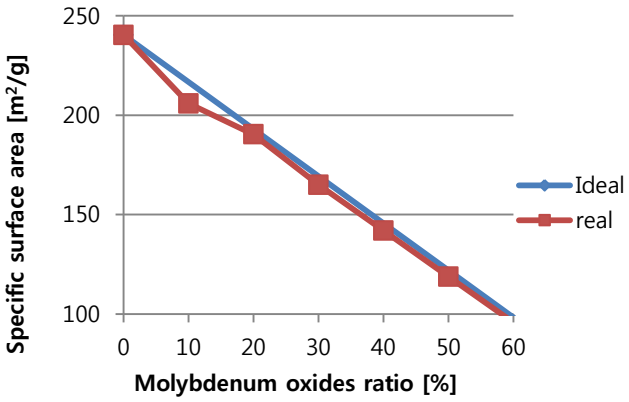

Fig.7 BET results of MoO_3+$(Ti,Zr)_2O_4$ catalyst prepared by MM method.

From the specific surface area (SSA) of bare MoO_3 and $(Ti,Zr)_2O_4$, the SSA of catalysts prepared by MM method can be calculated. It was based on the ratio of each constituents (Ideal value). But as shown in Fig.7, the real value of SSA showed lower value compared to calculated value of SSA. It was thought that MoO_3 particles enter the pores of $(Ti,Zr)_2O_4$, thus the actual SSA value was lower than the calculated one.

3.3 The Effect of Water Vapor

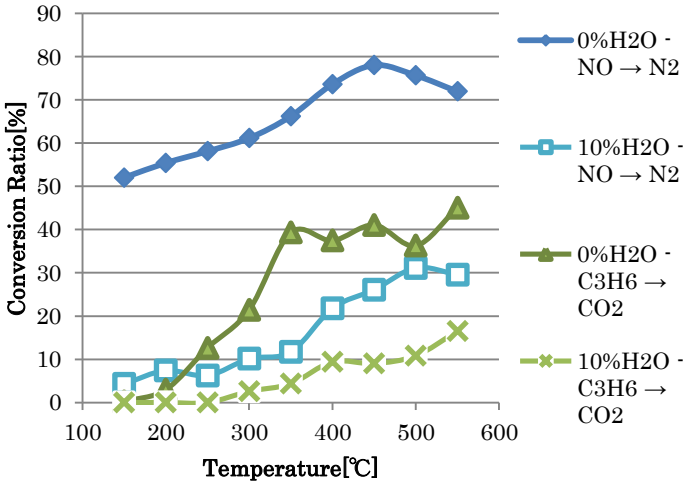

Fig.8 The effect of Water vapor to the NO_x reduction and C_3H_6 oxidation performance of 30%MoO_3+$(Ti,Zr)_2O_4$ catalyst

Fig.8 showed the influence of water vapor to the performance of the catalyst. The presence of water vapor makes not only lower the reduction of NO to N_2, but also lower the oxidation of C_3H_6 to CO_2.

3.4 The Reusability of the Catalyst

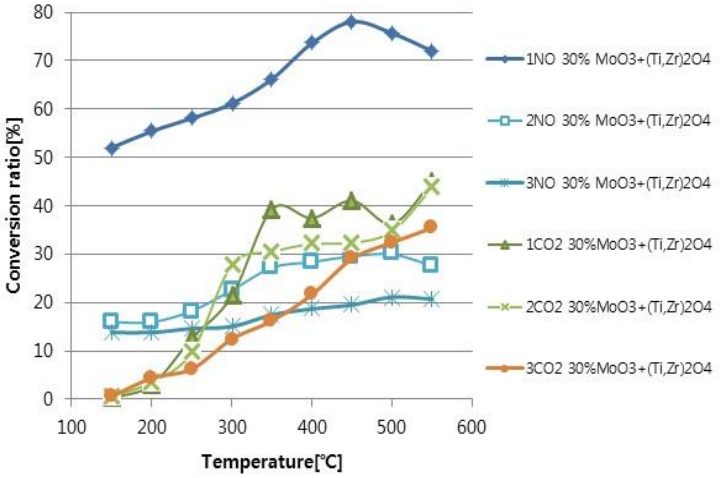

Fig.9 Comparison of NO reduction and C_3H_6 oxidation activity of catalyst at first, second, third time usage

The comparison of activity of catalyst during the first time, second time and third time usage is shown in Fig.9. The NO reduction performance decreased with the number of use, and C_3H_6 oxidation also shown the same pattern. However, at 500℃, despite the decrease in NO reduction performance, C_3H_6 oxidation performance not changed. It was thought that for repetitive usage, the NO reduction mechanism via NO_2 become weaker, thus, the decrease in NO conversion did not followed by decrease in C_3H_6 conversion.

4 Conclusions

The catalyst prepared MM method MoO_3+$(Ti,Zr)_2O_4$ catalyst showed catalytic activity towards selective catalytic reduction of NO to N_2 with C_3H_6 as reducing agent. Compared to the IM method, catalyst prepared by MM method exhibited higher catalytic activity. The catalysts prepared by MM method showed optimum ratio of Mo addition at 30%. It is possible that MoO_3 high oxidation ability improved the catalytic activity of MoO_3+$(Ti,Zr)_2O_4$ as suggested by previous study. Manually mixed WO_3 or $(Mo,W)_xO_y$ with $(Ti,Zr)_2O_4$ catalyst showed catalytic activity loss compared to the bare $(Ti,Zr)_2O_4$ because of its formation of binary-type oxides on the catalyst surface.

References

[1] Norio Arai Techno-System Corp (1997)
[2] R.Burch et al, Appl.Catal.B, 11, (1997) 207
[3] Ch.Fountzoula et al, Appl, Catal. B, 35, 295 (2002)
[4] P.Forzati et al, Catal. Today, 62 (2000) 51
[5] M.Haneda et al, Catal. Today, 42, 127-135 (1998)
[6] B.M.Reddy et al, Appl. Catal. A, 228 (2002) 269-278
[7] J.Mitadera, Master Thesis, Tokyo Institute of Technology (2003)
[8] H.Kawai, Master Thesis, Tokyo Institute of Technology (2004)
[9] M.Makii, Master Thesis, Tokyo Institute of Technology (2008)

Wastewater Treatment by Adsorption with Activated Carbon from Wood Residues in Rubberwood Sawmilling Process

Student Number: 12M18169 Name: Xiao HAN Supervisor: Ryuichi EGASHIRA

ゴム木材製材プロセスにおける残材由来活性炭を用いた吸着による排水処理

韓 笑

東南アジアのゴム木材製材プロセスの改善ために、残材の熱処理生成物である木酢液を木材の防腐剤, 活性炭を防腐剤の排水を処理するための吸着剤として利用する新たなプロセスに対し、使用済み活性炭の処理について検討した。ゴム木材おが屑を熱処理して得られた活性炭及び使用済み活性炭を熱再生して得られた再生活性炭のキャラクタリゼーション及びフェノールとクレゾールを含むモデル排水に対する回分式吸着実験を行った。再生活性炭の吸着性能は未使用活性炭よりも低い吸着性能であった。使用済み活性炭の処理を考慮した製材プロセスのシミュレーション計算を行い, 必要なおが屑の量が実現可能な範囲内にあることを示した。

1. Introduction

In Southeast Asian countries, rubberwood furniture manufacturing is an important industry. The current sawmilling process includes the process shown by black boxes in **Fig.1**. Rubberwood logs are cut, preserved and dried, then molded into products. Two major problems were reported in the existing process; the utilization of toxic preservatives, and large amount of wood residues [2]. The preservatives contain the harmful compounds such as boric acid and mixture of borax pentahydrate and the workers are exposed to these harmful compounds. In addition, the waste water, containing the preservatives, is discharged without any treatment, which causes soil and water pollutions.

To solve these problems, the utilization of the products from thermal treatment of wood residues (WR) was proposed. The proposed process is shown in **Fig.1**. It was suggested that the wood residues were thermally treated to produce pyroligneous acid (PA), activated carbon (AC), and off-gas, and these products were effectively utilized in the process [1][2]. Pyroligneous acid was characterized to contain the components effective for preservations, and it can be used as preservative agent instead of the current purchased preservative agent. However some of the chemical components in pyroligneous acid are necessary to be removed from the wastewater of the preservation. So, the wastewater is treated by the prepared activated carbon to meet the regulation of the wastewater. After treatment of the wastewater, the spent activated carbon (SAC) should be obtained and the treatment of it has not been discussed in previous studies.

In this work, the waste water treatment using activated carbon was studied, in which the treatment of the spent activated carbon was incorporated in the process. The virgin activated carbon (VAC) was obtained by thermal treatment of WR sawdust, and spent activated carbon was prepared by adsorption of phenol with virgin activated carbon. Thermal regeneration of spent activated carbon was carried out to obtain the regenerated activated carbon (RAC). The adsorption of phenol and p-cresol in the aqueous solution by virgin activated carbon and regenerated activated carbon were conducted to measure the change in the adsorption capability. Then the process incorporating the treatment of spent activated carbon was evaluated based on the material and heat balances.

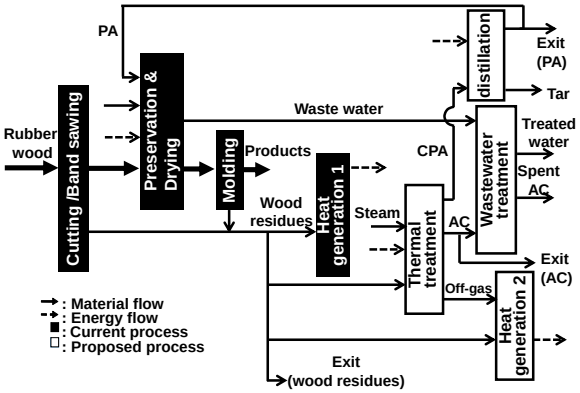

Fig. 1 Current and proposed process of sawmilling: material and heat flows

2. Activated Carbon from Wood Residues

2.1 Experimental

Wood residue, obtained from Malaysia, was thermally treated under steam atmosphere by the thermal treatment equipment, as shown in **Fig. 2** [3], to obtain the virgin activated carbon. Virgin activated carbon was treated by adsorption with phenol

aqueous solution to obtain spent activated carbon. Next, thermal regeneration of spent activated carbon was carried out using the same equipment shown in **Fig. 2** to prepare regenerated activated carbon under N_2 atmosphere. Thermal regeneration was chosen in this study because it was a commonly used regeneration method. **Table 1** and **2** show the principal conditions of thermal treatment and regeneration.

Experiments were also conducted to examine the characterization of the activated carbons. Scanning electron microscope (SEM) was used to observe the appearance of the activated carbon surface. The elemental analysis was conducted to measure the composition of the activated carbons. The specific surface area was measured by a surface area measuring instrument.

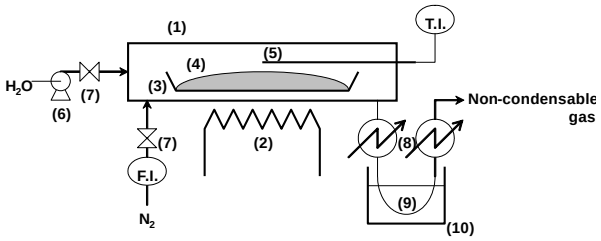

Fig. 2 Schematic diagram of thermal treatment apparatus: (1) tubular reactor; (2) electric tubular furnace; (3) sample holder; (4) feed/solid product; (5) NiCr-Constantan thermocouple; (6) micro-plunger pump; (7) valves; (8) condensers; (9) liquid product trap; (10) iced bath (275~277 K); F.I. flow indicator; T.I. temperature indicator

Table 1 Principal conditions for thermal treatment of wood residues

Feed	WR
Mass of feed [g]	30.0 ± 1.0
Atmosphere	N_2, H_2O
Flow rate of atmospheric gas [$m^3 \cdot h^{-1}$]	<473 K 0.003 (N_2) >473K0.0012(N_2), .003(H_2O)
Temperature [K]	873
Holding time [h]	1

Table 2 Principal conditions for thermal treatment of SAC

Feed	SAC
Mass of feed [g]	12.0 ± 1.0
Atmosphere	N_2
Flow rate of atmospheric gas [$m^3 \cdot h^{-1}$]	<473 K 0.003 (N_2)
Temperature [K]	1223
Holding time [h]	0

2.2 Results and Discussion

Thermal treatment of wood residues produced crude pyroligneous acid, virgin activated carbon and off-gas. The colour of crude pyroligneous acid was dark brown and water content was about 80%. It was because it contained a lot of tar components. All wood residues were evenly treated to virgin activated carbon. Virgin activated carbon was black in color and lighter in mass if compared with feed wood residues. Off-gas was non-coloured gas with a bad smell. Mass of obtained virgin activated carbon, crude pyroligneous acid, and off-gas were about 21%, 35% and 44% of the feed sawdust, respectively. Mass of off-gas was derived based on material balance.

From the SEM pictures of virgin activated carbon and regenerated activated carbon, it was found that particle size of the regenerated activated carbon was smaller than that of the virgin activated carbon. The results of elemental analysis were showed in **Table 3**. The content of oxygen could not be measured this time because too much ash content in them. In the case of activated carbon made from plants, it usually had a low content in sulphur and nitrogen [4]. The results of this experiment agreed with this trend. Specific surface area of virgin activated carbon, spent activated carbon and regenerated activated carbon were 582.54, 42.91, 271.19 m^2/g, respectively. After adsorption of phenol, the surface area of virgin activated carbon was obviously reduced. The possible reason was that phenol might occupy the pores of the activated carbon.

Table 3 Element analysis of RW, AC and RAC

Element	[wt%]		
	RW	AC	RAC
C	45.8	87.27	92.5
O	44.77	-	-
H	5.61	1.72	0.39
N	0.19	0.4	0.47
Ash	0.7	3.9	2.7

3. Batch adsorption of Model Wastewater by Activated carbon from Wood Residues

3.1 Experimental

In this study, in order to compare the adsorption performance of virgin activated carbon and regenerated activated carbon, phenol or p-cresol solution was chosen as the model wastewater, because they were typical harmful substances of the pyroligneous acid. Activated carbon was washed, dried, ground and sieved before adsorption experiments to equalize the properties of it. The batch adsorption experiment was conducted using a vessel with magnetic stirrer. Contacting time was decided as 120 hours according to pervious study [3].

After reaching adsorption equilibrium, the sample solutions were analyzed by gas chromatograph (GC-2010 with FID, Shimadzu Co., Ltd.) to determine the concentration of the solution. The experimental conditions are shown in **Table 4**.

Table 4 Principal conditions for adsorption with stirring vessel

Feed solution	Aqueous solution of phenol Aqueous solution of p-cresol
Volume of feed solution [m^3]	250×10^{-6}
Concentration of phenol in feed solution,, C_0 [$g \cdot m^{-3}$]	540
Adsorbent	AC
Particle radius AC, d_p [μm]	0.15-0.35
Concentration of adsorbent, C_{AC} [$g \cdot m^{-3}$]	30000
Stirring speed [rpm]	500
Contacting time [h]	120
Contacting temperature [K]	303

3.2 Results and Discussion

The mass balance relation in the adsorption experiments can be expressed as,

$$L_0 C_0 = L_0 C_1 + S_0 q_1$$

L_0, C_0 , C_1 , S_0 , and q_1 are the volume of feed solution [m^3], feed concentration [g/m^3], concentration of the solution after equilibrium [g/m^3], mass of the activated carbon [g], and amount of adsorbate on activated carbon [g/g-activated carbon], respectively. The adsorption amount of each sample was calculated by this equation.

Langmuir equation expressed blow was used to find saturated amount of adsorption:

$$q* = \frac{C_e q* K_L}{1 + C_e K_L}$$

C_e, q,q* ,K_L are concentration of the solution after equilibrium [g/m^3], adsorption amount for 1g adsorbent [g/g-activated carbon], the saturated amount of adsorption for 1g adsorbent, and Langmuir equilibria constant, respectively.

Based on the adsorption results, adsorption isotherms of phenol with virgin activated carbon and regenerated activated carbon are shown in **Fig. 3**, and those of p-cresol are shown in **Fig. 4**. The lines show adsorption isotherm calculated, and the plots show the experimental data. In this study, more than 80% of model harmful substance was adsorbed by virgin activated carbon, and adsorption isotherm could be described by Langmuir equation.

The saturated amount of adsorption is shown in **Table 5**. Adsorption amount of phenol and p-cresol were almost the same. The adsorption amount of regenerated activated carbon was about 10% of virgin activated carbon.

From the results mentioned above, we propose to treat spent activated carbon as energy source, because the efficiency of regenerating it is not very good.

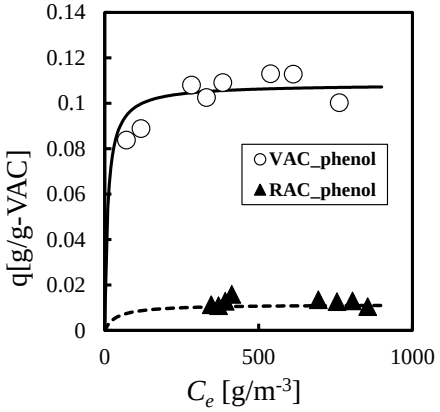

Fig.3 Adsorption isotherm for phenol by VAC and RAC

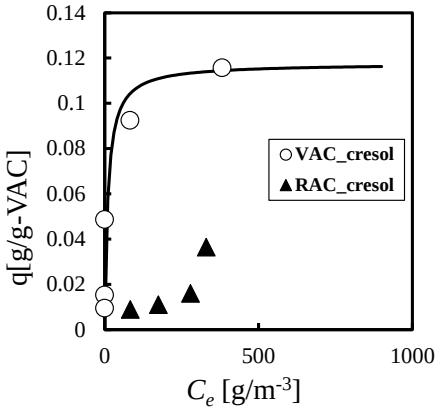

Fig. 4 Adsorption isotherm for p-cresol by VAC and RAC

Table 5 Saturated amount of adsorption

	VAC	RAC
$q*_{phe}$[g/g-AC]	0.10838	0.01147
$q*_{cre}$[g/g-AC]	0.12423	-

4. Improvement of Rubberwood Sawmilling Process

4.1 Overview of the process

In this study, the simulation calculation was based on the assumption that all the spent activated carbon is used as energy source in heat generation2 process. In heat generation2, off-gas and spent activated carbon will be used preferentially, then wood residues will be used. The rest of wood residues will get out of the system. Residue ratio $\alpha_{wr,Th}$ means the ratio of wood residues using for thermal treatment to total wood residues. Possible range of $\alpha_{wr,Th}$ was calculated from material balance and heat balance of the proposed process.

4.2 Calculation

In this study, toxic component in wastewater was assumed to be only phenolic components. The concentration of phenolic components in waste water was considered, because adsorption of unfavorable substance in wastewater was affected by not only activated carbon adsorption performance, but also the concentration of the substance. Since previous study reported that there were 2.7% of phenolic components existed in pyroligneous acid [1]. The concentration of that in wastewater could be calculated as 499ppm. The standard concentration of wastewater in Malaysia is 1ppm [1]. By using the data mentioned above, activated carbon amount in wastewater treatment process could be calculated.

Flow rate of feed rubberwood was supposed to be 1000 ton of a year.

The yield and other characteristics of products were based on experimental results of this study and previous study [3].

4.3 Results and Discussion

$F_{Wr,Exit}$ means the flow rate of wood residues which get out of the system, and the change of it is shown in **Fig.6**. In this figure, if $F_{Wr,Exit}$ become minus, it means the necessary heat for the whole process can't be covered by using the products from thermal treatment of wood residues. Maximum residue ratio could be calculated from this figure as 0.53. In this case, no wood residue is left, 749 ton/year excess amount of pyroligneous acid and 102 ton/year excess amount of activated carbon could be obtained.

If excess amount of pyroligneous acid is 0, namely, the amount of pyroligneous acid produced equal to the amount of pyroligneous acid required. In this case, activated carbon produced couldn't cover the requirement.

If excess amount of activated carbon is 0, namely, the amount of activated carbon produced equal to the amount of activated carbon required. In this case, 32 ton/year excess pyroligneous acid could be obtained, and 772 ton/year wood residues will be left. Minimum residue ratio could be calculated as 0.044 in this case.

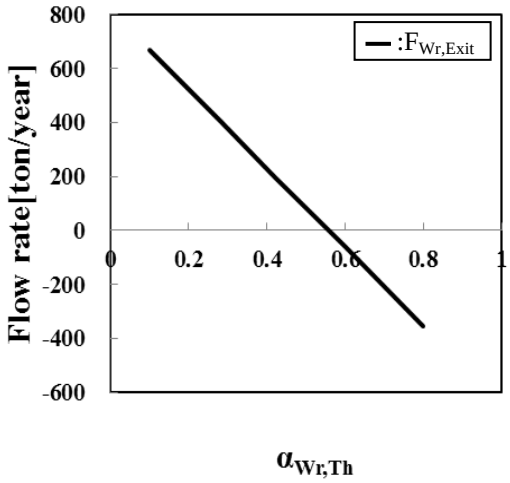

Fig. 6 Flow rate change of exited wood residues

5. Conclusion

Model harmful substance could be removed by activated carbon made from wood residues.

The adsorption isotherm results showed that the adsorption amount of regenerated activated carbon was about 1/10 of that of virgin activated carbon. Therefore, it is concluded that regenerated activated carbon didn't have sufficient adsorption capacity compare to virgin activated carbon. So spent activated carbon was proposed to be used as energy source.

Based on the experimental data obtained from this study, the possible range of residue ratio$\alpha_{wr,Th}$ was calculated. In some cases, excess amount of pyroligneous acid and activated carbon could be obtained. The process was proposed to solve the environment problems in rubberwood sawmilling process.

References

[1] Rizafizah OTHAMAN, Kean Giap LIM, Shunsuke KONISHI, Masayuki SATO, Nan SHI and Ryuichi EGASHIRA, "Thermal Treatment of Wood Residues and Effective Utilization of Its Products to Improve Rubberwood Manufacturing Process," Journal of Chemical Engineering of Japan, pp. 1149–1158 (2008)

[2] Rizafizah Binti Othaman, Doctor Thesis, Tokyo Institute of Technology (2009)

[3] Mitani Saori, Master Thesis, Tokyo Institute of Technology (2011)

[4] 真田雄三・鈴木基之・藤元薫；活性炭　基礎と応用，講談社サイエンティフィック（2007）

Recycling of valuable metals by solvent extraction using carboxylic acid as extractant

Student number: 12M18100 Name: Kazuma NAKAMURA Supervisor: Ryuichi EGASHIRA

カルボン酸抽出剤を用いた溶媒抽出法による有価金属のリサイクル

中村 数馬

安価であり分子中にリンを含まないことで廃溶媒の焼却処分が可能なカルボン酸の一種であるネオデカン酸を抽出剤として，希土類磁石構成金属元素であるジスプロシウム，ネオジム，コバルト，および鉄の回分平衡抽出を行った．他の金属と比較して鉄の分配比は著しく高く容易に除去でき，この性能は現在工業的に利用されている有機リン酸系抽出剤の場合に比較して高かった．また，有機溶媒相からの金属の逆抽出に利用する酸の量を低減できた．最後に，希土類磁石リサイクルにおけるカルボン酸抽出剤の利用を提案した．

1. INTRODUCTION

Recovery of valuable metals such as rare metals is greatly attracted because of increasing their demands and escalating their prices. But recycling them is difficult and costly. Therefore, large number of research activities has been reported to improve the recycling technology [1] [2]. The recovery of valuable metals from Nd-Fe-B magnets scrap is a representative example, and the solvent extraction with acidic organophosphorous ester as extractant has been intensively studied. **Table1** shows the typical composition of Nd-Fe-B magnets[3]. Acidic organophosphorous ester, such as PC-88A and D2EHPA are most popular extractants in the industrial application and they have high selectivity between rare earth metals, but they cause waste water pollution because they has phosphor in their structure. Moreover, due to their strong affinity with major impurity, Fe^{3+}, the recovery of Fe^{3+} from the loaded organic solution should require large amount of acids.

In this study, the recovery of valuable metals in Nd-Fe-B magnet was studied by the solvent extraction with carboxylic acid as extractant. Carboxylic acid can be incinerated, and stripping of Fe^{3+} was easier than that with organophosphorous ester extractants[1]. Fe^{3+}, Dy^{3+}, Nd^{3+} and Co^{2+} were selected as representative elements in the magnet to investigate the solvent extraction with neo-decanoic acid, one of carboxylic acid. The extraction equilibria of single and binary metal solutions were measured to study the effects of the experimental conditions on the extraction and stripping behaviors for the purpose to make the valuable metal recycle process from Nd-Fe-B magnet scrap by using carboxylic acid as extractant.

Table1 Typical composition of Nd-Fe-B magnets

	Fe	B	Co	Cu	Rare earth			
					Nd	Dy	Pr	Tb
ave[wt%]	66	1	2	0	23	5	3	0
					31			
max	69.6	1.11	3.66	0.23	27.6	7.67	6.48	1.61
min	61.6	0.95	0.54	0.11	18.6	2.97	0.26	0

2. EXPERIMENTAL

The experimental conditions of extraction equilibrium are shown in **Table 2**. Neo-decanoic and naphthenic acids are mixtures of carboxylic acids. PC-88A (2-ethylhexyl phosphonic acid mono-2-ethylhexyl ester) and D2EHPA (Bis(2-ethylhexyl) phosphoric acid) are acidic organophosphorous ester extractants. Kerosene was used as the diluent of the extractant. The aqueous solutions of the metals were prepared by dissolution of metal chloride in deionized water. The *p*H in the aqueous phase was adjusted by NaOH and HCl. The experimental condition of stripping equilibrium is shown in **Table 3**. The feed organic phases of 10vol% extractant loaded by single metal ion were prepared by extracting the metal from the aqueous solution. HCl or HNO_3 was used as stripping reagent.

All experiments were carried out in a 50mL conical flask with screw top. Equal volumes (10mL) of aqueous and organic solutions were stirred with thermostatic bath for 3hours at 303K to attain the equilibrium. After equilibrium, these two phases were separated by separating funnel. The *p*H value in the aqueous phase was measured by digital *p*H meter (F-52, HORIBA). The concentration of metal in aqueous phase was determined using ICP-AES (SPS7800, SII Nano Technology), and that in organic phase was calculated by material balance.

Table2 Experimental conditions of batch extraction equilibrium

Solute	M^{n+}(Fe^{3+},Dy^{3+},Nd^{3+},Co^{2+})chloride
Extractant	Neo-decanoic, naphthenic (NA) PC-88A, D2EHPA
Diluent	kerosene
Initial metal concentration in aqueous phase ,$C_{i,aq,0}$[kmol･m^{-3}]: 0.001	
Extractant concentration in organic phase [vol%]: 10~30	

Table3 Experimental conditions of stripping experiment

Solute	M^{n+}(Fe^{3+},Dy^{3+},Nd^{3+}, Co^{2+})chloride
Extractant	Neo-decanoic acid, PC-88A
Stripping agent	HCl, HNO_3
Initial metal concentration in organic phase,$C_{i,org,2}$[kmol･m^{-3}]: 0.001	
Initial extractant concentration in organic phase [vol%]: 10	
Initial concentration of stripping agent,$C_{HCl,aq,2}$ or$C_{HNO3,aq,2}$ [kmol･m^{-3}]: 0.01~7	

3. RESULTS AND DISSCUSSTION

3.1. Solvent extraction with various extractant

The material balance equations for extraction and stripping equilibrium measurements can be expressed as,

$C_{i,aq,0}V_{aq}+C_{i,org,0}V_{org} = C_{i,aq,1}V_{aq}+C_{i,org,1}V_{org}$

$C_{i,aq,2}V_{aq}+C_{i,org,2}V_{org} = C_{i,aq,3}V_{aq}+C_{i,org,3}V_{org}$

The distribution ratio, extraction yield, and stripping yield of component *i*, were defined respectively as,

$$\boldsymbol{D_i} = \frac{C_{i,org}}{C_{i,aq}} \quad \text{Eq(1)}$$

$$\boldsymbol{E_i} = \frac{C_{i,org,1}V_{org}}{C_{i,aq,0}V_{aq}} \quad \text{Eq(2)}$$

$$\boldsymbol{Y_i} = \frac{C_{i,aq,3}V_{aq}}{C_{i,org,2}V_{org}} \quad \text{Eq(3)}$$

$C_{i,org,1}$ and $C_{i,org,3}$ were calculated with an assumption that the volumes of aqueous and organic phases were constant before and after the experiment.

The separation factor of component *i* relative to component *j*, $\beta_{i,j}$ was defined as,

$$\boldsymbol{\beta_{i,j}} = \frac{D_i}{D_j} \quad \text{Eq(4)}$$

The half extraction *p*H values ($pH_{1/2}$) for the extraction with single metal solutions with various extractant are listed in **Table 4**. The $pH_{1/2}$ was defined as the *p*H value at D_i=1. Neo-decanoic acid could preferably extract Fe^{3+} in the range of high acidity relative to other metal ions, such as Dy^{3+}, Nd^{3+} and Co^{2+}. PC-88A showed the better performance to separate Dy^{3+} and Nd^{3+}.

Table4 List of $pH_{1/2}$ with each extractant (10vol%) on extraction of Fe^{3+}, Dy^{3+}, Nd^{3+}, Co^{2+}.

	Neo-decanoic	NA	PC-88A	D2EHPA
Fe^{3+}	2.36	2.21	-0.15	-0.48
Dy^{3+}	4.64	4.47	0.54	0.09
Nd^{3+}	5.01	4.89	1.29	0.60
Co^{2+}	6.39	6.21	3.37	2.79

3.2. Extraction equilibrium with neo-decanoic acid

As reported in previous paper [4], extraction equilibrium with carboxylic acid can be represented by Eq(5).

$$x_i M_i^{n_i+} + \frac{1}{2}(n_i + m_i)\overline{(RH)_2} \rightleftharpoons \overline{(M_i R_{ni} \cdot m_i RH)_{xi}} + n_i x_i H^+ \quad \text{Eq(5)}$$

where x_i, m_i, and n_i stand for polymerization number of extracted species, solvation number of extractant to extracted species, valence of metal, respectively. The extractants were assumed to exist as dimmer in the organic solution. The extraction equilibrium constant can be expressed as,

$$K_{ex,i} = \frac{\left[\left(M_i R_{n_i} \cdot m_i RH\right)_{x_i}\right][H^+]^{n_i x_i}}{[M_i^{n_i+}]^{x_i}[(RH)_2]^{\frac{(n_i+m_i)}{2}}} \quad \text{Eq(6)}$$

Eq. (6) can be written as,

$$\log C_{i,org,1} = x_i(\log C_{i,aq,1} + n_i pH) + \log\left(x_i K_{ex,i,1}\right) + \frac{(n_i+m_i)}{2}\log C_{RH,org,1} \quad \text{Eq(7)}$$

In this experiment, the concentrations of metal were much lower than that of extractant, $C_{RH,org}$ were assumed to be a constant. The $\log C_{i,org}$ was plotted against ($\log C_{i,aq}+n_i pH$) in **Fig. 1(a)**, and x_i was decided as unity. However, the plot of Fe^{3+}, Dy^{3+} and Nd^{3+} results didn't follow the slope in high acidity region. Different reaction might occur and the extraction was enhanced in this region. When x_i=1, Eq(7) can be written as,

$$\log D_i - n_i pH = \frac{n_i+m_i}{2}\log C_{RH,org} + \log K_{ex,i} \quad \text{Eq(8)}$$

The m_i and $K_{ex,i}$ could be obtained from the slope and intercept of the plots of $\log D_i$-$n_i pH$ against $\log C_{RH,org}$, (**Fig.1. (b)**) and they are listed in **Table 5**.

Eq(4) can be rewrite using $K_{ex,i}$ as,

$$\beta_{i,j} = \frac{K_{ex,i}}{K_{ex,j}} \times \left(C_{RH,org,1}\right)^{\frac{1}{2}(n_i-n_j)} \times \left(C_{H,aq,1}\right)^{(n_j-n_i)} \quad \text{Eq(9)}$$

Separation factor can be obtain by substitute $K_{ex,i}$ and n_i,n_j.

$$\beta_{Fe,Dy} = \frac{K_{ex,Fe}}{K_{ex,Dy}} = 5.10 \times 10^7$$

$$\beta_{Dy,Nd} = \frac{K_{ex,Dy}}{K_{ex,Nd}} = 7.24$$

$$\beta_{Nd,Co} = \frac{K_{ex,Nd}}{K_{ex,Co}} \times (C_{RH,org,1})^{\frac{1}{2}} \times (C_{H,aq,1})^{-1}$$

$= 2.25\times10^6$ (obtained by substitute $C_{RH,org}$=0.32, *p*H=5)

The separation factor of Fe^{3+} to Dy^{3+}, and that of Nd^{3+} to Co^{2+} were enough large to be possible to separate each other. Dy^{3+} and Nd^{3+} can be separated by using multistage extraction system.

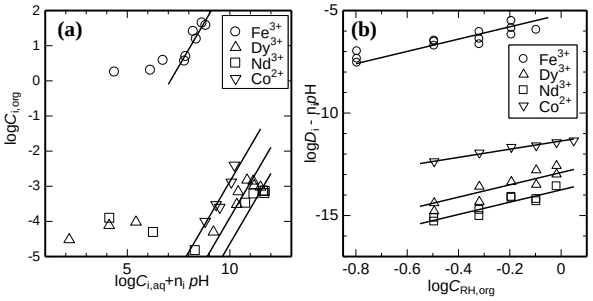

Fig.1 Extraction of Fe^{3+}, Dy^{3+}, Nd^{3+} and Co^{2+} with neo-decanoic acid as extractant

Table5. Composition of extracted species and obtained $K_{ex,i}$

i	Extracted species	$K_{ex,i}$
Fe^{3+}	$FeR_3\cdot3RH$	6.43×10^{-6}
Dy^{3+}	$DyR_3\cdot3RH$	1.26×10^{-13}
Nd^{3+}	$NdR_3\cdot3RH$	1.74×10^{-14}
Co^{2+}	$CoR_2\cdot2RH$	4.37×10^{-12}

3.3. Extraction of binary metal solution with neo-decanoic acid

Extraction of binary metal solution in some representative systems, such as (i) Fe^{3+} and Dy^{3+}, (ii) Fe^{3+} and Co^{2+}, (iii) Dy^{3+} and Nd^{3+}, (iv) Dy^{3+} and Co^{2+} were carried out to investigate the effect of coexistence metal on extraction equilibrium.

F.M.Doyle et.al.[5] reported that extraction of some metal ions(Ni^{2+}, Zn^{2+}, Cu^{2+} etc) increased with Fe^{3+} extraction in sulfuric acid solution at high acidity re-

gion when neo-decanoic acid was used as extractant.

Figures 2~5 show the effects of the acidity on the extraction yield and distribution ratio of metals. White and black plots represent the extraction results with single metal solution, and binary solution, respectively. Distribution of Co^{2+} increased with distribution of Fe^{3+} and Dy^{3+} in high acidity region and separation efficiency was reduced. It means that Co^{2+} is co-extracted with other metal such as Fe^{3+}, Dy^{3+}, and Nd^{3+}.

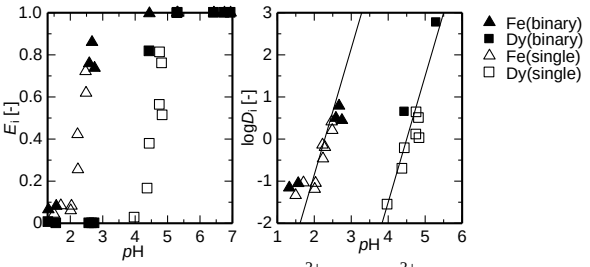

Fig. 2 Extraction behavior of Fe^{3+} and Dy^{3+} from binary or single metal solution by using neo-decanoic acid

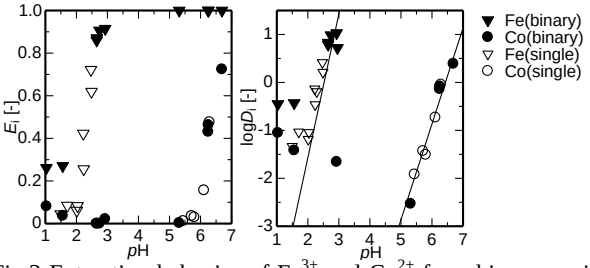

Fig.3 Extraction behavior of Fe^{3+} and Co^{2+} from binary or single metal solution by using neo-decanoic acid

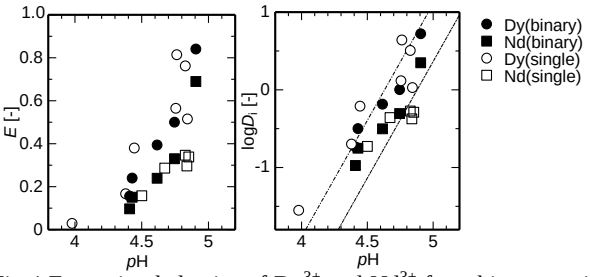

Fig.4 Extraction behavior of Dy^{3+} and Nd^{3+} from binary or single metal solution by using neo-decanoic acid

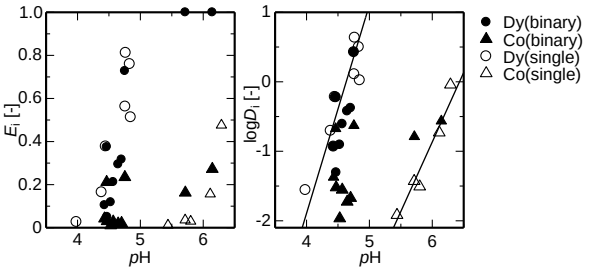

Fig.5. Extraction behavior of Dy^{3+} and Co^{2+} from binary or single metal solution by using neo-decanoic acid.

3.4. Stripping

Figures 6~8 show the effect of acid concentration on the stripping yields with neo-decanoic acid and PC-88A. The stripping yield of Fe^{3+} and Dy^{3+} from neo-decanoic acid solution was larger than that from PC-88A solution. The yields of Co^{2+} were same between neo-decanoic acid and PC-88A. It means that stripping from neo-decanoic acid solution was easier than that from PC-88A. Stripping of Fe^{3+} from PC-88A solution required higher acidity solution. However higher acidity solution should degrade the quality of organic solution and corrosion-resistance equipment should be necessary.

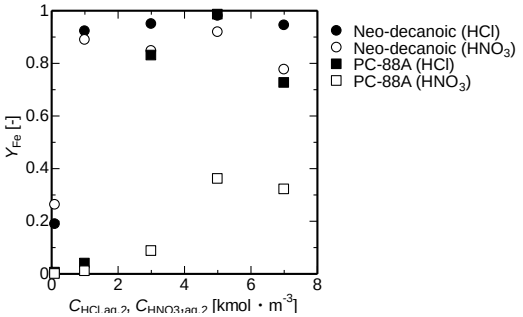

Fig.6 The effect of acid concentration on striping yield of Fe^{3+} Stripping reagent: HCl, HNO_3

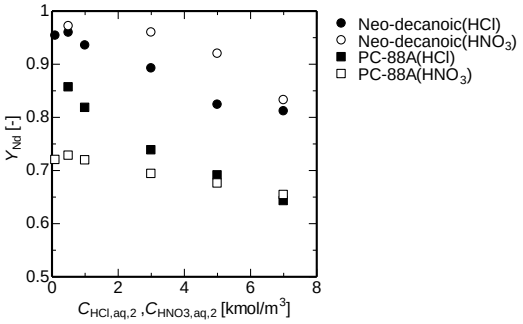

Fig.7 The effect of acid concentration on striping yield of Dy^{3+}. Stripping reagent: HCl, HNO_3

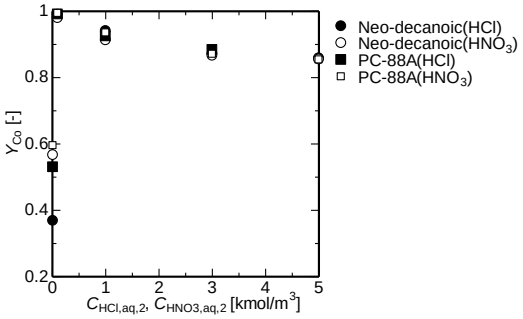

Fig.8 The effect of acid concentration on striping yield of Co^{2+}. Stripping reagent: HCl, HNO_3

3.5. Separation process

From the experimental results, we made a proposal of the separation process of Fe^{3+}, Dy^{3+}, Nd^{3+} and Co^{2+} from Nd-Fe-B magnets by using neo-decanoic acid as extractant, as shown in **Figure 9**. This separation process was proposed by the following rules; (i) to use low amount of NaOH or HCl to adjust the *p*H, (ii) to use relatively weak acid to strip the metal from organic phase, (iii) to remove major impurity, Fe^{3+}, first, (iv) to separate Dy^{3+} and Nd^{3+} in the last stage because it's

the most difficult in this process, (v) to consider the effects of co-extraction of Co^{2+} with Fe^{3+}.

After leaching the magnet scrap with 0.1~1.0M HCl, the major impurity, Fe^{3+}, and Co^{2+} are removed at pH2~2.5. Co^{2+} is co-extracted with Fe^{3+}. After stripping them, NaOH are added to the aqueous solution and $Fe(OH)_3$ are precipitated and Co^{2+} remain in the aqueous solution. Dy^{3+} and Nd^{3+} are separated by solvent extraction at pH5~5.5. Dy can be recovered from organic phase by stripping with 0.1M HCl.

4. CONCLUSIOIN

・ Using neo-decanoic acid as extractant could remove Fe^{3+} from other valuable metals (Dy^{3+}, Nd^{3+}, Co^{2+}) easier than using PC-88A.

・ Separation factor between Dy^{3+} and Nd^{3+} was enough for separation.

・ Stripping from metal loaded organic solution of neo-decanoic acid using hydrochloric acid or nitric acid was easy and it will suppress the decreasing of quality of organic solution.

・ Co^{2+} was co-extracted with other metals.

・ From the above, we made proposal of the separation process of valuable metals from Nd-Fe-B magnet using neo-decanoic acid as extractant.

Acknowledgement

PC-88A was supplied by Daihachi chemical industry corporation.

Nomenclatures

C_i	Concentration of i	[kmol・m^{-3}]
$K_{ex,i}$	Extraction equilibrium constant of i	[-]
D_i	Distribution ratio of i	[-]
E_i	Extraction yield of i	[-]
Y_i	Stripping yield of i	[-]
β	Separation factor	[-]
V	Volume	[m^3]
t	time	[min]
T	Temperature	[K]
x_i	Polymerization degree of extract species of i	
n_i	Valence of i	
m_i	Solvation number of extract species of i	

<Subscript>

0	at initial state of batch extraction experiment
1	equilibrium state of batch extraction experiment
2	at initial state of stripping experiment
3	equilibrium state of stripping experiment
aq	Aqueous phase
org	Organic phase
RH	Extractant
Fe	Fe^{3+}
Dy	Dy^{3+}
Nd	Nd^{3+}
Co	Co^{2+}
H	Hydroxide
HCl	Hydrochloric acid
HNO3	Nitric acid
NaCl	sodium chloride
i	Solute i
j	Solute j

References

[1] 小山和也，田中幹也; レアアースの最新技術動向と資源戦略，第三章，2(工場内)磁石廃材の湿式リサイクル技術 127-131

[2] 襷田榮一: リサイクル金属資源回収プロセスにおける溶媒抽出，レアメタル資源の分離回収技術と溶媒抽出，化学工学シンポジウムシリーズ60 101-110

[3] 平成22年度　廃棄物資源循環学会 レアメタルリサイクルに関する合同講演会 資料

[4] J.S.Preston, Solvent extraction of metals by carboxylic acids, Hydrometallurgy, 14(1985) 171-188

[5] F.M.Doyle, D.pouillon, Solvent extraction of metals with carboxylic acid acid-coextraction of base metals with Fe(Ⅲ) and characterization of selected carboxylate complexes, Hydrometallurgy,19(1988)289-308

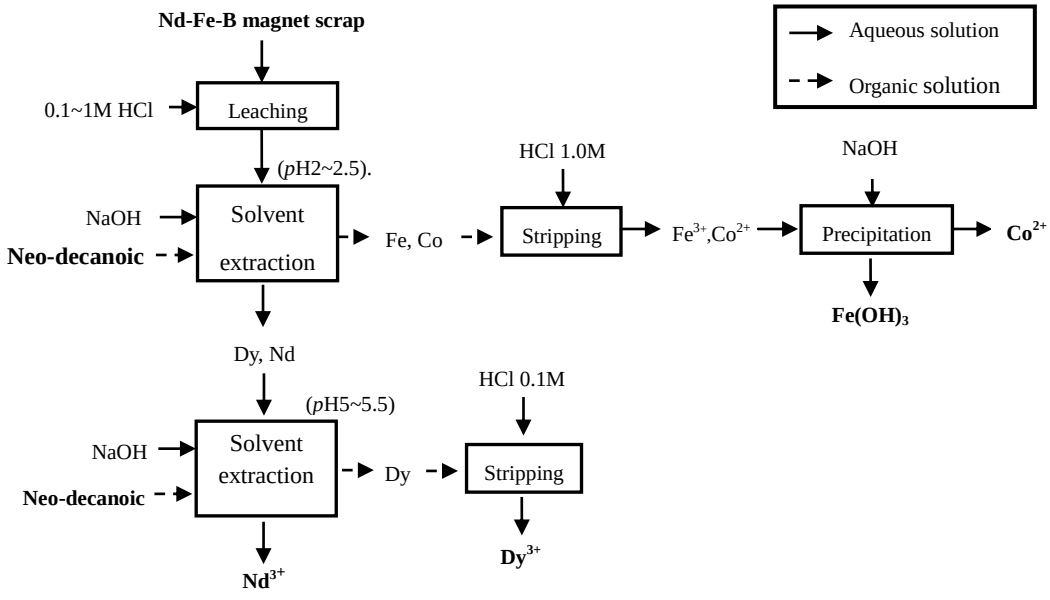

Fig.9. Separation process of Fe^{3+}, Dy^{3+}, Nd^{3+} and Co^{2+} from Nd-Fe-B magnet scrap.

Evaluation of UWB-BAN Coordinator with Multiple Antennas

Student Number: 12M18086 Name: Sho KOBAYASHI Supervisor: Jun-ichi TAKADA

複数アンテナを有するUWB-BANコーディネータに関する評価

小林 翔

ボディエリアネットワークは体内，体表，人体周辺での通信ネットワークを指し，医療等の様々な分野への応用が期待されている．その応用の一つであるセンサとコーディネータを利用したバイタルセンサネットワークでは，信頼性を向上させる手段として，遅延波を合成する rake ダイバーシチや，複数アンテナを用いたアンテナダイバーシチが利用される．本研究では BAN コーディネータノードに着目し，ベルト状に複数アンテナを取り付けた場合のダイバーシチ効果を評価した．

1 Introduction

BAN is the communication between sensors located in, on or around the human body. This is expected to manage wide applications in medical/health-care, sports, entertainment, and so forth. IEEE 802.15 TG6 standardized not only for the specification of narrow band system like typical vital sensors but also ultra wide band (UWB) system to provide high speed transmission to the wide band systems like capsule endoscope [1]. The UWB utilizes bandwidth of more than 500 MHz, and can realize high speed data transmission with low power within a short distance. Further, since UWB signals have very short pulse width, the multipath signals are resolvable.

In BAN systems, the channel response between the transmitter and receiver is inevitably influenced by the body posture and movement. Therefore a dynamic model of the propagation channel is required for proper evaluation of the system. In practice, BAN sensor node is restricted by installation space and battery life, so it is called reduced function device (RFD). However, the coordinator node is usually a full function device (FFD), hence it has much room for space and power. In this regard, diversity technique such as rake diversity which combines the delayed signals coherently, or antenna diversity which combines the independently received signals at different antennas can be used in the coordinator node to improve the performance. If such systems are applied, the antennas should be positioned optimally to achieve the best performance.

Existing studies discussed the propagation model when the coordinator antennas are attached at various places under static [2] and dynamic scenarios [3]. Moreover, the use of bracelets and waist belts are considered to attach the antennas on the body. However, the effect of the antenna position in a dynamic condition has not been discussed. Thus, this study investigates the effect of rake reception and antenna diversity when several antennas are attached on a waist belt. In UWB BAN system, the rake reception offers more reliable transmission by combining the multi-path signals. However, some significant multipath signals can still be shadowed due to any body movement and posture, and hence outage events can occur. Therefore, this study evaluate the performance gain of the antenna diversity as well as the rake reception for even more improving the outage performance.

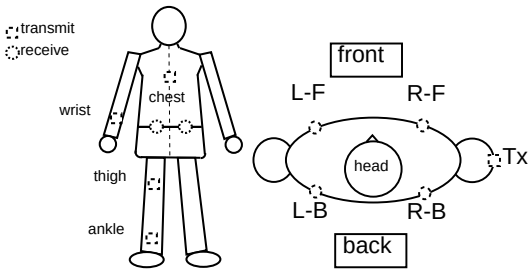

(a) Front view (b) Top view

Figure 1: Antenna position

This study measured the channel responses between multiple antennas of the coordinator node on a waist belt and the the sensor nodes. Then, several parameters were estimated from measured data. As well, the effect of rake reception and antenna diversity at each position are compared by evaluating outage probability.

2 Measurement Setup

In this study, a digital storage oscilloscope (DSO) was used to acquire a UWB pulse waveform. This system directly obtained the snapshots of the impulse response by measurement of UWB pulse signal in the time domain. Multiple on-body channels were measured using above the measurement system. Figure 1 presents the position of the sensor nodes (antennas). The transmit antennas of sensor nodes were attached on the wrist, ankle, thigh and chest. On the other hand, four receive antennas of the coordinator node were attached along the torso as shown in Figure 1. The antenna has an omni-directional radiation pattern in the horizontal plane. These antennas are attached about 1 cm away from the body surface by using polystyrene foam. This measurements were conducted two times for two subjects (165 cm, 68 kg and 180 cm, 65 kg) in the following scenarios. Two body movement scenarios were considered; one is walking on the spot, and the other is standing up/sitting down. This measurement was done in an experiment room which can be regarded as an office environment. Figure 3 shows the floor plan of the measurement room of which size is 5.5 m $\times$ 6.5 m, and its ceiling height is 2.7 $\sim$ 3.3 m. Table 1 presents the other measurement parameters.

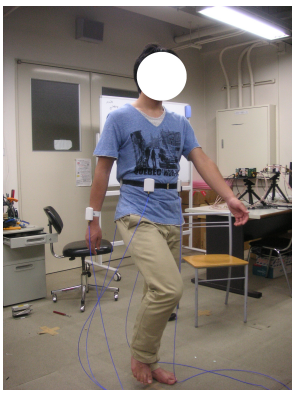

Figure 2: Scene of experiment

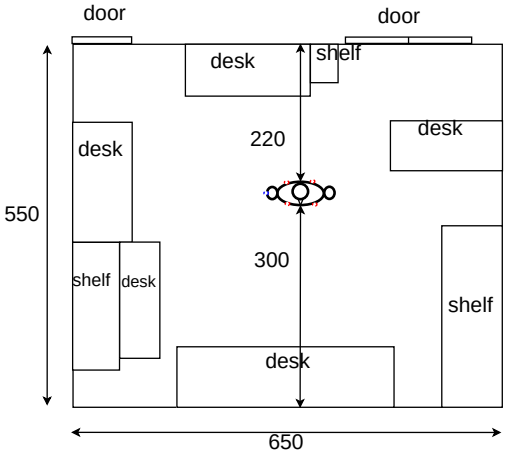

Figure 3: Measurement environment

3 Measurement result

This study obtained the waveform of the received signal in the measurement. By matched filtering of the received signal, the channel impulse responses were estimated.

3.1 Delay Profile

Figure 4 shows the delay profile when the transmit antenna is attached on the wrist which was calculated by averaging the power of the impulse responses over time. As can be seen, dominant arrival paths can be observed at 1 ns, 7 ns, and 22 ns. These signals are regarded as direct path, reflected path from the floor, and reflected path from wall based on the calculation of the arrival times for the corresponding travel distances of the waves. Since the distance between transmit antenna and receive antennas is about 15 $\sim$ 30 cm, the arrival time of the direct path falls into 1 ns. Similarly, the arrival time of the reflected path from the floor is about 7 ns because the distance was about 1 m. The reflected path from the wall arrived around 22 ns, and this corresponds distance of about 6.5 m. Here, dominant path is considered as the reflected signal from the wall of the lower side of Figure 3. This study deal with these three dominant arrival paths.

Table 1: Parameters

Sampling rate	25 Gsample/sec
Number of samples	1000/ 1 snapshot
Number of snapshot	100/sec
Measurement time duration	5 sec
Frequency	3.4$\sim$4.8 GHz

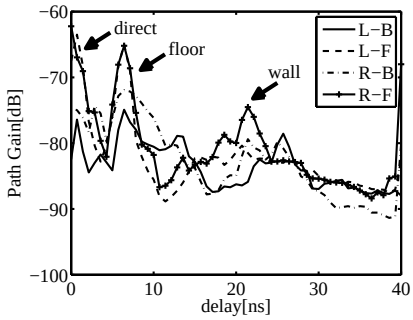

Figure 4: Delay profile

3.2 Path Gain

The path gain of each path were obtained. Firstly, the impulse response were calculated from measured data. Then, the 3 largest values were obtained, and sorted these based on arrival time. Figure 5 shows cumulative distribution function (CDF) of path gain of each arrival path in the case of wrist. For the direct path (first arrival path) case, the antennas attached in front of the body (R-F, L-F) tend to have higher average value than those far from the transmit antenna (R-B, L-B). This is because the swing width of the arm when the arm is in front of the body is larger than when arm is at the back. Therefore, these antennas are less attenuated by shadowing of the body when the arm is in front of the body. Reflected path from the floor (second arrival path) also shows the same tendency. On the other hand, reflected path from the wall (third arrival path) of each have almost the same average value. Furthermore, this path has lower variance than other two paths. Therefore, this path may contribute less for rake diversity.

3.3 Cross Correlation

If the diversity technique is applied, it is important to keep independence between each path. Therefore the cross correlation were calculated among the delayed paths and among the antennas Cross correlation value is calculated using Equation (1) [4], where h represents the path gain, x and y denote antenna indices, and i and j indicate delay tap indices. E[$\cdot$] denotes the expectation operator. Figure 6(a) shows the correlation among the delayed paths at R-F antenna's case. This shows very low correlation value among the delayed paths. It can be seen that the correlation between two paths of the same antenna are low due to different propagation mechanism. Thus, rake diversity can be applied for this situation. Next, the correlation between each pair of antenna were considered . Figure 6(b) shows the correlation between first arrival

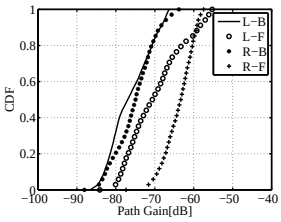

(a) Direct path

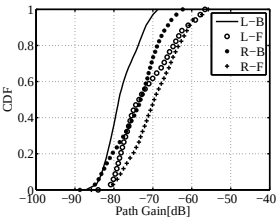

(b) Path from floor

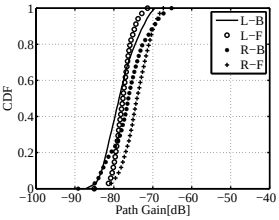

(c) Path from wall

Figure 5: CDF of path gain

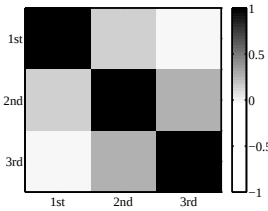

(a) Correlation of delayed paths (wrist, R-F)

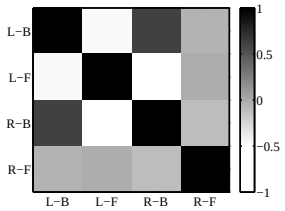

(b) Correlation of each antenna(wrist, direct path)

Figure 6: Cross correlation

paths of each antenna when the transmit antenna is on wrist . It was found that in most cases the cross correlations indicated low value, even if L-B and R-B were highly correlated. Also, the pair of L-F and L-B and the pair of L-F and R-B show inverse correlation. This is probably due to the arm swinging. This means that it may be ineffective to use the pairs of antennas located on the same side of the body in case of the arm swinging to improve performance by diversity combining.

4 Evaluation of transmission

4.1 Calculation method

This section evaluates the outage probability for rake and antenna diversity. Outage probability means the probability that the signal-to-noise ratio (SNR) becomes lower than a threshold by fading and shadowing. The error probability were calculated based on the measurement results [5]. Modulation scheme is assumed to be differential binary phase shift keying (DBPSK). Firstly, bit-error ratio P_b is calculated as following

$$P_b = \mathrm{erfc}(\sqrt{\gamma_b}), \tag{2}$$

Table 2: Parameters in calculation

Parameter	Value
Bandwidth	499.2 MHz
Modulation scheme	DBPSK (Synchronous detection)
Packet size(N_b)	250 Bytes
Noise figure(NF)	12 dB
Implementation loss(Loss)	8 dB
Bit rate (BR)	487 kbps

where γ_b represent SNR per bit. This γ_b is expressed as

$$\gamma_b = \frac{E_b}{N_0} = \frac{P_r}{BR} \cdot \frac{1}{N_0} \tag{3}$$

P_r is receive power, E_b is energy per bit, N_0 is noise power density, and BR is bit rate. Then, P_r can be calculated by path gain PG from experiment, and is expressed as following equation.

$$P_{r\mathrm{dB}} = P_{t\mathrm{dB}} - NF - Loss + PG_{\mathrm{dB}} \tag{4}$$

This is processed in dB scale. P_t, NF, and $Loss$ denote the transmit power , noise figure, and implementation loss, respectively. Path gain indicates the combined one of 3 paths (3-finger rake) or 4 different antennas. Also, N_0 can be obtained by multiplication of Boltzmann's constant(1.38×10^{-23}[J/K]) and the temperature(25 ℃). Next, PER P_p is calculated using P_b.

$$P_p = 1 - (1 - P_b)^{N_b} \tag{5}$$

N_b is the packet size. Outage probability P_{out} is obtained as the probability that P_p become lower than threshold Γ_p.

$$P_{\mathrm{out}} = \mathrm{prob}(\Gamma_p < P_p) \tag{6}$$

This study set Γ_p to 0.05. Figure 2 represents parameters which are used in calculation.

4.2 Result

This study specifically evaluates the outage probability when the maximum allowed radiated power of UWB is used. According to the regulation of Federal Communications Commission (FCC) the power level is limited to −41.3 dBm/MHz. Since this research use the bandwidth of 500 MHz, it becomes −14.3 dBm. Therefore, this study obtained the outage probability at −14.3 dBm.

Figure 7 represents the outage probability when not using any special scheme. R-F antenna shows good performance. This can achieve an outage probability of less than 10% for all transmit antennas. This is because this antenna has high path gain. On the other hand, the antennas attached on the back side (R-B, L-B) has high outage probability for all antennas (more

$$\rho_{(ix,jy)} = \frac{\mathrm{E}[(|h_{ix}|_{\mathrm{dB}} - \mathrm{E}[|h_{ix}|_{\mathrm{dB}}])(|h_{jy}|_{\mathrm{dB}} - \mathrm{E}[|h_{jy}|_{\mathrm{dB}}])]}{\sqrt{\mathrm{E}[(|h_{ix}|_{\mathrm{dB}} - \mathrm{E}[|h_{ix}|_{\mathrm{dB}}])^2]\mathrm{E}[(|h_{jy}|_{\mathrm{dB}} - \mathrm{E}[|h_{jy}|_{\mathrm{dB}}])^2]}} \tag{1}$$

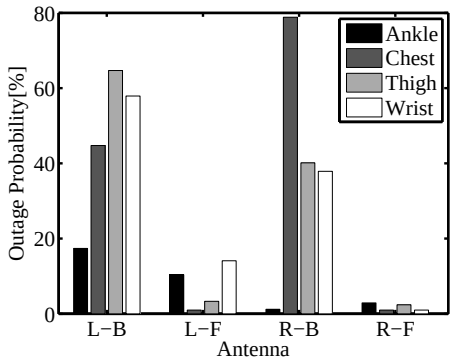

Figure 7: Outage probability without any scheme

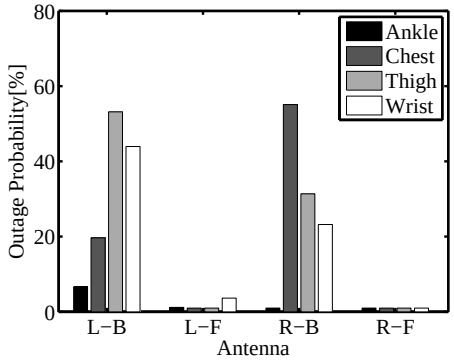

Figure 8: Outage probability using rake diversity

than 20 %). Next, 3 delayed signals of each antenna were combined to consider the effect of rake diversity. Figure 8 presents the result. Improvement of each antenna can be observed due to low correlation. Notably, the front side antennas (R-F, L-F) achieve less than 1% for all transmit antenna. However, the back side antennas (R-B, L-B) do not experience much improvement.

In addition, the effect of diversity combining using multiple antennas were verified. Figure 9 shows the result when using two antennas diversity. This result also shows improvement of each antenna pair. In many cases, achieve less than 1% outage probability was achieved. However, back side antennas (R-B, L-B) are not improved much because both antennas basically have lower gain than others. As well, this is due to high correlation between the antennas attached on the same side.

Next, the effect of both scheme were compared. To see the result clearly, the result at 10 dB below the maximum power (−24.3 dBm) were compared. Figure 10 represents the result when the best antenna or the best pair is used for each transmit antenna. This indicates that 2 antenna diversity can gain more improvement than rake using 3 delayed signal. This is probably because the gain of delayed paths are lower than the largest path of each antennas. Antenna diversity results in a relatively large improvement for the ankle and wrist cases. Antenna diversity results in a relatively large improvement for the ankle and wrist cases. Since these two positions move greatly due to body motion, the effect of attenuation by fading and shadowing at one antenna increases. Therefore, it is observed that diversity scheme can make up for this attenuation.

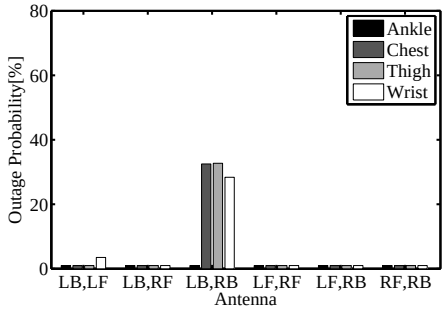

Figure 9: Outage probability using 2 antennas diversity

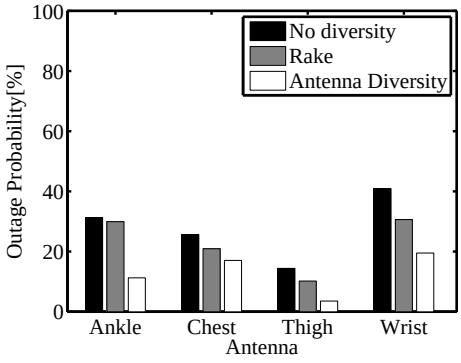

Figure 10: Comparison of both scheme

5 Conclusion

In this study, the channel responses were measured in case that the multiple antennas of the coordinator node on a waist belt receive a signal from the sensor node. From the received signal, the radio channel properties such as the delay profile, path gain, and cross correlation were characterized. Further, the effect of rake and antenna diversity was investigated by evaluation of the outage probability. As a conclusion, 2 antenna diversity can bring improvements larger than rake using 3 delayed signal. Also, sufficient performance cannot be achieved with two antennas on the back side of the body. This is due to low path gain and high correlation.

References

[1] IEEE 802.15 WPAN Task Group 6 (TG6) Body Area Networks. [Online]. Available : `http://www.ieee802.org/15/pub/TG6.html`

[2] S. V. Roy, C. Oestges, F. Horlin, and P. D. Doncker, "A Comprehensive Channel Model for UWB Multisensor Multiantenna Body Area Networks," IEEE Trans. Antennas. Propag., Vol. 58, No.1, pp. 163–170, Jan. 2010.

[3] M. Kim, and J. Takada, "Statistical Model for 4.5-GHz Narrowband On-Body Propagation Channel With Specific Actions," IEEE Antennas Wireless Propag. Let., Vol. 8, pp.1250–1254, Dec. 2009.

[4] J. Keignart, C. Abou-Rjeily, C. Delaveaud, and N. Daniele, "UWB SIMO Channel Measurements and Simulation" IEEE Trans. Microw. Theory Tech., Vol. 54, No. 4, pp. 1812–1819, Apr. 2006.

[5] J. Wang, K. Masami, and Q. Wang, "Transmission Performance of an In-body to Off body UWB Communication Link," IEICE Trans. Commun., Vol. E94-B, No. 1, pp. 150–157, Jan. 2011.

Visualization of the propagation channels and interpretation of the mechanisms in macro cellular environments at 11 GHz

Student number: 12M18092 Name: Rieko TSUJI Supervisor: Jun-ichi TAKADA

11 GHz 帯における市街地環境での伝搬特性可視化と伝搬メカニズムの解釈

辻　理絵子

本論文では，伝搬測定およびシミュレーションから得られた伝搬特性を環境写真と重層することで，伝搬路の可視化を行った．測定は 11 GHz 帯，市街地環境で実施した．シミュレーションで使用した建物モデルは，伝搬環境における周辺構造物をレーザープロファイラを用いて取得した点群データを基に構築した．両者の比較により，見通し波や反射波の影響を測定とシミュレーションの両方で確認した．一方，シミュレーションでは再現されないが，測定では無視できない影響を持つ散乱波の存在を確認した．

1 Introduction

The demand for high capacity and high bit rates has been increasing in recent years. To satisfy this demand, MIMO technique can be a key solution. MIMO technique utilize multi path component. The multi antenna is used in the both of base station (BS) and mobile station (MS), each antenna transmit different signal and through propagation channel, the signals were received. The performance of MIMO is strongly depends on accuracy of separation the signal. Thus, directional properties of propagation channel and its phenomena are need to be analyzed [1].

On the other hand, there is a methodology enable comprehensive understandings of angular characteristics of propagation channel. That is "visualization". Visualization means that the 360 degree panoramic photo which are superimposed angular power spectrum [2]. The conventional methodology such as comparing power spectrum and environmental information separately is quite laborious and costly. However, only visualization of measurement data is deficient because measurements have the limitation to estimate parameters. The resolution of the measuring equipment make accurate analysis hard. Thus, simulation that can provide us propagation path information make up the limitation. Ray-tracing method is often used to simulate propagation characteristics, but ray-tracing simulators generally model only specular reflection, edge diffraction and penetration. However, according to the literature [3], the contribution of the scattering is still significant and should not to be ignored. Therefore, comparing with the measurement and the ray-tracing simulation results by visualization method is helpful to understand the propagation phenomena.

This paper shows that the procedure of building visualization tool and both of the limitation of measuring equipment and ray-tracing simulation, and interpretation of the propagation phenomena in urban environments at 11 GHz.

2 Framework

Figure 1 shows the flowchart of this research. First, the measurement was carried out and the transfer function was obtained in the urban environment at 11 GHz. At the same place, also measured the point cloud data

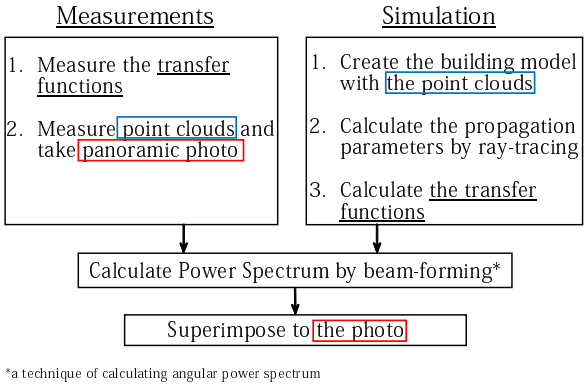

Figure 1: Flowchart

of the objects surrounding the MS by a laser scanner, the location data by GPS, and panoramic photo. The obtained point cloud data are then converted into the polygon data to use in the ray-tracing simulation. After the ray-tracing simulation, the transfer function is calculated with the path parameters generated by ray-tracing. Subsequently, for both of the measurement and the simulation results, angular power spectrum is calculated by beam-forming method. In this paper, I consider vertical polarization only at both of the BS and the MS.

The beam-forming is performed as

$$G(k,\phi,\phi^{'},\theta,\theta^{'}) = \frac{\mathbf{a}_k^H(\phi^{'},\theta^{'})\mathbf{H}_k\mathbf{a}_k^*(\phi,\theta)}{|\mathbf{a}_k(\phi^{'},\theta^{'})|^2|\mathbf{a}_k(\phi,\theta)|^2}$$

where G represents the angle-resolved transfer function, and $\mathbf{a}$, $\mathbf{H}$, k, ϕ, ϕ', represents the antenna response, the matrix of the transfer function, the number of the sub-carrier, direction of departure (DoD), and direction of arrival(DoA), respectively. The Azimuth Elevation Power Spectrum (AEPS), and Delay Power Spectrum (DPS) are calculated respectively by

$$\text{AEPS }:p(n,\phi,\theta) = \sum_n\sum_{\phi'}\sum_{\theta'}|g(n,\phi,\phi^{'},\theta,\theta^{'})|^2$$

$$\text{DPS }:p(n) = \sum_{\phi}\sum_{\theta}\sum_{\phi'}\sum_{\theta'}|g(n,\phi,\phi^{'},\theta,\theta^{'})|^2$$

where $g(n,\phi,\phi^{'},\theta,\theta^{'})$ denotes the impulse response which is obtained by the inverse Fourier transform of $G(k,\phi,\phi^{'},\theta,\theta^{'})$.

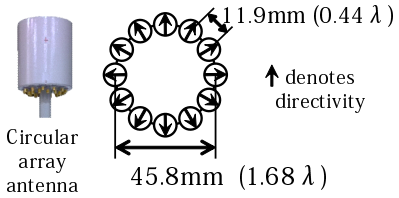

Figure 2: detail of the circular antenna array

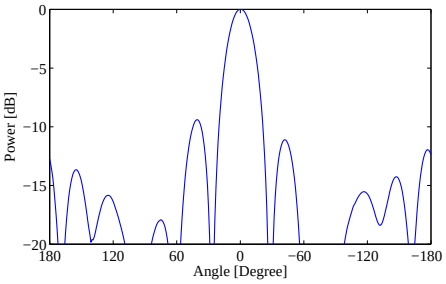

Figure 3: Radiation pattern

To superimpose the angular power spectrum to the panoramic photo, I have to calculate elevation and do data matching. Panoramic photo were made by capturing a frame the video clip of the measured route environment and each photo have the data of the objects in the photo and GPS location. For calculating elevation, the distance and height of the objects and Pythagorean theorem is utilized. For data matching, location data and also measured data snapshot's GPS location data is utilized. calculating the distance between panoramic photo frame and measured data snapshot, the nearest data was chosen. For the simulation data matching, I just selected the same number of the measured data snapshot.

3 Measurement Campaign

3.1 Channel sounder

Both of the BS and the MS use the same type of antennas (12-elements uniform circular antenna array) as shown in Figure 2. This antenna has both vertical and horizontal polarized elements. Each element is spaced by 11.9 mm (0.44λ). The radiation pattern of the antenna by beam-forming is shown in Figure 3. The resolution is approximately 60 degree. The transmit signal is the unmodulated multi-tone signal having 2048 tones (2.5 ns resolution in delay domain), center frequency 11 GHz, and 400 MHz bandwidth. The transmit power is 24 dBm. Table 1 shows the measurement parameters. More detailed specifications of the channel sounder are presented in [4].

3.2 Measured route

The measurement campaign was conducted in the city of Ishigaki, Japan. The BS antenna was placed in the roof top of the building approximately 28 m. Figure 4 shows the prospective view from the BS towards the MS. The MS antenna was placed in approximately 3 m above the roof top of the vehicle which was driven

Table 1: Measurement specifications

Parameters	Value
Uniform circular array	Dual-polarized patch element Gain: 6 dBi UCA spaced by 11.9 mm
Carrier frequency	11 GHz
Signal bandwidth	400 MHz
Transmit power	24 dBm
No. tones	2048
Delay resolution	2.5 ns
Measured interval time	1.128 s

Figure 4: View from the BS

at 5 km/h and transmit signal with 1.128 s interval along the route denoted as the arrow in Figure 5. The distance between the BS and the MS is approximately ranging from 330 m to 450 m. As shown in Figure 4, the average height of the building in measured route is 7 m, and it was the line-of-sight (LoS) environment throughout the route.

4 Simulation

4.1 Building model

At the same place of the measurement, the buildings surrounding the MS were scanned by IP-S2 Lite, which is a 3D laser scanner developed by TOPCON Corp. The point cloud data obtained from the scanning is converted into the polygonal data for ray-tracing simulation. In addition, the polygon model is further simplified by flattening the building surface and removing the small objects such as utility pole and trees as shown in Figure 6, because ray-racing is based on Fresnel zone principal, thus the detailed surface should not considered. After the simplification, the number of the surface are reduced from 5616 to 90 as shown in Table 2.

4.2 Ray-tracing simulation

The simulation was carried out by using Wireless Insite, ray-tracing simulator developed by Remcom Inc. From the simulation, I can obtain received power, delay time, angle of arrival, and angle of departure.

Figure 5: Measurement area

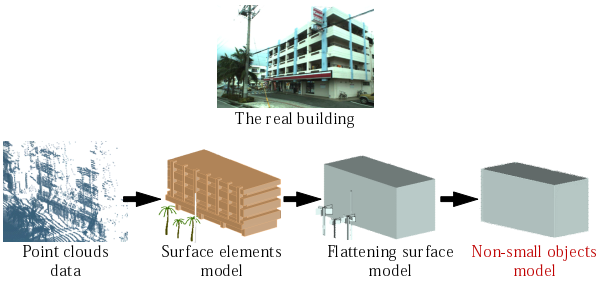

Figure 6: The example of the model simplification

Figure 7 shows the calculation area, in which 13 reconstructed buildings are included. The MS was set along the red route with 1.67 m interval at 3 m height, and the BS was set on right lower side at 28 m height without building model in Figure 7. Thus the number of the snapshot is 71. All the buildings are assumed to be made of concrete. The ground material was set as asphalt [5]. Table 3 shows the parameters of the simulation.

4.3 Data processing

The matrix of the transfer function is reconstructed as

$$\mathbf{H}_k = \sum_{l=1}^{L} \gamma_l \mathbf{a}_k^{'}(\phi_l^{'}, \theta_l^{'}) \mathbf{a}_k^{T}(\phi_l, \theta_l) e^{-j2\pi f_c \tau_l}$$

where the prime denotes the value in receiver, and γ_l, L, τ_l denote l-th path gain, total number of paths, and l-th path delay time, respectively.

5 Results and Discussion

5.1 Distance-delay characteristics

Figure 8 shows distance-delay power spectrum of the measurement and the simulation results. Two major paths are observed in both the measurement and the simulation results. From the simulation, these two paths (Path 1 and Path 2) are confirmed to be the direct wave and the reflected wave from the backward building A as shown in Figure 9. Figure 9 shows the simulated paths where the left and right side figures show the strongest received power of 7 and 25 paths,

Table 2: Number of the surface

Model type	The number of the surface
Surface elements	5616
Flattening surface	841
Non-small objects	90

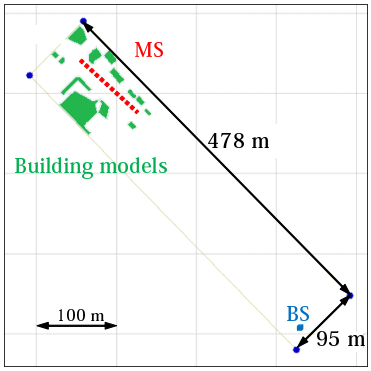

Figure 7: Simulation area

respectively. Good agreement between the measurement and the simulation results is observed. However, there are some waves which are not confirmed from the simulation results.

5.2 Angular-power spectrum

Figure 10 and Figure 11 shows a frame of the visualization movie. The angular power spectrum reproduced between 25 degree to −25 degree in elevation, since the spectrum out of the range is not efficient to analyze because of the antenna design. Figure 10 shows the AEPS at the delay time when the direct wave arrived. From this figure, it is confirmed that ray-tracing method can reproduce direct wave appropriately.

Figure 11 shows DoD which means $\sum_n$AEPS, at the point of approximately 370 m away from the BS. We can observed direct wave at near 0 degree in Figure 11. The path around -180 degree, which is confirmed to be a reflection wave from backward building A as shown in Figure 9, is also observed in both the measurement and the simulation results.

However, some discrepancies are observed. The path between −50 degree to −130 degree does not appear in the simulation result. Possible explanations are as follows. The effect of the reflected wave from the building B located near −100 degree might be under estimated in simulation. As shown in Figure 9, the reflected wave from building B actually exists but too small under −140 dB because of the parameter setting of the concrete material. Scattering effect also can be the reason. In addition, the resolution of the antenna is another candidate. From Figure 3, −3 dB power reduction resolution of the antenna is approximately 60 degree. If the channel sounder received both of the coming wave from −50 degree and −120 degree at the same time, it is possible to measure the spread power between −50 degree to −130 degree.

Another discrepancy is around 90 degree to 140 degree. It is seen that ray-tracing cannot reproduced the waves. From this figure, this might be the effect of

Table 3: Simulation specifications

Parameters	Value
Carrier frequency	11 GHz
Signal bandwidth	400 MHz
Material constant	concrete ($\sigma = 0.015$, $\epsilon = 15$) asphalt ($\sigma = 0.0005$, $\epsilon = 5.72$)

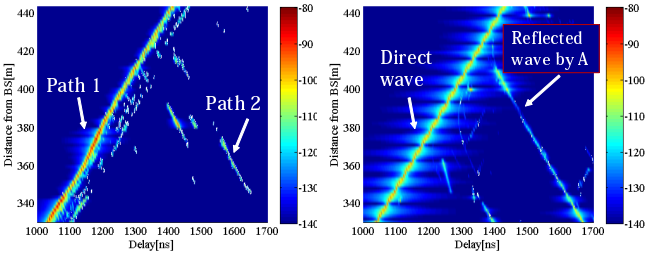

Figure 8: Distance-delay power spectrum (left: measurement, right: simulation)

scattering of the trees, but it is needed more detailed analysis.

6 Conclusion

This paper shows visualization method of the propagation channels both of the measurement and the simulation results. From the results, it is shown that the direct wave is appropriately reproduced in the simulation. However, were some possibility that the reflected waves are underestimated in simulation and some significant scattering effect might not be considered. For the future work, I plan to fit panoramic photos to the measurement and the simulation results more accurately, and some high-resolution parameter estimation algorithm will be applied for more precise evaluation. And finally, the effect of the scattering might be modeled.

References

[1] M. Kim, Y. Konishi, Y. Chang, and J. Takada "Large Scale Parameters and Double-Directional Characterization of Indoor Wideband Radio Multipath Channels at 11 GHz," *IEEE Trans. Antennas Propag.*, vol. 62, no. 1, pp. 430-441, Jan. 2014.

[2] J.M. Conrat, P. Pajusco, and A. Dunand, "On the use of panoramic photography for understanding propagation channel physical phenomena," *COST 2100*, No. 12024, Bologna, Italy, Nov. 2010.

[3] M. Ghoraishi, J. Takada, and T. Imai, "Identification of Scattering Objects in Microcell Urban Mobile Propagation Channel," *IEEE Antennas Propag.*, vol. 54, no. 11, pp. 3473-3480, Nov. 2006.

[4] M. Kim, Y. Konishi, Y. Chang, and J. Takada, "Novel Scalable MIMO Channel Sounding Technique and Measurement Accuracy Evaluation with Transceiver Impairments," *IEEE Trans. Instrum Meas.*, vol. 61, no. 12, pp. 2546-2550, Dec. 2012.

[5] Remcom Inc., *Wireless Insite 2.7.0 Reference Manual*, pp. 97-98, Nov. 2013.

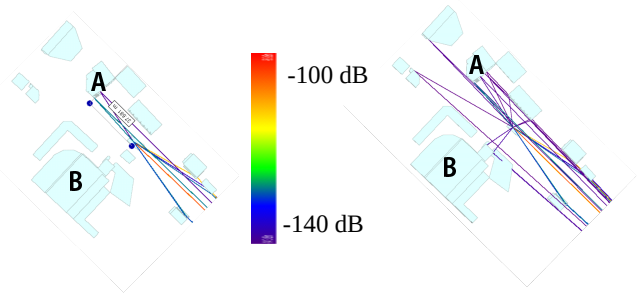

Figure 9: Strongest 7 path (left) and 25 path (right) calculated by the simulation

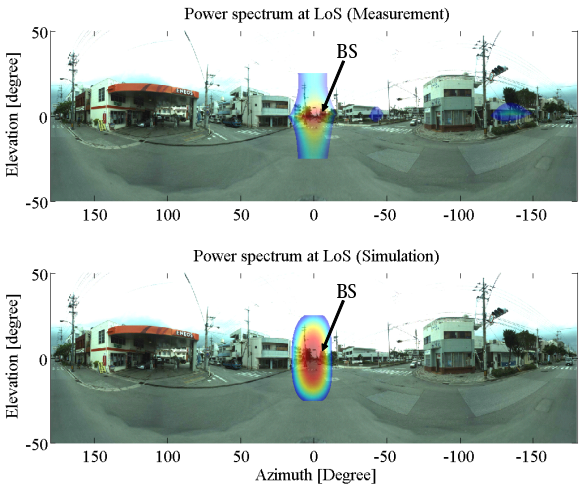

Figure 10: AEPS at LoS delay time (top: measurement, bottom: simulation)

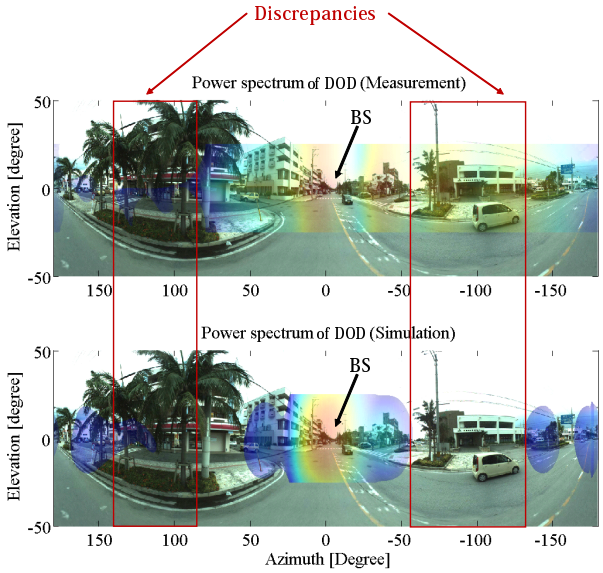

Figure 11: DoD (top: measurement, bottom: simulation)

Fracture criterion between a multi-beam structure and rough adhesive surface

Student Number : 12M18028　Name : Kazuhito EMURA　Supervisor : Kunio TAKAHASHI

梁集合体構造と粗さのある凝着表面における破壊条件

江村和仁

先端平面とウレタンシートとの間に凝着界面を持つ剛体に様々な角度で力を加え、垂直応力とせん断応力に関する脱離条件を実験的に求めた。最大凝着力を幾何形状から界面に対する垂直荷重と水平力に分解する。剛体は根元を固定され界面における垂直・せん断応力分布は一様であるとし破壊条件を垂直応力とせん断応力に関して見積もった。この破壊条件をもとに、先端面で凝着する弾性梁の垂直荷重と水平力に関する脱離条件を導出した。

1. Introduction

Geckos can quickly climb walls and ceilings with adhesion force. They have a lot of micro-nano hairs on their fingers surface, which are called setae and spatulae. The hairs can absorb surface roughness and generate large adhesion force [1]. This adhesion mechanism was studied well and the application of the mechanism was already made [2][3].

This mechanism cannot explain how geckos can move quickly, because it is difficult to break strong adhesion interface. A multi-beam structure [4] is inspired from the hairs. The structure consists of many elastic beams and adhesives applied on the tips of the beams. The structure is intended to grip a rough surface with adhesion force and control detachment from the surface. Because adhesion force is generated at any surfaces, grip and release devices with adhesion force are expected for application in various surrounding compared to magnetic chuck and vacuum chuck. The detachment mechanism of the multi-beam structure is treated as a superposition of the mechanism of single beam. The mechanism of single beam was discussed with a beam theory and a rough assumption about a fracture criterion of the adhesion interface [5]. The mechanism was experimentally investigated [6][7]. The experimental result couldn't be explained with this model.

In the present study, the fracture criterion is experimentally investigated with a rigid body and adhesives. With the fracture criterion and the beam theory, the detachment mechanism of an elastic beam is suggested.

2. Model

A multi-beam structure that consisted of many elastic beams and adhesives applied on tips of the beams holds an object at adhesion interface between a surface of the object and the tips as shown in Figure 1. The detachment mechanism of the structure is treated as superposition of the mechanism of single beam. Normal load F_n and tangential force F_t are applied to each of the beams as shown in Figure 2. F_n is corresponded to the weight of the object.

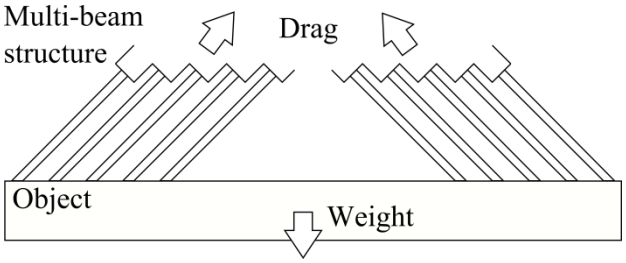

Figure 1. A multi-beam structure holds an object.

Normal stress distribution is generated at the interface. The distribution is evaluated from a beam theory. Using contact area S, section modulus Z, angle of the beam θ and length of the beam l respectively, maximum normal stress $\sigma_{n,max}$ at the interface is expressed as Equation 1.

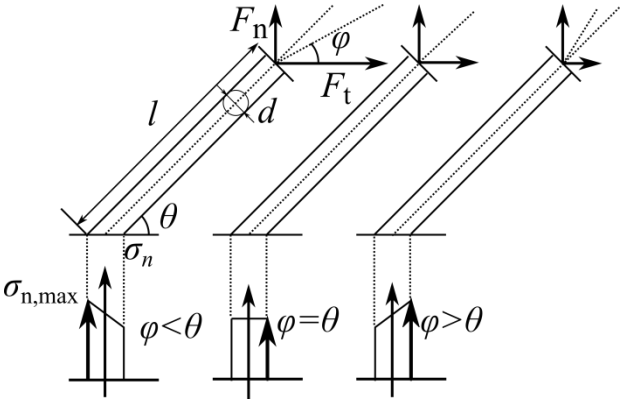

Figure 2. Normal stress distribution at adhesion interface.

$$\sigma_{n,max} = \frac{F_n}{S} + \frac{\left|F_n l\cos\theta - F_t l\sin\theta\right|}{2Z} \qquad (1)$$

The adhesion interface is broken and the beam detach from the surface when $\sigma_{n,max}$ is larger than critical value $\sigma_{cr}(\tau)$ i.e.,

$$\sigma_{n,max} \geq \sigma_{cr}(\tau) \qquad (2)$$

If F_t is changed, $\sigma_{n,max}$ is changed as shown in Figure 2. The detachment from the surface is controlled by F_t. The fracture criterion of the adhesion

interface is defined as $\sigma_{cr}(\tau)$. The detachment criterion of an elastic beam is defined as F_n and F_t when detachment occurs. The fracture criterion is not studied well. The fracture criterion concern with shear stress should be investigated experimentally.

3. Experiment

3.1 Experimental system

The experimental system is shown in Figure 3 and Table. The rigid body is fixed firmly to an arm of the of the rotation stage(e) by double nut. Tilting angle of the table φ is same as the angle of resultant of F_n and F_t to the surface.

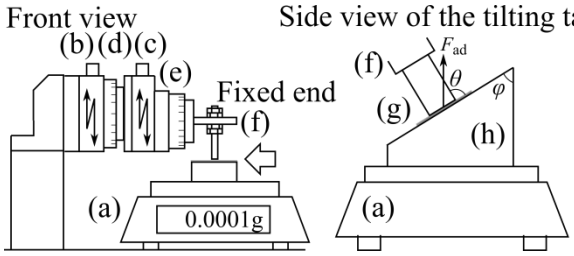

Figure 3. The experimental system.

Table Experimental system.

(a)AY-220 SHIMADZU	Electric balance Resolution:0.1mg
(b)KZL060 SURUGA SEIKI	Motorized stage Resolution: 1μm
(c)B11-60D SURUGA SEIKI	X axis crossed roller guide stage Resolution: 0.5μm
(d)B43-60N (e)B43-38N SURUGA SEIKI	Manual rotation stage Resolution: 0.2°
(f)	Screw, SUS304, 9.75mm length 1.85mm in diameter
(g)CT-03-500 EXSEAL Corp.	Adhesives Urethane sheet 0.2mm thick
(h)	Tilting table, angle φ :5deg to 90deg at 5deg intervals

3.2 Process of experiment

Then experimental process is shown in Figure 4.

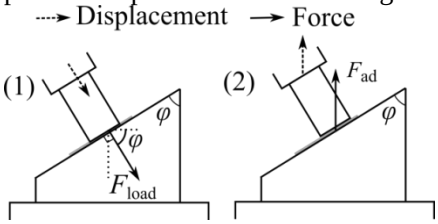

Figure 4. The experimental process.

The body is (1)adhered to the surface and loaded vertically to the surface (2)Removed from the surface at 1μm/sec vertically.

Figure 5 shows that maximum adhesion force F_{ad} is plotted when loading force F_{load} is applied to the flat surface. The threshold of F_{load} is needed and determined as $F_{load} \geq 0.40(\mathrm{N})$ to keep the same condition through the experiments.

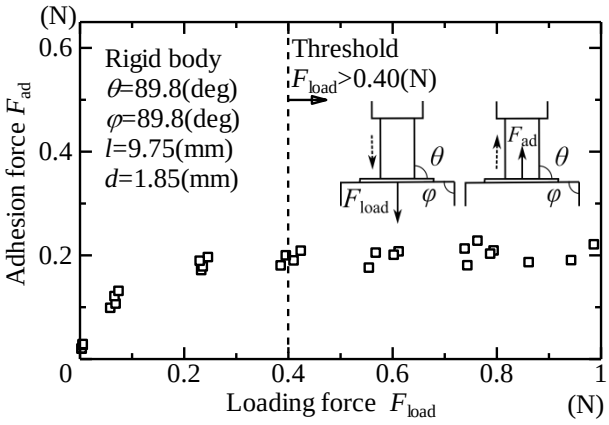

Figure 5. The threshold of F_{load}.

4. Result

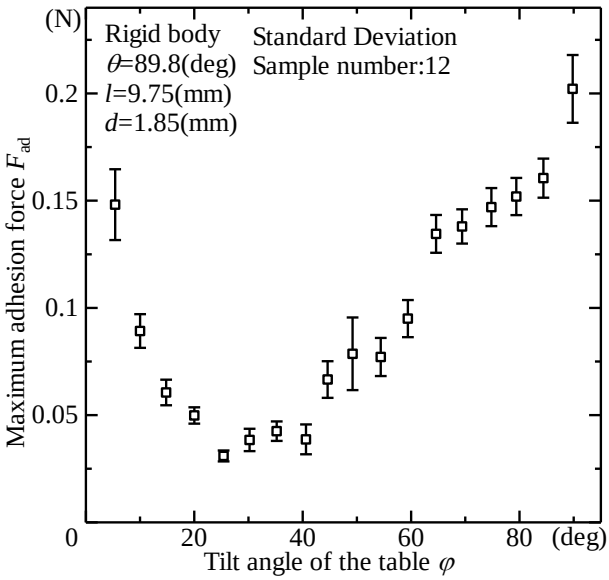

Figure 6. The maximum adhesion force F_{ad} with tilt angle of the table φ.

Experimental result is plotted as relation of F_{ad} and φ in Figure 6. The number of the sample is 12 at each φ. The plotted points are the mean value of F_{ad}. The error bars is evaluated from standard deviation.

5. Discussion

5.1 Fracture criterion of adhesion interface

With assumption of fixed end between the rigid body and the arm, the effect of the bending moment at the interface is ignored and the normal and shear stress distribution is assumed uniform as shown in Figure 7. The normal stress σ_{ave} and shear stress τ_{ave} is

evaluated from the mean value of F_{ad} and Equation 3 and 4.

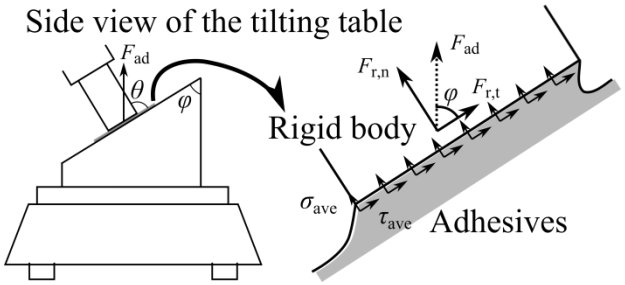

Figure 7. Normal and shear stress distribution between the rigid body and tilting surface.

$$\begin{cases} F_{r,n} = F_{ad}\sin\varphi \\ F_{r,t} = F_{ad}\cos\varphi \end{cases} \tag{3}$$

$$\begin{cases} \sigma_{ave} = F_{r,n}/S \\ \tau_{ave} = F_{r,t}/S \end{cases} \tag{4}$$

The fracture criterion is plotted as relation of σ_{ave} and τ_{ave} as shown in Figure 8. When τ_{ave} is around 20kPa, the detachment occur at many values of σ_{ave}. It is suggested that the fracture mode is different at each value of σ_{ave} at the detachment point.

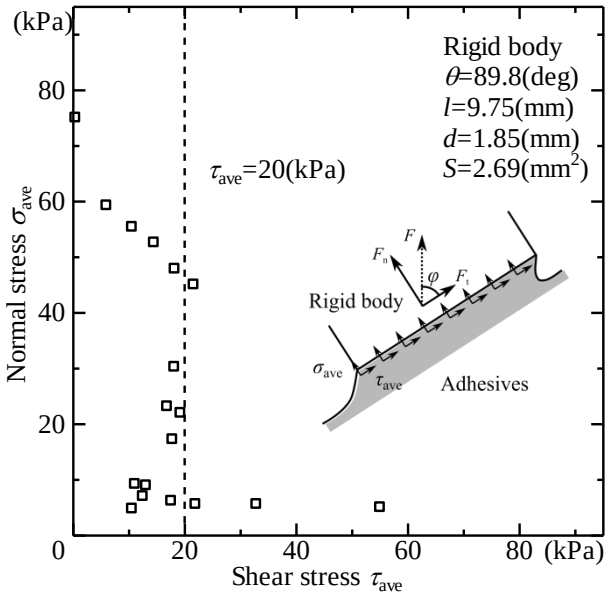

Figure 8. The fracture criterion of adhesion interface.

5.2 Detachment criterion of an elastic beam

Using the fracture criterion, the detachment criterion of an elastic beam is modified. The beam is adhered to a surface. When F_n and F_t is applied to the beam, $\sigma_{n,max}$ is expressed as Equation 1. Shear stress is assumed uniform over the interface, so τ is expressed as Equation 5.

$$\tau = F_t/S \tag{5}$$

From Equation 1 and 5, F_n and F_t are expressed as Equation 6.

$$\begin{cases} F_n = \dfrac{S\left(\sigma_{n,max} \pm 4\, l/d \sin^2\theta\tau\right)}{1 \pm 4\, l/d \sin\theta\cos\theta} \\ F_t = S\tau \end{cases} \tag{6}$$

When $\sigma_{n,max}$ and τ satisfy a fracture criterion, the beam is detached from the surface and Equation 6 express the detachment criterion. Figure 9 shows the detachment criterion at (a) $\theta = 30^\circ$, (b) $\theta = 45^\circ$, (b) $\theta = 60^\circ$; the solid lines show the conventional detachment criterion when $\sigma_{n,max}$ satisfy a fracture criterion expressed as constant value of $\sigma_{cr}(\tau) = \sigma_{cr}(0)$. The plotted points show the present detachment criterion when $\sigma_{n,max}$ satisfy the proposed fracture criterion as shown in Figure 8. When the resultant force of F_n and F_t increases in the direction φ at the lines or plotted points, the beam is detached from the surface.

As shown in Figure 9, both F_n and F_t at $\varphi = \theta$ take the largest values in each angle of the detachment criterion. Because the angle of the resultant of $\sigma_{n,max}$ and τ at $\varphi = \theta$ agrees with θ, the maximum normal load at $\varphi = \theta$ is expressed as $S\sigma_{cr}$. σ_{cr} decreases as the angle of the stress resultant decreases as shown in Figure 10. It is suggested that the structure can grip a heavy object when θ is large.

6. Conclusion

To investigate the detachment mechanism of a multi-beam structure, the fracture criterion of adhesion interface is experimentally investigated with the rigid body and the tilting tables. The maximum adhesion force between the rigid body and the elastic body is measured with the electric balance and the fracture criterion is evaluated from the maximum adhesion force. The detachment criterion of an elastic beam is evaluated from the proposed fracture criterion and a beam theory. With comparison of the detachment criterion of various beam angles, it is suggested the multi-beam structure can grip a heavier object when the angle of the beam is large.

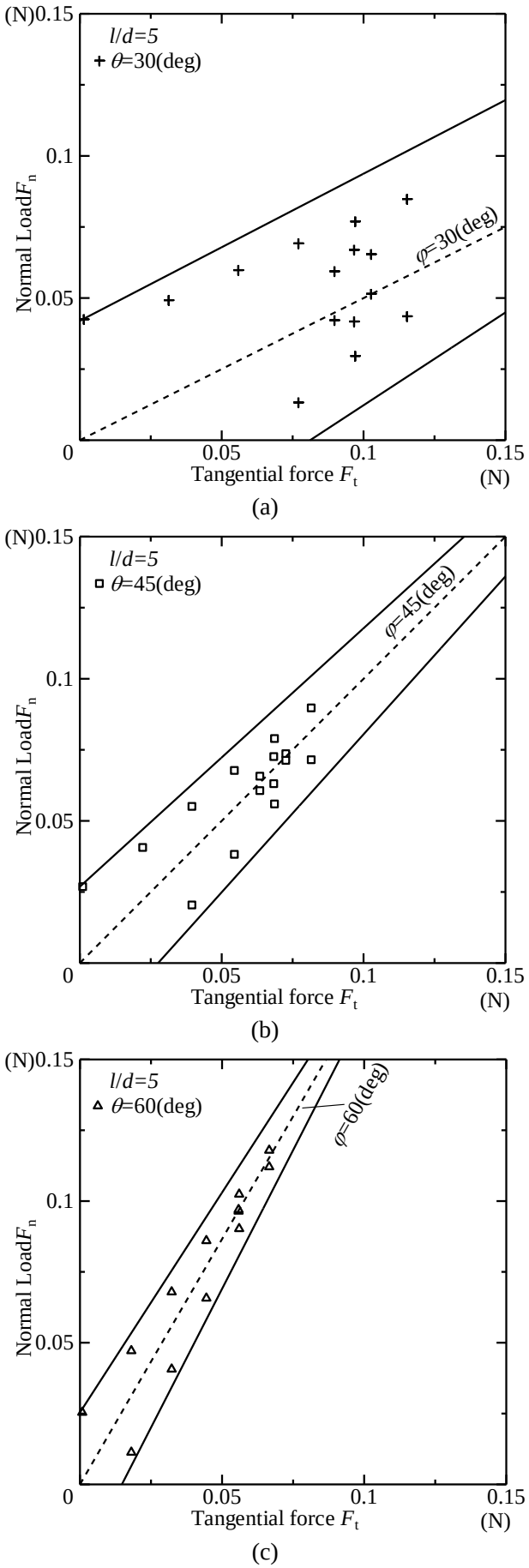

Figure 9. The detachment criterion of an elastic beam at various beam angles θ .

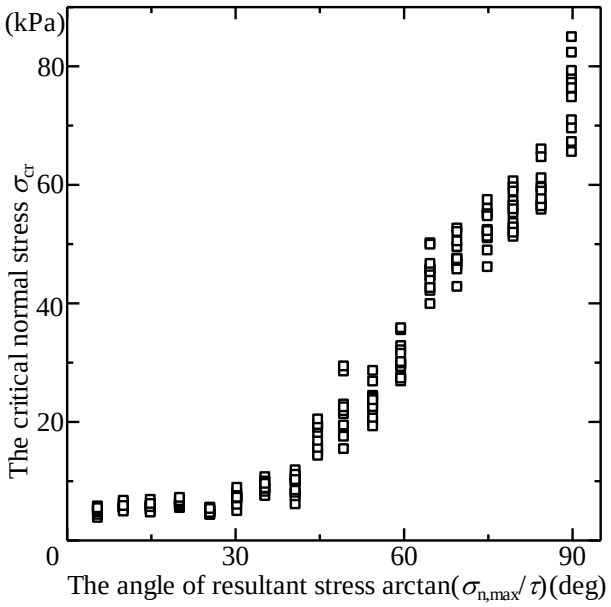

Figure 10. The fracture criterion about normal stress and the angle of the resultant stress.

References

[1] K.Autumn, et.al., 2002. PNAS 99(19): 12252-12256

[2]Geim, et.al., Nature Materials.2 (2003): pp.461-463

[3] S. Kim, et.al., IEEE Transactions on Robotics, Vol. 24, February 2008. pp.65-74

[4] K.Takahashi, et.al., International journal of adhesion & Adhesive 26 (2006) pp.639-64

[5] J. Watanabe, et.al., 14th symposium on Microjoining and Assembly Tech in Electronics Feb 5-6 2008 Yokohama pp.369-372

[6]M.Wang, et.al., 16th symposium on Microjoining and Assembly Technology in Electronics, Vol.16 2010 pp.435-438.

[7] K.Emura, et al., The 4th Multidisciplinary International Student Workshop (MISW2012), pp. 91, 2012, Aug.

Mechanism of Adhesion Hysteresis in the Elastic Contact between a Silicone Rubber and a Silica Glass Lens

Student Number: 12M18264 Name: Dooyoung BAEK Supervisor: Kunio TAKAHASHI

シリコーンゴムと石英ガラスレンズ間の弾性接触における凝着ヒステリシスのメカニズム

白 斗永

シリコーンゴムと石英ガラスレンズ間の接触における凝着ヒステリシスのメカニズムが研究された．実験により変位，力，接触半径の三つのパラメータが厳密に測定された．測定系の剛性を考慮した TMO モデルが実測値の解析に用いられた．三つの測定値が線形弾性理論に基づいた力の釣り合い式を満たすことが確認された．その結果，外部仕事，弾性，界面，剛性，散逸の各々のエネルギー変化項の計算が可能となり，エネルギー散逸が解析され，凝着ヒステリシスのメカニズムは接触部の円周状亀裂長さの変化量に比例するパラメータの導入で説明可能となった．

1 INTRODUCTION

Understanding the adhesion phenomena is significant and essential for designing the application using the adhesive force, e.g. grip-and-release devices [1]. A point contact model of contacting between a parabolic punch and a semi-infinite body is the most basic model for analyzing the adhesion phenomenon theoretically and experimentally. For theoretical analysis of this model, Johnson, Kendall and Roberts suggest the JKR theory [2] which consist in compressing an elastic parabolic punch against a flat rigid surface or, conversely, a hard parabolic punch against a flat elastic substrate. This theoretical model rely on basic assumptions of elastic theory [3]. From this reason, the experimentalist has to check the theory and experimental condition strictly before attempting to anlyze their experimental results for their reliability. In this perspective, Takahashi, Mizuno and Onzawa suggest the TMO theory [4] which consider the stiffness of the measurement system. And, Johnson [5] point out that in many practical situations the high intensity stress of adhesive forces gives rise to inelastic-viscoelastic or plastic-deformation of the solids, notably in the separation zone at the edge of the contact. This influences the apparent work of adhesion and gives rise to a difference between loading and unloading process which referred to as an adhesion hysteresis. This adhesion hysteresis which is different from the mechanical hysteresis is classified and defined by Silverzan et al. [6], and they suggest that the adhesion hysteresis is raised from a chemical reaction, namely the formation of a hydrogen bond, across the interface. Differences between theoretical model and experimental behavior mainly in the viscoelastic materials are also reviewed by Shull [7] and Barthel [8]. The adhesion hysteresis has been studied by many authors [3, 5-13], and factors that cause the adhesion hysteresis can be classified in two types. The first one is raised from the state of the bulk of the materials. If the bulk is non-elastic materials such as viscoelasticity, the time dependence and nonlinearity of the materials affects the whole process of contact. The second one is raised from the state of the interface between the materials. In this case, chemical reaction, molecular bonding, surface roughness and dangling chains could affects the adhesion hysteresis. From this, the reason of occurring the adhesion hysteresis cannot be generalized, however, it is clear that the energy is dissipated during loading and unloading the contact.

The mechanism of the adhesion hysteresis is still on discussion steps. Therefore, objective of the present study is to investigate the mechanism of the adhesion hysteresis. As an approach to achieve our objective, we measured the parameter of the displacement, the force and the contact radius respectively by experiment, and then evaluating essential parameters using the TMO theory for calculating each energy terms, i.e. elastic energy, interface energy, stiffness energy and external energy without any assumption of equilibrium state of total energy. From this process, the energy dissipation as a surplus of total energy relation can be calculated. And, the mechanism of the adhesion hysteresis is analyzed and discussed from the results.

2 THEORETICAL CONSIDERATION

Figure 1 shows a schematic illustration of the TMO model which consider the stiffness of the experimental system [4]. A rigid parabolic punch assumed to contacts on a perfectly semi-infinite elastic body. The rigid punch is assumed an axisymmetric parabolic body and the friction of the interface between two bodies is negligible.

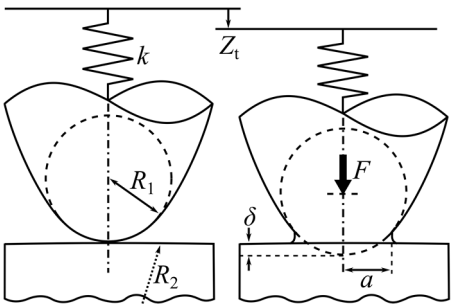

Figure 1. Schematic illustration of the TMO model, where Z_t is gross displacement, k is stiffness of the experimental system, R_1 is radius of curvature of the rigid parabolic punch, R_2 is radius of curvature of the semi-infinite elastic body, F is force between the rigid parabolic punch and the semi-infinite elastic body, δ is vertically deformed displacement of the semi-infinite elastic body, a is radius of contact area raised by contacting. Notably, direction of the gross displacement here is opposite direction from the TMO theory.

The theory of the point contact can be expressed using the JKR theory [2]. We, however, need to consider the practical limit of a real experimental system theoretically to anlyze the experimental results. First of all, it is hard to guarantee the equilibrium state of total energy of experimental results, because realizing the perfectly static state of an experimental process is nearly impossible. Secondly, the elastic materials used in the experiment is the polymeric materials which does not guarantee the perfectly linear elasticity. Thirdly, the radius of curvature R_2 in Figure 1

need to be considered, because the surface of polymeric materials does not guarantee the perfectly flat surface. In Figure 1, the force between the rigid parabolic punch and the semi-infinite elastic body are balanced as a relation of F=P_H-P_B when the displacement δ is given, where P_H is the Hertz force and P_B is the Boussinesq force [4]. So, this force can be expressed as

$$F = \frac{2Ea}{1-v^2}\left(\delta - \frac{a^2}{3R}\right) \quad (1)$$

which shows the relationship among the force F, the contact radius a, and the displacement δ, where E and v is Young's modulus and Poisson's ratio of the semi-infinite elastic body, and R is radius of curvature, i.e.

$$\frac{1}{R} = \frac{1}{R_1} + \frac{1}{R_2} \quad (2)$$

where R_1 and R_2 is each of radius of curvature in Figure 1. And, a force due to the stiffness of the measurement system can be expressed as

$$F = k(Z_t - \delta). \quad (3)$$

From eliminating the displacement δ using equations (1) and (3), the force in Figure 1 can be derived as

$$F = \frac{2kEa}{2Ea + (1-v^2)k}\left(Z_t - \frac{a^2}{3R}\right) \quad (4)$$

which means the relations among the force F, the contact radius a, and the gross displacement Z_t considering the stiffness k. Using equation (4), the Young's modulus E, the stiffness k and the radius of curvature R can be evaluated by measuring the three parameters, the force F and the contact radius a and the gross displacement Z_t, simultaneously in the experiment. In the same manner, the elastic energy stored in the semi-infinite elastic body can be evaluated as

$$U_{\text{el.}} = \frac{4Ea^5}{45(1-v^2)R^2} + \frac{1-v^2}{4Ea}F^2 . \quad (5)$$

It is important that equations (4) and (5) can be derived based on the elastic theory without any assumption of equilibrium state of total energy. The interface energy is defined as the energy reduction due to the contact, expressed as

$$U_{\text{int.}} = -\pi a^2 \Delta\gamma \quad (6)$$

where $\Delta\gamma$ is work of adhesion, i.e. the required work to separate unit area of the interface. The stiffness energy is defined as

$$U_{\text{stif.}} = \frac{F^2}{2k} \quad (7)$$

which is the energy stored in the stiffness of the measurement system. And, the external work is defined as the work given from the outside, expressed as

$$U_{\text{ext.}} = \int F \mathrm{d}Z_t . \quad (8)$$

In the processes of loading and unloading of the gross displacement, there exists the energy dissipation, therefore, the relations of variation of the energy dissipation can be assumed as

$$\Delta U_{\text{dis.}} = \Delta U_{\text{ext.}} - \Delta U_{\text{el.}} - \Delta U_{\text{int.}} - \Delta U_{\text{stif.}} \quad (9)$$

where $\Delta U_{\text{dis.}}$, $\Delta U_{\text{ext.}}$, $\Delta U_{\text{el.}}$, $\Delta U_{\text{int.}}$, $\Delta U_{\text{stif.}}$ is the variation of the energy dissipation, the external work, the elastic energy, the interface energy, and the stiffness energy.

3 EXPERIMENT

In the experiments, the gross displacement Z_t is controlled by vertical motorized stage, and the force F and the contact radius a are measured simultaneously by the digital balance and the microscope as shown in Figure 2. The measurement system was set in the clean bench on the vibration isolation table. And, room temperature was set in 20°C and humidity was 35%.

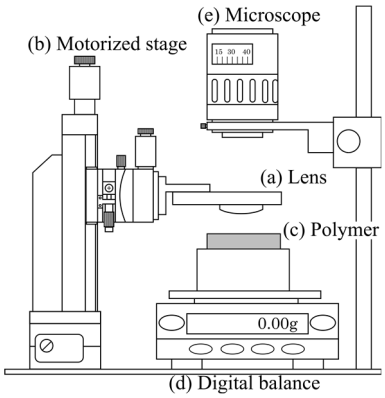

Figure 2. Schematic illustration of the experimental system. (a) Lens: silica glass lens with radius of curvature R_1=0.2076m and diameter of 40mm, (b) Motorized stage: motorized vertical movement with resolution 1μm/s, (c) Polymer: silicone rubber sheet with thickness 10mm and Young's modulus E=0.6-0.7MPa from tensile tester, (d) Digital balance: strain gauge type with resolution of 0.01g, (e) Microscope: resolution of 1600×1200pixcel.

In the present study, the loading process is defined as increasing of the gross displacement which means a downward direction of the motorized stage as positive. On the other hand, the unloading process is defined as decreasing of the gross displacement. The experiment need to be performed as static state as possible. So, the gross displacement is controlled by a step of 1μm/s, and waiting duration between steps is 60 seconds. The force and the contact radius are measured moment to moment per second, and data to be plotted are picked up just before the displacement changes. The loading and the unloading process are measured as a one cycle. And, the maximum loading displacements are chosen to be 30, 60 and 120μm for each cycle because there might be the region that the linear elasticity is not satisfied.

4 RESULTS AND DISCUSSIONS

The experimental results of 30, 60 and 120μm of each cycle are plotted as a relation of the gross displacement-force in Figure 3 and the gross displacement-contact radius in Figure 4. In the loading process of Figure 3, the tensile force is observed as an adhesive force at the initial contact, and then increasing of compressive forces between the lens and the silicone rubber are observed with increasing of the displacement. And, the increasing of the contact radius are also observed as shown in Figure 4. In the unloading process of Figure 3, the compressive forces are decreased until the maximum adhesive forces, and then the lens is detached from the silicone rubber. And, in the same process of Figure 4, the constant area of contact radius are observed at first, and progress of decreasing of the contact radius are observed. From this experimental results, the adhesion hysteresis, which is the differences in the loading path and the unloading path, is clearly observed in the each cycle. And, a dependence of the maximum loading displacement on the adhesion hysteresis is also observed in all the cycles.

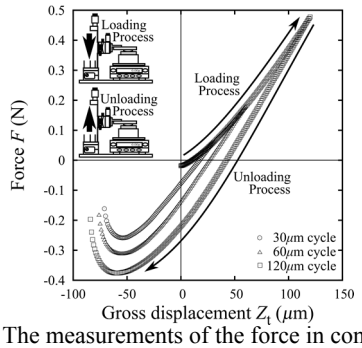

Figure 3. The measurements of the force in control of the gross displacement of the 30, 60 and 120μm cycle.

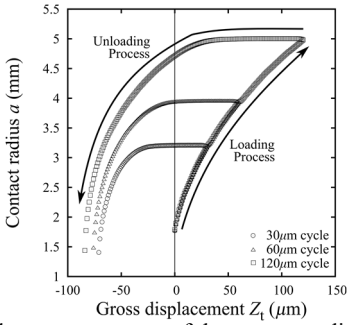

Figure 4. The measurements of the contact radius in control of the gross displacement of the 30, 60 and 120μm cycle.

4.1 EVALUATION OF R, E, k

Although the results of the each cycle in Figure 3 and 4 are not the equilibrium state of total energy, the balanced force of equation (4) as a function of gross displacement and contact radius must be satisfied in the linear elasticity area of the silicone rubber. Therefore, the unknown parameters R, E and k need to be evaluated using equation (4) with the measurements. First of all, the silicone rubber which is used in the experiment might not insure a perfectly flat surface. In case of the perfectly flat surface, R_2=∞ in equation (2) and R=R_1 is satisfied. If the silicone rubber is not a perfectly flat surface, however, R_2 affect the radius of curvature R. This affected R can be evaluated using equation (10) which is derived from equation (4) in condition of F=0 as

$$R = \left.\frac{a^2}{3Z_t}\right|_{F=0} \tag{10}$$

where the contact radius a and the gross displacement Z_t are the measured values of when the force F is zero in the gross displacement Z_t-intercept of Figure 3. Then, the radius of curvature R and R_2 are evaluated as shown in table 1.

Table 1. The radius of curvature.

R	Lens, R_1	Silicone rubber, R_2
0.1965m	0.2076m	3.6751m

R_2 of silicone rubber is larger than R_1 about 1700% in table 1 which shows a reasonable value in practical scale. Second, we need to evaluate the parameters of Young's modulus E and stiffness k. These two values are correlated each other as shown in equation (4). From fitting between the experimental results and equation (4) as a function of displacement and contact radius with E and k, therefore, finding the most well matched results by feedback adjustment of E and k simultaneously in the valid range of the E=0.6-0.7MPa. And, the results of fitting between the experimental results and equation (4) with evaluated parameters R, E, k as a function of displacement and contact radius are shown in Figure 5.

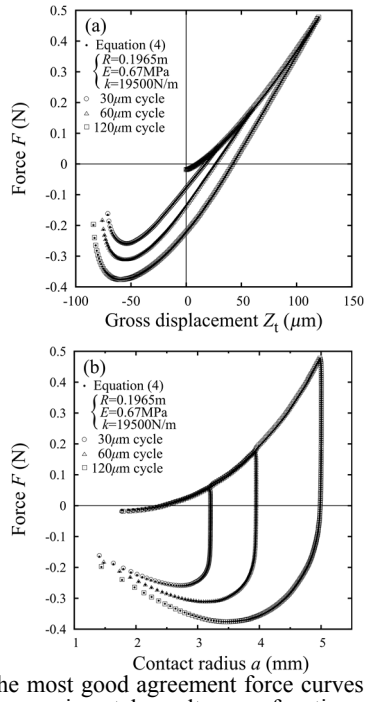

Figure 5. The most good agreement force curves of equation (4) with the experimental results as a function of the gross displacement (a) and the contact radius (b). Almost all plotted dots with R=0.1965m, E=0.67MPa and k=19500N/m are well matched with the measurements in (a) and (b). Also, this results means that the linear elasticity of the silicone rubber is satisfied in the deformation range of 120μm cycle or less.

4.2 EVALUATION OF $\Delta\gamma$

Each equation of the elastic energy (5), the stiffness energy (7) and the external work (8) can be calculated from using the experimental results and the evaluated values of R, E, k in Figure 5. In case of calculation of the interface energy (6), however, it is necessary to evaluate the work of adhesion $\Delta\gamma$ previously. So, from equations (6) and (9), equation (11) which have a term of $\Delta\gamma$ can be derived as

$$-\frac{\Delta U_{\text{ext.}} - \Delta U_{\text{el.}} - \Delta U_{\text{stif.}}}{\Delta(\pi a^2)} = \Delta\gamma - \frac{\Delta U_{\text{dis.}}}{\Delta(\pi a^2)} \tag{11}$$

where $\Delta U_{\text{ext.}}$, $\Delta U_{\text{el.}}$, $\Delta U_{\text{stif.}}$, $\Delta(\pi a^2)$ on the left-hand side can be calculated from using the experimental results and the evaluated values of R, E, k. The right-hand side of equation (11) can be divided for two term. The first term is the work of adhesion $\Delta\gamma$ defined as a physical property which has a constant value. And, the second term means the dissipated energy per unit changes of the contact area as a function of the contact radius. In briefly, the first term is constant and the second term is variable. The right-hand side of equation (11) can be observed as its left-hand side is already known. The work of adhesion might be evaluated from observing the variation state of the calculation results of equation (11). And, the calculation results of equation (11) as a function of the contact radius is shown as Figure 6. From Figure 6, the constant value is observed in the loading process. On the other hand, the variation is observed in the unloading process. This means that the constant value in the loading process can be assumed as the first term: the work of adhesion $\Delta\gamma$, because the variation of the second term cannot be observed in the loading process although Figure 6 is plotted as a function of the contact radius. Therefore, the work of adhesion can be evaluated as a $\Delta\gamma$=0.021J/m^2 from its loading process, and this physical property value will be constant in all the process of experiment.

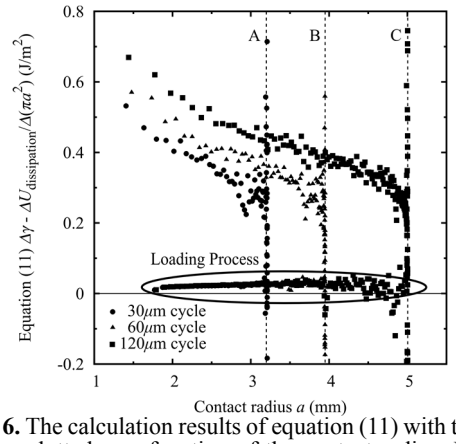

Figure 6. The calculation results of equation (11) with the each cycle are plotted as a function of the contact radius. Each of dotted line A, B, C is the constant area of contact radius of the initial unloading process as shown in Figure 3. So, the divergent along the A, B, C is observed, because the variation of contact area $\Delta(\pi a^2)$ is extremely small. The constant value observed in the loading process is circled.

5 ENERGY DISSIPATION AND CONCLUSION

Each equation of the elastic energy (5), the stiffness energy (7), the interface energy (6) and the external work (8) can be calculated from previous sections. So, the energy dissipation $U_{\text{dis.}}$ can be calculated from an integration of equation (9) as shown in Figure 7. From the results of Figure 7, the energy dissipation looks nearly zero in all the loading process. A tendency of linearly increase of dissipated energy as a function of the contact radius in the unloading process is observed. Therefore, this tendency of the energy dissipation can be written as

$$-\frac{\Delta U_{\text{dis.}}}{\Delta(2\pi a)} \qquad (12)$$

for its physical meaning that the dissipated energy of proportional to the variation of circumferential crack length of the contact area. The calculation results of equation (12) can be plotted as shown in Figure 8. The calculation results of equation (12) is nearly zero in the loading process. On the other hand, the results in the unloading process looks nearly constant that it can be approximated as a line D.

Therefore, it can be cleared that Figure 8 can schematically approximated to Figure 9. This shows that the energy dissipation is nearly zero in the loading process from $a_{\text{ini.}}$ to $a_{\text{max.}}$, and then the energy is dissipated as proportion to the circumferential crack length of the contact area as the constant value of equation (12) in the unloading process from the $a_{\text{max.}}$ to $a_{\text{det.}}$. Therefore, the energy is dissipated per unit length of variation of the circumferential crack only in the unloading process. From the results, the adhesion hysteresis can be explained as shown in Figure 10, which means that an unknown factor of the contact edge prevent the peeling between the lens and the rubber. This effect is non-reversible between the loading and unloading processes, and it can be suggested that this factor might be occurred due to the state of the interface between the materials, i.e. molecular bonding, surface roughness, dangling chains. Finally, the predictability of the adhesion hysteresis can be suggested from introducing the constant.

REFERENCES

[1] Y. Sekiguchi, et al.: *J. Adhesion Sci. Technol*., Vol. 26, No. 23 (2012), 2615
[2] K. L. Johnson, et al.: *Proc. R. Soc. London A* 324 (1971), 301
[3] M. Deruelle, et al.: *J. Adhesion Sci. Technol.*, Vol. 12, No. 2 (1998), 225
[4] K. Takahashi, et al.: *J. Adhesion Sci. Technol.*, Vol. 9, No. 11 (1995), 1451
[5] K. L. Johnson: *Tribology International,* Vol. 31, No.8 (1998), 413
[6] P. Silberzan, et al.: *Langmuir*, 10 (1994), 2466
[7] K. R. Shull: *Mater. Sci. Eng. R.* 36 (2002), 1
[8] E. Barthel: *J. Phys. D: Appl. Phys*., Vol. 41 (2008), 163001.
[9] Y. L. Chen, et al.: *J. Phys. Chem.*, Vol. 95, No. 26 (1991), 10736
[10] G. Y. Choi, et al.: *Langmuir*, Vol. 13, No. 23 (1997), 6333
[11] H. She, et al.: *Langmuir*, Vol. 14, No. 11 (1998), 3090
[12] Z. Wei, et al.: *J. Adhesion Sci. Technol.*, Vol. 24, No. 6 (2010), 1045
[13] H. Kesari, et al.: *Philos. Mag. Lett.*, Vol. 90, No. 12 (2010), 891

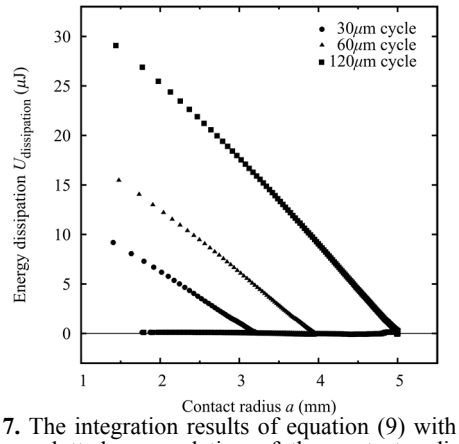

Figure 7. The integration results of equation (9) with all the cycles are plotted as a relation of the contact radius. The dissipated energy is nearly zero in the loading process of each cycle. On the other hand, the increasing of the energy dissipation are observed linearly with decreasing of the contact radius in the unloading process.

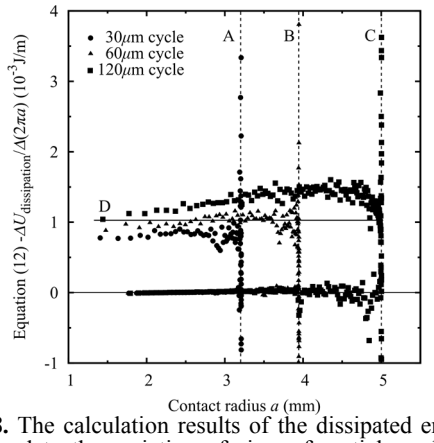

Figure 8. The calculation results of the dissipated energy of proportional to the variation of circumferential crack length (12). In each of dotted line A, B, C shows the divergent along the line in the constant area of contact radius of the initial unloading process. And, the factors that cause the energy dissipation in the unloading process of Figure 8 can be approximated as a line D.

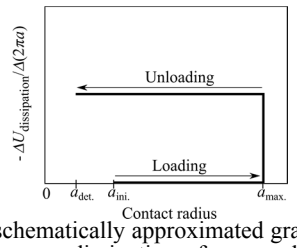

Figure 9. The schematically approximated graph of the factor that cause the energy dissipation of one cycle, where $a_{\text{ini.}}$ is initial contact radius, $a_{\text{max.}}$ is the radius when the maximum loading displacement, $a_{\text{det.}}$ is the radius when detached.

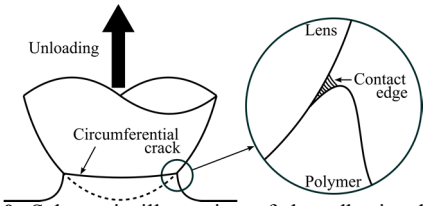

Figure 10. Schematic illustration of the adhesion hysteresis which is raised by the factor of the contact edge on the circumferential crack in the unloading process.

RADIO CHANNEL PARAMETER ESTIMATION USING SAGE ALGORITHM

Student Number: 12M18258 Name: PHAM Van Hue Supervisor: Jun-ichi TAKADA

SAGE アルゴリズムを用いたチャネルパラメタ推定法

Abstract

新無線伝送技術を開発するにあたり, 時空間電波伝搬特性の解明が重要な基盤となる. それに向け, 本研究では MIMO (Multiple-Input Multiple-Output) チャネルサウンダにおける高分解能伝搬パス推定法を開発した. 具体的には、パラメトリックモデルと多次元最尤推定を用いた SAGE (Space Alternating Generalized Expectation Maximization) アルゴリズムを用いて, 2.5ns の遅延分解能と 1 度の角度分解能を実現した. さらに, 開発した手法を用いて屋内環境における伝搬路特性を解析した.

1 Introduction

Recently, various applications of wireless services such as Mobile phones, Wi-Fi, Cellular data service, wireless sensor networks, wireless energy transfer, etc. are occupying most favorable electromagnetic spectrum for wireless communication (below 6 GHz band). Then, the design of future mobile radio networks (beyond the fourth generation-4G) requires research toward the characteristics of channels at higher frequencies where we could occupy a larger bandwidth. In addition, by using multiple antennas at both the transmitting and receiving sides of the communication link, MIMO systems are able to exploit the spatial diversity induced by the rich multipath environment, increase data rates and improve the quality of wireless link transmission. However, the performance of MIMO communication systems is strongly dependent on MIMO channel condition. In the radio channel model shows in Fig.1a, although the array antennas part and the propagation environment of the radio channel are complete different elements, they are treated as a single model. The array antennas part is a part of the transceiver and the engineer can design them as they want. On the other hand, the propagation environment is a natural phenomenon and we can not design or control it. Therefore, we come up with double directional channel model (Fig.1b). In this research, we focus on radio channel parameters estimation, which play a vital role in the process of double directional channel modeling.

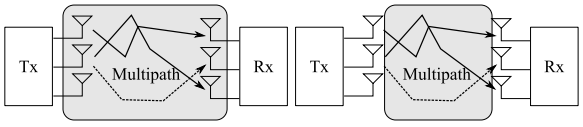

(a) Radio channel model (b) Double directional channel model

Figure 1: The distinction between radio channel model and double directional channel model

Parameter	Value
Carrier Frequency	11 GHz
Signal Bandwidth	400 MHz
No. of multitones	2048

Table 1: Specification of channel sounder

Figure 2: Channel Sounder

2 Radio channel measurement

The channel sounder is a device which is used to measure the radio channel. By using it, the time-variant impulse response is obtained. The channel sounder (Fig. 2), which has been used in this research, is prototyped firstly in [1]. Then it was developed for various purposes such as multilink channel measurement and double direction measurement. One of the important properties of this channel sounder is high multipath resolution, which can be seen from two aspects, spatial resolution and time-delay resolution. By using Uniform Circular Array (UCA) antennas with optimal design of beam in radiation pattern, it could achieve a high spatial resolution and maximum excess delay time of $5.12\mu s$ with very small delay-time resolution of $2.5ns$. An important factor which may affect measurement results is phase noise in signal source. Assuming that perfect frequency synchronism is possible between transmitter and receiver, the outputs of two quadrature demodulators results in a received signal vector with constant amplitude and fixed phase angle. However, this is in case of ideal frequency sources, which is almost impossible in implementation. We tried to reduce this effect as much as possible by using Cesium local oscillator as frequency source. The UCA antennas used in this research are dual-polarized micro-strip, has 12 vertical-polarized and 12 horizontal-polarized ports, which allow us to measure 24×24 MIMO channel. Radiation pattern is measured in an anechoic chamber in advance, and is used for radio channel parameter estimation process.

3 Radio channel estimation

3.1 Wide-band MIMO channel model

We introduce narrow-band MIMO channel model for single frequency bin [2] as follows

$$\mathbf{H}(f) = \sum_{l=1}^{L} \mathbf{a}_{\mathrm{R},l}\left(\varphi_{\mathrm{R},l}, \theta_{\mathrm{R},l}, f\right) \mathbf{\Gamma}_l \mathbf{a}_{\mathrm{T},l}^{T}\left(\varphi_{\mathrm{T},l}, \theta_{\mathrm{T},l}, f\right) e^{-\mathrm{j}2\pi f \tau_l}, \quad (1)$$

where $\mathbf{H}(f) \in \mathbb{C}^{M_{\mathrm{R}} \times M_{\mathrm{T}}}$, L is total number of paths considered in a environment, and $M_{\mathrm{T}}, M_{\mathrm{R}}$ is number of antennas elements at transmitter and receiver side, respectively. We also consider about dual-polarized complex path weight for each l-th path, given in tensor form

$$\mathbf{\Gamma}_l = \begin{bmatrix} \gamma_{\mathrm{VV},l} & \gamma_{\mathrm{VH},l} \\ \gamma_{\mathrm{HV},l} & \gamma_{\mathrm{HH},l} \end{bmatrix} \in \mathbb{C}^{2\times 2}. \quad (2)$$

Notice that the complex path weight $\mathbf{\Gamma}_l$, which is dual-polarized complex gain of the l-th path describes all effects which can be treated as frequency independent such as free space path loss, loss on scattering or reflection points, and so on. In the channel model (Eq.1), $\mathbf{a}_{\mathrm{R}}\left(\varphi_{\mathrm{R},l}, \theta_{\mathrm{R},l}, f\right)$ is array response at receiver which is expressed as a function of receive-azimuth ($\varphi_{\mathrm{R},l}$), co-elevation ($\theta_{\mathrm{R},l}$) and frequency f, and $\mathbf{a}_{\mathrm{T}}\left(\varphi_{\mathrm{T},l}, \theta_{\mathrm{T},l}, f\right)$ is array response at transmitter which is expressed as a function of transmit-azimuth ($\varphi_{\mathrm{T},l}$), co-elevation ($\theta_{\mathrm{T},l}$) and frequency f. The delay time τ_l corresponds to electrical length of propagation path of l-th path. This model is only applicable to narrow-band channels, but we are considering the wide-band channel model with bandwidth of interest $2B$. By reforming the matrix form of eq.1 to vector form and defining M_f as number of sampling points in frequency domain, we obtain the wide-band MIMO channel model as below.

$$\mathbf{s} = \mathfrak{B}(\boldsymbol{\mu}) \cdot \boldsymbol{\gamma} \in \mathbb{C}^{M_{\mathrm{R}}.M_{\mathrm{T}}.M_f \times 1} \quad (3a)$$
$$\mathfrak{B}(\boldsymbol{\mu}) \in \mathbb{C}^{M_{\mathrm{R}}.M_{\mathrm{T}}.M_f \times 4L}$$
$$\boldsymbol{\gamma} \in \mathbb{C}^{4L\times 1}$$

The matrix valued function $\mathfrak{B}(\boldsymbol{\mu})$ is a description of the structure of the radio channel. Here, we denote the nonlinear parameters $\boldsymbol{\mu} = \left[\boldsymbol{\tau}^T, \boldsymbol{\varphi}_{\mathrm{T}}^T, \boldsymbol{\theta}_{\mathrm{T}}^T, \boldsymbol{\varphi}_{\mathrm{R}}^T, \boldsymbol{\theta}_{\mathrm{R}}^T\right]^T$ also as structural parameters. The complex path weights matrix $\boldsymbol{\gamma} = [\gamma_{\mathrm{VV}}, \gamma_{\mathrm{HV}}, \gamma_{\mathrm{VH}}, \gamma_{\mathrm{HH}}]^T$ are linear weight for this model, which will be referred as linear parameters.

3.2 EM-based SAGE algorithm

3.2.1 Signal model

The general problem of interest here may be characterized by using the follow model

$$\mathbf{x} = \mathbf{s}(\boldsymbol{\theta}) + \mathbf{n} \quad (4a)$$
$$= \mathfrak{B}(\boldsymbol{\mu}) \cdot \boldsymbol{\gamma} + \mathbf{n} \in \mathbb{C}^{M\times 1} \quad (4b)$$
$$\mathfrak{B}(\boldsymbol{\mu}) \in \mathbb{C}^{M\times 4L}$$
$$\boldsymbol{\gamma} \in \mathbb{C}^{4L\times 1}$$

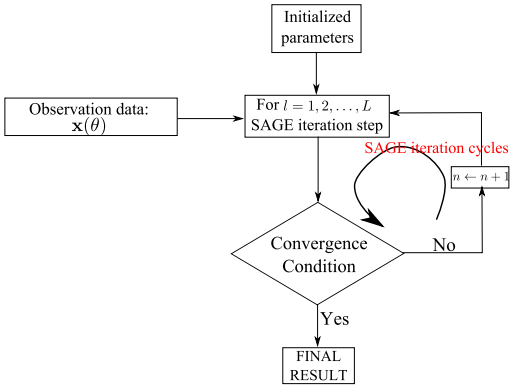

Figure 3: Signal flow chart of SAGE algorithm

with $M = M_{\mathrm{R}} \cdot M_{\mathrm{T}} \cdot M_f$. The desired signal is interrupted by additive white Gaussian noise, then the likelihood function or the probability density function (p.d.f) of $\mathbf{x}(\boldsymbol{\theta})$ is

$$p\left(\mathbf{x}; \boldsymbol{\theta}\right) = \frac{1}{(\pi)^M \det(\sigma^2 \mathbf{I})} \exp\left[-\frac{1}{\sigma^2}\left(\mathbf{x} - \mathbf{s}(\boldsymbol{\theta})\right)^H \left(\mathbf{x} - \mathbf{s}(\boldsymbol{\theta})\right)\right], \quad (5)$$

and the maximum likelihood estimation of $\boldsymbol{\theta}$ becomes

$$\hat{\boldsymbol{\theta}} = \arg\min_{\boldsymbol{\theta}} \left[\left(\mathbf{x} - \mathbf{s}\right)^H \left(\mathbf{x} - \mathbf{s}\right)\right]. \quad (6)$$

In order to solve Eq. 6, we come up with the SAGE algorithm.

3.2.2 SAGE algorithm

The SAGE algorithm, which is applied for radio channel parameters estimation [3], is a twofold extension of the Expectation Maximization (EM) algorithm. The basic concept of SAGE is *each iteration is an EM iteration to re-estimate not all but only a subset component of $\boldsymbol{\theta}_l$ while keeping the estimates of the other components fixed.* Figure 3 shows the signal flow chart of SAGE algorithm. Here, the *SAGE iteration step* is one EM iteration for an individual signal component. The *SAGE iteration cycle* consists of L *SAGE iteration step*s and we repeat SAGE iteration cycle until the likelihood function (Eq. 5) converges to its maximum value.

There are two major problems of SAGE algorithm. The first problem is how to initialize parameters as the input of SAGE. The second problem is how to manage the parameter search procedure. To deal with the first one, we use *Successive Interference Cancellation based Initialization Procedure (SIC-SAGE)*. The basic idea behind the SIC-based produced is as follows: The parameters vectors of the L waves are estimated successively. To estimate the parameter vector of l-th wave, an estimate of the interference caused by the previously estimated waves is calculated and subtracted from the measurement data. To do this, we are using the first SAGE iteration cycle to detect strong path and remove it from measurement data. The second one could be solved with Initialization and Search Improved (ISI-SAGE) by using *adaptive grid search*, a search procedure with grid size being decreased during the search produce.

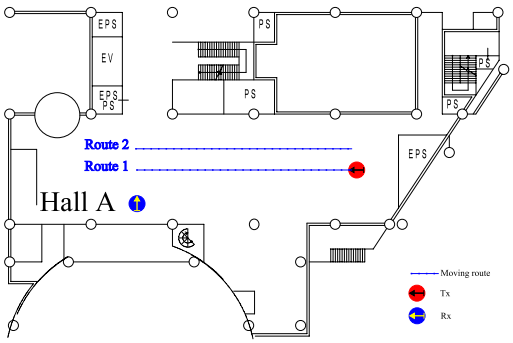

Figure 4: Floor plan view of the measurement environment

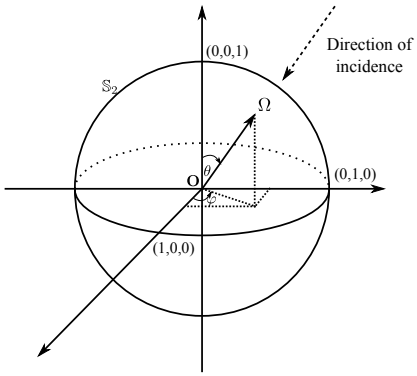

Figure 5: Characterization of an incidence direction

We will apply this algorithm and using channel model in Eq.3a for real channel measurement data in the next section.

4 Indoor environment analysis

4.1 Measurement campaign

The measurement environment layout is shown in Fig.4. The measurement campaign was carried out in a wide area, which could be used for large events. The material of hall A is reinforced concrete, and some areas have metal plate flooring. On each route (20m-long route), transmit antennas are moving on these route, we take a total of 280 snapshots, and distance between two snapshots is about 7 cm (about 2.5λ). We only choose measurement points which has distance of 10λ for further analysis because of computation complexity. This scenario is considered as a stationary environment, meaning there are no moving objects (the measurement was taken on holiday). The red and blue circles represent the position of transmitter and receiver antennas, respectively. The direction of arrows in these circles represent the direction of the first element of UCA, which means the direction of zero degree direction of each local coordinate.

4.2 Characterization of radio channel

4.2.1 Direction spread

To characterize the direction spread, we have to consider both azimuth and co-elevation [4]. We describe a direction as a unit vector $\mathbf{\Omega}$ with the initial point at $\mathbf{O}$ and the terminal point is located on a sphere $\mathbb{S}_2$. This vector has unit radius as shown in Fig.5. The vector unit $\mathbf{\Omega}$ is uniquely determined by its spherical coordinates $(\varphi, \theta) \in [-\pi, \pi) \times [0, \pi]$ according to the relation

$$\mathbf{\Omega} = e(\varphi, \theta) = [\cos\varphi \sin\theta, \sin\varphi \sin\theta, \cos\theta]^T \ . \quad (7)$$

The path weight of each direction is normalized by the total path weight, then the mean direction could be expressed by

$$\mu_{\mathbf{\Omega}} = \frac{1}{P_{sn}} \sum_{l=1}^{L} \{e(\varphi_l, \theta_l) \cdot P_l\} \ . \quad (8)$$

The mean of azimuth $\bar{\varphi}$ and the mean of co-elevation $\bar{\theta}$ are obtained from $\mu_{\mathbf{\Omega}}$ as the solution of the nonlinear equation

$$e(\bar{\varphi}, \bar{\theta}) = \frac{1}{|\mu_{\mathbf{\Omega}}|} \mu_{\mathbf{\Omega}} \ . \quad (9)$$

The rms direction spread can be finally expressed as

$$\sigma_{\mathbf{\Omega}} = \sqrt{\frac{1}{P_{sn}} \sum_{l=1}^{L} \left\{ \|e(\varphi_l, \theta_l) - \mu_{\mathbf{\Omega}}\|^2 \cdot P_l \right\}} \quad (10)$$

$$\sigma_{\mathbf{\Omega}} = \sqrt{1 - \|\mu_{\mathbf{\Omega}}\|^2} \ . \quad (11)$$

From Eq. 11, we obtain $\sigma_{\mathbf{\Omega}} = 0$ and $\sigma_{\mathbf{\Omega}} = 1$, if and only if $|\mu_{\mathbf{\Omega}}| = 1$ and $\mu_{\mathbf{\Omega}} = 0$, respectively.

4.2.2 Cluster Identification

The clustering of paths is a problem that has recently drawn a lot attention. Visual clustering has been used for long time, but visual identification of clusters contains a certain level of uncertainly and interpretation, also very difficult to deal with huge amount of data. In this section, we represent an automatic clustering algorithm for estimated paths. In this research, we are using a definition of cluster which was used in COST 259: A cluster is a group of paths with similar propagation characteristics. The clustering algorithm will be used here is *K-means clustering algorithm* [5]. This algorithm gives a locally optimal solution with the given number of clusters. The idea of this algorithm, an iterative algorithm, is *minimizing* the total sum of the *distance of paths* to their clusters centroid. However, one drawback of this algorithms is numbers of cluster should be determined before clustering identification, then we introduce Kim-Parks Index to decide the number of cluster. This index measures the ratio between the global intra-cluster spread and inter-cluster minimum distance, which should be minimized.

4.3 Result

Individual propagation paths have been extracted from measurement snapshots using SAGE algorithm developed in Section 3. For each measurement snapshot, 100 paths were detected. We used a global search for initialized parameters, and in order reduce computation time, search grid size becomes half for each SAGE iteration cycle. Each snapshot converges after 8-12 SAGE iteration cycles. For Route 1, the mean of residual power is about 37.8%.

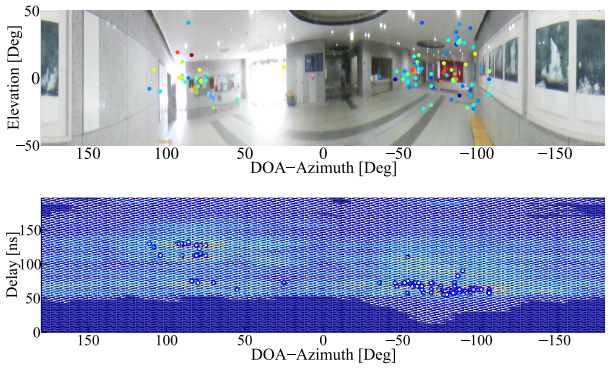

Figure 6: Matching SAGE detected-paths with panorama view from Rx and comparison with beamforming result

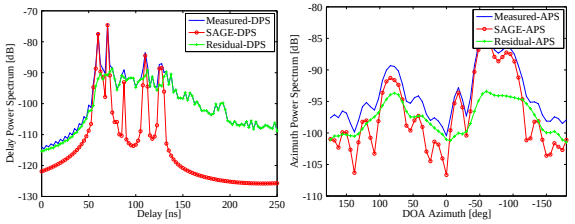

(a) DPS (b) APS

Figure 7: Measured, SAGE reconstructed and the residual DPS and APS

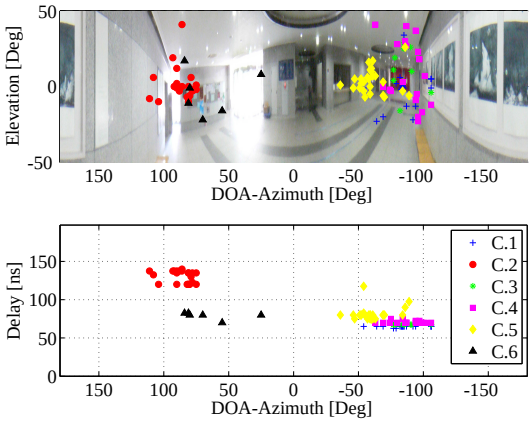

Figure 8: Cluster identification with $K = 6$

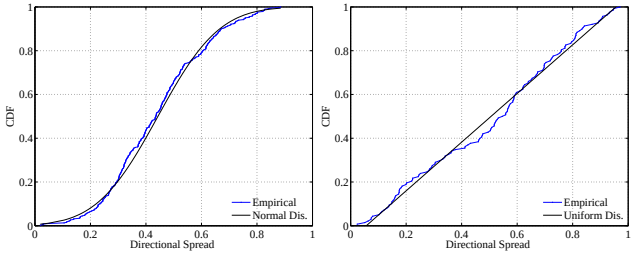

(a) Intra Cluster (b) Inter Cluster

Figure 9: CDF of rms direction spread of all clusters on Route 1

An example of path extraction is given in Fig. 6 with the color represent the path weight in power. We lay over the SAGE-detected paths on the panorama picture of environment and compare between SAGE-detected paths and beamforming result. We could see that detected paths are almost matched well with beamforming result. Furthermore, Fig. 7 shows the Delay Power Spectrum (DPS) and the Azimuth Power Spectrum (APS) of measured channel and reconstructed channel using SAGE estimation result. The strongest delay bins are estimated correctly in Fig. 7a. This is very important because in transmission, only strong signals are used. Figure 7b shows the directivity of channel, and we could see that the signals mostly come from the Line of Sight direction, reflected by side walls and back walls. We also did the cluster identification for Route 1; the result for first snapshot is shown in Fig. 8 with number of cluster $K = 6$. The number of clusters vary from 2 to 7. Finally, rms direction spread for intra-cluster and inter-cluster is shown in Fig. 9. From the cumulative distribution function (cdf) of them, we find that rms direction spread for intra-cluster follows the normal distribution, but rms direction spread of inter-cluster follows the uniform distribution.

5 Conclusions and future work

As conclusions in this research, we have shown the implementation of SAGE algorithm for wide-band radio channel parameters estimation and analysis of indoor radio channel spatial domain based on SAGE estimation result and cluster-based model. For future work, in terms of *radio channel estimation*, the estimation accuracy could be increased by reducing the mismatch of proposed channel model with reality, as well as the calibration of used UCA. One more point, in terms of *estimation algorithm*, the SAGE is an iterative algorithm to solve the optimal problem, but the waste of computing resource can not be denied. Gradient-based algorithm is well known as a better method to solve this problem mathematically. However, it requires a continuous information of antennas mathematically, which is difficult in implementation.

References

[1] Y. Konishi, M. Kim, M. Ghoraishi, J. Takada, S. Suyama, and H. Suzuki, "Channel Sounding Technique using MIMO Software Radio Architecture," *Eur. Conf. Antennas Propag.*, pp. 2546-2550, 2011.

[2] A. Richter, "Estimation of radio channel parameters: Models and algorithms," Doctoral Thesis, Ilmenau University of Technology, 2005.

[3] B. H. Fleury, M. Tschudin, R. Heddergott, D. Dahlhaus, and K. I. Pedersen, "Channel parameter estimation in mobile radio environments using the SAGE algorithm," *IEEE J. Sel. Areas Commun.*, vol. 17, no. 3, pp. 434-450, 1999.

[4] B. H. Fleury and S. Member, "First- and Second-Order Characterization of Direction Dispersion and Space Selectivity in the Radio Channel," *IEEE Trans. Inf. Theory*, vol. 46, no. 6, pp. 2027-2044, 2000.

[5] J. MacQueen, "Some methods for classification and analysis of multivariate observations," *Proc. fifth Berkeley Symp. Math. Stat. Probab.*, vol. 233, no. 233, pp. 281-297, 1967.

STUDY ABOUT ANTENNA DE-EMBEDDING FROM 2-DIMENSIONAL PROPAGATION CHANNEL AROUND SCATTERING OBJECT

Student Number: 12M18146 Name: Osamu Watanabe Supervisor: Jun-ichi TAKADA

二次元モデルを用いた散乱体近傍でのアンテナと伝搬路の分離に関する研究

渡邉 修

送受信のアンテナを伝搬環境と切り離す方法であるアンテナディエンベディングを行うために、送信アンテナ、受信アンテナが互いに非常に接近している状況を考える際に、離れている状況とどのような変化が現れるかを必要になるモードの数と、それによって現れる受信点での推定誤差の変化を観察した。なおシミュレーションには境界要素法で二次元電磁界シミュレータを構築し利用した。

1 Introduction

As one of the method to separate simulation domain into antenna domain and environment domain there is a technique called antenna de-embedding. Antenna de-embedding is a technique to separately model antennas and propagation channel. Radio channel consists of transmitter (Tx) antenna, propagation channel, and receiver (Rx) antenna. Among these three elements, Tx and Rx antennas are the parts of the radio equipments which can be optimally or suboptimally designed. In contrast, propagation channel is a kind of natural phenomenon which can not be controlled nor designed. Therefore, the antenna de-embedded propagation channel can be used to evaluate the influence of antennas to radio channel property.

Antenna de-embedded propagation channels have been modeled as double-directional channel model [Steinbauer], represented by direction of departure at Tx antenna and direction of arrival at Rx antenna, assuming plane waves. This model is matching with the representation of antenna radiation pattern in angular domain. Recently, an alternative approach of using spherical wave functions has been proposed [Nakai, Miao]. In this approach, antenna radiation characteristics are represented by sum of spherical wave functions (mode), and the propagation channel is represented as the coupling matrix between Tx antenna mode and Rx antenna mode. The advantage of this approach is the natural truncation of modes due to the cut-off property of spherical wave function determined by size of antenna.

The objective of this study is to examine the applicability of propagation channel modeling by using spherical wave function when scatterer is in proximity to either or both of antennas. A typical example is a wireless body area channel where wearable devices communicate each other. Instead of using full three-dimensional (3D) model, this study handles simplified two-dimensional (2D) model for fast simulation. The cut off properties of spherical and cylindrical modes are very similar, and results of this study can be easily applicable for 3D case. Antenna areas are modeled by circles, and the fields at the perimeter of them are modeled by using cylindrical wave functions.

Specifically, this study tried to know the influences of the scatterer in proximity to antenna(s) on 1) the required number of modes and 2) the required sampling interval on the circular perimeter, to accurately model the channel response.

Transmitted wave is decomposed into certain number of order of cylindrical eigenmodes and the channel. Propagation matrix in terms of Tx and Rx eigenmodes.

2 Theory of Antenna De-embedding in 2D

Conducting the antenna de-embedding, first Tx antenna and Rx antenna is expressed with sum of cylindrical wave functions (modes) Next, antenna de-embedded propagation channel is introduced in the form of the matrix. Then error is defined so that accuracy of the method can be estimated quantitatively.

2.1 Cylindrical wave function expansion

As the homogeneous solution of Helmholtz equation in the cylindrical coordinates

$$\mathbf{E} = \sum_{n=-\infty}^{\infty} q_n Z_n(k_0\rho)e^{jn\varphi} \tag{1}$$

$\mathbf{E}$ is electromagnetic field, ρ is distance form the center of coordinate and φ is its angle. k_0 is wave number in a medium. Z_n is a nth order of Bessel function and q_n is a coefficient at the order. arbitrary electric field outside the antenna region can be represented as

$$\varphi = \sum_{-M}^{M} C_n H_n^{(2)}(k_0\rho)e^{jn\varphi}. \tag{2}$$

M is natural number which can be given depend on the size of the boundary region. When information of the electromagnetic field at the boundary is provided, field information inside the antenna region is fixed, the theory known as field equivalent theory.

Let us set the boundary in a shape of circle and find the coefficients q_n of the electromagnetic field inside antenna region. When the field at the boundary is written as $\mathbf{E}^{\mathrm{Bound}}$. Let us assume we have some $\mathbf{F}$ provides transformation

$$\mathbf{E}^{\mathrm{Bound}} = \mathbf{F}\mathbf{q}^{\mathrm{Bound}} \tag{3}$$

We can obtain q_n by solving

$$\mathbf{q}^{\mathrm{Bound}} = \mathbf{F}^{-1}\mathbf{E}^{\mathrm{Bound}} \tag{4}$$

$\mathbf{F}$ is actually written as

$$F_{nm} = Z_n(\rho)e^{jn\phi_m}. \tag{5}$$

and ϕ_m is discretized as follows

$$\phi_m = (m-1)\Delta\phi,\ \ \Delta\phi = 2\pi/M \tag{6}$$

Bessel function Z_n have to be selected depend on the existence of singular point inside antenna region. $H_n^{(2)}$ is used to satisfy the radiation condition at Tx antenna side, while J_n is used to represent the non-singular field at Rx antenna side.

2.2 Modeling of propagation channel by using mode-to-mode coupling

When Tx and Rx antenna's radiation characteristic is represented by modes, we can assume there to be exist mode-to-mode coupling as a relationship between Tx and Rx antenna modes. If we have boundary around Tx and Rx antenna to measure the boundary field at the boundary, by naming electric field at the boundary of Tx antenna as $\mathbf{E}^{\mathrm{TX}}$ and electric field at Rx antenna as $\mathbf{E}^{\mathrm{RX}}$. $\mathbf{q}^{\mathrm{TX}}$ and $\mathbf{q}^{\mathrm{RX}}$is written as

$$\mathbf{q}^{\mathrm{TX}} = \mathbf{F}^{-1}\mathbf{E}^{\mathrm{TX}} \tag{7}$$

$$\mathbf{q}^{\mathrm{RX}} = \mathbf{F}^{-1}\mathbf{E}^{\mathrm{RX}}. \tag{8}$$

Assuming $\mathbf{M}$ exists which satisfy mode-to-mode coupling between $\mathbf{q}^{\mathrm{RX}}$ and $\mathbf{q}^{\mathrm{RX}}$. The equation is written as

$$\mathbf{q}^{\mathrm{RX}} = \mathbf{M}\mathbf{q}^{\mathrm{TX}} \tag{9}$$

$\mathbf{M}$ becomes the matrix which embed the information of propagation channel. When this matrix $\mathbf{M}$ satisfy arbitral $\mathbf{q}^{\mathrm{TX}}$ and $\mathbf{q}^{\mathrm{RX}}$, once $\mathbf{M}$ derived channel propagation will be calculated without simulating Tx and Rx antenna directly.

This matrix $\mathbf{M}$ is derived below. When the n th mode is desired number of mode, total number of mode that the field decomposed into becomes $2n+1$ which is between $-n$ to n. Therefore the size of the each vector $\mathbf{q}^{\mathrm{TX}}$, $\mathbf{q}^{\mathrm{RX}}$ becomes $2n+1$. Thus $\mathbf{M}$ becomes square matrix size of $(2n+1)\times(2n+1)$ Assuming the $\mathbf{M}$ is regular, solving simultaneous equation,

$$(\mathbf{q}_1^{RX}, \cdots, \mathbf{q}_{2n+1}^{RX}) = \mathbf{M}(\mathbf{q}_1^{TX}, \cdots, \mathbf{q}_{2n+1}^{TX}) \tag{10}$$

$\mathbf{M}$ is obtained.

Using the equations (7) to (9) the relationship between $\mathbf{E}^{\mathrm{TX}}$ and $\mathbf{E}^{\mathrm{RX}}$ can be expressed as

$$\mathbf{E}^{\mathrm{RX}} = \mathbf{F}^{(\mathrm{RX})}\mathbf{M}\mathbf{F}^{(\mathrm{TX})-1}\mathbf{E}^{\mathrm{TX}}. \tag{11}$$

2.3 Definition of error

Errors which can occur related to antenna de-embedding has some reason. One is due to the cutting off at the choice of highest modes. Others is due to error at the calculation of (11) rooted from error at $\mathbf{M}$. To evaluate the accuracy of the antenna de-embedding method, it is reasonable to focus on the error at derived electromagnetic field at the boundary of Tx and Rx antenna. NMSE(Nomralized Mean Square Error) is derived as written in equation

$$\mathrm{NMSE} = \frac{\sqrt{\sum_{n=1} |E_{\mathrm{n}}^{-\mathrm{B(rec)}} - E_{\mathrm{n}}^{-\mathrm{B}}|^2}}{\sqrt{\sum_{n=1} |E_n^{-\mathrm{B}}|^2}} \tag{12}$$

$E_n^{-\mathrm{B}}$ is ideal electric field at the boundary in a discreet notation at the boundary E^{Bound}. $E_{\mathrm{n}}^{-\mathrm{B(rec)}}$ is reconstructed wave using mode information $\mathbf{q}$

3 Simulation result

In this section, the error related to the cutoff of the modes and accuracy of antenna de-embedding in certain situation will be discussed.

3.1 Calculation of error due to cutoff

Error related to reconstruction of the electric field at the boundary is largely related to the size of the boundary to be used as observation. However even in the case that the size of the boundary circle to observe field is fixed, higher order of modes observed when there is large disturbance of the field exists near observer. To estimate how many order of modes are required at certain situation, parameter study have conducted. Distance between Tx antenna, Rx antenna and scattering object have changed.
Study have done changing,
1) Distance between Tx antenna and Rx antenna without existence of scattering object.
2) Distance between scatting object and Rx antenna when Tx antenna is located at far away.
3) Distance between Tx antenna and Rx antenna with scattering object located near the Tx antenna.

Error have calculated defined in 2.3. Distance is taken in x axis. Threshold have set in the NMSE values of 0.05 and 0.01 and minimum number of mode to satisfy this accuracy is taken as Y axis.

3.1.1 1) Distance change between Tx antenna and Rx antenna without scattering object

Figure 1 shows minimum required number of modes to satisfy error NMSE lower than 0.05 and 0.01 each. x axis is the distance between Tx and Rx antenna. Required number of modes increases when the distance between Tx and Rx antenna get closer when the distance is closer than 0.1λ.

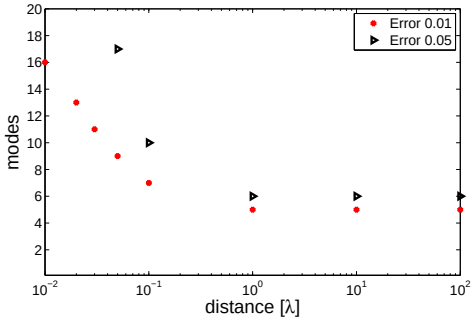

Figure 1: Required number of mode with change of distance between Rx and Tx antenna (without scatting object)

3.1.2 2) Distance change between Scatting object and Rx antenna when Tx antenna is located at far away

Figure 2 is the case of Tx antenna is located far away the distance of (100λ) from scattering object and Rx antenna both. As a scattering object circular object with diameter of 2λ perfect electric conductor. Minimum required number of modes to satisfy error NMSE lower than 0.05 and 0.01 each. x axis is the distance between scatting object and Rx antenna. Figure 2 does not show huge change in minimum required modes for both case of 0.05 and 0.01, with

the change of distance between Rx antenna and scattering object. It can be said that scattering object does not disturb the field large enough to create higher mode around Tx antenna because the size of scattering object is relatively large compare to the wave length.

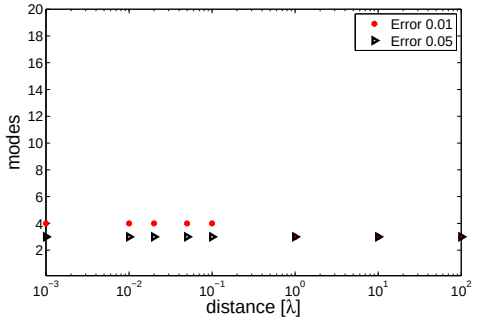

Figure 2: Required number of mode with change of distance between Scatting object and Rx antenna (Tx antenna located far)

3.1.3 3) Distance between Tx antenna and Rx antenna with scattering object located near the Tx antenna.

Figure 3 is the case of Tx antenna and Scattering object is located with distance of 0.1λ from Tx antenna. As a scattering object, circular object with diameter of 2λ perfect electric conductor is used. x axis is the distance between Tx and Rx antenna.

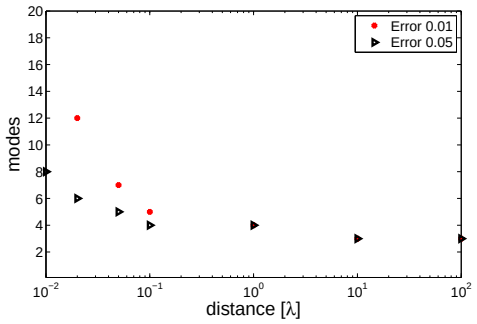

Figure 3: Required number of mode with change of distance between Tx and Rx antenna (Scattering object located close)

3.2 Estimation of mode-to-mode coupling matrix

Matrix $\mathbf{M}$ is derived here which is the most important for antenna de-embedding process. Then using the obtained matrix $\mathbf{M}$ is used to obtain $\mathbf{E}^{\mathrm{RX}}$ by using only using $\mathbf{E}^{\mathrm{TX}}$ as the Tx antenna information.

3.2.1 Preparation of initial wave

To estimate M written in Section2.2, it is necessary to obtain set of vector $\mathbf{q}^{\mathrm{TX}}$、$\mathbf{q}^{\mathrm{RX}}$ as much as $2n+1$ and they have to be independent each other. To achieve this initial wave is located as figure 4 shows. By illuminating initial wave at different location one by one, I have tired to create independent $2n+1$ number of vector.

Radius of 0.1λ is used as observation boundary circle. Inside the circle sampling initial wave is placed at over the circle of 0.9 times of the observation boundary. The distance between each sampling initial wave is equally placed by shifting θ. TX_1、TX_2 are sample of them.

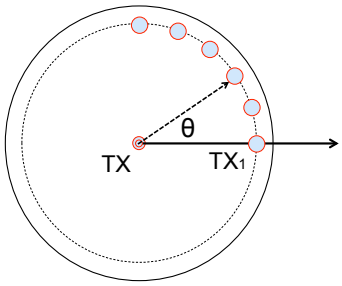

Figure 4: Location of sampling initial wave

3.2.2 Estimated Matrix

Using the vectors $\mathbf{q}^{\mathrm{TX}}$、$\mathbf{q}^{\mathrm{RX}}$ obtained in 3.2.1, $\mathbf{M}$ can be derived. By simply mapping them 5 can be obtained to represent relationship between Tx antenna and Rx antenna modes.

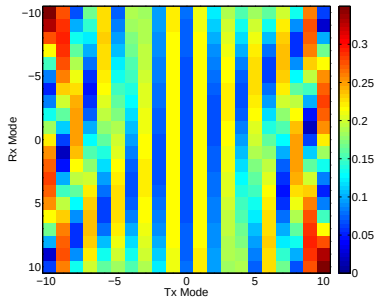

Figure 5: Colour map

This shows which mode is highly related to one mode.

3.2.3 Reconstruction of waves

Once matrix is derived shown as 図 5 smaller order of mode can be estimated with Rx antenna. By using it, receiving mode can be translated into Rx field at the boundary. There is a result calculating receiving wave when it is assumed that the sampling of the wave have done enough dense.

Figure 6 is the prepared mode as a sample Tx mode to conduct estimation of Rx field using antenna de-embedding method. Estimated wave using antenna de-embedding method and result of electromagnetic field directly calculated is compared in figure 7

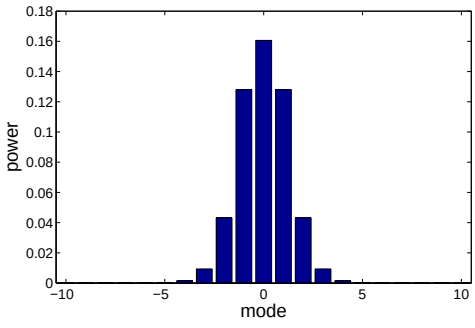

Figure 6: Sample wave to test antenna de-embedding

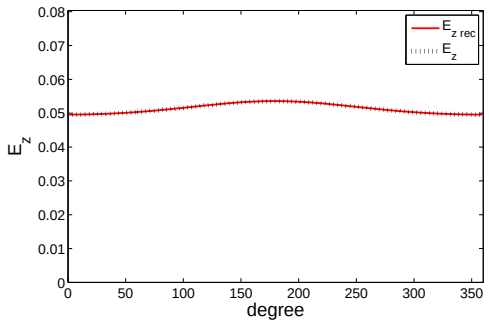

Figure 7: Comparison of ideal field and reconstructed field

Figure 7 shows the almost perfect fit with estimated field and ideal field. When the NMSE is calculated in this case, NMSE $=6.1 \times 10^{-7}$ is obtained which mean perfectly the wave is reconstructed.

4 Result and future work

Required mode considering 2D antenna de-embedding have estimated for NMSE of 0.01 and 0.05. Shown the antenna de-embedding's applicability near the scattering object when the sampling point is taken enough dense.

There will be need of conducting research using dielectric material and in the case of 3D situation which is more realistic situation.

References

[1] C. A. Balanis, "Advanced Engineering Electromagnetics," John Wiley Sons, 1989.

[2] N. Morita et al, "Integral Equation Methods for Electromagnetics," Artech House, 1991.

[3] R. E. Collin, "Evaluation of Antenna Q" IEEE Transactions on antennas and propagation., pp. 23-27,1964.

[4] Kenji. N et al, "Double-directional channel with the spherical harmonics" Technical Report of IEICE., pp. 113-117,2010.

Development of MIMO Antenna Evaluation Method using Channel Capacity and LTE throughput utilizing Extended Kronecker Model

Student Number: 12M18123 Name: Yuta Maruichi Supervisor: Jun-ichi TAKADA

拡張クロネッカモデルを用いたチャネル容量及び LTE スループットによる MIMO アンテナ評価手法の開発

学籍番号: 12M18123 氏名: 丸一 雄大 指導教官: 高田 潤一

MIMO 技術に使用されるアンテナの性能は、周囲の環境の影響を強く受けるので、アンテナの評価のためには、アンテナ単体だけではなく、通信路容量、スループットなどシステム全体を評価する指標を使う必要がある。本論文では、MIMO チャネルモデルとして拡張クロネッカモデルを用い、LTE シミュレータを使用して MIMO 通信路の固有値と LTE スループットを予め対応表として作成しておくことで LTE スループットを簡易的に推定する方法を提案し、通信路容量と LTE スループットにより MIMO アンテナを評価した。

1 Introduction

Recently, many people use smartphones and tablets and demand for higher data rate is still growing. To satisfy this increase in demand, MIMO (Multiple Input and Multiple Output) technique, which uses multiple transmitter antennas and receiver antennas, has been adopted for many systems such as Wireless LAN (Local Area Network) and LTE (Long Term Evolution). Of course, to maximize the MIMO system performance , we have to select the best MIMO antenna from antenna candidates, so we have to evaluate those antennas by some antenna evaluation criteria.

Antenna directivity and efficiency are widely used as the fundamental parameter for SISO(Single-Input Single-Output) antenna evaluation parameters. However, these parameters are not sufficient for MIMO antenna evaluation because MIMO system performance is dependent on the field environment. So, the antenna should be evaluated considering the environment by the whole system evaluation parameters such as channel capacity, and throughput. Particularly, throughout is a more realistic criterion than capacity, hence research which calculate the throughput for MIMO antennas evaluation are very actively conducted[1].

To measure the throughput, which are three estimation methods, field measurement, MIMO-OTA(Over The Air) test, and software simulation, are mainly used. For the first one, field measurement, we directly measure the throughput through field measurements. The throughput is the actual user throughput and a much more realistic parameter, but it needs a lot of costs for measurements. Moreover, it is difficult to get reproducibility in field measurements because the actual user throughput is dependent on the number of users in a cell. The second one, MIMO-OTA test, is where we construct a room which models an outdoor environment and measure the throughput in the room. The room is fixed, so we can get the reproducible throughput, but the room construction cost is not negligible. The third one, simulation software, is where we get throughput by using computing software. It has flexibility that we can change any environment parameters, but even simulation software needs software development /purchasing costs. Thus, the current estimation methods are not cost efficient to estimate the throughput.

In this research, a simple LTE throughput estimation method that utilizes eigenvalues of the MIMO channel matrix is proposed. In addition, in the software simulation, it is necessary to model a real environment, and the Kronecker model is one popular method to simulate a MIMO channel in a NLOS (non-line-of-sight) environment. However, the conventional Kronecker model does not include polarization effects, so the model should be extended for general usage. Thus, the extended Kronecker model is introduced. Finally, the real antennas attached on a car are evaluated by the proposed method and LTE throughput is compared with channel capacity.

2 Antenna evaluation criteria

For single antenna evaluation, directivity and efficiency are used as classical parameters. Directivity is the parameter which expresses the directive gain of an antenna, and efficiency expresses the ratio between total radiated power from an antenna and the power that an antenna receives from the transmitter. Those parameters represent fundamental performance of a single antenna.

However, for MIMO antenna evaluation, those parameters are not enough to evaluate the performance, because the whole system performance of MIMO is dependent on the multi-path environment. To include the multi-path environment, angular power spectrum (APS) should be included in addition to directivity and efficiency. Mean effective gain (MEG) and antenna correlation are introduced as parameters which include the APS model[2]. MEG is calculated by the following equation,

$$\begin{aligned} G_e &= \frac{1}{1+X}\int_0^{2\pi}\int_0^{\pi}\left\{X|E_\theta(\theta,\phi)|^2 P_\theta(\theta,\phi)\right. \\ &+ \left.|E_\phi(\theta,\phi)|^2 P_\phi(\theta,\phi)\right\}\sin\theta d\theta d\phi, \end{aligned} \quad (1)$$

where X denotes the cross correlation ratio, E_θ and E_ϕ denote the directivity of vertical polarization and horizontal polarization respectively, and P_θ and P_ϕ denote the normalized vertical APS and horizontal APS,

respectively. In the same manner as MEG, the antenna correlation can be derived from the following equation,

$$\rho_{i,j} = \frac{1}{1+X}\left|\int_0^{2\pi}\int_0^{\pi}\left\{X\frac{E_{\theta i}(\theta,\phi)E^*_{\theta j}(\theta,\phi)P_\theta(\theta,\phi)}{G_{ei}G_{ej}} + \frac{E_{\phi i}(\theta,\phi)E^*_{\phi j}(\theta,\phi)P_\phi(\theta,\phi)}{G_{ei}G_{ej}}\right\}\sin\theta d\theta d\phi\right|^2, \quad (2)$$

where i, j denotes the antenna number, and $\otimes$ denotes the Kronecker product. In general, MIMO antennas which have high MEG shows better performance, and MIMO antenna combinations which have high antenna correlation harms the system performance.

3 MIMO channel model

3.1 Stochastic MIMO channel

The narrowband MIMO transmission model with N_{BS} base station antennas and N_{UT} user terminal antennas is given as

$$\mathbf{y}(t) = \mathbf{H}\mathbf{x}(t) + \mathbf{n}(t), \quad (3)$$

where $\mathbf{y}(t)$ denotes the N_{BS} dimensional received signal vector, $\mathbf{x}(t)$ denotes the N_{BS} dimensional received signal vector, $\mathbf{n}(t)$ denotes N_{UT} dimensional receiver noise, and $\mathbf{H}$ denotes $N_{\mathrm{UT}} \times N_{\mathrm{BS}}$ dimensional MIMO channel matrix.

In the NLOS environment, each element of $\mathbf{H}$ follows the Rayleigh fading. To characterize the statistics of $\mathbf{H}$, MIMO fading correlation matrix $\mathbf{R}_{\mathrm{MIMO}}$ is defined as

$$\mathbf{R}_{\mathrm{MIMO}} = E[\mathrm{vec}(\mathbf{H})\mathrm{vec}(\mathbf{H})^H], \quad (4)$$

where

$$\mathrm{vec}(\mathbf{H}) = [h_{11}, \cdots, h_{N_{\mathrm{UT}}1}, h_{12}, \cdots, h_{N_{\mathrm{UT}}N_{\mathrm{BS}}}]^T. \quad (5)$$

3.2 MIMO channel capacity

MIMO channel matrix can be decomposed by singular value decomposition(SVD) as equivalent multiple SISO channels as

$$\mathbf{H} = \mathbf{U}\mathbf{\Sigma}\mathbf{V}^H, \quad (6)$$

where Σ is a real diagonal matrix, $\mathbf{V}$ and $\mathbf{U}$ are $N_{\mathrm{UT}} \times N_{\mathrm{UT}}$ dimensional and $N_{\mathrm{BS}} \times N_{\mathrm{BS}}$ dimensional unitary matrix respectively. So, the MIMO channel capacity can be calculated by the sum of multiple SISO channels, which has element gain of $\mathbf{\Sigma^2}$ as

$$C = \log_2 \det(\mathbf{I} + \frac{\gamma}{N_{\mathrm{BS}}}\mathbf{\Sigma^2}), \quad (7)$$

where γ denotes signal-to-noise ratio (SNR).

3.3 Kronecker model

In outdoor NLOS environments, the correlation between the Base Station(BS) and User Terminal(UT) array elements is observed to be independent. In this case, the MIMO correlation matrix is expressed as the Kronecker product between BS and UT correlation matrices as

$$\mathbf{R}_{\mathrm{MIMO}} = \mathbf{R}_{\mathrm{BS}} \otimes \mathbf{R}_{\mathrm{UT}}. \quad (8)$$

This is the Kronecker model. Here, each element of correlation matrices can be calculated by the directivity and the normalized APS as [4],

$$R^{\alpha}_{i,j} = \int_0^{2\pi}\int_0^{\pi} E^{\alpha}_i(\theta,\phi)E^{\alpha *}_j(\theta,\phi)P^{\alpha}(\theta,\phi)\sin\theta d\theta d\phi, \quad (9)$$

where α denotes UT or BS, and i, j denotes the antenna number. Thus, from the directivity and the APS, MIMO correlation matrix can be evaluated.

By using $\mathbf{R}_{\mathrm{MIMO}}$, the channel matrix including antenna characteristics can be easily implemented in the Monte-Carlo simulation as

$$\mathrm{vec}(\mathbf{H}) = \mathbf{R}^{\frac{1}{2}}_{\mathrm{MIMO}}\mathbf{h}_{\mathrm{i.i.d.}}, \quad (10)$$

where $\mathbf{h}_{\mathrm{i.i.d.}}$ is zero mean, unit variance, complex, circular symmetric i.i.d. gaussian random vector. By repeating this loop, the average MIMO channel capacity can be obtained (See Fig.1).

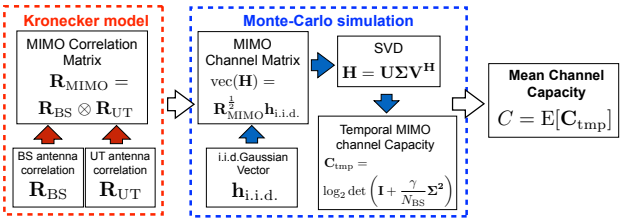

Figure 1: Block chart of channel capacity estimation

4 Extended Kronecker model

The classical Kronecker model does not include polarization [3]. In this work, the model is split into 4 independent single polarization combinations to extend the model as [3]. To simplify the model, it is assumed that vertical and horizontal polarizations have same APS and each APS is independently distributed. From these assumptions, Kronecker model can be applied to each polarization combination as

$$\mathbf{R}_{\mathrm{Vv,Vv}} = \mathbf{R}_{\mathrm{VV}} \otimes \mathbf{R}_{\mathrm{vv}}, \ \mathbf{R}_{\mathrm{Hh,Hh}} = \mathbf{R}_{\mathrm{HH}} \otimes \mathbf{R}_{\mathrm{hh}}$$
$$\mathbf{R}_{\mathrm{Vh,Vh}} = \mathbf{R}_{\mathrm{VV}} \otimes \mathbf{R}_{\mathrm{hh}}, \ \mathbf{R}_{\mathrm{Hv,Hv}} = \mathbf{R}_{\mathrm{HH}} \otimes \mathbf{R}_{\mathrm{vv}}, \quad (11)$$

where capital letters and small letters in the subscript show the polarization at BS side and UT side respectively. By considering the cross polarization ratio X, MIMO correlation matrix is expressed as

$$\tilde{\mathbf{R}}_{\mathrm{MIMO}} = \frac{X}{X+1}\mathbf{R}_{\mathrm{Vv,Vv}} + \frac{X}{X+1}\mathbf{R}_{\mathrm{Hh,Hh}} + \frac{1}{X+1}\mathbf{R}_{\mathrm{Vh,Vh}} + \frac{1}{X+1}\mathbf{R}_{\mathrm{Hv,Hv}}. \quad (12)$$

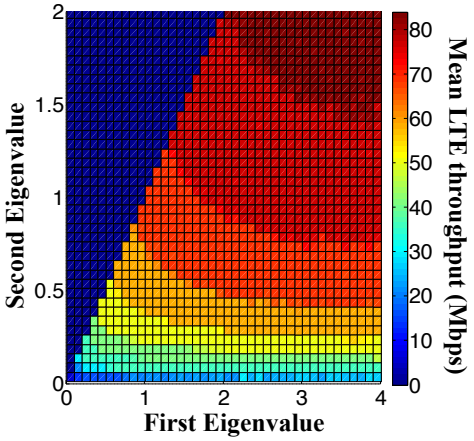

Figure 2: Eigenvalues vs. LTE throughput map (Generated by Vienna University LTE link level simulator)

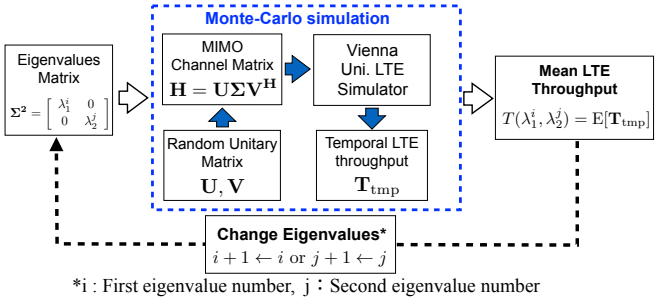

Figure 3: Block chart to bulid throughput vs. eigenvalues map

5 Throughput estimation using throughput vs. eigenvalues map

As explained above, most of throughput estimation methods are costly and time consuming, therefore there is a demand for a simple evaluation method. In this work, to satisfy this demand, it is proposed that a LTE throughput vs. eigenvalues map is generated in advance using a LTE simulator, and LTE throughput is estimated by utilizing the map in almost the same manner as the channel capacity estimation (See Fig.4).

5.1 Throughput vs. eigenvalues map

To use the proposed method, it is necessary to create the map by using a LTE simulator. In this work, Vienna University LTE link level simulator is used[5]. This is a Matlab based simulation software and free for academic usage. The procedure to make the map is shown in Fig.3.

1. Decide the target eigenvalues.
   Here, (Eigenvalue) = (Singular value)^2.
2. Make a MIMO channel matrix using the eigenvalues and random unitary matrices, and input it into the LTE simulator.
3. Calculate the temporal throughput, and repeat step 2. as a Monte-Carlo simulation to get average throughput.

Table 1: Parameter of throughput vs. eigenvalues map

LTE simulator	Vienna University LTE link level Simulator[5]
MIMO	2×2 MIMO(Open loop)
Number of user	1 (Single user)
Bandwidth	10 [MHz]
H-ARQ	No
Cyclic prefix	Normal
Channel Estimation	Soft Sphere Decoder
Cyclic prefix	Normal
Rank	2 (Fixed)
Number of trials at each eigenvalue	25
SNR normalization	14 [dB] (at $\mathrm{Tr}(\mathbf{\Sigma}^2) = 1$)

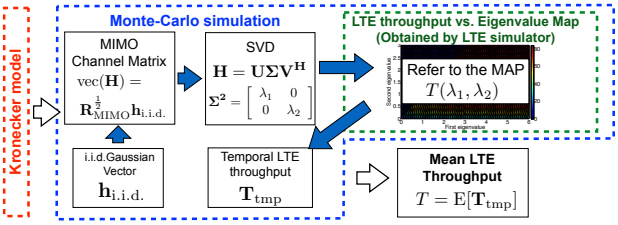

Figure 4: Block chart of LTE throughput estimation (Proposed method)

4. Save the average throughput at given eigenvalues, and change eigenvalues.

By repeating steps 1.∼4., the map can be created. The map created using Table 2 settings is shown in Fig.2.

5.2 Proposed estimation method

After making the map, it is possible to estimate LTE throughput in the same manner as the calculation of the channel capacity. The procedure is shown in Fig.4. After eigenvalues are gotten in the same manner as the channel capacity estimation, temporal LTE throughput is estimated by referring to the map.

One of the advantages of the proposed method is that once the map is created, it is not necessary to use LTE simulator which needs a long simulation time. Actually, if the map is published, it is possible to estimate LTE throughput without using LTE simulator. The disadvantage is the lack of flexibility. The throughput of the map is the average of the LTE throughput, so the evaluation must be conducted by the average value. In addition, the throughput is dependent on the simulator settings, so the new map needs to be created when those simulator parameters are changed .

5.3 Characteristics of LTE throughput and channel capacity

The process of proposed method is quite similar to the channel capacity estimation. To distinguish those parameters and show the effect of proposed method, the relation of those parameters is examined. Figure 5 shows the correlation of those parameters when the

Table 2: Simulation setting

Target antenna	Inpane, Shark
Map setting	Same as Table 2
Directivity	Measured data (Fig.6)
APS model	Taga model
Mean	10 [deg]
Standard deviation	20 [deg]
XPR	6[dB]
Average SNR	20 [dB]
Number of trials	5000

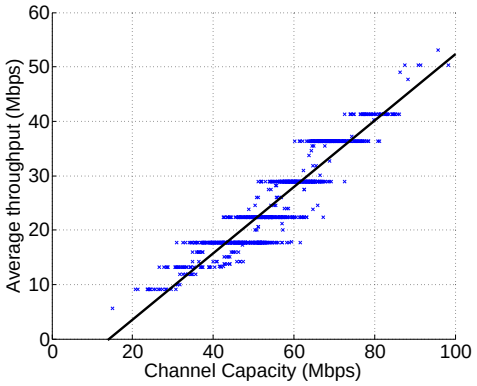

Figure 5: Correlation of Capacity and LTE throuhgput (SNR = 20dB, MIMO channel matrix : i.i.d.Gaussian)

i.i.d. gaussian channel is inputed as the MIMO channel matrix. From the figure, it is obvious that channel capacity does not correspond to LTE throughput one-to-one, actually even for the same capacity, there is about 10∼15Mbps variance in LTE throughput, so those parameters can be treated as different parameters, and from [6], it is shown that higher correlation and antenna gain imbalance of antenna make the variance larger.

Finally, 2 real MIMO antenna sets, an antenna attached on the instrumental panel of a car (called "Inpane") and an antenna attached on the roof of a car (called "Shark") , are evaluated by the channel capacity and the LTE throughput. The characteristics of the antenna sets are summarized in Fig.6. Shark has large MEG, but the antenna correlation is higher than that of Inpane. Using Table 2 settings, the channel capacity and LTE throughput are calculated as Fig.7 - Fig.8. For both measure, Shark showed better performance and correctly evaluated the MIMO antenna sets.

6 Conclusions

As a conclusion, the research has demonstrated the simpler LTE throughput estimation method, and the LTE throughput was compared with the channel capacity and showed little difference. Finally, real antennas were evaluated by both measures and showed the same tendency.

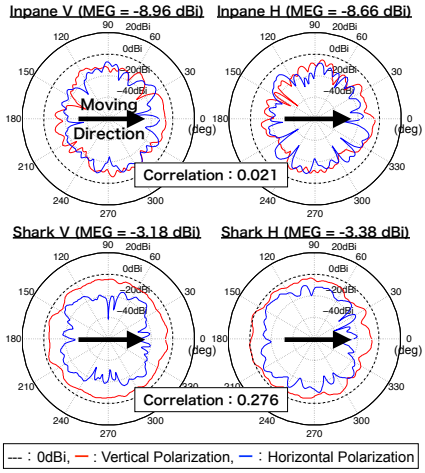

Figure 6: Characteristic of target MIMO antennas ($\theta = 0$[deg], XPR = 6[dB], and V polarization is main.)

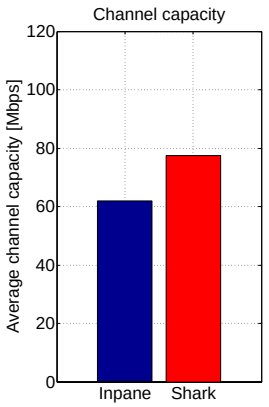

Figure 7: Simulation result (Channel capacity)

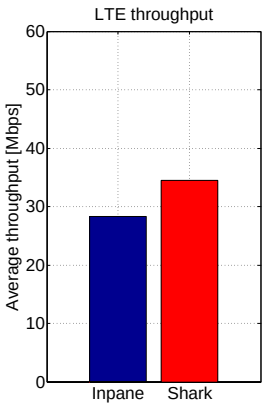

Figure 8: Simulation result (LTE throughput)

References

[1] 小川晃一, "携帯端末アンテナシステムの評価・解析・高性能化技術" , 電子情報通信学会論文誌 B, Vol. J93-B, No. 9, pp. 1100-1114, 2010.

[2] T. Taga, "Analysis for mean effective gain of mobile antennas in land mobile radio environments, " IEEE Trans. Veh.Technol., vol. 39, No. 2, pp. 117-131, May 1990.

[3] J.P. Kermoal, L. Schumacher, F. Frederiksen, and P.E. Mogensen, "Polarization diversity in MIMO radio channels: experimental validation of a stochastic model and performance assessment," Proc. 2001 Fall IEEE Veh. Tech. Conf., pp. 22-26, 2001.

[4] J. Takada, "Propagation Modeling for Performance Evaluation of MIMO Antennas," Microwave Workshop and Exhibition Digest, Yokohama, Japan, 2007, CD-ROM.

[5] C. Mehlfhrer, M. Wrulich, J. C. Ikuno, D. Bosanska and M. Rupp, "Simulating the Long Term Evolution Physical Layer," in Proc. of the 17th European Signal Processing Conference (EUSIPCO 2009), Aug. 2009, Glasgow, Scotland.

[6] 丸一 他, 信学技報, RCS2013-282, Jan. 2014.

COOPERATIVE COMMUNICATION IN NARROW-BAND WIRELESS BODY AREA NETWORK: CHANNEL AND PERFORMANCE STUDY

Student Number: 12M18287 Name: KARMA Wangchuk Supervisor: TAKADA Jun-ichi

狭帯域無線ボディエリアネットワークにおける協調伝送方式の検討

Abstract

To improve the reliability of narrow-band wireless body area network operating at 2.4 GHz ISM band, cooperative communication is proposed in this work. Using an off-the-shelve ZigBee radio transceiver multi-link channel measurements in a full mesh topology for most probable sensor node locations on the body were made. After statistically modeling these channels the performance gains due to three cooperative schemes, simple decode-and-forward relaying, cooperative decode-and-forward relaying, and incremental decode-and-forward relaying were evaluated. Performance gains in the order of 16 dB with incremental decode-and-forward relaying has been demonstrated when the statistically best cooperator was selected. These findings will be useful in actual body area network design.

1 Introduction

The continued advancements in wireless communication technology has meant it has become so ubiquitous it is now a part of our everyday lives. It is then no surprise that the versatility and mobility afforded by wireless communication technology combined with the progresses made in miniaturization of wireless transceivers and electromechanical body sensors is foreseen to revolutionize, besides others, the healthcare industry - which the finalization of the IEEE 802.15.6 BAN standard seeks to accelerate. Besides health care there is a huge opportunity for application of BAN in many different fields like sports, military, space applications, business and entertainment among others [1]. However reliability issues arising due to channel characteristics, environment, and other factors such as interference needs to be addressed.

2 Body Area Network

A network of sensors, actuators and radio transceivers communicating in the vicinity of, or inside, a human body (but not limited to humans) is defined as wireless body area network (BAN) [2]. Different from the personal area networks (PANs) BAN is characterized by the requirement of short-range, low power and highly reliable wireless communication at data rates up to 10 Mbps in close proximity to or inside a human body, all the while keeping the electromagnetic radiation into the body, given as specific absorption rate (SAR) at a safe minimum [3]. A conceptual BAN for healthcare application, in a star topology where various body sensors communicate centrally to a coordinator node which in turn connects to a network or the internet via a gateway device is illustrated in Fig.1.

2.1 BAN Challenges

The main challenges in wireless body area network arises from the fact that for it to be ubiquitously adopted the nodes should be small, comfortable and safe for the subject while being reliable at the same time. Reliability for BAN healthcare applications is vitally important [**?**]. The BAN nodes therefore must be:

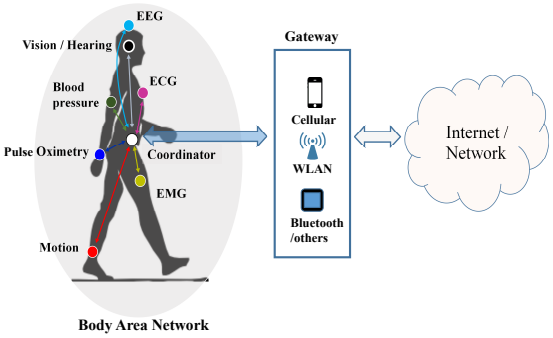

Figure 1: A conceptual BAN connected to the internet

1. Highly energy efficient: because the sensor nodes must be small, it will have small batteries that should last on the order of days to years, which in turn means low transmit power.

2. Very robust against interference: interference from Wireless LAN, Bluetooth and other sources is a huge concern especially for BAN operating at the ISM band.

3. Capable of meeting wide application requirements: depending on the application, BAN needs to support wide range of data rates ranging from 1 Kbps to 10 Mbps, while still satisfying high reliability and low-latency requirements.

4. Capable to cope with the unique characteristics of BAN channels: the affect of body, body posture and motion on radiation pattern of the transmitting and receiving antenna and on propagation of the electromagnetic waves make BAN channels very unique and difficult to characterize. This is even more complicated by the affect of the surrounding environment. Also the on-body BAN channel is dominantly slow fading and prone to burst errors [4] that can not be corrected with error correction codes of reasonable complexity.

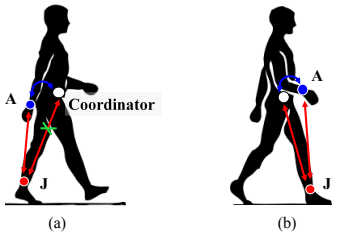

Figure 2: (a) Three node BAN showing simple relaying scenario (b) Cooperative diversity combining scenario

Given these challenges a narrow-band BAN could face severe reliability issues, which are exacerbated at ISM bands due to interference from other wireless systems. We therefore need ways to mitigate this reliability issue.

2.2 Cooperative Communication

In wireless networks, signal fading arising due to channel impairment can be mitigated through the use of diversity [5]. Space, time, and frequency diversity and the their combinations thereof have been shown to offer dramatic performance gains. In contrast to conventional from of space diversity, recently another form of diversity technique known as cooperative diversity have gained huge popularity [6] [7]. In cooperative communication a node takes advantage of the other nodes in the network to relay its message to the final destination by exploiting the broadcast nature of wireless channels. This has the effect of turning the cooperating nodes into virtual antenna arrays. Therefore the ultimate receiver receives copies of the same signal over multiple paths which can be combined using any of the diversity combining techniques such as maximal ration combining (MRC), equal gain combining (EGC) and selection combining (SC), resulting in the channel variations caused by fading, shadowing and other forms of interference to be averaged.

It has be demonstrated that cooperative diversity can provide full spatial diversity translating into greatly improved robustness to fading for the same transmit power, or dually reduced transmit power for the same performance. Power savings of up to 12 dB for outage probabilities around one in thousand has also been shown to be possible [6].

2.2.1 Motivation: Cooperative Communication in BAN

Given that a BAN is expected to have one or more sensor nodes operating in the vicinity of each other and communicating to a central coordinator, it is quite obvious that one could make the nodes cooperate and thereby exploit the possible gains from cooperative diversity. Fig.2(a) illustrates a three node BAN with coordinator located at Navel and the sensor nodes located at J:Ankle and at the A:Wrist. Now, when the node at the Ankle is trying to communicate with the coordinator node, if because of interference, environment, body motion and posture or combination of all, the link is severely attenuated that the nodes are not able to communicate, then the other node in the network at A:Wrist, could cooperate and relay the message to the coordinator. This could help improve the reliability of the network.

Figure 3: Different motion scenarios (from left-right, clockwise): descending steps, walking along the hallway, standing still, sitting and working at the desk

To take this concept further, in Fig.2(b) even when the direct link from the J:Ankle node to the Navel node is not undergoing deep fading, the node at the A:Wrist to still cooperate and forward the message to the coordinator node. At the coordinator node there are now two copies of the same signal, which could be combined using any of the diversity techniques such as MRC, EGC and SC to obtain some performance gains. As mentioned earlier the possible gains could be stated dually as: improvement in data communication reliability,such as outage probability or average error rate, at the same transmit power or reduction in the required transmit power to achieve the same reliability. In this work only decode-and-forward operation at the cooperator and SC at the coordinator are considered as these are most practical and easily implementable in current digital radio transceivers without much modification.

3 Multi-Link Channel Measurement and Channel Modeling

In order to be able to study the performance gains due to cooperative communication in 2.4 GHz BAN the channels channels between the different nodes needs to be measured and modeled. The conventional approach to measure on-body BAN channels was to use long cables and multiport Vector network analyzers (VNA) and measure the S_{12} and S_{21} transmission coefficients. However this approach severely limits the motion scenarios and environment the measurements can be made in. To overcome this in this work a channel sounder for the 2.4 GHz ISM band using off-the-shelve ZigBee transceivers was developed. With this wearable channel sounder, measurements in any environment and any motion scenarios could be made. The downside of the sounder is that phase information of the channel can not be obtained. The Fig.3 shows the four different motion scenarios considered, constituting everyday motion scenarios in a typical office environment. For health care application the major sensor nodes locations are already known, as shown in Fig.1, therefore in this

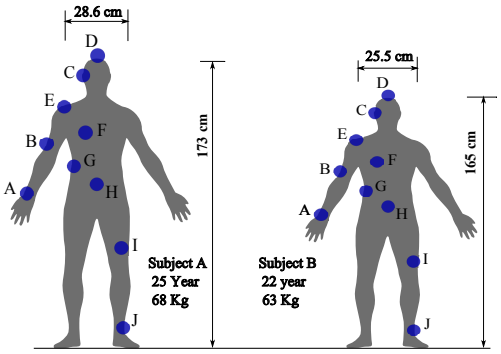

Figure 4: Subject information and node locations

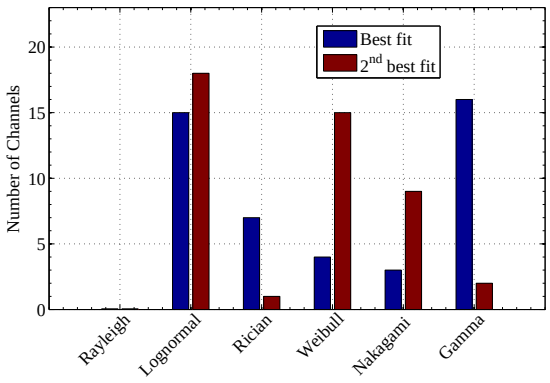

Figure 5: Number of links described by each statistical distribution

work all the possible channels between all these nodes and for few more locations in a full mesh topology were measured. The respective node location and the details of the two measurement subjects are given in Fig.4

3.0.2 Modeling

It was found that the modeling of the path-loss components of the channel as a function of distance with some path loss exponent gave large modeling errors and contradictory results. Also some of the links with longer distance had lower path loss compared to few links that were separated by shorter distance. Therefore in this work the path-loss values have been taken as deterministic values and dependent on the node position. Unlike in other wireless channels in BAN the fading component could not be separated into small scale fading and large scale fading components. This was further complicated because the effects of the antenna can not be de-embedded from the channel measurement [8]. The fading component of the BAN channel were therefore modeled as a composite of both the small scale and large scale fading. The common approach of fitting statistical distribution to the measurement data was adopted to model the fading components using log-normal distribution, Rayleigh distribution, Riciean distribution, Nakagami-m distribution, Weibull distribution and Gamma distribution.The distribution parameters were extracted using maximum likelihood estimator. For selecting the model Akaike Information Criterion with correction $AICc$ was utilized. It was found that the log-normal distribution provided the best fit or the second best fit among the different distribution considered for majority of the links. For the 45 channels fitted the results are shown in Fig.5 The final channel model consisted of deterministic path-loss component and long-normal fading component.

4 Cooperative Transmission Schemes and Performance Evaluation

For comparison four different transmission schemes: Direct transmission, Simple decode-and-forward (S-DF) relaying, Cooperative decode-and-forward (C-DF) relaying, and Incremental decode-and-forward (I-DF) relaying were evaluated. The difference between S-DF and C-DF was that in C-DF the transmission from the cooperating node and the source were combined at the coordinator using SC. MRC and EGC were not considered as the real system would only support non-coherent differential BPSK modulation as per the IEEE802.15.6 PHY specifications. In I-DF the coordinator node broadcast a request for transmission from the cooperator, such as a negative-Acknowledgment(NAK) message, when the direct transmission is received in failure. The cooperator then retransmits the message it received from the source. For illustration the equivalent channel for I-DF relaying is shown in Fig.6

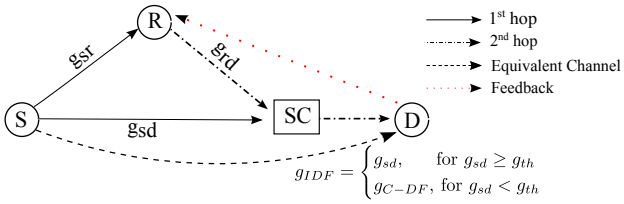

Figure 6: Equivalent channel for I-DF relaying

4.1 Performance Gain

As performance measure we focused on SNR-outage probability give as:

$$P_{out} = \int_0^{\gamma_{th}} p_\gamma(\gamma) d\gamma \quad (1)$$

where γ is the instantaneous received SNR. For equal power transmission at all the nodes (1) is in fact the value of cumulative distribution function (CDF) of the channel gain, substituting g for γ and g_{th} for γ_{th}.In this work this is referred to as SNR-outage performance to differentiate from the rate outage probability commonly used to compare the efficiency of different cooperative schemes. After comparing the SNR-outage probability due to the statistically best cooperator, not surprisingly the I-DF gave greater performance gain compared to the S-DF and the C-DF as seen in Fig.7. The gains due to C-DF and S-DF when employing the best cooperator are not very different, especially when the S-DF equivalent channel is better than the direct channel. It can therefore be concluded that the gains are mainly because of improvement in path loss due to relaying and not due to diversity combining. From Fig.7 it is also clear that on average there is always some gain due to cooperative communication. For instance with I-DF relaying for any destination (or coordinator) location there is on average a minimum of 5.58 dB gain over direct transmission and 5.52 dB average gain over direct transmission

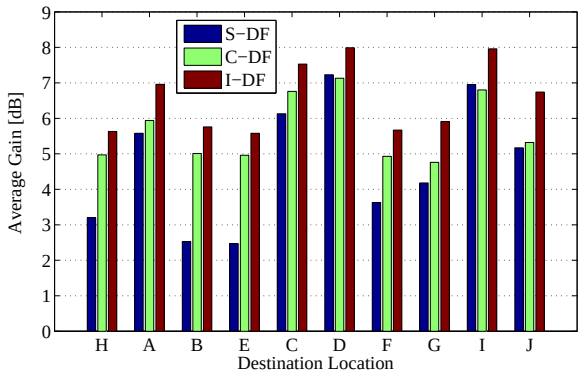

Figure 7: Average gain with best cooperator for different destination locations (at 10% outage probability)

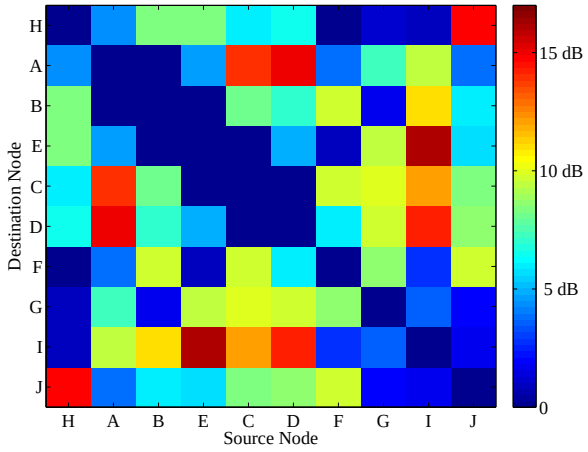

Figure 8: I-DF relaying gain with best cooperator at 10% outage probability

for any source location. On checking the improvement in the outage threshold at 10% outage with all schemes, the threshold was the highest when the destination node was located at E: Shoulder. This suggests that if cooperative communication is employed in BAN the best position for the coordinator node or the hub is at the shoulder.

In Fig.8 the gains due to I-DF with best cooperator for all combination of source, cooperator, destination node is shown in It is clear that with carefully selected cooperator there are almost up to 16 dB gains to be had at 10% outage probability.

5 Conclusions and Future Research

In this work its has been demonstrated that in a BAN with realistically located sensor nodes by employing cooperative communication there is substantial performance gains in terms of improvement in outage threshold which would directly translate into SNR or transmit power, or equivalently the reliability. Up to 16 dB improvement in the outage threshold at 10% outage probability and a minimum of 5.58 dB average gain for any coordinator node location can be achieved with I-DF relaying. The best location for the coordinator node is the shoulder. With carefully chosen cooperator reliability can be greatly improved in a BAN with cooperative communication.

Future Research

Evaluating the gains and the energy consumptions due to cooperative communication in BAN based on actual hardware would be very useful. Actual implementation of cooperative communication would require more careful considerations not just in the PHY layer but also upper layers of communication protocol. Cross layer optimization of transmission schemes would be a challenging and useful area of future work.

References

[1] M. Chen, S. Gonzalez, A. Vasilakos, H. Cao, and V. C. M. Leung, "Body Area Networks: A Survey," *Mobile Networks and Applications*, vol. 16, pp. 171–193, Aug. 2010.

[2] *802.15.6-2012 - IEEE Standard for Local and metropolitan area networks - Part 15.6: Wireless Body Area Networks*. No. February, 2012.

[3] TG6-draft, "IEEE802.15-10-0245-06-0006," 2010.

[4] M. Kim and J. Takada, "Experimental investigation and modeling of shadow fading by human movement on body surface propagation channel," in *2009 IEEE Antennas and Propagation Society International Symposium*, pp. 1–4, IEEE, June 2009.

[5] J. Proakis, *Digital Communications*. McGraw-Hill Book Company, 2nd ed., 1989.

[6] J. N. Laneman, *Cooperative Diversity in Wireless Networks : Algorithms and Architectures*. PhD thesis, Massachusetts Institute of Technology, 2002.

[7] A. Sendonaris, E. Erkip, and B. Aazhang, "User cooperation diversity-part II: implementation aspects and performance analysis," *IEEE Transactions on Communications*, vol. 51, pp. 1939–1948, Nov. 2003.

[8] J. Takada, T. Aoyagi, K. Takizawa, N. Katayama, T. Kobayashi, K. Y. Yazdandoost, H. Li and R. Kohno, "Static Propagation and Channel Models in Body Area," in *Cooperation in Science and Technology (COST)*, (Lille, France), 2008.